ABSTRACT

ELLWEIN, LAURA MARIE. Cardiovascular and Respiratory Regulation, Modeling and Parameter Estimation. (Under the direction of Mette Sofie Olufsen.)

Short-term cardiovascular responses to postural and carbon dioxide challenges involve complex interactions between global and local regulatory mechanisms, which regulate blood pressure and perfusion. Mathematical models can be used to extract clinical markers that characterize these interactions which cannot be assessed noninvasively. To predict one such marker, cerebrovascular resistance, we present several lumped parameter compartmental models that can analyze dynamic changes in beat-to-beat arterial blood pressure, middle cerebral artery blood flow, and expiratory partial pressure of carbon dioxide. The cardiovascular submodels utilize compartments to describe blood pressure, blood flow, compliance, and resistance in the heart and systemic circulation. The respiratory submodel contains compartments describing tissue and pulmonary gas concentrations. Results of studies using models predicting postural change from sitting to standing showed that it is possible to predict cerebrovascular resistance, yet these studies did not allow unique identification of this physiological quantity.

The size and complexity of the compartmental models discussed above led us to develop novel tools for more certain estimation of model parameters, including cerebrovascular resistance. To do so we combined nonlinear optimization with sensitivity analysis and subset selection. Sensitivity analysis allowed us to rank candidate parameters from the most to least sensitive, with the most sensitive parameters retained during model reduction. Subset selection was used to identify a set of independent candidate parameters that can be estimated given limited data. Combining these tools allowed us to choose a set of sensitive and identifiable parameters that could be estimated using nonlinear optimization. Using these two tools we were able to quantify cerebrovascular resistance (among other parameters), and showed as expected that resistance is increased in healthy aging.

Cardiovascular and Respiratory Regulation, Modeling and Parameter Estimation

by
Laura Marie Ellwein

A dissertation submitted to the Graduate Faculty of
North Carolina State University
in partial fullfillment of the
requirements for the Degree of
Doctor of Philosophy

Applied Mathematics

Raleigh, North Carolina

2008

APPROVED BY:

Dr. C. Tim Kelley	Dr. Vera Novak
Dr. Mette S. Olufsen Chair of Advisory Committee	Dr. Hien Tran

DEDICATION

This work is dedicated to my parents and my grandmother for having faith that I could accomplish anything.

BIOGRAPHY

Laura Marie Ellwein was born and raised in Milwaukee, Wisconsin. She always enjoyed mathematics, competing in math competitions from grade school through high school. She graduated from the University of Wisconsin - Madison in 1999 with a BS in chemical engineering. After graduating, she spent four years at General Mills in Iowa and Illinois as a quality engineer. A series of events led her to leave the corporate life to enroll in graduate school in applied mathematics at North Carolina State University (NCSU) in 2003. She developed a specific interest in applications in cardiovascular fluid dynamics which led to an interdisciplinary concentration in physiology.

Laura has made the most of her five years away from the Midwest both in her academic career and extracurricular activities. She was an active member of the Research Group on Heart-Brain Control Systems which gave her opportunities for participating in workshops in Denmark and Austria. She was invited to present her work at international conferences in San Diego and Philadelphia. The summers gave Laura opportunities for training fellowships at Harvard Medical school and Merck and Co. Inc., as well as mentoring roles as part of the NCSU Research Experience for Undergraduates. When not in pursuit of her academic path, Laura participated in the Raleigh Ringers, a critically acclaimed handbell choir, and attended Resurrection Lutheran Church, where she found a second family. After completing her PhD, she will return to her hometown of Milwaukee for a postdoctoral research position in the biomedical engineering department at Marquette University.

ACKNOWLEDGMENTS

I first must wholeheartedly thank my advisor, Dr. Mette Olufsen. In ways that I still do not fully understand, she perfected the gift of pushing me when I needed it and encouraging me during the toughest parts of the journey. Through her I had amazing opportunities made available to me, including overseas travel and summer internships.

Thank you also to each member of my committee: Dr. Novak, my invaluable physiology expert; Dr. Kelley, who supported computational aspects of my work; and Dr. Tran, who gave great insight into every aspect of my studies. Further I would like to acknowledge the support I received from SAMSI, NSF, NIH (through my training fellowship at Harvard Medical School) and the mathematics department at NCSU during my graduate career.

The data used in my studies were made available came from the laboratories of Dr. Novak, Beth Israel Deaconness Medical Center, Boston; Dr. Lipsitz, Hebrew Rehabilitation Center, Boston; and Dr. Xie, University of Wisconsin. Without their data this work would have not been possible.

My success would not have been as great without the help of others. I am grateful for the contributions of Cheryl Zapata, an exceptional undergraduate student, and Scott Pope, a fellow graduate student and my primary numerical expert. Thanks also go to Dr. Ottesen, Roskilde University, Denmark, and Dr. Heldt, Massachusetts Institute of Technology, for discussions on development of heart models and subset selection. Finally, special thanks go to Dr. Batzel, University of Graz, Austria, my best resource on respiratory regulation.

Finally, I would like to thank all my friends in the math department. Those that went before me showed me the ropes and proved that it was indeed possible to finish. Those that experienced it with me were there during classes, qualifying and preliminary exams, and through to the end, not to mention football, beach trips, and general good times. I cannot imagine my time here without this support system. I especially acknowledge my friend and wonderful roommate Sarah (Grove) Muccio who was a blessing through my time here at NCSU.

And finally, many thanks to all of family, who supported me not only during my graduate studies but also in all of my life endeavors.

TABLE OF CONTENTS

LIST OF TABLES

LIST OF FIGURES

Chapter 1

Introduction

During the last decades a large number of lumped parameter differential equations models have been developed to study dynamics and control of the cardiovascular system, see e.g., [43], [73], [74], [77], [78], [93], and [109]. Typically, these models predict blood pressure and flow in and between compartments using electrical circuits with capacitors and resistors. In recent years the complexity of these models has increased to more accurately account for the underlying physiological dynamics. For example complex nonlinear models have been developed to describe the pulsatile pumping of the heart, e.g., [22], [74], and [79], and the blood flow and pressure regulation, [39], [72], [74], and [109]. Modelers often praise these models for their complexity and biological relevance, while experimentalists criticize the same models for being of little use for prediction.

One of the main problems is that it is difficult using large comprehensive models to identify model parameters and compare these over several datasets. These complex nonlinear models often include hundreds of parameters, While physiological knowledge can be used to determine nominal values for some of these parameters, several parameters can only be estimated based on observations from animal studies, and some parameters cannot be determined at all. Simulations using nominal parameter values may provide insight into the overall model dynamics and the behavior for a given group of subjects, but since physiological properties are known to vary significantly between subjects, such simulations cannot provide patient specific information. Standard deviations in parameters can be large, in particular because such models often contain insensitive and interdependent parameters that hamper parameter estimation.

In these studies, we focus on developing lumped-parameter compartmental mod-

els of the cardiovascular and respiratory systems in order to analyze the dynamics of blood pressure and flow regulation under several test conditions. Our models predict dynamics of cerebral blood flow velocity, arterial blood pressure, and expiratory carbon dioxide levels for individual subjects using patient-specific model parameters. Parameter values are estimated using standard nonlinear least-squares optimization methods including direct search and gradient-based algorithms. For large models such as those described in these studies, nonlinear optimization can be both computationally costly and doesn't guarantee unique parameter values. To address these issues we seek to reduce the parameter space of each model by using a combination of sensitivity analysis, which examines the impact of individual parameters on the model solution, and subset selection, which identifies parameter dependencies.

In Chapter 2 we introduce the physiological background necessary for developing our models. General model components and parameter estimation methods are developed in Chapter 3. Chapter 5 presents an 11-compartment cardiovascular model designed to predict blood pressure and flow dynamics during a postural change from sitting to standing. Sensitivity analysis is used to reduce the model for analysis of the sitting portion of the data. Subset selection is introduced in Chapter 6. This chapter uses subset selection and sensitivity analysis to estimate 5 parameters in a 5-compartment model. Parameters are estimated using cerebral blood flow and finger blood pressure data from 24 healthy young and healthy elderly subjects. Finally, the respiratory system is added to the model in Chapter 7 as a first attempt towards modeling the effect of CO_2 challenges on cardiovascular dynamics.

Chapter 2

Physiological Background

In this chapter we present an overview of the physiology involved in modeling cerebrovascular control. General information comes from Boron and Boulpaep [13], Berne and Levy [11], and Smith and Kampine [103]. Sections 2.1 and 2.2 dicuss the relevant features of the cardiovascular and respiratory systems, and Section 2.3 discusses generally accepted control mechanisms.

2.1 Cardiovascular System

The cardiovascular system forms a closed network with arteries, veins, and capillaries, connected by the heart. The system can be separated into two parts, the systemic circulation and the pulmonary circulation. They are connected by the heart which generates the blood pressure differential for each system necessary to drive blood through the system, see Figures 2.1 and 2.2. In the systemic circulation, oxygen-rich blood is pumped from the left ventricle at pressures between 80 and 120 mmHg. Blood is transported by the systemic arteries to the systemic capillary bed, where oxygen (O_2) and nutrients diffuse across the capillaries into the tissues while carbon dioxide (CO_2) and other metabolites diffuse in the reverse direction into the bloodstream. Subsequently, the blood is transported to the right atrium by the systemic veins. As blood travels from the arteries to the veins, the pressure falls to $\sim$5 mmHg [13], see Figures 2.1 and 2.2A.

In contrast to the systemic circulation, the pulmonary system operates at relatively low pressure, with a right ventricular pressure of $\sim$25 mmHg and venous pressures at $\sim$3 mmHg, see Figure 2.2B. Carbon dioxide rich blood ejected from the right ventricle flows

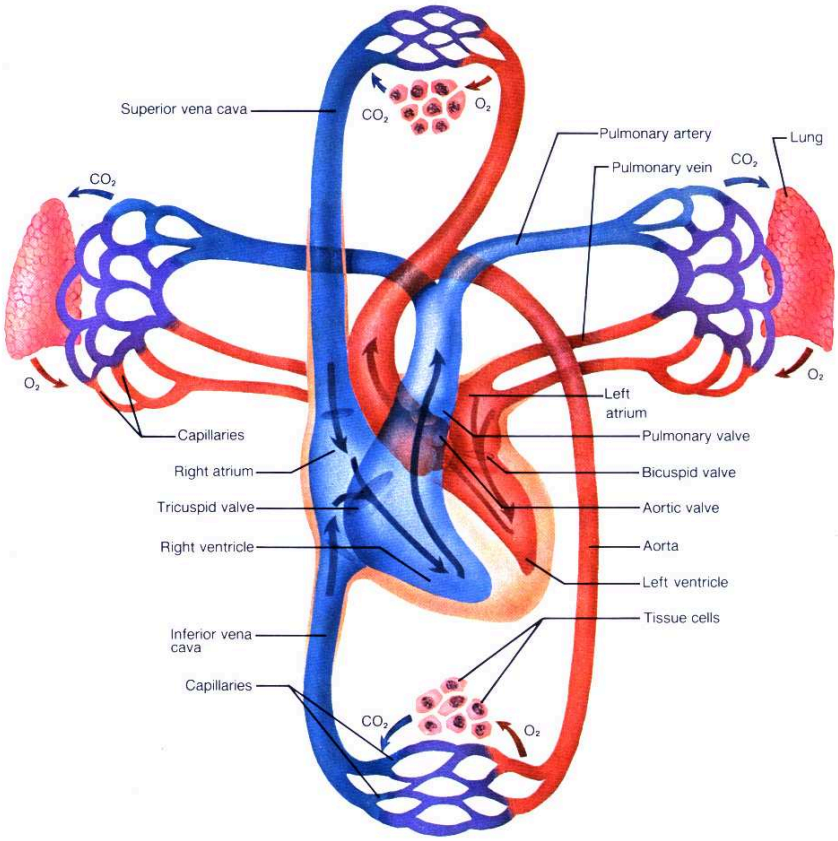

Figure 2.1: Blood flows from the left ventricle through the systemic arteries and veins to the right atrium. It is ejected from the right ventricle and pumped through the pulmonary circulation back to the left atrium. Systemic arteries and pulmonary veins contain O_2-rich, CO_2-poor blood, while systemic veins and pulmonary arteries are low in O_2 and high in CO_2. Reprinted from [32].

through the pulmonary arteries to the pulmonary capillary bed, where CO_2 diffuses into the lungs for expiration and inspired O_2 diffuses into the capillaries. The oxygenated blood flows through the pulmonary veins back to the left atrium to re-enter the systemic circulation.

The greatest proportion of total blood volume resides in the systemic veins, about 64%. The systemic circulation as a whole carries 84% of total blood volume, the pulmonary circulation 9%, and the heart 7% [36]. Veins act as the storage vessels and the arteries function to regulate pressure and flow to the capillaries. The distensibility of vessels results in changes in vessel volume in response to pressure changes. Total blood volume in a typical 70 kg man is $\sim$5 liters.

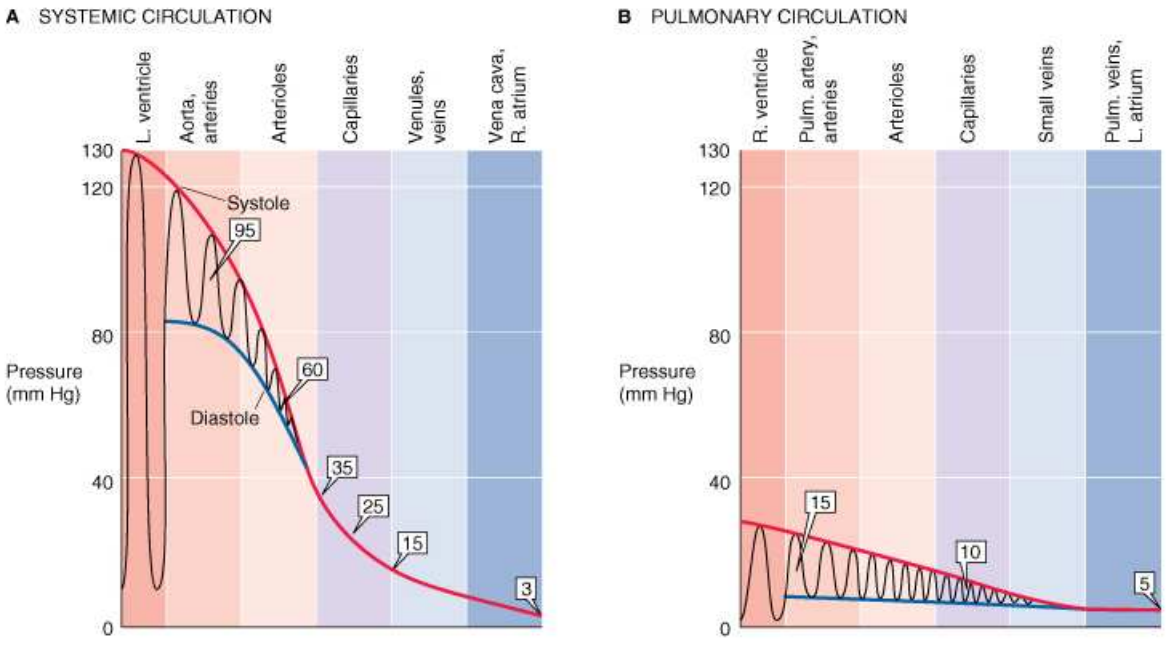

Figure 2.2: A: Typical pressures n the systemic circulation. Note, mean pressure decreases exponentially. B: Typical pressure in the pulmonary circulation. Mean pressure decreases linearly. Reprinted from [13]. ©Elsevier Ltd. Boron and Boulpaep; Medical Physiology, Updated Edition.

In this study we develop cardiovascular models representing the entire system discussed above. Our models present the cardiovascular system using compartmental models in which all vessels in a particular portion of the circulation are lumped together as one unit and are assumed to have the same characteristics. All compartments are considered to be spatially homogenous but have dynamic volumes and pressures. Each model has high pressure arterial compartments and low pressure venous compartments, connected in a closed loop by at least one cardiac compartment. Metabolite exchange occurs in tissue and lung compartments connecting arterial and venous components.

2.1.1 Heart

The heart is divided into four chambers, two each for the left and right hearts, which feed into the systemic and pulmonary systems respectively, see Figures 2.1 and 2.3. Each side of the heart consists of an atrium and a ventricle, the former acting as a primer for the latter. The two sides of the heart output the same volume of blood per unit time,

called the cardiac output (CO) [ml/s]. Valves at the inlet and outlet of the ventricles allow pressure to build up within the ventricles and prevent back-flow of blood. Atrioventricular valves separate the atria and the ventricles and semilunar valves are located at the exit of the ventricles. In the left ventricle these are named the mitral and aortic valves, and in the right ventricle they are the tricuspid and pulmonary valves.

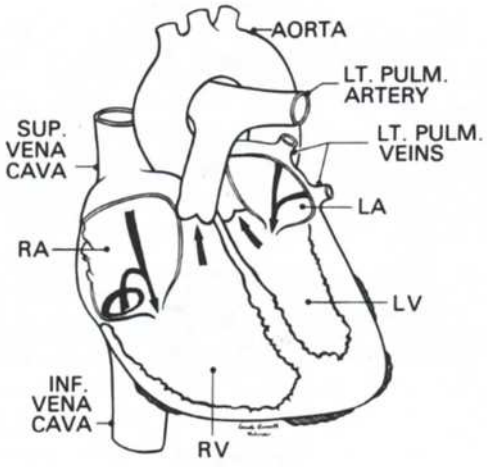

Figure 2.3: The four chambers of the heart and connecting vessels. LA: left atrium. LV: left ventricle. RA: right atrium. RV: right ventricle. SUP: superior. INF: inferior. LT: left. Reprinted from [103].

The heart chambers work in synchrony due to the electrical coupling of the cardiac muscle fibers. All cardiac cells have intrinsic pacemaker ability, i.e., they are able to spontaneously generate nerve impulses. In healthy individuals it is primarily the sinoatrial node cells that play the pacemaker role. The interior of these cells spontaneously grows less negative than at rest, causing the cell membrane to depolarize. At a threshold level of depolarization, an action potential is generated which causes the concentration of intracellular calcium to increase, precipitating cardiac muscle cell contraction. The electrocardiogram (ECG) measures the dynamical changes in the electrical activity of the heart. It is comprised of the P wave, the QRS complex, and the T wave, each corresponding to portions of the cardiac cycle, see Figure 2.4. The upward P wave is caused by depolarization of the atria, marking the start of atrial contraction. Ventricular depolarization marking the onset of ventricular contraction is seen in the QRS complex, a combination of upward and downward waves caused by the spread of electrical current throughout ventricles in several directions. Finally, the T wave represents repolarization of ventricular cells marking the be-

ginning of the relaxation phase of the cardiac cycle. A complete cardiac cycle typically lasts 0.8 s. This corresponds to an average heart rate of 75 beats/min [13, 103]. It is typically measured as the timespan between two R waves on the ECG, called the R-R interval.

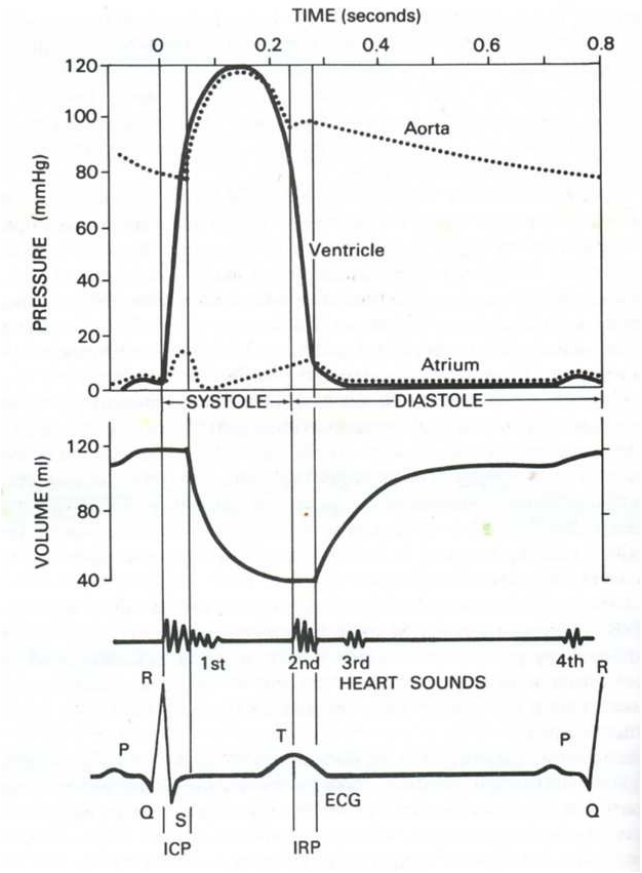

Figure 2.4: Diagram of a typical cardiac cycle. The top graphs show the pressures in the left ventricle, the left atrium, and the aorta. The middle graph shows the ventricular volume. The bottom graph shows the ECG. In addition, heart sounds are shown between the middle and bottom graphs. Note that both valves are closed during the isovolumic contraction period (ICP) and the isovolumic relaxation period (IRP). Reprinted from [103].

At the onset of the cardiac cycle, at a volume of about 50 ml, the aortic valve is closed while the mitral valve is open, allowing blood to enter the left ventricle at a low pressure, see Figures 2.4 and 2.5. At the end of ventricular filling, at about 120 ml, the ventricular muscle contracts to raise the pressure inside the ventricle. As the ventricular pressure exceeds that of the atrium, the mitral valve closes. Ventricular contraction continues to increase ventricular pressure until it exceeds pressure in the aorta, causing the aortic

valve to open and blood to be ejected into the aorta. The aortic valve closes when the pressure in the aorta exceeds that in the ventricle. At this point the majority of the blood has been ejected. After a period of ventricular relaxation at low ventricular volume the cardiac cycle is completed. The contraction and ejection phases comprise systole, whereas the relaxation and filling are called diastole. It should be noted that for healthy individuals at no time are both valves open. The dynamics of the right ventricle mirrors that of the left ventricle except the systolic pressure is about 25 mmHg [13, 36].

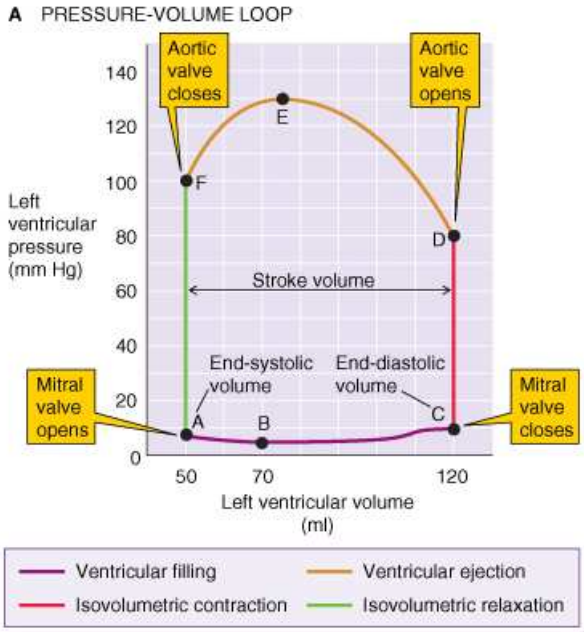

Figure 2.5: Pressure-volume loop showing the four phases of the cardiac cycle. Line segments represent AC: diastole, CD: contraction, DF: systole, FA: relaxation. Reprinted from [13], ©Elsevier Ltd. Boron and Boulpaep; Medical Physiology, Updated Edition.

In this study we derive and discuss a number of heart models developed to predict ventricular pressure using an activation function. Each of these models has at least one ventricular component for generation of the pressure differential necessary for blood flow. An atrial component may be included as well, which increases accuracy of the model but also introduces complexity. Valves must be included so we generate the pressure and volume changes that occur during the cardiac cycle. Because the two sides of the heart operate together, we model them with the same timing. Finally knowing the standard ventricular pressures and volumes allows us to parameterize and validate the cardiac models accordingly.

2.1.2 Vasculature

Blood vessels are composed of elastin, smooth muscle cells, collagen, and endothelial cells. The aorta and large arteries have the highest elastin content of all the vessels, making them the most distensible. All arteries contain some amount of elastin, but the proportion decreases as the arteries decrease in diameter closer to the tissue. The arterioles have the highest proportion of vascular smooth muscle cells, which have the ability to contract in response to stimulation from the nervous system. This creates active tension which causes the arterioles to constrict, thereby increasing the resistance to blood flow. Hence the arterioles are often referred to as "resistance vessels" [13], while larger arteries are referred to as "conduit vessels". Both arteries and veins branch in a bifurcating tree-like structure before reaching the capillary bed for a given tissue. The number of vessels and the total cross-sectional area of the vasculature increases exponentially as blood travels toward capillaries, see Figure 2.6.

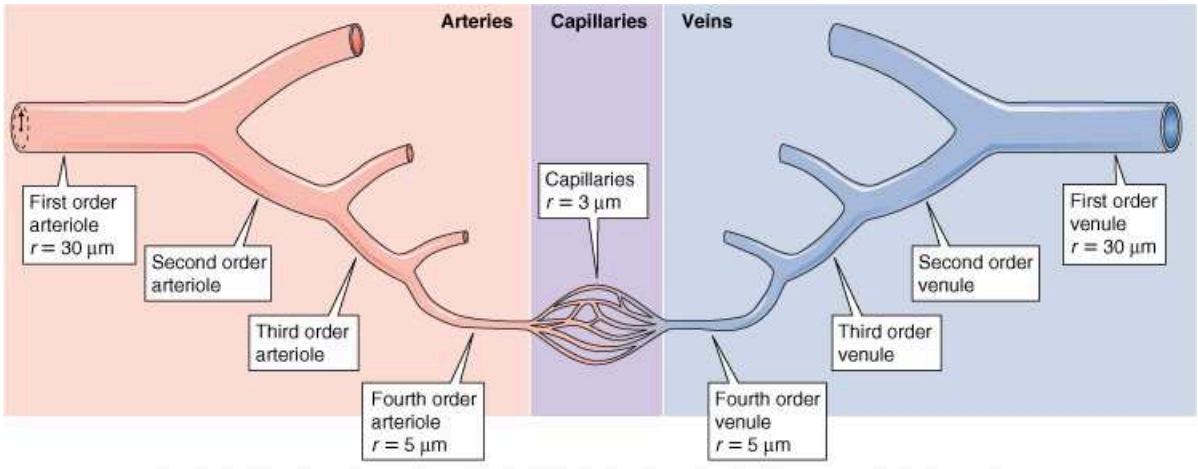

Figure 2.6: Branching structure of a typical vascular bed. Reprinted from [13], ©Elsevier Ltd. Boron and Boulpaep; Medical Physiology, Updated Edition.

The systemic capillaries receive blood from the arterioles for distribution throughout the tissues. Their vessel wall is thin, made up mostly of endothelial cells. A single capillary is just wide enough to accommodate individual red blood cells (about 2-5μm) carrying metabolites, with the blood flowing at a relatively slow rate. This combination of factors allows for the easy diffusion of metabolites between the capillaries and tissue [11]. Unlike the arteries, the network of capillaries forms a mesh-like structure, see Figure 2.6.

The primary function of the systemic veins is to act as a conduit for metabolite removal from the tissues. The veins are primarily collagen, a non-elastic connective tissue protein that only stretches about 3-4% [13]. Their high compliance, i.e., ability to store a large volume of blood while incurring only minimal pressure change, gives them the name "capacitance vessels" [13]. They grow into a branching structure reversed from that of the arterial tree, see Figure 2.6. As blood volume and pressure decreases, veins undergo a shape change from circular to eliptic, and at very low pressures they may completely collapse. Similarly, as blood volume and pressure increase the veins become circular, increasing the cross-sectional area of the vessel without changing its circumference. A rounded vein does not stretch due to the contribution of the stiff collagen to the vessel wall tension. This gives the veins an apparent compliance that at low volumes and pressures occurs not because of any change in wall tension but purely as a result of a change in geometry. At high pressures, however, the stiffer collagen causes the wall tension to rise sharply and the vein to appear uncompliant, see Figure 2.7.

The differences in vessel composition guide our modeling efforts. All vessel components have a characterizing resistance and compliance which may change as a result of active vasoregulation. Components representing the arterioles are modeled using a dynamic resistance regulated in response to changes in pressure or CO_2 concentrations. Similarly the veins are modeled using dynamic compliances.

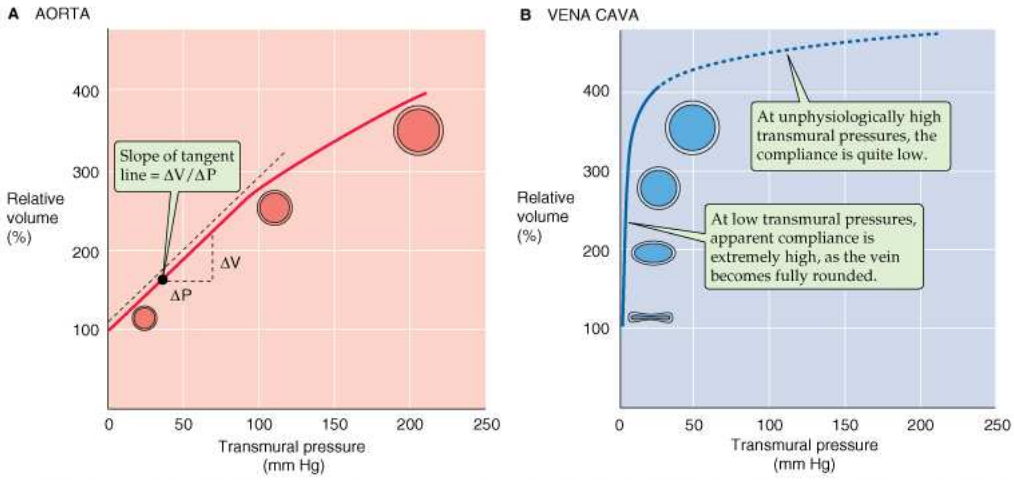

Figure 2.7: Compliance in the aorta (A) and the vena cava (B) depicted as relative volume percentage with respect to transmural pressure. Reprinted from [13], ©Elsevier Ltd. Boron and Boulpaep; Medical Physiology, Updated Edition.

2.2 Respiratory system

The respiratory system transports gases between the environment and the tissues, see Figure 2.10. At the start of the respiratory cycle, air consisting of approximately 21% O_2 and 79% nitrogen (N_2) and a trace amount of CO_2 is inspired through the nose and mouth. The circulatory system transports the gases either carried by red blood cells or dissolved in the blood plasma. The O_2-rich air travels through the branches of the lungs to the alveoli, the gas exchange sites in the lungs. Their close contact with the pulmonary capillaries allows for O_2 diffusion into the capillary bed. O_2-rich (CO_2-poor) blood flows from the pulmonary veins through the left heart and systemic arteries to the systemic tissue capillary beds. From there O_2 diffuses from the systemic capillaries to the cells, with CO_2 diffusing from the cells to the capillaries for removal. Systemic veins carry the O_2-poor (CO_2-rich) blood back through the right heart and pulmonary arteries to the lungs, where CO_2 diffuses out of the capillaries back to the alveoli. This CO_2-rich gaseous mixture is expelled back through the lung airways during expiration. In these studies we model the dynamics of O_2 and CO_2, ignoring inert gases such as N_2 that are not metabolized.

2.2.1 Lungs

The lungs provide a pathway for gas exchange between the external atmosphere and the circulatory system. Air enters the single trachea and flows into multiple bronchi, both types of airways consisting of cartilage. At about generation 11, the airways are free of cartilage as they turn into bronchioles. Alveoli start to appear on the bronchioles around generation 16 and continue to increase in frequency until the branches are made up entirely of alveolar sacs. The lung airways branch to approximately 23 generations before the alveolar sacs [13], see Figure 2.8. The conducting airways, i.e., those that do not participate in gas exchange, are designated as anatomical dead space V_D [ml]. The volume of the dead space in milliliters for a given person is approximately equal to their weight in pounds [11], which for a normal 70 kg (154 lb) man is approximately 150 ml. This is small compared to the total lung capacity of about 6 liters [11, 13]. The amount of air inhaled in one breath is called the tidal volume V_T [ml] and is about 500 ml [13]. Formulas for these volumes as functions of anthropometric data can be found in the review by Stocks and Quanjer [106].

Lung muscles drive the pumping action required for inspiration. Inspiration is

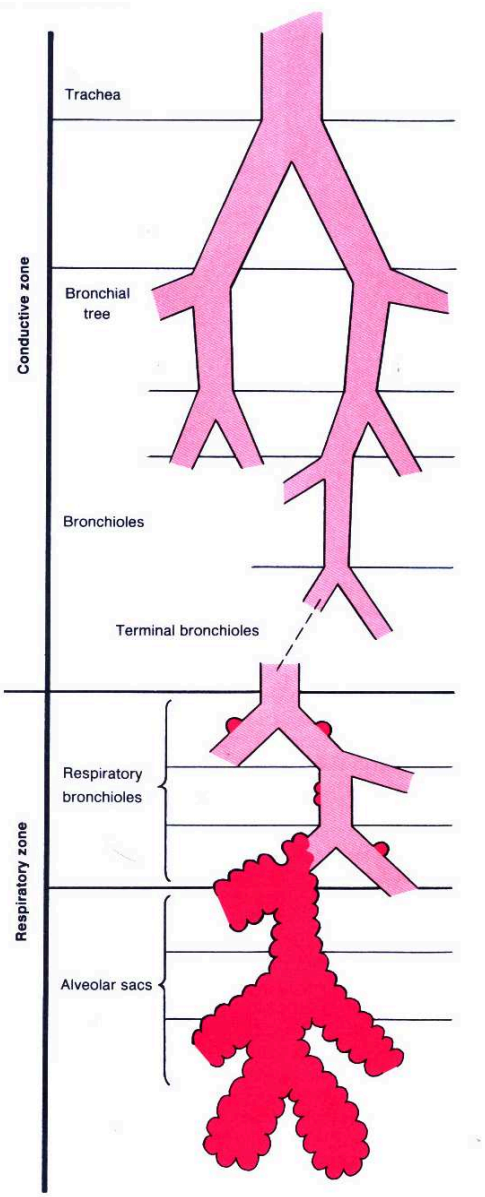

Figure 2.8: Diagram of the branching structure of the lungs. The airways in the conducting zone are primarily cartilage. Those in the respiratory zone are made up of alveolar sacs and participate in gas exchange. Reprinted from Fox [32].

driven actively by the contraction of the diaphragm and external intercostal muscles, see Figure 2.9. Contraction stimulated by the phrenic and spinal nerves causes the diaphragm to move downwards towards the abdomen and the external intercostals to stabilize and rotate the ribs, thus increasing the volume and lowering the pressure in the intrathoracic

cavity between the chest cavity and the lungs. The pressure in the intrathoracic cavity reflects the pressure in the intrapleural space between the two pleural membranes. The lower pressure in the intrathoracic cavity creates a vacuum which draws air into the alveoli. Forced inspiration recruits additional secondary muscles. In contrast, relaxed exhalation is purely a passive process and occurs when the inspiratory muscles relax and return to their resting positions.

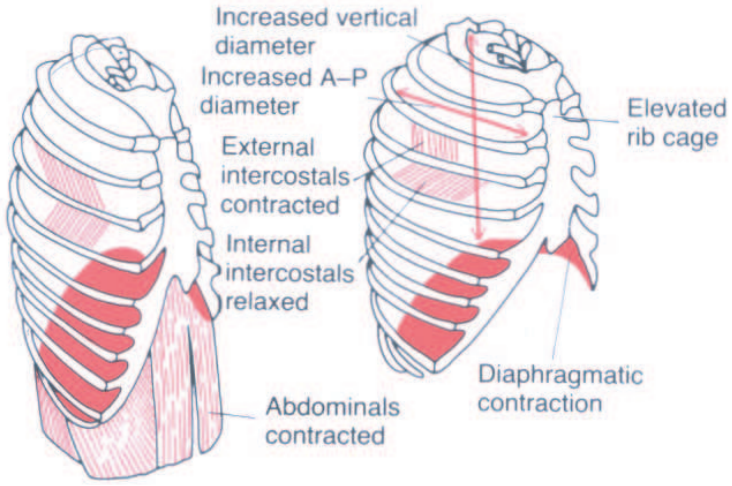

Figure 2.9: Muscle activity during the respiratory cycle. During inspiration, the diaphragm and external intercostal muscles contract, and the internal intercostals relax. As a result, the vertical and anterior-posterior (A-P) diameters of the lung cavity increase, and the rib cage elevates. Reprinted from Guyton [36].

Though we do not model the complex geometry of the lungs, it is important to understand the different lung components. The alveoli change volume during the respiratory cycle, suggesting a model of the alveolar compartment with dynamic volume. In contrast, a fixed volume is appropriate for a model of the dead space given that these airways are composed of rigid cartilage. Literature values for lung volumes aid in the parameterization of the model. The movement of the diaphragm and corresponding changes in alveolar volume account for respiratory effects on vascular pressure changes.

2.2.2 Gas transport

In order to model the dynamics of CO_2 and O_2 we discuss the fundamentals of gas transport in the circulation. The two gases behave as ideal gases in vapor form, but their concentrations in blood are highly dependent on their solubility and their affinity for

hemoglobin (Hb), a protein in red blood cells. We first present the standards for measuring gas concentrations in vapor and follow with a description of the primary transport mechanisms for CO_2 and O_2 in blood.

The fraction of gas in a gaseous mixture is usually expressed as a partial pressure p_{gas}, defined as the pressure a quantity of gas would have if it filled its volume void of any other gases. Dalton's Law states that each of the partial pressures in a mixture add up to the total pressure exerted by the mixture, therefore the partial pressures of O_2, CO_2, N_2, and water vapor add up to atmospheric pressure, 760 mmHg. As air travels into the nasal passages it becomes humidified to 100% humidity, i.e., partial pressure of water at 47 mmHg, and warmed to 37^{O} (300 K), conditions known as BTPS, "body-temperature-pressure-saturated". Other measurement conditions include ATPS, "ambient-temperature-pressure-saturate", for expired air saturated with water vapor at atmospheric pressure that has cooled to the ambient temperature, and STPD, "standard-temperature-pressure-dry", for air at 0^{O}C (273 K), atmospheric pressure, with no water vapor. Respiratory quantities are conventionally reported under a variety conditions so conversions for model calculations are made as needed.

The gas fraction in blood is expressed as a concentration c_{gas} [$\mathrm{ml}_{gas}/\mathrm{ml}_{blood}$]. To a first approximation, the volume of gas dissolved in the blood is proportional to p_{gas} [mmHg]. If p_{gas} increases, c_{gas} will increase proportionally. This is known as Henry's law,

$$p_{gas} = kc_{gas}, \tag{2.1}$$

where k is the Henry's Law constant dependent on the type and temperature of the solvent, i.e., the solubility. The concentration of CO_2 in blood closely follows Henry's law due to its high solubility. Carbon dioxide exists in equilibrium with other compounds, as seen for example with carbonic acid in the CO_2 hydration reaction

$$\mathrm{CO_2}+\mathrm{H_2O} \rightleftharpoons \mathrm{H_2CO_3} \rightleftharpoons \mathrm{H^+}+\mathrm{HCO_3^-}. \tag{2.2}$$

Oxygen is transported primarily by Hb, therefore the amount of O_2 in blood is highly dependent on its affinity to Hb. Because Henry's law only addresses concentration of dissolved gases, it does not accurately reflect the total concentration $c_{O_2,total}$ of O_2 present in the blood. The relationship between p_{O_2} and $c_{O_2,total}$ must be treated as nonlinear for O_2.

We assume in our modeling efforts that concentrations of CO_2 and O_2 are independent of each other. In reality, the saturation level of Hb with O_2 depends on the pH, the temperature, and the amount of CO_2 in the blood. In turn, we see from (2.2) that an increase in CO_2 shifts the hydration reaction to the right, causing the formation of H^+ and decreasing pH. Higher levels of CO_2 cause a lower saturation of Hb with O_2 at the tissue. Similarly, more O_2 at the lungs causes less saturation of Hb with CO_2. These interdependencies could be explicitly modeled using a variety of dissociation equations, e.g. see [80]. However, characterizing these complex relations would require additional parameters that we may not be able to quantify for a given person. Thus, in this study we chose a simple linear dissociation equation for CO_2 (reflecting Henry's law) and a nonlinear equation for O_2 to relate p_{gas} and $c_{gas,total}$. These have been used successfully in other studies, see e.g. [9].

The transport of gases between the alveoli and the pulmonary capillary bed occurs primarily via passive diffusion, and as such is driven by the concentration differential across the thin alveolar wall. Under steady-state conditions, the rate of O_2 leaving the alveoli equals the rate of O_2 taken up by the capillaries, known as Fick's law,

$$\dot{V}_{O_2} = q_p(c_{a,O_2} - c_{v,O_2}),$$

where q_p [ml/s] is the flowrate in the pulmonary circulation, $\dot{V}_{O_2}$ [ml/s] is the rate of O_2 diffusing out of the alveoli, and $c_{a,O_2} - c_{v,O_2}$ [$\text{ml}_{gas}/\text{ml}_{blood}$] is the arterial-venous concentration gradient. The same relationship is considered true for CO_2 diffusing into the alveoli from the pulmonary capillaries. We consider Fick's law when modeling diffusion across the alveolar wall and neglect spatial dependence of diffusion on local concentration gradients.

2.3 Regulation

Internal mechanisms control the condition of any particular property of the human body when a stimulus disturbs it from its baseline condition. This ability to regulate to stability is termed "homeostasis". In negative feedback regulation, the sensor in a system senses the disturbance in a property and sends correcting information via the integrator to the effector, which acts to to bring the property back to its homeostatic level. A generic sensor-integrator-effector system is shown in Figure 2.11. One of the main global feedback control mechanisms found in the body is the autonomic regulation of heart rate, cardiac contractility, and vessel resistance, and vascular tone. Autonomic regulation utilizes por-

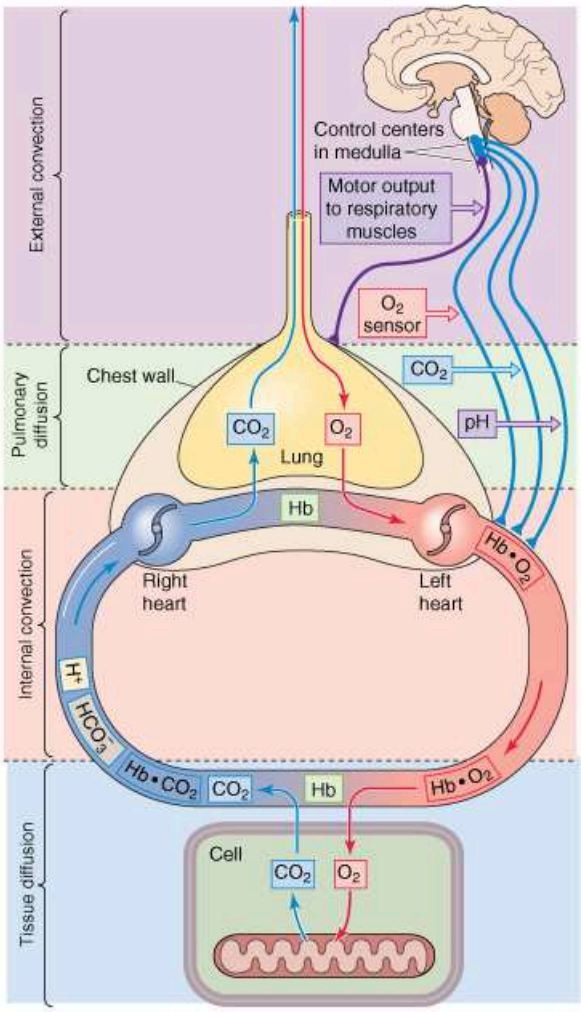

Figure 2.10: Schematic of the major components of the respiratory system. Gases are exchanged by several transport processes: external convection between the body and the atmosphere; pulmonary diffusion; internal convection through the circulatory system; and tissue diffusion. Oxygen-rich blood flows from the lungs to the tissues, and carbon-dioxide-rich blood flows from the tissues to the lungs. Information about concentrations of arterial O_2, CO_2, and pH, sensed by the peripheral chemoreceptors, are integrated in the control centers of the medulla to produce an output that alters ventilation accordingly. Reprinted from [13], ©Elsevier Ltd. Boron and Boulpaep; Medical Physiology, Updated Edition.

tions of the central nervous system (CNS) for signal integration and the peripheral nervous system (PNS) for signal dissemination. In addition to global feedback controls there are local controls. An important local feedback control is autoregulation, which regulates vascular resistance in specific tissues independent of the central nervous system. Blood pressure

and blood gas concentrations are controlled as a result of these feedback mechanisms.

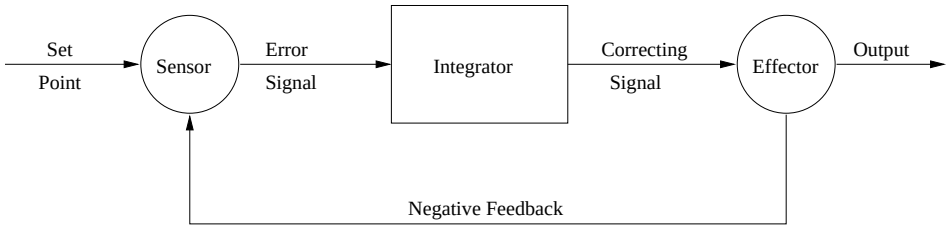

Figure 2.11: Diagram illustrating negative feedback control. The sensor sends information to the integrator about the difference between the current output and the target output, called the error signal. The integrator sends the correcting signal to the effector to change the output to return it to its target level.

2.3.1 Autonomic regulation

In autonomic regulation, information about blood pressure and blood gas concentrations, sensed by the baroreceptors and chemoreceptors respectively, is sent to control centers in the CNS via afferent sensory neurons. Note that the term "center" defines not an anatomically distinct set of cells, but rather a common functionality. Integration of many signals by these centers produces an output signal which is sent to the appropriate areas of the body via efferent motor neurons. In the CNS, cardiovascular activity is regulated by the cardiovascular center of the medulla, and similarly the respiratory center is responsible for the control of ventilation. The cardiovascular center is further divided into the vasomotor center, which causes vasomotion, and cardiac centers (cardioacceleratory and cardioinhibitory), which change heart rate (HR) and cardiac contractility [13, 103]. The pool of motor neurons in the PNS effecting these changes is divided into sympathetic and parasympathetic pathways, which have opposing effects on the body, i.e., when one system is stimulated, the other is suppressed.

Cardiovascular regulation

The baroreceptors, located in the carotid sinus and the aortic arch, respond to changes in vessel wall distention due to changes in arterial pressure. Decreased arterial pressure decreases vessel wall distention, which decreases the baroreceptor nerve firing rate sent to the medulla. The medulla generates a correcting signal and disseminates it through the sympathetic and parasympathetic systems of motor neurons. The sympathetic system

is activated in response to decreased baroreceptor firing rate. Increased sympathetic outflow gives rise to an increase in norepinephrine, which in turn leads to peripheral vasoconstriction, decreased vascular compliance, increased HR, and increased cardiac contracility within approximately 6-8 cardiac cycles. As a result, stroke volume and cardiac output increase, leading to a increase in blood pressure. The decrease in baroreceptor firing rate also decreases the activity to the cardioinhibitory center of the medulla and the parasympathetic nerve pathways. Parasympathetic inhibition leads to a decrease in the release of acetylcholine, which speeds up cardiac electrical conduction resulting in an increased HR within 1-2 cardiac cycles [11] .

It is thought that there is little to no autonomic innervation in the cerebral vasculature [13, 103], although this claim is disputed. Richardson [92] claims that sympathetic control in the brain is minimal. Shepherd observed vasodilation via a parasympathetic efferent pathway although its effect is thought to be slight [101]. In contrast, Hamel [37] and Zhang *et al.* [117] have found evidence suggesting autonomic control of the cerebral circulation.

Respiratory regulation

The autonomic respiratory control response is mediated via peripheral and central chemoreceptors. Peripheral chemoreceptors, located in the aortic and carotid bodies, are sensitive to the arterial partial pressures of O_2 (p_{a,O_2}) and CO_2 (p_{a,CO_2}), and pH. A decrease in p_{a,O_2}, decrease in pH, or an increase in p_{a,CO_2} increases nerve firing of the chemoreceptors [13]. These afferent signals are sent to the medullar respiratory center, which after integrating them sends efferent signals to the diaphragm and intercostal muscles to increase their contraction. As a result, ventilation increases either through faster respiration rate (f_R) or larger tidal volume (V_T), both of which increase p_{a,O_2} and decrease p_{a,CO_2}. The increase in ventilation removes CO_2. This shifts the reaction in (2.2) to the left and reduces the concentration of H^+, i.e., increasing pH [8, 13, 29]. Thus the feedback loop is completed. The peripheral chemoresponse accounts for 20-30% of the total response [11]. It is most likely that the receptors respond to a decrease in pH caused by the increase p_{a,CO_2}, rather than p_{a,CO_2} itself, and this response is activated before that for p_{a,O_2}. The latter only occurs under severe hypoxia (low O_2) [40].

Central chemoreceptors are located near the surface of the medulla, surrounded

by brain extracellular fluid (BECF). They are stimulated by increased cerebral tissue p_{aCO_2} via concomitant decrease in pH [94], but do not respond to changes in cerebral p_{a,O_2}. They are responsible for 70-80% of the response to blood gas changes [11]. Cerebral vascular CO_2 can diffuse from the vessel lumen to the BECF across the blood-brain barrier (BBB), the tight endothelial cell wall of the vessels, which protects the brain from potentially harmful compounds while allowing essential nutrients to reach cerebral tissue. The increase in p_{a,CO_2} drives the reaction (2.2) to the right, thereby increasing the concentration of H^+ ions in the BECF and lowering the pH. Therefore an excess concentration of CO_2 in the blood corresponds to a lower than normal pH, triggering the central chemoreceptor response. This is an example of *respiratory acidosis* which results in an increase in ventilation. However, H^+ ions cannot cross the blood-brain barrier (BBB), therefore a highly acidic blood environment, as would be seen in metabolic acidosis, does not promote ventilation increase.

Interaction of Cardiovascular and Respiratory Autonomic Controls

The cardiovascular and respiratory controls influence each other both mechanically and neurally, see Figure 2.13. The downward contraction of the diaphragm during inspiration reduces the pressure in vessels in the intrathoracic cavity while simultaneously adding pressure to abdominal vessels. Thus intrathoracic arterial blood pressure decreases during inspiration and increases during expiration due to this mechanical stimulus [29]. The pressure differential between the systemic veins and the right atrium increases, which increases venous return, thereby raising cardiac output by the Starling mechanism [20, 29]. On the neural side, the mechanical action of inspiration stimulates pulmonary stretch receptors, which in turn inhibit parasympathetic activity and possibly sympathetic activity as well, leading to increased HR [29] and lowered blood pressure. Figure 2.12 shows the interplay between these mechanisms during normal breathing.

In addition, a decrease in p_{a,O_2}, an increase in p_{a,CO_2}, or a decrease in pH sensed by the chemoreceptors also stimulates the vasomotor and cardioinhibitory centers. The intrinsic cardiovascular responses are peripheral vasoconstriction, causing increased peripheral resistance, and bradychardia (slower HR) [11, 13]. However, the increased ventilation resulting from the chemoresponse inhibits the cardioinhibitory center in two ways. Increased ventilation stimulates the pulmonary stretch receptors, and removal of CO_2 resulting from increased ventilation causes p_{a,CO_2} to decrease and pH to increase in the brain extra-cellular

fluid [13]. The net result is inhibition of parasympathetic activity, leading to tachycardia (faster HR) and increased myocardial contractility [8, 29].

2.3.2 Autoregulation

Autoregulation can be described as the ability of a vascular bed to maintain constant perfusion in spite of fluctuations in blood pressure. Alternatively, it can refer in general to the set of local regulatory mechanisms that operate on a particular vascular bed [36, 84]. It is a factor most prominently in the skin, renal, and cerebral vessels. Several hypotheses exist to explain these autoregulatory mechanisms, including the myogenic hypothesis, a response to changes in vessel wall stretch or tension, and the metabolic hypothesis, a response to changes in levels of metabolites. While regulation of the peripheral vasculature occurs both locally and via the autonomic nervous system, regulation of the cerebrovasculature occurs primarily by autoregulation. We use the second definition of autoregulation for the studies presented here, and focus on those factors that affect cerebral autoregulation.

Cerebral autoregulation

The myogenic effect refers to the response to increased transmural pressure, but its mechanism is not well understood or agreed upon. It has been observed that an increase in pressure stretches the vessel wall and increases wall tension. In an elastic vessel, the diameter would increase, which would reduce resistance to blood flow and induce a blood flow increase following Ohm's law [13]. In autoregulation, wall stretch resulting from increased blood pressure and flow instead causes contraction of vascular smooth muscle cells [36, 84], which constricts the vessel lumen to reduce blood flow [101]. It is possible that contraction is triggered by increased calcium levels due to stretch-activated cell membrane cation channels, although other mechanisms have been proposed [84, 13, 51]. Berne and Levy [11] contend that it is not wall stretch but wall tension that activates the myogenic response, while Aaslid [1] found evidence to negate the myogenic hypothesis.

The various regions of the brain continuously change their metabolic needs. Resultant changes to regional blood flow have been observed. The strongest metabolic effect is a response to changes in p_{a,CO_2}. A higher metabolic demand implies a greater utliization of O_2 and excess formation of CO_2. Carbon dioxide is a vasodilator, and as such an increase causes local vasodilation which helps increase blood flow. High p_{a,CO_2} as well as low p_{a,O_2}

often results from decreased ventilation. The p_{a,CO_2} drives the hydration reaction (2.2) to produce more H^+ and lower pH, evoking vasodilation. In this way blood flow is increased in order to remove CO_2 and deliver necessary levels of O_2. Note that this is counter to the systemic vasoconstrictor effect [13, 29]. By this mechanism CBF is maintained. The effect of vasodilation dampens central chemoreceptor activity [116]. For example, with decreased p_{a,CO_2}, autoregulatory vasoconstriction occurs as does inhibition of ventilation. However, the resultant lower CBF causes less removal of H^+ by blood and pH remains or returns to a lower level. This counters the inhibition of ventilation.

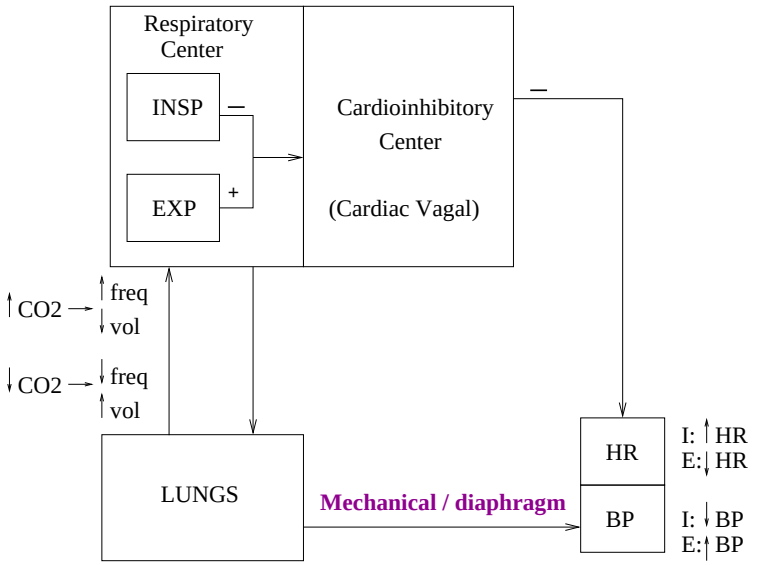

Figure 2.12: Cardiovascular regulation during normal breathing. During inspiration at a normal breathing rate, heart rate increases and blood pressure decreases, with the opposite effects occurring during expiration. A high concentration of CO_2 stimulates breathing at a higher breathing frequency f_R [1/s] but with a lower tidal volume V_T [ml] (short shallow breaths).

2.3.3 Summary of regulation

Regulation of cardiovascular and respiratory processes is complex with much interaction between the two systems and their control mechanisms. We present the regulatory processes relevant to the models we study:

- Decreased arterial blood pressure induces sympathetic activation (vasomotor center) and parasympathetic withdrawal (cardioinhibitory center), inducing faster HR, in-

creased cardiac contractility, increased peripheral resistance, and decreased compliance in order to restore blood pressure.

- Increased CO_2 increases the firing rate of the chemoreceptors, activating the vasomotor, cardioinhibitory, and respiratory centers. The result is increased peripheral resistance, decreased HR, and increased ventilation, in order to restore CO_2 levels.

- Inspiration induces parasympathetic withdrawal and decreased intrathoracic pressure, causing increased HR and decreased blood pressure in intrathoracic vessels.

- Changes in vascular resistance are modulated locally as responses to changes in pressure and CO_2. Increased CO_2 decreases resistance by vasodilation. Increased pressure increases resistance by inducing contraction of vascular smooth muscle cells as a response to vessel wall stretch.

Figure 2.13 summarizes the regulatory mechanisms as described in Section 2.3. Many volumes of literature have been published detailing the attempts to separate the various mechanisms and fully understand the underlying details. These mechanisms previously described are generally agreed upon by physiologists and will be utilized in our studies. It should be kept in mind that the details are still under deliberation as more studies are performed.

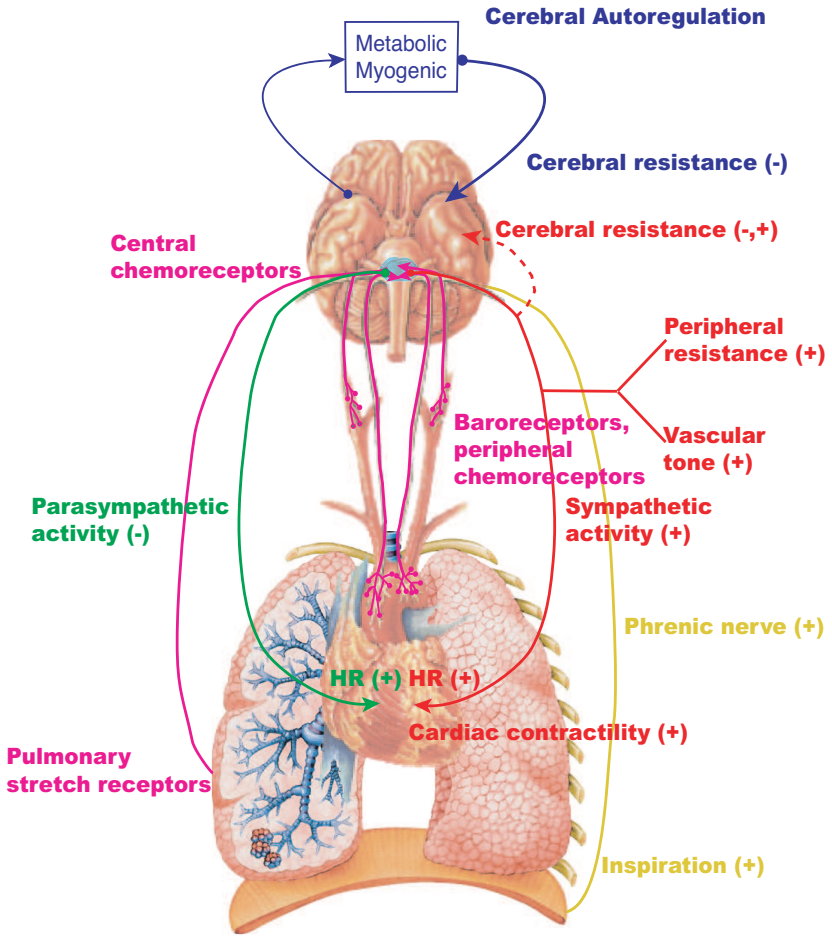

Figure 2.13: Interaction of cardiovascular and respiratory controls. A decrease in arterial pressure leads to a decrease in baroreceptor firing rate, activating the the vasomotor center and inhibiting the cardioinhibitory center. Sympathetic activation and parasympathetic withdrawal increase heart rate, cardiac contractility, peripheral resistance, and vascular tone. Increased CO_2, decreased O_2, or decreased pH leads to increased firing rate of central and peripheral chemoreceptors, stimulating the vasomotor, cardioinhibitory, and respiratory centers. This increases peripheral resistance, vascular tone, and ventilation. Heart rate increases as well after a transitory decrease. In addition, increased firing of pulmonary stretch receptors during inspiration inihibits the cardioinhibitory and respiratory centers, increasing heart rate and decreasing ventilation. Furthermore, the cerebral autoregulatory response to increased CO_2 leads to decreased cerebrovascular resistance.

Chapter 3

Cardiovascular Compartmental Models

The complexity of the cardiovascular system and its control makes it difficult to model it in its entirety. Simplifying assumptions are made according to the purposes of a given study. The cardiovascular system can be modeled using methodologies ranging from elaborate three-dimensional models of local structure to system-level models assuming spatial homogeneity. Similarly, the cardiovascular control can be modeled using anything from empirical models down to detailed molecular models.

Multi-dimensional spatially distributed models are typically of benefit for examining local flow behavior on a smaller scale. This is ideal when modeling fluid dynamics of a specific artery or the heart. For example, Stroud *et al.* examine blood flow through a portion of a stenotic artery using the two-dimensional Navier-Stokes equations [107]. In this study the impact of turbulence and non-Newtonian effects could be seen under both steady and pulsatile flow. McQueen and Peskin [85] discuss a three-dimensional model for blood flow in the heart, using the immersed boundary method to numerically solve the three-dimensional Navier-Stokes equations. Though the complexity of depth of such models gives excellent insight into a specific portion of the body, their use is constrained to such isolated investigations. In addition, these models are often constructed as open-loop models which do not accurately mimic the closed-loop nature of the circulatory system. It is only recently that studies have addressed the difficult task of multiscale modeling. For example, Formaggia *et al.* [30] discuss the general mathematical issues of multiscale modeling in the

cardiovascular system, and Kerckhoffs *et al.* [46] address the specific problem of coupling a finite element 3D model of the heart with a lumped parameter vascular model in a closed loop.

A system-level model can more easily incorporate closed-loop phenomena and feedback controls. In system-level models, several regions of the body are often "lumped" together to represent a spatially-averaged component. Typically, these models predict blood pressure and flow in and between compartments representing locations in the cardiovascular system using electrical circuits with capacitors, resistors, and inductors. Lumped parameter compartmental models can have states that represent quantities that pulse with cardiac dynamics or mean values averaged over the timespan of an entire cardiac cycle. Many of the latter are based on predictions of mean values of states such as blood pressure [41, 43, 75, 113] and have been developed to study dynamics and control of the cardiovascular system, see e.g., [43, 74, 73, 77, 78, 93, 109]. Kappel and Peer [43] build a model consisting of two arterial, two venous, and two cardiac compartments to predict mean pressures during baroreflex response under a submaximal workload. In this model the blood flow was non-pulsatile, which made it feasible to use optimal control and verify existence, uniqueness, and stability. Ottesen's baroreflex model [77] is another example which assumes non-pulsatile blow and cycle-averaged state quantities. His model is an open-loop model, with one arterial and one venous component and the left and right ventricles acting as the source and sink of the model. Though the model is easily analyzed in the same manner as Kappel's model, the open-loop nature neglects effects of regulatory responses propagating via the circulation.

In recent years the complexity of these models has increased to more accurately account for the underlying physiological dynamics. For example, complex nonlinear models have been developed to describe the pulsatile pumping of the heart. The time-varying elastance model for ventricular pressure proposed by Suga *et al.* [108] is standard for many physiological models. More recently, Danielsen and Ottesen [22, 79] build off of a model proposed by Mulier [59] to describe both isovolumic and ejecting heart properties. Heldt *et al.* [39] adopt the elastance model in their closed-loop model of the regulatory response to orthostatic stress, whereas Olufsen *et al.* used the Danielsen version for their model [72, 74] as discussed further in Chapter 5. Greater complexity is introduced in large systems via the number of equations, the size of the associated parameter space, and nonlinearities.

Similar model constructs have been used to study cardiorespiratory dynamics. As

an example, diffusion can be represented with a spatially-distributed model, such as in the analysis of the Valsalva maneuver investigated by Lu *et al.* [54]. In this study compartmental models are used to describe time-varying respiratory dynamics in the lungs as well as the components of the cardiovascular system. In contrast, Fink *et al.* [28] models diffusion with a simple volumetric flow rate in their optimal control model used to study the barorereflex response to orthostatic stress, and consider all cardiovascular and respiratory rates as mean values.

We combine principles from these studies to develop pulsatile closed-loop models of the cardivascular and respiratory systems. Our models enable us to study the effect of regulatory responses on cerebrovascular dynamics, under both pressure and CO_2 challenges. In Section 3.1 we present the basic components of lumped parameter cardiovascular models. Section 3.2 is a treatment of the two aforementioned ventricular pressure functions used in our studies. We also introduce lumped parameter construction of respiratory compartments and the necessary nomenclature for understand gas dynamics in Section 3.3.

3.1 Cardiovascular models

Blood is driven from the heart through the vasculature by the pressure differential Δp [mmHg], following hemodynamic principles for fluid flow. Blood pressure p_i [mmHg], also referred to as transmural pressure, is defined as the difference between intravascular pressure p_{int} and extravascular pressure p_{ext}, i.e. $p_i = p_{int} - p_{ext}$, at a given location i in the vasculature. Extravascular pressure is generally constant at atmospheric pressure, so the convention is to set $p_{ext} = 0$ and assume all intravascular pressures are relative to atmospheric, i.e., $p_i = p_{int}$. The pressure differential $\Delta p = (p_i)_{in} - (p_i)_{out}$ gives the difference in transmural pressure between the inlet $i = in$ and outlet $i = out$ of a segment of vasculature, also called the perfusion pressure.

Blood flows from high arterial pressure to low pressure, opposed by resistance characterized by properties of both the vessel and the fluid. This relationship is described by the physiological analog of Ohm's law,

$$q = \frac{\Delta p}{R}, \tag{3.1}$$

where q [ml/s] is volumetric flow rate and R [mmHg·s/ml] is the resistance of the vessel to blood flow. The differential Δp is often calculated using mean pressures. The pulmonary

circulation has a lower mean pressure differential (15-5=10 mmHg) than the systemic circulation (95-3=92 mmHg), as seen from Figure 2.2. Given that both sides of the circulation have the same cardiac output, Ohm's law predicts a lower total resistance in the pulmonary circulation. The perfusion of tissues is regulated by altering arteriole resistance to effect changes in blood flow to tissues as required, i.e., lowering R increases q. We use Ohm's law for hemodynamics as the primary relationship for building our models.

In a straight rigid cylindrical tube with a Newtonian fluid, laminar flow can be predicted by a simplification of the Navier-Stokes equations known as Poiseuille's law, which includes an explicit form for resistance [49, 65]

$$R = \frac{8\eta L}{\pi r^4}, \tag{3.2}$$

where r is the radius of the vessel, η is the viscosity of the blood, and L is the length of the cylindrical vessel. In reality, blood flow is unsteady and viscosity depends on the flow rate (in particular for the smaller vessels), thus the flow is neither Newtonian nor laminar. However, for the large vessels, viscosity is approximately constant, and away from entry-regions the flow is approximately laminar, thus using the Poiseuille law for a system level model is a reasonable assumption [65, 103]. Since we do not have spatial information in our models, we do not use Poiseuille's law explicitly, but instead use it as a qualitative basis for development of models for vessel dynamics.

The lumped parameter compartmental models discussed in these studies are designed in a similar manner to an electrical circuit. In these types of models, transmural pressure $p(t)$ [mmHg] is analogous to voltage and volume $V(t)$ to charge, with volumetric flow rate $q(t)$ [ml/s] playing the role of electrical current. Each compartment has a compliance element $C(t)$ [ml/mmHg], similar to electrical capacitance, representing the change in volume given a change in pressure for a given compartment. For each of these compartments i, the stressed volume $V_{i,str}(t)$ is given by

$$V_{i,str}(t) = V_i(t) - V_{i,unstr} = C_i(t)(p_i(t) - p_{atm}), \tag{3.3}$$

where $V_i(t)$ [ml] is the time-dependent total volume and $V_{i,unstr}$ [ml] is the unstressed volume, at zero transmural pressure. The pressure p_{atm} [mmHg] is the constant extravascular atmospheric pressure, set to 0 mmHg as described above, and $p_i(t)$ are set accordingly. For the remainder of these studies, "pressure" refers to transmural pressure across the vascular

wall and "pressure differential" refers to the perfusion pressure between two locations in a vessel.

Flows between adjacent compartments have a resistive element $R(t)$ [mmHg·s/ml]. Incorporating Ohm's law for hemodynamics (3.1) and letting $R(t)$ be a function of time, we write the net change in volume for each compartment as

$$\frac{dV_i(t)}{dt} = q_{in}(t) - q_{out}(t), \quad q_{in(t)} = \frac{p_{i-1}(t) - p_i(t)}{R_{in}(t)}, \quad q_{out}(t) = \frac{p_i(t) - p_{i+1}(t)}{R_{out}(t)}. \tag{3.4}$$

It is possible for $q_{in}(t)$ or $q_{out}(t)$ to be the sum of several flows, for example the flow from the aorta into multiple arteries. The notations $i-1$ and $i+1$ refer to upstream and downstream compartments respectively. A representative segment is shown in Figure 3.1.

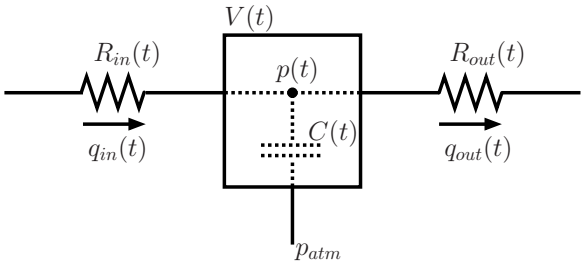

Figure 3.1: Representative vascular compartment of the cardiovascular system. V: volume [ml]; p: transmural pressure [mmHg]; p_{atm}: atmospheric reference pressure = 0 mmHg; C: compliance [ml/mmHg]; R: resistance [mmHg·s/ml]; q_{in}, q_{out}: volumetric blood flow rates into and out of the vascular compartment [ml/s].

A system of differential equations is obtained by differentiating (3.3) and equating with (3.4)

$$\frac{dp_i(t)}{dt} = C_i(t)\frac{dp_i(t)}{dt} + p_i(t)\frac{dC_i(t)}{dt} = q_{in}(t) - q_{out}(t). \tag{3.5}$$

An equation of this form is associated with each vascular compartment. An explicit form can be used for the heart pressure as a function of volume. Hence the heart compartments are described by volume conservation as

$$\frac{dV_i(t)}{dt} = q_{in}(t) - q_{out}(t), \quad i = la, lv, ra, rv, \tag{3.6}$$

where flows are determined similarly to (3.4).

For the remainder of these studies, all pressure, volumes, and blood flows are assumed to be time-dependent quantities and we may denote them by p, V, and q except where noted. The parameters $R(t)$ and $C(t)$ can be set as constants or modeled as functions of time, pressure, or other relevant physiological quantities.

3.2 Cardiac models

As described in Section 2.1.1, the left heart generates pressure for the systemic circulation and the right heart for the pulmonary circulation. Each side has an atrium which acts as a primer pump and a ventricle for pressure development. The same mathematical ventricular function should be used for each heart chamber within a given cardiovascular model, the differences arising in parameter values that characterize the model function. In this study two approaches are investigated in depth, the time-varying elastance model and a polynomial activation function model.

In the time-varying elastance model, the left ventricular pressure $p_{lv}(t)$ [mmHg] is defined as

$$p_{lv}(t) = E_{lv}(t)[V_{lv}(t) - V_d], \tag{3.7}$$

where $E_{lv}(t)$ [mmHg/ml] is time-varying elastance, the reciprocal of compliance. This is one of the most commonly used models, developed first by Suga and Sagawa as the end-systolic pressure-volume relation $p_{v,ES} = E_{v,ES}(V_{v,ES} - V_d)$ [96, 108]. Ventricular pressure p_{ES} at end-systole (ES) is linearly related to ventricular volume V_v for a family of pressure-volume (P-V) loops by the elastance $E_{v,ES}$ as the slope and V_d as the volume-intercept, see Figure 3.2. Each P-V loop represents ventricular dynamics under different constant afterload (pressure opposing ejection). This empirical function is completely independent of ventricular end-diastolic volume and is built using data collected during ventricular ejection. It is therefore a more reasonable approximation to the systolic phase of the cardiac cycle than the diastolic phase [96]. However, this model in its time-varying form (3.7) has been used extensively and performed well within several cardiovascular modeling efforts, e.g., [80, 93, 104, 109]. The beauty of this function lies its simplicity and ease of use. Its small number of characterizing parameters make it computationally more versatile. Also, a change in contractility of the heart, i.e., during regulation, could be represented by a change in parameters representing the maximum or timing of the elastance function.

It appears that the physiological meaning of V_d is still under question and its value varies widely. As described above, it is defined as the volume intercept of the end-systolic P-V linear relationship of a family of P-V loops for a given subject. Ottesen [80] and Schroff *et al.* [98] describe it as the volume at zero end-systolic pressure and give it the value 10 ml for a human heart and about 5 ml for a canine heart, respectively. Several other sources [99, 102] give average values for V_d in canines at around 0 ml. Heldt [38]

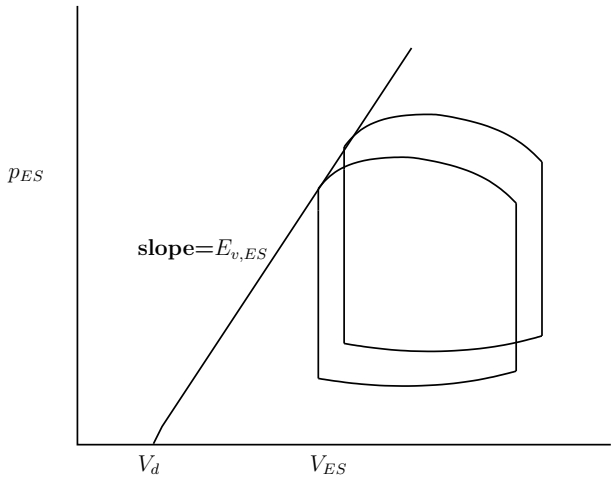

Figure 3.2: Diagram depicting two P-V loops under different constant afterloads (pressure opposing ejection), showing $E_{v,ES}$ [mmHg/ml] as the slope of the line formed by connecting points of end-systolic pressure p_{ES} [mmHg] at end-systolic volume V_{ES} [ml] between loops. The parameter V_d [ml] is the volume-intercept of this line.

discusses it as an unstressed volume and uses values ranging from 14 to 55 ml for the four heart chambers. The parameterization of V_d will be discussed in more detail in Chapter 6.

The ventricular function used for these analyses must be able to accept a variable HR (H [1/s]), and include a defined time for the start of relaxation. The second requirement is met by setting the time when minimum elastance is achieved. The function of choice is a modification of a function proposed by Heldt [38]:

$$E(t) = \begin{cases} E_{min} + (E_{max} - E_{min}) \left[1 - \cos\left(\dfrac{\pi t}{T_M}\right)\right] /2 & 0 \le t \le T_M \\ E_{min} + (E_{max} - E_{min}) \left[\cos\left(\dfrac{\pi (t - T_M)}{T_r}\right) + 1\right] /2 & T_M \le t \le T_M + T_r \\ E_{min} & T_M + T_r \le t \le T. \end{cases} \quad (3.8)$$

The parameters T_M and T_r are time for maximum (systolic) elastance and remaining time to relaxation respectively. These can be expressed as fractions of the length of the cardiac cycle T [s], thus allowing for variable H. The minimum and maximum elastance parameters are E_{min} and E_{max}. Since maximum elastance is the maximum slope from the P-V loops, which occurs at the point of end-systole, peak elastance and systolic pressure occur at approximately the same time.

Mulier explored a new approach in 1994 [22, 59], in which he described the ventricular pressure in the isovolumic (non-ejecting) heart. His model was based on the Frank-

Starling mechanism asserting that isovolumic pressure increases with increased volume. The ventricular pressure can be represented as the sum of the diastolic and developed pressure as a function of time t and ventricular volume V_v

$$p_v(t, V_v) = p_d(V_v) + [p_s(V_v) - p_d(V_v)]\, f(t),$$

where pressure p_d and p_s are diastolic and systolic pressure, respectively, and developed pressure across the timespan of the cardiac cycle is described by an activation function $f(t)$. Mulier modified this equation using physiological criteria to be

$$p_v(t, V_v) = a(V_v(t) - b)^2 + (cV_v(t) - d)f(t). \tag{3.9}$$

In this equation, the parameter a [mmHg/ml] represents the ventricular elastance during relaxation and b [ml] represents the ventricular volume at zero diastolic pressure. The parameters c [mmHg/ml] and d [mmHg] relate to the volume dependent (contractility) and volume independent components of the developed pressure.

This function is designed for an isovolumic heart, i.e., one that increases pressure through cardiac muscle contraction without injection-induced volume decrease. Though this is not the natural behavior of an active heart, several studies have shown that this function does indeed mimic both isovolumic and ejecting properties of the heart throughout the cardiac cycle when it is connected to a model of the cardiovascular system [22, 79, 81]. Although modifications have been made to better model ejection, we use the function in its original form.

Ottesen and Danielsen [79] discuss a variety of activation functions in the context of data collected by Regen [91] for a dog. They are presented as $g(t)$ with magnitude $\neq 1$, then normalized by $g(t_p)$, the value at the time for peak pressure, to attain a maximum value of 1 for $f(t)$. Below we summarize several activation functions:

a) Mulier:

$$g(t) = \begin{cases} (1 - e^{-(t/\tau_c)^\alpha}) & 0 \le t \le t_b \\ (1 - e^{-(t/\tau_c)^\alpha}) e^{-((t-t_b)/\tau_r)^\alpha} & t_b < t < t_h, \end{cases}$$

where τ_c and τ_r are contraction and relaxation parameters. The parameter α is an overall rate constant. The times t_b and t_h are the time for the start of relaxation and the length of the cardiac cycle.

b) Gamma distribution:

$$g(t) = (t - t_d)^{\mu-1} e^{\mu-1-(t-t_d)/\alpha},$$

where t_d, μ, and α are ventricular parameters, but do not have rigorous physiological interpretation.

c) Combined exponentials:

$$g(t) = \frac{\xi(t - t_d)}{e^{1+\epsilon-(t-t_d)^\alpha} + e^{t-t_d-1}}.$$

Again, the characterizing ventricular parameters ξ, t_d, ϵ, and α lack physiological interpretation.

d) Product of Hill functions:

$$g(t) = \left[\frac{(t - t_d)^\alpha}{A^\alpha + (t - t_d)^\alpha}\right]\left[\frac{B^\beta}{B^\beta + (t - t_d)^\beta}\right].$$

The ventricular parameters α, β, A, B, and t_d are again generic ventricular parameters.

The majority of these activation functions are designed using parameters that have no physiological meaning. They do have the benefit of closely agreeing with experimental data, however, a common limitation is that they do not provide compact support. These functions never attain zero but approach zero towards the beginning and end of the cardiac cycle. Therefore p_{lv} never returns to p_d and there is no definite end to the contraction. Canine data from a study by Regen [91] has shown that the ventricular pressure waveform widens with decreasing H, indicating a longer period of contraction with a longer cardiac cycle. Therefore, Ottesen and Danielsen developed a polynomial expression with compact support by which they were able to explicitly express the end of contraction coinciding with a return to diastolic pressure, thus representing the ventricular pressure waveform as a function of H [79].

Their activation function $f(t, H)$ is described by a polynomial of the form

$$f(t, H) = \begin{cases} p_p(H)\dfrac{(t - \alpha)^n(\beta(H) - t)^m}{n^n m^m[(\beta(H))/(m + n)]^{m+n}}, & \alpha \le t \le \beta(H) \\ 0, & \beta(H) < t < T, \end{cases} \tag{3.10}$$

where T [s] is the period of the cardiac cycle, $f(t) = g(t)/g(t_p)$, and $g(t) = (t-\alpha)^n(\beta-t)^m$. Ottesen and Danielsen utilized Regen's data to establish an increasing sigmoidal relationship

for peak pressure p_p and decreasing sigmoidal relationship for time for peak pressure t_p with respect to H [beats/s]. Given that $f'(t_p) = 0$, we obtain

$$\begin{aligned} \beta(H) &= \frac{n+m}{n} t_p(H) - \frac{\alpha m}{n} \\ p_p(H) &= p_{min} + \left[\frac{H^\eta}{H^\eta + \phi^\eta}\right](p_{max} - p_{min}) \\ t_p(H) &= t_{min} + \left[\frac{\theta^\nu}{H^\nu + \theta^\nu}\right](t_{max} - t_{min}). \end{aligned} \tag{3.11}$$

The parameters ϕ and θ give the median peak pressure and time to peak pressure, while η and ν represent the steepness of the slopes of the sigmoids. The min and max parameters represent the minimum and maximum of the appropriate sigmoids. The function is reset to zero with every heart beat, i.e., every cardiac cycle uses a prescribed diastolic pressure for the given volume. The parameter α defining the beginning of contraction is set to zero in this analysis. Though the polynomial ventricular pressure model given in (3.10) has more physiological basis, the large number of parameters (14) puts the polynomial ventricular pressure model (3.10) at a computational disadvantage during numerical optimization.

The two ventricular pressure functions are shown in Figure 3.3. The forms of the two functions are similar. We see though that the elastance function displays a similar rate of increase and decrease because it is made up of cosines, whereas the polynomial function has a steeper increase in pressure during systole and less steep decrease between peak systole and relaxation.

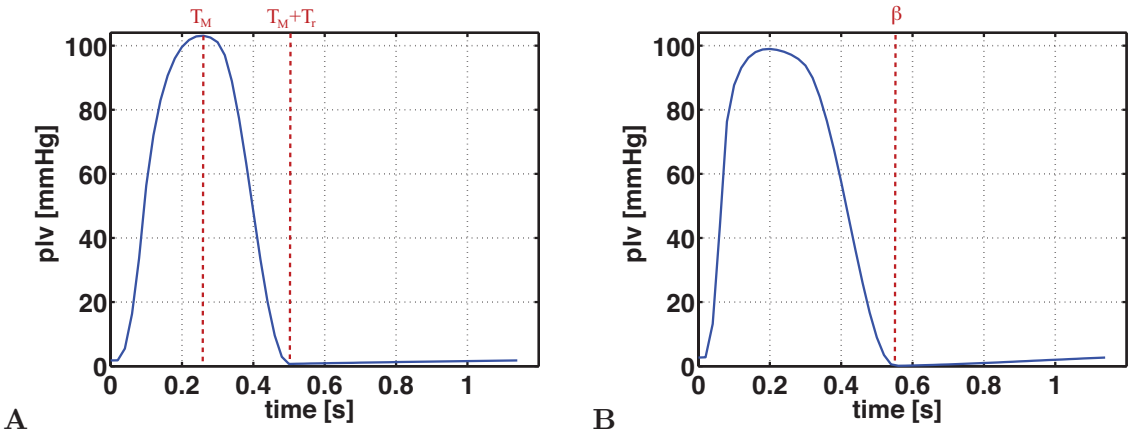

Figure 3.3: Ventricular pressure modeled using (A) the elastance heart model, (3.8) and (B) the polynomial heart model (3.9).

The ventricular function describes the pressure in the atria and ventricles, but not the control of flow between the heart and the surrounding vessels. The human heart utilizes valves to direct and restrict blood flow as described in Section 2.1.1. This action of the valves introduces quasi-discrete behavior into the model, since the flow out of the left ventricle is either negligible (when the valve is closed) or a non-zero function of the pressure drop between the heart and the aorta, e.g., $q_{av} = (p_{lv} - p_a)/R_{av}$. One way to account for the valves is by introduction of an on-off "switch" triggered by changes in pressure. In Olufsen *et al.* [72], the switch value was set to zero when the valve was closed and one when the valve opened, allowing for the flow function to be activated. Hoppensteadt and Peskin use this approach as well [41]. However, the physical behavior of a valve is not discrete as this model portrays. In addition, this mathematical construct is not smooth which does not allow for gradient-based analysis.

Another approach, introduced by Rideout [93] and used by Olufsen *et al.* [74], is to model the succession of opening and closing of the valves as a resistance that varies with pressure. This can be done using a small baseline resistance to define the "open" valve and a resistance that is several orders of magnitude larger to define the "closed" valve, with an exponential function describing the degree of openness as a function of the pressure gradient. The effective resistance of a valve is then defined by

$$R_{valve} = \min\left[R_{valve,open} + e^{-k(p_{in}-p_{out})}, R_{valve,closed}\right], \tag{3.12}$$

where k describes the speed of the transition from open to closed, and $R_{valve,closed}$ is a value large enough to give negligible blood flow. In this equation, the transition from open to closed is more gradual but still has distinct open and closed phases. An exponential function is used to describe the amount of "openness" as a function of the pressure differential across the valve. Values in the exponent are chosen to ensure that the valve closes efficiently and that the flow is virtually zero while the valve is closed. It is important to note that this function is non-smooth at the junctions of the exponential and $R_{valve,closed}$. A smoothing function is considered in Chapter 6 to ensure differentiability during gradient-based optimization.

3.3 Respiratory models

The change in the amount of gas within a particular compartment is represented by a material balance. We consider the transport of gases by convection (via blood or air flow), the utilization of CO_2 / formation of O_2 by metabolism, and the diffusion of O_2 out of and CO_2 into the lungs. Gas exchange occurs in tissue capillary beds, modeled as compartments located between arterial and venous pressures compartments for a given branch of the circulation. The compartments consist of two sections, one for blood flow and one for the tissue gas volume, depicted in Figure 3.4.

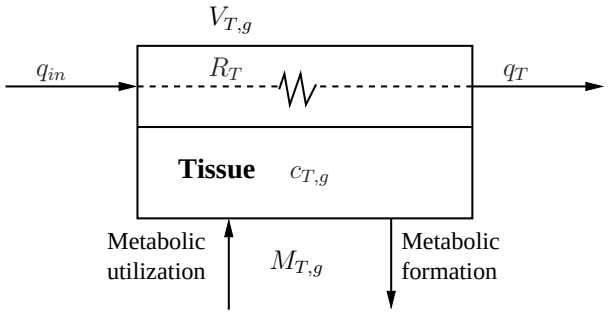

Figure 3.4: Representative tissue compartment of the cardiorespiratory system. R_T [mmHg·s/ml]: resistance of tissue vasculature; $V_{T,g}$ [ml]: effective tissue volume for each gas; q_{in}, q_{out} [ml/s]: blood flow into and out of tissue vasculature; $M_{T,g}$ [ml/s]: metabolic rate of each gas in the tissue.

In the systemic circulation, O_2 is used and CO_2 is formed during cell metabolism. We use constant rates $M_{T,g}$ [ml/s] prescribed by literature for this study, where the subscript T denotes the particular tissue and g is the gas. In addition, gases accumulate or are removed with the flow of blood. The total volume of gas into and exiting systemic tissue are given by $q_{in}c_{in,g}$ and $q_T c_{T,g}$, where c [$\text{ml}_{gas,STPD}/\text{ml}_{blood}$] is the concentration of gas, q_{in} is the particular inlet blood flow, and q_T is blood flow exiting the tissue. We use the same compartment description for gas exchange in the lungs, with the blood flow component representing the pulmonary capillaries and the gas volume component representing the alveoli. Convection via blood flow is modeled in the same manner as for systemic capillaries except that a mixed venous concentration c_v enters the tissue and the arterial concentration c_a exits. Gases enter the alveolar compartment with inspiration and exit with expiration. Their fractional levels are regarded as partial pressures $p_{i,g}$ [mmHg]. Anatomical dead space compartments in the lungs are modeled assuming that gas concentrations are changing

via convection only. Representative equations for gas dynamics are developed in detail in Chapter 7, but we discuss here the conventions for units and notation used in those equations.

The ideal gas law states that $pV = nRT$, where p [mmHg] is pressure, V [ml] is volume, n [mol] is number of molecules, and in this formula T [K] is temperature and R [ml·mmHg/(K·mol)] is the universal gas constant. The convention is to consider O_2, CO_2, and water vapor as ideal gases. Therefore to examine the same quantity of gas under two sets of conditions, we set $p_1V_1/T_1 = p_2V_2/T_2$. The volume that a given gas takes up will depend on its pressure and temperature. As introduced in Chapter 2, "standard-temperature-pressure-dry", or STPD, is air at 0^{o}C=273K at standard sea level atmospheric pressure of 760 mmHg. The conditions are considered dry because of the absence of water vapor. Volumes for metabolic rates and blood gas concentrations are given in V_{STPD}. Body-temperature-pressure-saturated, or BTPS, describes the conditions in the human body estimated at $37^{\text{o}}\text{C} = 310\text{K}$ and air pressure of $760 - 47 = 713$ mmHg, where 47 mmHg is the vapor pressure at this temperature. Alveolar volumes is given under these conditions.

For volume unit consistency, conversions must be made between these two systems. We set up the ideal gas law as

$$\frac{p_{STPD}}{T_{STPD}}V_{STPD} = \frac{p_{BTPS}}{T_{BTPS}}V_{BTPS}$$

and insert the pressures and temperatures at the two conditions

$$\frac{760}{273}V_{STPD} = \frac{713}{310}V_{BTPS}.$$

We rearrange to obtain the conversion factors used in Chapter 7,

$$\begin{aligned} V_{STPD} &= 0.826V_{BTPS}, \\ V_{BTPS} &= 1.21V_{STPD}. \end{aligned} \tag{3.13}$$

Chapter 4

Parameter Estimation

Complex physiological nonlinear models such as those discussed in Chapter 3 often include hundreds of parameters. While physiological knowledge can be used to determine values for some of these parameters, several parameters can only be estimated based on observations from animal studies, and some parameters cannot be determined at all. Simulations using nominal parameter values may provide insight into the overall model dynamics and the behavior for a given group of subjects, but since physiological properties are known to vary significantly between subjects, such simulations cannot provide patient specific information.

Examples of complex models include the PNEUMA model developed by Fan and Khoo [26] and the cardiorespiratory model developed by Lu *et al.* [54]. Fan and Khoo combined cardiovascular, respiratory, and control models to simulate sleep apnea. The cardiorespiratory model by Lu *et al.* was developed to predict the response to forced vital capacity and Valsalva maneuvers. Each of these models comprises more than 100 differential equations and as many characterizing parameters. However, neither model has been validated against clinical data for the purpose of subject specific predictions. Combined with experimental data, these models could be used to estimate parameters that cannot directly be measured experimentally.

The simplest methodology for identifying model parameters for a specific subject is to use manual tuning of parameters to predict observed or known model responses, see e.g., Heldt *et al.* [39] or Olufsen *et al.* [71]. For large models with many states and parameters and for multiple subject-specific studies this method becomes intractable, and it may not guarantee optimal solutions. A more robust approach uses nonlinear optimization

techniques to estimate a set of model parameters that minimize the least squares residual between computed and measured quantities, i.e., solving the inverse problem. For example, Olufsen *et al.* [72, 74] used the Nelder-Mead method [62] to predict parameters in a complex cardiovascular model developed to predict blood flow regulation during postural change from sitting to standing. In these studies, the objective was to develop a model that could predict dynamics observed in individual subjects. But given the size of the model (27 differential equations and more than 100 model parameters) this approach was only used to study dynamic behavior of one subject. In another study, Neal and Bassingthwaighte [61] used a multi-step procedure for estimating subject-specific values for 74 parameters to examine cardiac output and total blood volume during hemorrhage. This model was parameterized against 14 sets of porcine pre-injury hemodynamic datasets, and then used to study post-injury data taken from the same animals. The parameterization process took 24 hours per animal, a time frame not feasible for clinical applications. In physiological studies, these techniques have mostly been used for simpler problems with a small number of parameters or for problems where most of the internal states can be determined.

For complex nonlinear problems with many states and parameters, where only a limited number of states are observable, optimization techniques may give rise to non-unique solutions and often result in numerical problems since the differential equations may be stiff, contain delays, or be ill-posed. The use of numerical optimization techniques therefore necessitates important considerations. Any given set of optimal parameters only represents a local solution to the minimization problem. Parameters defining this local minimum may or may not be within physiological range, and there may be multiple sets of parameters that define the same model states. Thus, it is essential to compute initial, or nominal, parameter values using *a priori* knowledge such as subject height and weight, literature information, or experimental data. Second, the solution may be insensitive to some of the model parameters, i.e., a small change in some parameters may give rise to almost no change in the output states. We showed in Ellwein *et al.* [24] and in Chapter 5 that it may not be feasible to estimate insensitive parameters, neither from a physiological nor from a numerical perspective [45]. Furthermore, if any of the insensitive parameters are physiologically important, designing additional experiments may be necessary to estimate these parameters. Finally, model parameters that the solution is sensitive to may depend on each other. For example, given a mean flow through two resistance vessels, an infinite combination of resistances from each vessel could combine to give the same overall resistance,

thus both parameters can not be identified even though the solution will be sensitive to both parameters.

Sensitivity analysis methodologies can be formulated either using a stochastic or a deterministic approach, examining local or global behavior. We restrict our discussion to deterministic methods because our models contain no stochastic components. In addition, we start with considerable knowledge about each of our nominal parameters, near which we want to know the behavior of our models, so a local analysis is appropriate. To our knowledge this type of analysis has not been used extensively for the analysis of physiological models. Previous studies include work by Ebert [23], who performed a local sensitivity analysis using analytic derivatives to understand what parameters had the greatest impact on sea urchin growth, and a study by Carmichael *et al.* [17] who compared three local sensitivity methods, all using automatic differentiation, to analyze the impace of parameter perturbations on atmospheric ozone. Rabitz *et al.* [89] discuss both local and global methods in the context of a system of ordinary differential equations that describe chemical kinetics.

In one physiological study, Olansen *et al.* [70] used open-chest dog data combined with gradient-based optimization and sensitivity analysis to parameterize a cardiovascular model for studying right-left ventricular interaction. However, it was not clear how parameters were ranked in their sensitivity analysis method. We used classical sensitivity analysis (as described by Eslami [25] and Frank [33]) to rank parameters according to sensitivity [24]. We adopted a similar procedure as Banks and Bortz [7] and Bortz and Nelson [14], but took the analysis a step further using the sensitivity ranking results to shorten the parameter identification computational time and simplify the model. This ranking was used to separate parameters into two groups: one group consisted of parameters to which the solution was sensitive, and another group consisted of parameters to which the solution was insensitive. Ignoring the group of insensitive parameters gave rise to improved parameter estimates that produce a similar model output.

None of the previously mentioned studies attempted to identify dependencies between model parameters. Parameter interdependencies can cause problems during numerical optimization due to near singularities of the Jacobian matrix used in gradient-based optimization. Multiple combinations of parameters leading to the same solution may cause the optimizer to not be able to settle on an optimal parameter set. Studies by Burth, Verghese and Velez-Reyes [16, 110] used a subset selection algorithm first presented by Golub [34] to extract an independent set parameters that can be estimated given a set of data (we

define these parameters as identifiable) in a generator model for power systems. However, this study did not address the sensitivity of the model solution to its parameters. In a more recent study, Heldt [38] used both sensitivity analysis and the subset selection method when predict quantities in a beat-to-beat cardiovascular system model. A ranking system of local sensitivities was employed for each cycle-averaged model output for model analysis. Subequently, subset selection was performed to aid in parameter estimation. Though both methods were explored extensively, they were not used together to reduce the model to a simpler form.

We introduce sensitivity analysis and subset selection as methods for estimating key parameters given limited experimental cata. A multi-step parameter identification scheme is proposed to clearly identify independent, sensitive parameters that uniquely characterize a complex system. In Section 4.1 we present the general equations for calculating nominal values for model parameters. The inverse problem is discussed in Section 4.2. Section 4.3 gives two classes of optimization algorithms and their use in these studies. Finally, in sections 5.6 and 4.5 we present the two methods used to aid in parameter identification, sensitivity analysis and subset selection. Combinations of these are used in the different studies discussed in upcoming chapters.

4.1 Parameter values

Anthropometric data for a particular subject was used in conjunction with literature information to determine subject-specific initial conditions for states and nominal values for parameters. The general process followed throughout each of the following studies is delineated here, but since many formulas are available for specific measures, the formulas used in a specific study will be addressed within that study.

Total blood volume V_{tot} [ml]can be estimated using a number of formulas that are functions of height, weight, and/or body surface area [5, 57, 60, 90]. Using V_{tot} and based on the estimate that the systemic volume circulates in one minute [13], the total volumetric blood flow, or cardiac output (CO), is estimated as $q_{tot} = V_{tot}/60$ [ml/s]. Alternatively, recent studies have appeared that derive estimates of CO based on measurements of arterial blood pressure [58, 83, 112]. The disadvantage of these studies is that their models must be calibrated against actual CO measurements. These may be explored in future work, however we use the above estimate for all current work.

Blood volume and blood flow distributions are taken from Beneken and DeWit [10], one of the only studies we are aware of that distributes flow and volume by organ and gives bothstressed and unstressed volumes. Unstressed volume V_{unstr} is the volume stored in a given vascular bed at zero relative pressure, and stressed volume V_{str} is the volume that develops with pressure increase. Total volume $V_{tot} = V_{str} + V_{unstr}$. Table 4.1 gives these volumes and percentages for an individual with a total blood volume of 4544 ml. These are scaled according to the subject being studied. The blood flow distribution used to find flow rates in each portion of the body is also taken from Beneken and DeWit's work, in which 20% of the cardiac output flows to the head and arms and the other 80% to the rest of the systemic circulation. Several studies provide information on blood flow to the different regions of the body, e.g., [10, 12, 55]. For consistency with estimates on unstressed volumes we used values from Beneken and DeWit, scaled using the subject's blood volume to estimate average blood flow rates $\bar{q}_i$ to each compartment. Smith and Kampine [103] also present a breakdown of blood volumes but they were not defined to the level desired for our purposes.

Nominal values for resistances and compliances are then calculated using estimated volumetric blood flows and blood volumes. Resistances are found using Ohm's law (3.1) for hemodynamics using the mean flow and the pressure differential across a given vascular resistance

$$R = \frac{\Delta p}{\bar{q}}.$$

Stressed volume percentages are used to calculate stressed volumes for each vascular bed. Nominal values for compliances are calculated as the ratio of stressed volume to estimated mean pressure,

$$C = \frac{(V - V_{unstr})}{\bar{p}} = \frac{V_{str}}{\bar{p}},$$

where $\bar{p}$ is estimated from literature values, discussed further below.

Finally, nominal parameter estimates for ventricular function are taken from a variety of sources and modified for the specific purpose of each study. For studies using the polynomial ventricular pressure model, parameters were taken from Ottesen and Danielsen [79]. Parameter values were scaled for the atria and right heart in order to obtain appropriate literature pressures. Heldt [38] and Ottesen *et al.* [80] were used as sources for the elastance model parameters. Depending on the study, parameter values could be used "as is" from these studies or found as combinations of the two. Note since

Table 4.1: Blood volumes and percentage of total blood volume, from Beneken and DeWit [10]. Volumes are scaled to a total blood volume is 4544 ml.

Vessel	Volume [ml]	Total %	Stressed volume %
Ascending aorta	82	1.80	35.4
Thoracic arch	91	2.00	33.0
Thoracic aorta	89	1.96	33.7
Abdominal aorta	78	1.72	25.6
Intestinal arteries	23	0.51	26.1
Leg arteries	75	1.65	16.0
Head arteries (est.)	87	1.91	22.4
Arm arteries (est.)	60	1.32	22.4
Pulmonary arteries	119	2.62	58.0
Abdominal veins	315	6.93	3.2
Intestinal veins	649	14.28	6.5
Leg veins	295	6.49	12.9
Head veins (est.)	353	7.78	7.6
Arm veins (est.)	244	5.36	7.4
Inferior vena cava	530	11.66	7.9
Superior vena cava	530	11.66	7.9
Pulmonary veins	514	11.31	10.5
Left ventricle	125	2.75	–
Right ventricle	125	2.75	–
Left atrium	80	2.716	–
Right atrium	80	1.954	–

T_M and T_r are given relative to the length of the cardiac cycle, they were set up as fractions $T_{M,frac} = T_M/T$ and $T_{r,frac} = T_r/T$.

Initial values for pressures were either scaled with respect to the maximum systolic pressure for each subject studied or estimated based on literature. Systemic arterial pressures are set close to the maximum systolic pressure. Because we have no experimental data for systemic venous pressures, they were set based on average literature values. Smith and Kampine [103] state that the systemic venous pressures range from 10 mmHg in the smallest veins next to the capillaries to 0 mmHg at the entrance to the heart. Beneken and DeWit [10] also include mean pressures in their table of values, which range from 2 mmHg in the abdominal veins to 5 mmHg in the vena cava, and 8 mmHg in the lower body. It is therefore reasonable to set the minimum left ventricle pressure $p_{l,d}$ at 2 mmHg, and the vena cava pressure p_v at 5 mmHg. Cerebral venous pressure is set close to intracranial pressure, $\sim$10 mmHg [13]. In our later studies, literature values for venous pressures were used to scale venous pressure estimates for a particular subject. Initial conditions for the

heart volumes are also related to the subject and are study dependent.

Pulmonary pressures are set in a similar manner as the systemic pressures. Boron and Boulpaep [13] give a mean pulmonary arterial pressure of 15 mmHg and mean pulmonary venous pressure of 5 mmHg, entering the left heart. Smith and Kampine agree with these estimates [103]. These values were used to scale mean and initial pressures in the respiratory study. More details on this process and the parameterization of the respiratory system are discussed in Chapter 7.

In general, model parameters are collected into a vector which we denote μ, the elements of which are denoted by μ_k, $k = 1$ to Y. The pressures and volumes comprise the states of the model, denoted byX_j, $j = 1$ to Z and written together as the vector X. Physiological data, or observations, are denoted as y, and may represent one state or a combination of states in the model. With these designations we set up the computational aspects of the parameter estimation problem.

4.2 The inverse problem

In our model simulation, the set of parameters μ is related to the observations y, by way of a physiologically-based model X, such that $y = X(\mu)$. The observations (data) in these modeling efforts include arterial blood pressure (ABP) measured in the finger, cerebral blood flow velocity (CBFV) measured in the middle cerebral artery (MCA), and expiratory partial pressure of CO_2 (p_{exp,CO_2}). When solving the forward problem, the parameters and model are known *a priori* and are used to generate model output that simulates the observations. In the inverse problem, however, the model is hypothesized while the parameter values are unknown. By solving the inverse problem, we identify parameter values that generate model output that best simulates the observations. In practice, $y = X(\hat{\mu}) + \epsilon$, where ϵ represents error that could be a combination of noise in the measurements, model inaccuracies, or system variability. We aim to find the set of parameters $\hat{\mu}$ that minimizes the error ϵ and gives the computed model output as a function of time $X(t, \hat{\mu})$.

A least-squares formulation is used for the cost function describing the error between the computed model output $X(t, \hat{\mu})$ and the data $y = y^d$. This cost can be minimized using an optimization algorithm in order to estimate parameters which best fit the model

to the available data. The general least-squares form cost function J can be written as

$$J = \sum_{i=1}^{N} \left| \frac{y_i^d - X(t_i, \hat{\mu})}{\omega} \right|^2 . \tag{4.1}$$

Data y^d and model output $X(t, \hat{\mu})$ are sampled at times t_i, $i = 1$ to N, where N is the total number of data samples. The parameter ω is a normalization factor specific to the particular study, such as the number of data points or the mean of the data. The computed values $X(t, \hat{\mu})$ were interpolated at the data time points in the cost function evaluation. The vectors y and X may consist of multiple components.

All computations are done with MATLAB (©MathWorks). Solving the ODEs required MATLAB's stiff differential equation solver `ode15s` to capture the resolution of the solutions. Linear time-independent systems can be characterized as stiff if all eigenvalues of the coefficient matrix are negative but the largest and smallest eigenvalues differ greatly in magnitude. This same characterization is not as well defined for nonlinear and time-dependent systems. In fact, most authors do not come to a common conclusion. As an example, Quarteroni states that "ad hoc techniques" are necessary to determine stiffness [88]. In our investigation we found that non-stiff Runga-Kutta solvers were not able to solve our systems of equations, but the stiff solver `ode15s` worked well and was efficient enough for our purposes.

4.3 Numerical optimization algorithms

We use numerical optimization to find the set of parameters that meet the criteria

$$J(\hat{\mu}) \leq J(\mu) \tag{4.2}$$

for all μ near $\hat{\mu}$, where $\hat{\mu}$ is considered the local minimizer. Both gradient-based and direct-search (derivative-free) algorithms were used in these studies. Our earlier studies [74, 24] made use of direct-search algorithms because they are easy to use without needing to know much about the function being evaluated. As our knowledge of the system grew, the more robust gradient-based optimization algorithms became easier to use and therefore were the methods of choice.

4.3.1 Direct search methods

Direct-search algorithms are generally used with noisy functions and do not require the use of a gradient. They make their choice of parameters based on evaluating the function J at an original sample set of parameters, then choosing a new parameter sampling based on the previous information. This is a convenient first choice of algorithm for large systems because the gradients in such systems may be difficult to evaluate. Because the gradient is not necessary, direct search algorithms are attractive for systems with discontinuities. The simplicity of the algorithms can be an advantage, but the computational time needed for evaluations in larger problems can become prohibitive as will be seen with the model examined in Chapter 5 [45, 86].

One commonly used direct-search algorithm is Nelder-Mead [62]. Nelder-Mead evaluates the function J at the vertices of a simplex of parameters, orders the function values, replaces the worst value with a better one based on a set of rules, and repeats until a user-prescribed error tolerance has been reached. The user may also set the number of functions evaluations allowed as exit criteria instead of an error tolerance. A simplex is an N+1 vertex object in N dimensions. For the parameter set $\mu \in \mathbb{R}^Y$, the simplex S is a matrix of dimension $Y \times m$, where $m = Y + 1$. The simplex matrix has the nominal parameter set $\mu_{(0)}$ as its first column, or vertex, with the remaining columns being perturbations of this parameter set according to the `simpgen` algorithm [45]. The pseudocode presented below is adapted from Kelley [45], with the values for α_i chosen from the sequence $-1 < \alpha_{ic} < 0 < \alpha_{oc} < \alpha_r < \alpha_e$. Note that the notation $\mu_{(n)}$, $n = 1$ to $Y+1$ refers to one vector iterate of parameters, as opposed to μ_k which is one element of a parameter vector set.

1. Evaluate J at the vertices of S and sort the vertices such that $J(\mu_{(1)}) \leq ... \leq J(\mu_{(Y+1)})$, $\mu_{(1)}$ referred to as the best vertex and $\mu_{(Y+1)}$ the worst.

2. While $|J(\mu_{(Y+1)}) - J(\mu_{(1)})| > \tau$, τ defined by the user,

   a) Compute the centroid $\bar{\mu} = \frac{1}{Y}\sum_{n=1}^{Y} \mu_(n)$ of the simplex.

   b) Compute the reflected point $\mu_{(r)} = (1 + \alpha_r)\bar{\mu} - \alpha(\mu_{(Y+1)})$ of $\mu_{(Y+1)}$, and $J_r = J(\mu_{(r)})$.

   c) Reflect: If $J(\mu_{(1)}) \leq J_{(r)} < J(\mu_{(Y)})$, replace $\mu_{(Y+1)}$ with $\mu_{(r)}$.

   d) Expand: If $J_{(r)} < J(\mu_{(1)})$, then compute $\mu_{(e)} = (1 + \alpha_{(e)})\bar{\mu} - \alpha(\mu_{(Y+1)})$, and

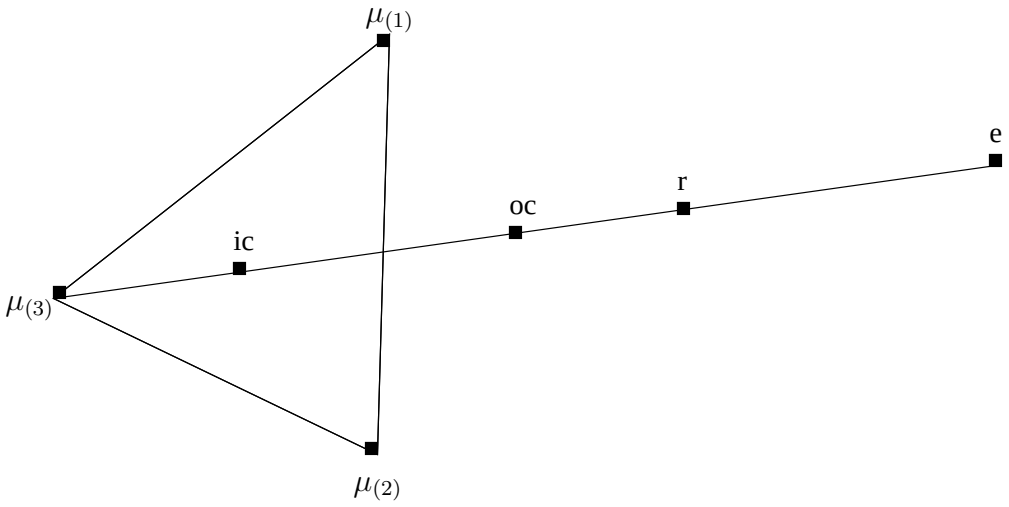

Figure 4.1: Representation of the Nelder-Mead simplex method in N = 2 dimensions. Subscripts include r: reflection; e: expansion; oc: outside contraction; ic: inside contraction.

$J_{(e)} = J(\mu_{(e)})$. Then if $J_{(e)} < J_{(r)}$, replace $\mu_{(Y+1)}$ with $\mu_{(e)}$ and go back to step 1.

e) Outside contraction: If $J(\mu_{(Y)}) \leq J_{(r)} < J(\mu_{(Y+1)})$, compute $\mu_{(oc)} = (1 + \alpha_{(oc)})\bar{\mu} - \alpha(\mu_{(Y+1)})$, and $J_{(oc)} = J(\mu_{(oc)})$. Then if $J_{(oc)} < J_{(r)}$, replace $\mu_{(Y+1)}$ with $\mu_{(oc)}$ and go back to step 1.

f) Inside contraction: If $J_{(r)} \geq J(\mu_{(Y+1)})$, compute $\mu_{(ic)} = (1+\alpha_{(ic)})\bar{\mu} - \alpha(\mu_{(Y+1)})$, and $J_{(ic)} = J(\mu_{(ic)})$. Then if $J_{(ic)} < J(\mu_{(Y+1)})$, replace $\mu_{(Y+1)}$ with $\mu_{(oc)}$ and go back to step 1.

g) Shrink: If none of the above apply, then set $\mu_{(n)} = \mu_{(1)} - (\mu_{(n)} - \mu_{(1)})/2$, compute $J(\mu_{(n)})$, and return to step 1.

4.3.2 Gradient methods

When the cost function is easily differentiable, a gradient-based local optimization method can be used. These methods use the gradient of the cost function to determine where the cost is at a minimum. We present several variants on the standard iterative Newton's method [45]. We consider the quadratic model

$$m_{(n)}(\mu) = J(\mu_{(n)}) + \nabla J(\mu_{(n)})^T(\mu - \mu_{(n)}) + (\mu - \mu_{(n)})^T \nabla^2 J(\mu_{(n)})(\mu - \mu_{(n)})/2$$

about the iterate $\mu_{(n)}$. For the minimizer $\hat{\mu}$,

$$\nabla m(\hat{\mu}) = 0 \tag{4.3}$$

and $\nabla^2 J(\hat{\mu})$ is positive definite. Therefore in a Newton iteration, the new candidate set of parameters $\mu_{(n+1)}$ is calculated from the current set $\mu_{(n)}$ by

$$\mu_{(n+1)} = \mu_{(n)} - \nabla^2 J(\mu_{(n)})^{-1} \nabla J(\mu_{(n)}) \tag{4.4}$$

We then refer to $s = -\nabla^2 J(\mu_{(n)})^{-1} \nabla J(\mu)$ as the *step* s. The Gauss-Newton algorithm modifies Newton's method to be used on the nonlinear least squares problem. An approximation for the Hessian $\nabla^2 J$ is obtained by first writing the least squares cost as a function of the residual

$$R = (r_1, ..., r_N), \text{ where } r_i = (y_i^d - \hat{y}(t_i))/\omega. \tag{4.5}$$

The cost becomes

$$J(\mu) = \sum_{i=1}^{N} ||r(\mu_i)||^2 = R(\mu)^T R(\mu). \tag{4.6}$$

Then the gradient and Hessian are written as

$$\begin{aligned} \nabla J(\mu) &= 2R'(\mu)^T R(\mu), \\ \nabla^2 J(\mu) &= 2\left[R'(\mu)^T R'(\mu) + \sum_{i=1}^{N} r_i(\mu)^T \nabla^2 r_i(\mu) \right]. \end{aligned}$$

It is acceptable to eliminate the factor of 2 as it does not change the minimization problem [86]. Gauss-Newton uses only the first term of the Hessian, thus the step s is written as

$$s = -(R'(\mu_{(n)})^T R'(\mu_{(n)}))^{-1} R'(\mu_{(n)})^T R(\mu_{(n)}).$$

A variation that is of benefit when we start far from the minimizer $\hat{\mu}$ is the Levenberg-Marquardt algorithm. The theory supporting this method predicts convergence even when the initial parameter estimates are far from the solution, and rapid convergence when near the solution. A non-negative regularization damping parameter ν is added to the step to give

$$s = -(\nu_{(n)} I + R'(\mu_{(n)})^T R'(\mu_{(n)}))^{-1} R'(\mu_{(n)})^T R(\mu_{(n)}).$$

This is most useful when the matrices $R'(\mu)^T$ and $R'(\mu)$ are not of full column rank, uniformly bounded, or well-conditioned [45]. Then the matrix $-(\nu_{(n)} I + R'(\mu_{(n)})^T R'(\mu_{(n)}))$

is positive definite as required. We present the pseudocode for the Levenberg-Marquardt method with trust region, adapted from Kelley [45], p. 57. Parameters $\alpha_0 \leq \alpha_{low} < \alpha_{high}$ set the criteria for whether the trial step s should be rejected or ν should be adjusted. Parameters $0 < \omega_{down} < 1 < \omega_{up}$ designate the size and direction of the adjustment. Given the actual reduction in the cost $ared = J(\mu_{(n)}) - J(\mu_{(n+1)})$ and the predicted reduction $pred = -\nabla J(\mu_{(n)})^T s/2$, if $ared/pred$ is large, we can lower ν. The Gauss-Newton algorithm is recovered when ν is zero.

1. $z = \mu_{(n)}$.
2. Do while $z = \mu_{(n)}$,
   a) $ared = J(\mu_{(n)}) - J(\mu_{(n+1)})$, $s = \mu_{(n+1)} - \mu_{(n)}$, $pred = -\nabla J(\mu_{(n)})^T s/2$.
   b) If $ared/pred < \alpha_0$ then set $z = \mu_{(n)}$, $\nu = \max(\omega_{up}\nu, \nu_0)$, and recompute the trial point with the new value of ν.
   c) If $\alpha_0 \leq ared/pred < \alpha_{low}$, then set $z = \mu_{(n+1)}$ and $\nu = \max(\omega_{up}\nu, \nu_0)$.
   d) If $\alpha_{low} \leq ared/pred$, then set $z = \mu_{(n+1)}$.
   If $\alpha_{high} < ared/pred$, then set $\nu = \omega_{down}\nu$.
   If $\nu < \nu_0$, then set $\nu = 0$.
3. $\mu_{(n+1)} = z$.

4.4 Sensitivity analysis

The models can be described by a system of coupled nonlinear ODEs as presented in Chapter 3 that can be written as

$$\frac{dX}{dt} = F(X, t, \mu), \tag{4.7}$$

where $X(X, t, \mu) = [X_1, ..., X_Y]$ denotes the Y state variables and $\mu = [\mu_1, ..., \mu_Z]$ denotes the Z parameters to be identified. The differential equation analysis approach described by Eslami [25] and Frank [33] is used to derive sensitivity equations for the system of equations (4.7). The dynamic relative sensitivity S_{jk} of the state X_j to parameter μ_k, non-dimensionalized by X_j/μ_k, is defined as

$$S_{jk}(t, \mu)|_{\mu=\mu_0} = \left.\frac{\partial X_j(t, \mu)}{\partial \mu_k} \frac{\mu_k}{X_j(t, \mu)}\right|_{\mu=\mu_0}, \; X_j, \mu_k \neq 0. \tag{4.8}$$

Here $\mu_0 = [\mu_{1,0}...\mu_{Z,0}]$ denotes a specific set of values for the parameters.

As a first step in separating model parameters into sensitive and insensitive groups, a relative sensitivity $\mathbf{S_k}$ is computed as a norm composite over all times i and states j for each parameter of the form

$$\begin{aligned} \mathbf{S_{jk}}(\mu) &= ||S_{jk}(t,\mu_0)|| = \left|\left|\frac{dX_j(t_i,\mu_0)}{d\mu_k}\frac{\mu_k}{X_j(t_i,\mu_0)}\right|\right|, \\ \mathbf{S_k} &= ||\mathbf{S_{jk}}||\,. \end{aligned} \tag{4.9}$$

For example, if data is available for finger pressure p_{af} and cerebral blood flow velocity $v_{acp} = q_{acp}/A_{acp}$, where $q_{acp} = (p_{ac} - p_{vc})/R_{acp}$, the norms could be computed either over the two outputs p_{af}, v_{acp} or three states p_{af}, p_{ac}, p_{vc}, depending on the study.

To compute the partial derivatives $\partial X_i/\partial\mu_j$, also referred to as quasi-state variables, each differential equation of the form of (4.7) is differentiated with respect to each parameter and the derivatives are commuted:

$$\frac{\partial}{\partial\mu_k}\frac{dX_j}{dt} = \frac{d}{dt}\frac{\partial X_j}{\partial\mu_k} = \frac{\partial}{\partial\mu_k}F_j(X,\mu). \tag{4.10}$$

The sensitivities in (4.10) are solved simultaneously with the state equations in (4.7). Together these two systems of equations result in a total of $Y + Y \times Z = Y(Z+1)$ equations for the states $\{p_j, V_j\}$ augmented with the quasi-state solutions $\partial X_j/\partial\mu_k$. The full solution is the Y states and $Y \times Z$ quasi-states.

Deriving sensitivity equations analytically can be tedious and error prone for large systems. Alternatively, sensitivities can be derived using a computational approach. A simple finite difference method gives a numerical approximation to the derivatives with an increment h designated by the user. We used both forward difference and central difference approximations within the scope of our study,

$$\frac{\partial X_j}{\partial\mu_k} \approx \frac{X_j(t,\mu + he_k) - X_j(t,\mu)}{h}, \tag{4.11}$$

$$\frac{\partial X_j}{\partial\mu_k} \approx \frac{X_j(t,\mu + he_k) - X_j(t,\mu - he_k)}{2h}, \tag{4.12}$$

where

$$e_k = [0\ldots0\hat{1}0\ldots0]^T$$

is the unit vector in the e_k^{th} component direction. These methods are cheap and easy to use and implement, however acceptable accuracy must be verified for a given study.

Another option for obtaining derivatives is automatic differentiation (AD). Instead of approximating derivatives numerically or calculating them symbolically, automatic differentiation implements implement operators that calculate exact derivatives to machine precision [27, 95]. To apply AD, equation (4.10) is rewritten using the chain rule as

$$\frac{\partial}{\partial \mu_k}\frac{dX_l}{dt} = \frac{\partial}{\partial \mu_j}F_l(X_1,\ldots,X_Y,\mu_1,\ldots,\mu_Z) = \sum_{k=1}^{Y}\left(\frac{\partial F_l}{\partial X_j}\frac{\partial X_j}{\partial \mu_k}\right) + \frac{\partial F_l}{\partial \mu_k}, \tag{4.13}$$

where the Jacobians $\partial F/\partial X$ and $\partial F/\partial \mu$ are calculated using AD, and $\partial X/\partial \mu$ are the quasi-state variables. The subscript l refers to the particular ODE. Thus, the right hand side of the system of ODE's in (4.10) is constructed with the components of the Jacobians and the quasi-state variables. Solutions to quasi-state equations give time-series for $dX_j(t_i)/d\mu_k$.

We have used two AD algorithms for MATLAB in these studies. Both MAD, commercially available through TOMLAB [95], and myAD, developed by Martin Fink [27] and available in the public domain, use operator overloading. A new data class is defined specific to automatic differentiation and standard operators such as addition and multiplication are redefined, or "overloaded". As an example, when the overloaded operator `times` see an AD class object, it treats it as a variable and performs the product rule rather than double precision multiplication. Alternatively, AD can be carried out with source transformation, which compiles the source code objective function into its derivative code. This is similar to symbolic computation and currently more prevalent in C++ and FORTAN [31]. Of the two algorithms that use operator overloading we found myAD to perform about six times faster with our source codes. However, this was still too slow for use with gradient-based optimization algoritihms.

4.4.1 Windkessel example

To illustrate some of the sensitivity methods, an analysis was done on a three-element Windkessel model commonly used in cardiovascular applications. Sensitivity equations are computed both analytically and with a central difference scheme using several difference increments. The two classes of optimization algorithms are compared as well. The discussion here is based on the model and data presented in Olufsen *et al.* [71].

The Windkessel model describes the blood flow through one arterial compartment, in this case the MCA. This is a three-parameter model that describes blood flow q_{MCA} [ml/s] through the MCA as a function of blood pressure in the MCA, assumed to be approximated

by blood pressure in the finger p_F [mmHg]. A resistance R_S and compliance C_S characterize the MCA with R_P describing peripheral resistance. Full detail is shown in Figure 4.2. Since $Y = 1$ and $Z = 3$, there are 1 state equation

$$\frac{dq_{MCA}}{dt} = \frac{1}{R_S}\frac{dp_F}{dt} + \frac{p_F}{R_S C_S R_P} - \frac{(R_S + R_P)q_{MCA}}{R_S C_S R_P} \tag{4.14}$$

and $1 \times 3 = 3$ sensitivity equations:

$$\begin{aligned}
\frac{d}{dt}\frac{\partial q_{MCA}}{\partial R_S} &= \frac{1}{R_P C_S}\left[\left(\frac{R_S + R_P}{R_S^2} - \frac{1}{R_S}\right) q_{MCA} - \frac{R_S + R_P}{R_S}\frac{\partial q_{MCA}}{\partial R_S}\right] - \frac{p_F}{R_P C_S R_S^2} - \frac{1}{R_S^2}\frac{dp}{dt}, \\
\frac{d}{dt}\frac{\partial q_{MCA}}{\partial R_P} &= \frac{1}{R_S C_S}\left[\left(\frac{R_S + R_P}{R_P^2} - \frac{1}{R_P}\right) q_{MCA} - \frac{R_S + R_P}{R_P}\frac{\partial q_{MCA}}{\partial R_P}\right] - \frac{p_F}{R_S C_S R_P^2}, \\
\frac{d}{dt}\frac{\partial q_{MCA}}{\partial C_S} &= \frac{1}{R_S R_P}\left[\left(\frac{R_S + R_P}{C_S^2}\right) q_{MCA} - \frac{R_S + R_P}{C_S}\frac{dq_{MCA}}{dC_S}\right] - \frac{p_F}{R_P R_S C_S^2}.
\end{aligned} \tag{4.15}$$

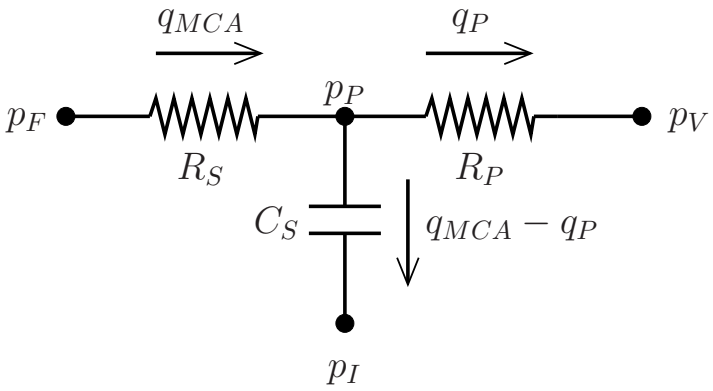

Figure 4.2: The Windkessel model represents flow through the middle cerebral artery q_{MCA} [ml/s] and its peripheral vasculature q_p [ml/s]. The parameters C_S [ml/mmHg] and R_S [mmHg·s/ml] are lumped representations of systemic compliance and resistance up to and including the MCA. Subscript P refers to vasculature in the cerebrovascular periphery. Pressures p_V and p_I [mmHg] are the venous pool and intracranial pressure. Reprinted from [71].

Nelder-Mead and Levenberg-Marquardt methods were used to estimate parameters predicting the data output $y = q_{MCA}$ with a nonlinear least squares residual cost function to quantifying the error between the data and the model q_{MCA}. A simple residual $R = q^d_{MCA,i} - q^c_{MCA,i}$ was used, such that the cost J became

$$J = \frac{\sum (q^d_{MCA,i} - q^c_{MCA,i})^2}{2}.$$

The data and model solution are shown in Figure 4.3 for time 10 to 20 seconds. As seen in Table 4.2, both methods return almost identical least-squares costs. Note however that final values for C_S are quite different from each other while values for R_S are almost the same. This is directly related to the sensitivity of the solution to these parameters as seen in the sensitivity analysis. We also observe that the CPU time for the Levenberg-Marquardt method is about five times that for the Nelder-Mead method, which may point to a benefit of simplex over gradient-based optimization methods for small systems.

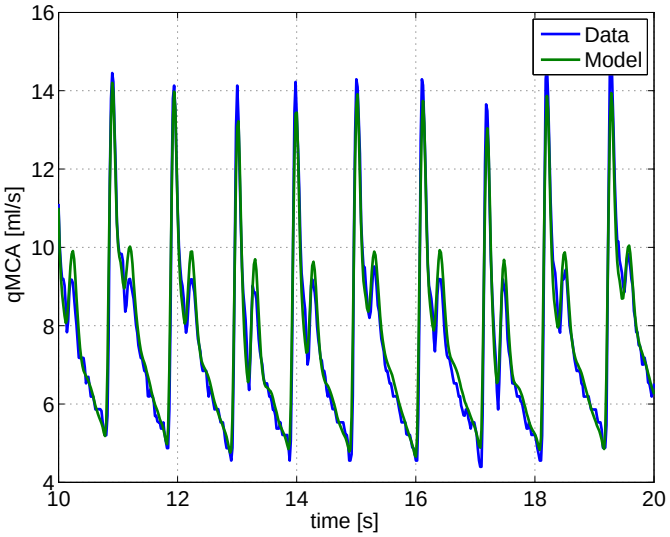

Figure 4.3: Model solution q_{MCA} compared to data for the windkessel model, (4.15). Data from Olufsen *et al.* [71].

Equations (4.15) were solved with the Nelder-Mead method using the optimized values found by Olufsen *et al.* [71]. The solutions give the sensitivity of the output state q_{MCA} to each of the parameters as a function of time. Results shown in Figure 4.4 reveal that the systemic resistance R_S is the most sensitive parameter, followed by the peripheral resistance R_P. The least sensitive parameter is C_S, which is virtually zero across the timespan of the analysis. The optimized values for C_S varied the most between two methods and R_S the least, consistent with the results in Table 4.2.

A central difference method (4.12) corroborated the findings of the analytical derivatives. Quasi-state sensitivity solutions were approximated where h was set at 10^{-4}, 10^{-6}, and 10^{-8}. An h of 10^{-6} was sufficient to produce solutions consistent with the analytical derivatives, see Figure 4.5.

Table 4.2: Optimized parameter values, least squares cost, and CPU time for the windkessel model. R_P, R_S in [mmHg·s/ml], C_S in [ml/mmHg].

Optimization Method	Least Squares Cost	CPU time [s]	$[R_S, R_P, C_S]$
Initial	670.17	n/a	[10.60, 5.40, 3.30]
Nelder-Mead	140.17	$2.23 \cdot 10^3$	[5.98, 5.52, 5.21]
Levenberg-Marquardt	141.17	$1.03 \cdot 10^4$	[5.94,5.40,6.36]

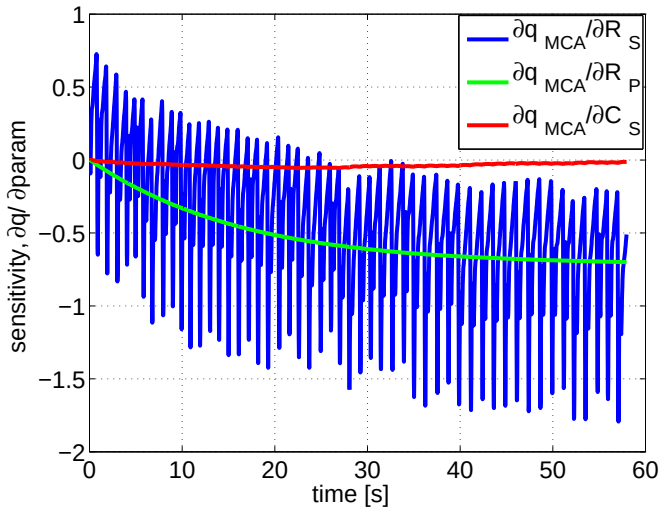

Figure 4.4: Sensitivities ($\partial q/\partial \mu$) of flow q_{MCA} with respect to windkessel parameters R_S [mmHg·s/ml], R_P [mmHg·s/ml], and C_S [ml/mmHg].

4.5 Subset selection

Subset selection is used to predict independent candidate parameters for numerical optimization. The result from the subset selection method is a list of identifiable parameters and a list of parameters that should be held constant at nominal parameter values during the optimization process.

Subset selection analyzes the Jacobian matrix ($dR/d\mu$) computed from the scaled residual vector R. The entry at row j and column k of the Jacobian is $\partial R_j/\partial \mu_k$. Using the Jacobian, singular value decomposition $R' = U\Sigma V^T$ is used to obtain a numerical rank [34] for R'. The numerical rank is then used to determine ρ parameters that can be identified given the model output $y = X(\hat{\mu})$ defined in Section 4.2. QR decomposition is used to determine the ρ identifiable parameters to which our system is sensitive *as a group*. This differs from sensitivity analysis, which finds independent parameters to which our system

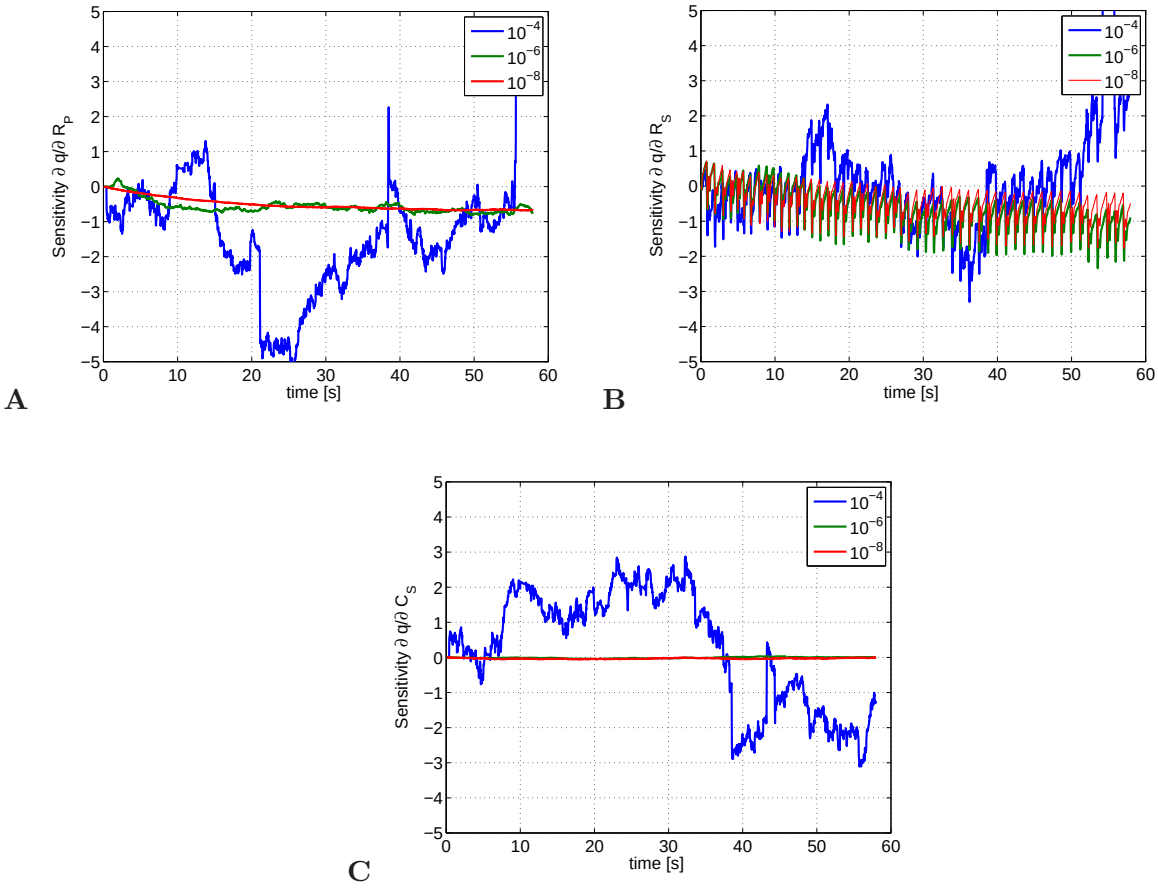

Figure 4.5: Sensitivities of q_{MCA} with respect to each of the three parameters, approximated with the centered difference method (4.12) using h=10^{-4}, 10^{-6}, and 10^{-8}. A: peripheral resistance R_p. B: systemic resistance R_S. C: systemic compliance C_S.

is *individually sensitive*. The subset selection algorithm proceeds as follows:

1. Given an initial parameter estimate, μ_0, compute the Jacobian, $R'(\mu_0)$ and the singular value decomposition $R' = U\Sigma V^T$, where Σ is a diagonal matrix containing the singular values of R' in decreasing order, and V is an orthogonal matrix of right singular vectors.

2. Determine ρ, the numerical rank of R'. This can be done by determining a smallest allowable singular value.

3. Partition the matrix of eigenvectors as $V = [V_\rho V_{Z-\rho}]$.

4. Determine a permutation matrix P by constructing a QR decomposition with column

pivoting, see [35] p. 235, for V_ρ. That is, determine P such that

$$V_\rho^T P = QR,$$

where Q is an orthogonal matrix and the first ρ columns of R form an upper triangular matrix with diagonal elements in decreasing order.

5. Use P to re-order the parameter vector μ_0 according to $\tilde{\mu}_0 = P^T \mu_0$.

6. Make the partition $\tilde{\mu}_0 = [\tilde{\mu}_{0,\rho} \tilde{\mu}_{0,Z-\rho}]$ where $\tilde{\mu}_{0,\rho}$ contains the first ρ elements of $\tilde{\mu}_0$. Fix $\tilde{\mu}_{0,Z-\rho}$ at the a priori estimate $\tilde{\mu}_{0,Z-\rho}$.

7. Compute the new estimate of the parameter vector $\hat{\mu}$ by solving the reduced-order minimization problem

$$\hat{\mu} = \arg\min_{\mu} J(\tilde{\mu}), \text{ with } \tilde{\mu}_{0,Z-\rho} \text{fixed at nominal values.}$$

Steps one and two are used to determine the numerical rank ρ of R'. It is possible to estimate a smallest acceptable singular value by analyzing the Jacobian error bound. Since the Jacobian is computed using forward differences, the error of the Jacobian is approximately the square root of the error tolerance of the ODE solver. Thus if ϵ is the Jacobian error, then, according to [35] p. 428, this error can change the singular values of the Jacobian by ϵ. Thus, we cannot trust any singular value smaller than ϵ, and consequently, we use ϵ as the smallest acceptable singular value. For example, if we set the absolute error tolerance to 10^{-6}, i.e., the error of the numerical model solution is of order 10^{-6}, then the error in the Jacobian matrix is approximately $\sqrt{10^{-6}} = 10^{-3}$. Consequently, singular values should not be smaller than 10^{-3} . Since the error of the Jacobian is an approximation, the smallest singular value that we accept is 10^{-2}. If errors are relative instead of absolute, the smallest acceptable singular values are $10^{-2}||R'||_2$. The latter condition is equivalent to choosing columns of R' that form a matrix with condition number no greater than 10^2.

Once the number of identifiable parameters has been determined, we find the most dominant parameters by performing a QR decomposition with column pivoting on the most dominant right singular vectors computed in step 4. The process begins by choosing the most sensitive parameter in a way similar but not identical to the sensitivity analysis of the previous section, the column with largest 2-norm is chosen. The algorithm chooses additional parameters in a way that keeps the condition number of the chosen columns small, for more detail see [35] p. 233-236.

Chapter 5

11-Compartment Cardiovascular Model

The goal of this study was to develop a mathematical model that predicted dynamics in observed CBFV and peripheral ABP data and propose mechanisms that can explain the interaction between autonomic and cerebral autoregulation. To validate the model, we compared model predictions with measurements of arterial finger blood pressure and middle cerebral artery blood flow velocity of a young subject, with methods proposed in Chapter 4. We study cerebrovascular regulation by examining pressure changes during a sit-to-stand maneuver. On the transition from sitting in a chair to standing, 300-800 ml of blood pools in the lower extremities as a result of gravitational forces [11, 53]. Venous return is reduced, which leads to a decrease in diastolic filling and thus stroke volume and cardiac output via the Frank-Starling effect. Arterial blood pressure declines and an immediate decrease in blood flow to the brain is seen. The baroreflex is activated as described in Section 2.3.1. This increases heart rate, cardiac contractility, and peripheral resistance, ultimately raising arterial blood pressure. Simultaneously, the cerebral autoregulatory response to decreased blood flow is vasodilation of cerebral arteries leading to increased cerebral blood flow (see Section 2.3.2). To study these phenomena, we developed a mathematical model that includes two submodels: 1. A cardiovascular model that can predict blood pressure and blood flow velocity during sitting, and 2. A control model that can predict the autonomic and cerebral regulatory mechanisms during the postural change from sitting to standing.

5.1 Model construction

The model, see Figure 5.1, is developed using an electrical circuit analog model described in Chapter 3. Using this analog, the thorax and lower body is represented by four compartments, two each for the upper and lower body, to model venous pooling and sympathetic effects on the different vascular beds. Two compartments model the cerebral circulation to allow the study of cerebral regulation and validate the model against CBF data measured in the MCA. A compartment for the finger arteries is included to allow for validation of the model against blood pressure data measured in the finger. The heart, which generates pressure to drive the blood flow through the circulation, is modeled by two compartments representing the left atrium and ventricle. The atrium ensures adequate filling of the heart and the ventricle generates the pulse pressure. The mitral and aortic valves are included as part of the left ventricle to ensure proper pressure development and direction of the blood flow. Finally, to close the loop and to determine cardiac output and venous return, the aorta and vena cava are modeled with distinct compartments. At each level, except the finger, veins and arteries are separate because of venous pooling in the veins and autonomic effects in the arteries.

The pulmonary circulation is not included in this model because the majority of the control mechanisms and the relevant data correspond to the systemic circulation only. Instead, the cumulative effects of the pulmonary circulation are combined into the resistance between the vena cava and the atrium. The effects of respiratory changes that may occur during the duration of the data collection are ignored.

5.1.1 State equations

As discussed in Chapter 3, the systemic circulation is depicted using an electrical circuit analog model. The model has 9 pressures $p_i(t)$ represented as state variables in the manner of (3.5), one for each of the arterial and venous pressures. For example, the rate of change of arterial finger pressure, dp_{af}/dt, is given by

$$\frac{dp_{af}}{dt} = \frac{1}{C_{af}} \left(\frac{p_a - p_{af}}{R_{af}} - \frac{p_{af} - p_v}{R_{afp}} \right), \tag{5.1}$$

where p_{af}, p_a and p_v represent model states and C_{af}, R_{af}, and R_{afp} are model parameters. A complete list of equations and model parameters is given in Appendix A.1.

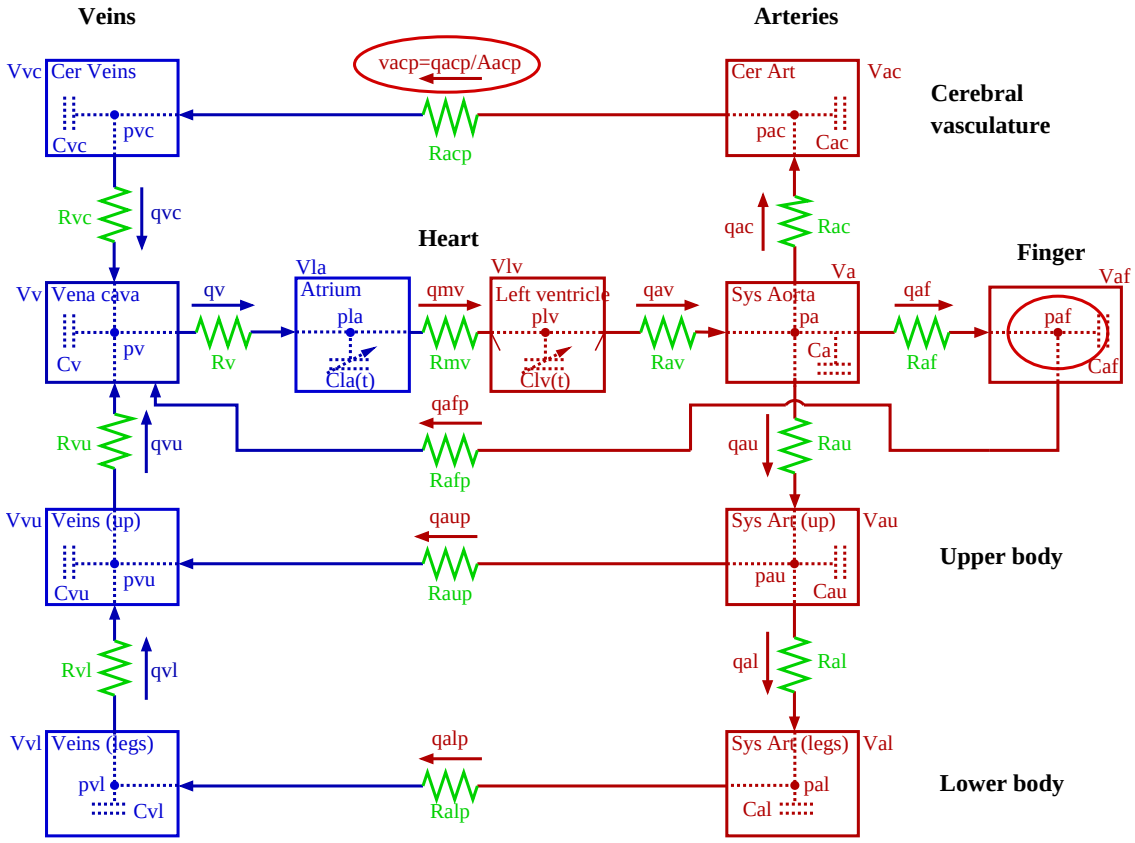

Figure 5.1: Compartmental model representing systemic circulation. The model contains 11 compartments, including: 5 systemic artery beds, 4 systemic venous beds, and the left atrium and left ventricle. Because the pulmonary system is not included, systemic veins are directly attached to the left ventricle. Each pressure compartment p [mmHg] includes a capacitor C [ml/mmHg] to represent compliant volume V [ml] of arteries or veins. All compartments are separated by resistors R [mmHg·s/ml] representing resistance of the vessels to blood flow Q [ml/s]. The compartment representing the left ventricle has 2 valves. Resistors are marked with zigzag lines, capacitors with dashed parallel lines inside the compartments, and aortic and mitral valves with short lines inside the compartment that represents the left ventricle.

The pressure in the left atrium (la) and ventricle (lv) are explicitly defined as described in (3.9) and (3.10). However they are functions of volume and therefore modeled by the simple volume conservation relation in (3.6). Only the mitral and aortic valves appear in this model as part of the left ventricle, and are represented by the equations in (3.12) with $k = 10$ and $R_{valve,closed} = 5000$.

Table 5.1: Initial and optimized parameter values used to predict the baseline dynamics. Subscripts v and a refer to ventricular and atrial parameters, see (3.10), (3.12).

Resistances and Compliances	Initial	Optimized	Heart	Initial	Optimized
R_{av} [mmHg·s/ml]	0.030	0.115	a_v [mmHg/ml^2]	0.0003	0.001
R_{au} [mmHg·s/ml]	0.072	0.185	b_v [ml]	5	4.912
R_{al} [mmHg·s/ml]	0.087	0.0043	c_v [mmHg/ml]	6.4	6.910
R_{af} [mmHg·s/ml]	0.183	0.546	d_v [mmHg]	1	0.831
R_{ac} [mmHg·s/ml]	0.409	0.318	n_v	2	3.666
R_{aup} [mmHg·s/ml]	1.565	1.857	m_v	2.2	1.737
R_{alp} [mmHg·s/ml]	6.522	7.585	ν_v	9.9	11.020
R_{apf} [mmHg·s/ml]	17.5	17.895	$\theta_v[1/s]$	0.951	0.921
R_{acp} [mmHg·s/ml]	6.696	7.084	η_v	17.5	17.666
R_{mv} [mmHg·s/ml]	0.007	0.0164	ϕ_v [1/s]	1	1.156
R_v [mmHg·s/ml]	0.033	0.037	$t_{min,v}$ [s]	0.186	0.131
R_{vu} [mmHg·s/ml]	0.001	0.000	$t_{max,v}$ [s]	0.280	0.231
R_{vl} [mmHg·s/ml]	0.174	0.119	$p_{min,v}$	0.842	1.107
R_{vc} [mmHg·s/ml]	0.957	1.288	$p_{max,v}$	1.158	1.239
C_a [ml/mmHg]	0.084	0.0732	a_a [mmHg/ml^2]	0.002	0.0002
C_{au} [ml/mmHg]	0.616	0.726	b_a [ml]	5	4.107
C_{al} [ml/mmHg]	0.940	0.988	c_a [mmHg/ml]	6.4	6.433
C_{af} [ml/mmHg]	0.174	0.235	d_a [mmHg]	1	1.167
C_{ac} [ml/mmHg]	0.159	0.0892	n_a	1.9	1.950
C_v [ml/mmHg]	2.931	2.518	m_a	2.2	1.977
C_{vu} [ml/mmHg]	15.276	15.453	ν_a	9.9	10.860
C_{vl} [ml/mmHg]	6.038	6.278	$\theta_a[1/s]$	1	2.000
C_{vc} [ml/mmHg]	2.847	2.301	η_a	17.5	16.539
			ϕ_a [1/s]	1	2.115
A_{acp} [cm^2]	0.142	0.208	$t_{min,a}$ [s]	0.186	0.249
α	1.429	2.322	$t_{max,a}$ [s]	0.280	0.356
			$p_{min,a}$	0.842	1.007
			$p_{max,a}$	0.990	1.210

5.1.2 Nonlinear resistances

To our knowledge, previous modeling contributions assume that, during steady state, i.e., sitting, the small resistances between compartments that represent large conduit vessels are constant (see Chapter 3 and [41, 93]). However, it is known from fluid mechanics that resistance is inversely proportional to vessel radius (see (3.2)) which in turn is proportional to the transmural pressure at the corresponding location within the vessel [103]. Such dependencies are important to include in regions that represent vessels with large diameters and high blood pressure (i.e., large arteries), whereas they are less important in regions of

low blood pressure (i.e., the venous system). Furthermore, these "passive" changes in diameters are also negligible in regions with small vessels (i.e., small arteries and arterioles), where autonomic responses are active and dominate the change in vessel diameters. In this section we will show the effect of including these nonlinear "passive" resistance changes in the larger arteries, then follow with a discussion of modeling the autonomic control in the smaller arteries.

To model these resistances, we base our derivation on Poiseuille's Law, see (3.2). The length l of a vessel can be assumed to be constant, which leads to the relation

$$\frac{1}{R} \propto r^4 \propto V^2 \propto p^2. \tag{5.2}$$

The first of these relations comes from Poiseuille's law, the second from the assumption of fixed vessel length l, and the third from the relation $V_{str} = Cp$. Since we use a compartmental model, and each compartment represents a number of vessels lumped together, we have no specific information about r for any particular vessel. Instead we build upon the relation in (5.2), recognizing that in a real artery, the resistance will saturate at minimum and maximum values. Hence this inverse relation is modeled with a decreasing sigmoidal function of the form

$$R = (R_M - R_m)\frac{p_0^k}{p^k + p_0^k} + R_m, \tag{5.3}$$

where R_M and R_m are the maximum and minimum values for resistance and p is the blood pressure in the compartment that precedes the resistance. The parameter k represents the steepness of the sigmoid. The parameter p_0 is calculated such that R returns to the value of the controlled parameter found during the steady-state, denoted R_s

$$p_0 = \bar{p}_{goal}\left[\frac{R_s - R_m}{R_M - R_s}\right]^{1/k}. \tag{5.4}$$

The mean pressure at which R_s is attained is $\bar{p}_{goal}$, set according to a sigmoidal function connecting the mean pressures from the sitting $\bar{p}_{sit}$ and standing $\bar{p}_{stand}$ portions of the data

$$\bar{p}_{goal} = \bar{p}_{sit} + \frac{\bar{p}_{stand} - \bar{p}_{sit}}{1 + e^{-k(t - T_{up} - \delta)}}.$$

For $k = 2$, the slope of the sigmoid approximates the relation in (5.2). However, this relation is valid only for a steady flow. Blood flow in arteries is unsteady, and the flow through a given vessel depends on the state of the vessel. Consequently, as shown in Table 5.2, k cannot be assumed to always be 2.

Table 5.2: Optimized parameters for nonlinear passive resistances and control equations. Units: p [mmHg], τ [s], h [cm], δ [s], R [mmHg·s/ml], C [ml/mmHg], k dimensionless.

Initial and optimized regulation parameters					
Parameter	Initial	Optimal	Parameter	Initial	Optimal
p_a	92.8	-	$k(c_a)$	2.0	4.58
p_{au}	90.0	-	$R_M(c_a)$	$4 \times c_v^{ss}$	11.99
τ_{Cv}	10.0	18.57	$R_m(c_a)$	$c_v^{ss}/4$	0.94
τ_{Ca}	10.0	13.67	$k(C_a)$	2.0	0.38
τ_R	5.0	23.03	$C_M(C_a)$	$4 \times C_a^{ss}$	4.3×10^{-2}
τ_S	5.0	0.076	$C_m(C_a)$	$C_a^{ss}/4$	4.8×10^{-4}
h_H	50.0	46.73	$k(C_{au})$	2.0	17.22
h_k	3.0	3.92	$C_M(C_{au})$	$4 \times C_{au}^{ss}$	1.01
δ	0.4	1.26	$C_m(C_{au})$	$C_{au}^{ss}/4$	0.42
$k(R_{al})$	5.0	1.48	$k(C_{al})$	2.0	13.90
$R_M(R_{al})$	$10 \times R_{al}^{ss}$	1.69	$C_M(C_{al})$	$4 \times C_{al}^{ss}$	15.25
$R_m(R_{al})$	$R_{al}^{ss}/10$	1.1×10^{-3}	$C_m(C_{al})$	$C_{al}^{ss}/4$	0.82
$k(R_{ac})$	5.0	8.79	$k(C_{ac})$	2.0	4.05
$R_M(R_{ac})$	$10 \times R_{ac}^{ss}$	2.49	$C_M(C_{ac})$	$4 \times C_{ac}^{ss}$	0.23
$R_m(R_{ac})$	$R_{ac}^{ss}/10$	1.3×10^{-2}	$C_m(C_{ac})$	$C_{ac}^{ss}/4$	7.0×10^{-2}
$k(R_{af})$	5.0	3.83	$k(C_{af})$	2.0	81.34
$R_M(R_{af})$	$10 \times R_{af}^{ss}$	1.5×10^{-1}	$C_M(C_{af})$	$4 \times C_{af}^{ss}$	0.46
$R_m(R_{af})$	$R_{af}^{ss}/10$	2.9×10^{-5}	$C_m(C_{af})$	$C_{af}^{ss}/4$	1.7×10^{-2}
$k(R_{aup})$	2.0	5.74	$k(C_v)$	3.0	0.47
$R_M(R_{aup})$	$4 \times R_{aup}^{ss}$	14.58	$C_M(C_v)$	$5 \times C_v^{ss}$	15.32
$R_m(R_{aup})$	$R_{aup}^{ss}/4$	0.13	$C_m(C_v)$	$C_v^{ss}/5$	0.52
$k(R_{alp})$	5.0	10.57	$k(C_{vu})$	3.0	12.90
$R_M(R_{alp})$	$10 \times R_{alp}^{ss}$	145.19	$C_M(C_{vu})$	$5 \times C_{vu}^{ss}$	55.86
$R_m(R_{alp})$	$R_{alp}^{ss}/10$	0.41	$C_m(C_{vu})$	$C_{vu}^{ss}/5$	1.93
$k(R_{afp})$	2.0	3.69	$k(C_{vl})$	3.0	47.93
$R_M(R_{afp})$	$4 \times R_{afp}^{ss}$	64.81	$C_M(C_{vl})$	$5 \times C_{vl}^{ss}$	277.94
$R_m(R_{afp})$	$R_{afp}^{ss}/4$	0.16	$C_m(C_{vl})$	$C_{vl}^{ss}/5$	0.17
$k(c_v)$	2.0	4.62	$k(C_{vc})$	3.0	15.71
$R_M(c_v)$	$4 \times c_v^{ss}$	17.27	$C_M(C_{vc})$	$5 \times C_{vc}^{ss}$	13.89
$R_m(c_v)$	$c_v^{ss}/4$	1.04	$C_m(C_{vc})$	$C_{vc}^{ss}/5$	0.19

Resistances of major arteries are computed as functions of mean pressure: $R_{al}(\bar{p}_{au})$, $R_{ac}(\bar{p}_a)$, and $R_{af}(\bar{p}_a)$. The resistance of the aorta (R_{au}) could also be modeled using this method. Initial investigations showed that other mechanisms, e.g., autoregulation or autonomic regulation, may also affect R_{au}. As a consequence, the initial approach was used to estimate R_{au}, discussed further in Section 5.1.4.

Mean arterial pressures $\bar{p}_i$, where i refers to either a or au, were defined as weighted

averages, where the present is weighted higher than the past:

$$\bar{p}(t) = \alpha \int_{-\infty}^{t} p(s) e^{-\alpha(t-s)} ds. \tag{5.5}$$

Differentiating, we obtain

$$\begin{aligned} \frac{d\bar{p}(t)}{dt} &= \alpha \left[\int_{-\infty}^{t} -\alpha p(s) e^{-\alpha(t-s)} ds + p(t) \right] \\ &= \alpha(-\bar{p}(t) + p(t)). \end{aligned} \tag{5.6}$$

Data for the time period from $-\infty \to 0$ does not exist, therefore we instead define the bottom limit in (5.5) to be 0 which gives the same result as (5.6). For $p(t) = 1$, this definition gives

$$\bar{p}(t) = \alpha \int_{0}^{t} e^{\alpha(t-s)} ds = \alpha \left[\frac{e^{-\alpha(t-s)}}{\alpha} \right]_{0}^{t} = 1 - e^{-\alpha t}.$$

Thus if we redefine the mean pressure as the scaled quantity

$$\bar{p}(t) = \frac{\alpha}{1 - e^{-\alpha t}} \int_{0}^{t} p(s) e^{-\alpha(t-s)} ds,$$

then $\bar{p} = 1$ when $p(t) = 1$, and

$$\frac{d\bar{p}(t)}{dt} = \frac{\alpha}{1 - e^{-\alpha t}} (-\bar{p}(t) + p(t)).$$

As seen in Figure 5.2, $\bar{p}_a$ oscillates with the same frequency as pressure p_a but with a smaller amplitude.

5.1.3 Gravity effects

Gravitational effects are essential during postural change from sitting to standing. We consider a cylindrical vessel with length Δz [cm], radius r [cm], and time-invariant cross-sectional area A [cm^2], i.e., $dA/dt = 0$, see Figure 5.3 and assume that velocity $v(r, z, t)$ [cm/s] is constant with respect to both spatial dimensions. Hence $v(t)$ only, therefore the volumetric flow rate becomes $q(t) = Av(t)$ [ml/s]. The blood pressure is assumed to be only a linear function of position along the vessel, i.e., dp/dz is constant, giving a pressure differential of $(p_{in} - p_{out})/\Delta z$.

A force balance coming from Newton's second law is used to derive the mathematical model [93]. The total force f_{total} to move the volume of blood in a characteristic vessel segment with length Δz and cross-sectional area A is

$$f_{total} = (p_{in} - p_{out})A.$$

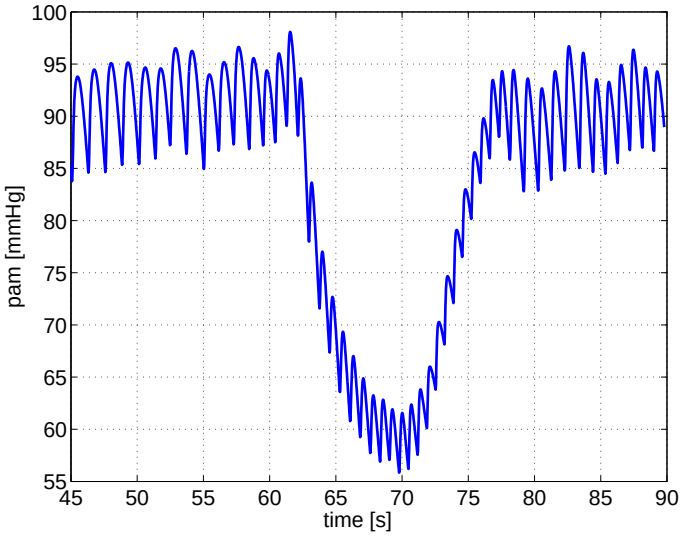

Figure 5.2: Mean arterial pressure $\bar{p}_a$ [mmHg], for $45 \leq t \leq 90$ s, computed using (5.6). Similar results were found for $\bar{p}_{au}$ [mmHg].

This must balance with the sum of the viscous resistance force f_{res}, the inertial force f_{iner}, and the gravitational force f_{grav}. As discussed in Section 2.1.2, the pressure drop due to resistance to flow is given by Ohm's law for hemodynamics, $\Delta p = qR$, see (3.1). Thus

$$f_{res} = qAR.$$

The inertial force f_{inert} is given by

$$f_{iner} = M\frac{dv}{dt} = \rho A \Delta z \frac{d}{dt}\left(\frac{q}{A}\right) = \rho \Delta z \frac{dq}{dt},$$

where ρ=1.055 [g/ml] is the density of the fluid and M [g] is the mass of the fluid contained in the characteristic vessel segment. Finally, f_{grav} is the product of the mass of the fluid and the component of the acceleration of gravity in the downward direction

$$f_{grav} = Mg\cos(\phi),$$

where $g = 981$ [cm/s^2] is the gravitational acceleration and ψ is the angle the vessel makes with the horizontal axis. Dividing by A, it follows that

$$p_{in} - p_{out} = L\frac{dq}{dt} + -\rho g \Delta h + qR,$$

where $L = \rho \Delta z / A$ [1/s^2] is inertance and $\Delta h = \Delta z \cos(\phi) = h_{in} - h_{out}$ [cm] is the vertical difference of the vessel inlet (at h_{in} where p_{in} and p_{out} represent pressure at the inlet and

outlet, respectively). We neglect inertial effects in this study, which reduces (5.1.3) to

$$q = \frac{(p_{in} + \rho g h_{in}) - (p_{out} + \rho g h_{out})}{R}. \tag{5.7}$$

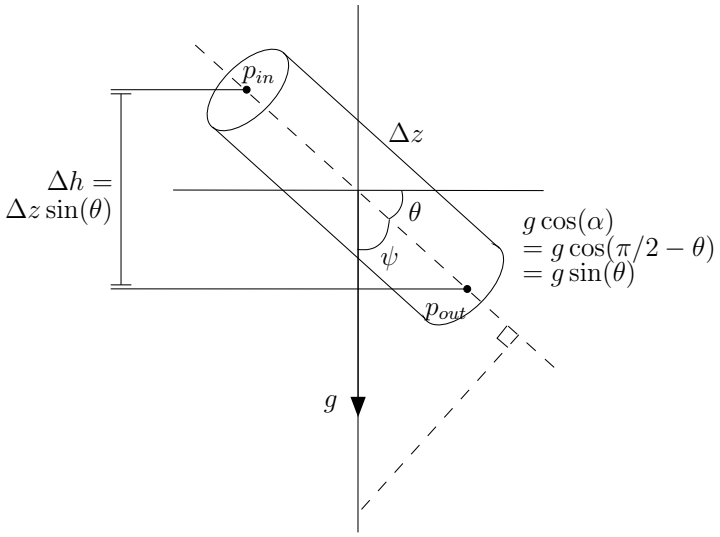

Figure 5.3: Vessel segment with cross-sectional area A [ml] and length Δz [cm]. Pressures at the vessel inlet and outlet are p_{in} and p_{out} [mmHg]. Vessel is at an angle θ with respect to the direction of gravity g [cm/s^2] and at an angle ψ with respect to the horizontal axis. Difference in vertical latitude is $\Delta h = \Delta z \cos(\phi)$ [cm].

When modeling postural change from sitting to standing, we substitute (5.7) for Ohm's law in the state equations. In the limit $g \to 0$, (5.7) approaches the normal form of Ohm's law. In the case of energy conservation, i.e., negligible viscous losses ($R \to 0$), Bernoulli's law for steady flow is recovered; as a result, $p_{in} + \rho g h_{in} = p_{out} + \rho g h_{out}$. Thus Ohm's law is still valid if we interpret p as the hydrostatic pressure $p + \rho g h$.

To capture the transition from sitting to standing, h is defined for the lower body compartments as the exponentially increasing function

$$h(t) = \frac{\Delta h}{1 + e^{-k(t - T_{up} - \delta)}}, \tag{5.8}$$

where T_{up} is the time at which the subject stands up, Δh [cm] is an estimated height difference for the sit-to-stand transition for the average subject, and δ [s] is the latency for the transition to standing. Because the pressure is measured in the finger held at the level of the heart, compartments that represent the heart and finger are not affected by gravity and we consider these to be at height $h = 0$. Compartments that represent the brain and

the upper body are exposed to constant hydrostatic conditions during sit-to-stand since the height difference between the heart and these two areas does not change during the maneuver. Therefore hydrostatic effects in these compartment were not included. However, the distance between legs and heart increases during standing so these compartments are affected by gravity. Consequently, equations for the flows q_{al} and q_{vl} were modified as described in (5.7)

$$q_{al} = \frac{p_{au} - (p_{al} + \rho g h)}{R_{al}},$$
$$q_{vl} = \frac{(p_{vl} + \rho g h) - p_{vu}}{R_{vl}}.$$

In the first of these equations, $h_{in} = 0$ and $h_{out} = h$, where h is computed using (5.8). In the second, $h_{in} = h$ and $h_{out} = 0$. The transition to standing is on the order of seconds, so it is assumed that vessels remain vertical, i.e. $\phi = 0$ and $\cos(\phi) = 1$. Thus h is just the estimated length of the vascular bed relative to the heart at a given time.

5.1.4 Regulation

The autonomic response to postural change regulates mean arterial blood pressure $\bar{p}_a$ by controlling cardiac contractility (c_a and c_v, mmHg/ml), peripheral systemic resistances (R_{aup}, R_{alp}, and R_{afp}, mmHg·s/ml) and systemic compliances (C_a, C_{au}, C_{al}, C_{ac}, C_{af}, C_v, C_{vu}, C_{vl}, and C_{vc}). Physiologically, HR is also regulated by the autonomic system, but we extract it from the data for use as an input to the ventricular pressure function so it is not modeled as a function of $\bar{p}_a$.

The change in the controlled parameters is modeled using a first-order differential equation with a set-point function dependent on $\bar{p}_a$

$$\frac{dx(t)}{dt} = \frac{-x(t) + x_{ctr}(\bar{p}_a)}{\tau}. \tag{5.9}$$

This equation ensures that as the controlled parameter $x_{ctr}(t)$ increases with an increase or decrease in mean pressure $\bar{p}_a$, dx/dt becomes more positive and $x(t)$ grows, thus bringing dx/dt back to zero. The reverse occurs when $x_{ctr}(t)$ decreases. The parameter τ [s] is a time constant that characterizes the time required for the controlled variable to obtain its full effect. Different values of τ are used for control of cardiac contractility, compliance, and resistance, representing the varying time scales of the corresponding responses.

To obtain increases in peripheral resistances (R_{aup}, R_{alp}, and R_{afp}) and cardiac contractility (c_a and c_v) in response to the decrease in arterial blood pressure, the following set-point function has been used

$$x_{ctr}(\bar{p}_a) = (x_M - x_m)\frac{p_0^k}{\bar{p}_a^k + p_0^k} + x_m, \tag{5.10}$$

where $x = R, c$ and x_M and x_m are the maximum and minimum possible values for each resistance or contractility parameter. Thus the sigmoidal set-point function reflects the passive effects during steady-state, see (5.3).

Vascular tone is increased in response to a decrease in arterial blood pressure, leading to a decrease in compliance. Thus, for the compliances $x = C$, the set-point function has the form

$$x_{ctr}(\bar{p}_a) = (x_M - x_m)\frac{\bar{p}_a^k}{\bar{p}_a^k + p_0^k} + x_m. \tag{5.11}$$

Equation (5.10) gives rise to a decreasing sigmoidal curve (i.e. for a decreasing pressure, the value of x_{ctr} will increase), whereas (5.11) gives rise to an increasing sigmoidal curve (i.e. for a decreasing pressure, the value of x_{ctr} will decrease). The parameter p_0 is calculated to ensure that $x(t)$ returns the value of the controlled parameters found during steady-state, similar to (5.4). Initial parameter values for k, x_m, and x_M are from Danielsen [21]. Note that $\bar{p}_a$ in these implementations is that described by (5.6).

During the transition to standing, cerebral autoregulation mediates a decline in cerebrovascular resistance (R_{acp}) in response to the decrease in arterial blood pressure, the opposite of the peripheral response. In addition, the autonomic nervous system may also play a role, by decreasing the resistance due to cholinergic vasodilation or by increasing the resistance due to release of norepinephrine [37, 117]. Consequently, it is not trivial to develop an accurate physiological model that describes cerebrovascular regulation. The strategy discussed here uses a piecewise linear function with unknown coefficients to obtain a representative function that shows the behavior of the time-varying response of the cerebrovascular resistance. Once such a function is obtained, the result is interpreted in terms of the suspected underlying physiology. To obtain such a function, the cerebrovascular resistance is parameterized using piecewise linear functions of the form

$$R_{acp}(t) = \sum_{i=1}^{n} \gamma_i h_i(t), \tag{5.12}$$

where h_i represents the standard "hat" functions given by

$$h_i(t) \begin{cases} \dfrac{t - t_{i-1}}{t_i - t_{i-1}}, & t_{i-1} \leq t \leq t_i \\ \dfrac{t_{i+1} - t}{t_{i+1} - t_{i-1}}, & t_i \leq t \leq t_{i+1} \\ 0, & \text{otherwise.} \end{cases} \tag{5.13}$$

The unknown coefficients γ_i are estimated together with the other control parameters in Table 5.2. The same method is used to estimate the behavior of the resistance R_{au}, which as a compartment representing large arteries may be affected not only by passive nonlinear resistances but also autonomic regulation.

5.2 Experimental data

Data for this study were collected in the laboratory of Dr. Lewis A. Lipsitz, Institute for Aging Research, Hebrew Senior Life, Boston. The 11-compartment model was validated against continuous physiological data from a young subject which included ABP measurements from the finger and arterial CBFV from the MCA [50]. The subject was instrumented with a three-lead ECG (Collins) to obtain HR and a photoplethysmographic cuff placed on the middle finger of the non-dominant hand supported at the level of the right atrium to obtain noninvasive beat-to-beat blood pressure (Finapres, Ohmeda). The middle cerebral artery was insonated by placement of a 2-MHz Doppler probe (Nicolet Companion) over the temporal window to obtain continuous measurements of blood flow velocity. The envelope of the velocity waveform was derived from the fast Fourier transform of the Doppler signal, as described by Aaslid et al [2]. All physiological signals were digitized at 500 Hz (Windaq, Dataq Instruments) and downsampled to 50Hz for this analysis.

The subject sat in a straight-backed chair with his legs elevated at 90^{O} in front of him for 5 minutes of baseline recording. The subject was then asked to stand, the standing motion taking about 2 seconds to complete. Recordings continued throughout the stand. This was performed three times, twice with one minute of standing and the third time with six minutes of standing. Standing was defined as the moment both feet touched the floor.

Figure 5.4 shows the characteristic features of the measured data. After the transition to standing at $t = 60$ s, blood pressure (systolic, diastolic, and mean values) dropped significantly. At the same time, mean blood flow velocity decreased during the transition

from sitting to standing (dark line through pulsatile velocity data). However, although systolic and diastolic values of pressure decreased, only the diastolic value of the blood flow velocity was diminished. The systolic values remained at baseline or were even slightly increased. This yields a significant widening of the flow pulse, a feature typical for young adults with normal regulatory responses [50].

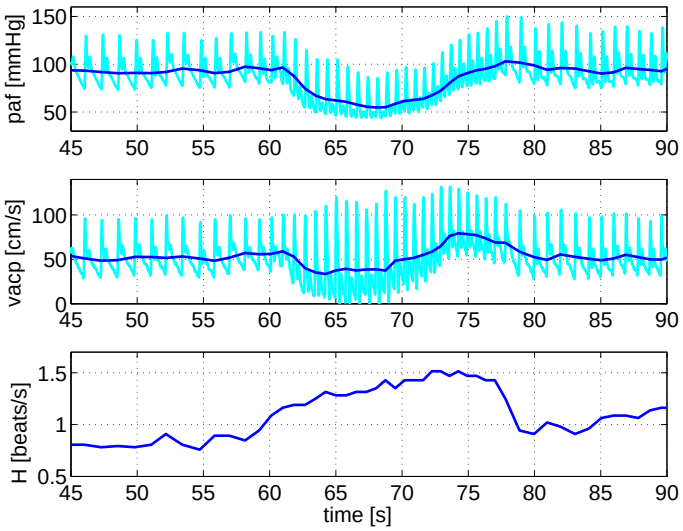

Figure 5.4: Measured arterial blood pressure in the middle finger p_{af}, cerebral blood flow velocity v_{acp}, and heart rate H for a young subject for $45 \leq t \leq 90$ s. Cyan traces, time-varying values; blue traces, corresponding beat-to-beat mean values. Heart rate is obtained as $H = 1/T$ [1/s], where T [s] is cardiac cycle duration. Immediately after transition to standing (at $t = 60$ s), pulsatile and mean blood pressure dropped significantly, mean blood flow velocity dropped, and pulsatile blood flow velocity widened (i.e., systolic value increased and diastolic value decreased). Initially, HR increased and then reached a new steady-state higher than during sitting.

5.3 Parameterization

For this study, estimation of model parameters was done in several steps. First, physiological properties of the system were used to determine nominal values for all state variables and parameters as described in Section 4.1. Initial values for the compliances and resistances are given in Table 5.1, as described in Section 4.1. Initial values for pressure and total and unstressed volumes are given in Table 5.3. This subject was assumed to have a blood volume of 5000 ml and cardiac output of 5 l/min, so all values were scaled

Table 5.3: Initial values for pressures and volumes.

Parameter	Pressure [mmHg]	Parameter	Total volume [ml]	Parameter	Unstressed volume [ml]
p_a	70	V_a	40	V_a^{unstr}	32
p_{au}	72	V_{au}	300	V_{au}^{unstr}	240
p_{al}	73	V_{al}	234	V_{al}^{unstr}	152
p_{af}	70	V_{af}	80	V_{af}^{unstr}	64
p_{ac}	70	V_{ac}	70	V_{ac}^{unstr}	56
p_v	2.0	V_v	183	V_v^{unstr}	169
p_{vu}	2.1	V_{vu}	1910	V_{vu}^{unstr}	1757
p_{vl}	2.2	V_{vl}	725	V_{vl}^{unstr}	652
p_{vc}	43	V_{vc}	391	V_{vc}^{unstr}	360
V_{lv}	68				
V_{la}	172				

accordingly.

Estimating parameters was done first for the baseline problem and then for the control problem. The 11 equations of the form of (3.5), given in their entirety in Appendix A.1, were solved for each compartment using the baseline (sitting) portion of the data ($t \leq 60$ s). During baseline, all resistances and compliances were kept constant; hence $dC/dt = 0$ and $dR/dt = 0$, i.e.,

$$\frac{dp}{dt} = \frac{1}{C}\frac{dV}{dt}.$$

Equations A.1 are combined with (3.9) and (3.10), which determine pressures in the left atrium and ventricle.

Finally, a constant factor A_{acp} was used to calculate cerebral blood flow velocity, $v_{acp} = q_{acp}/A_{acp}$, [cm/s]. The assertion that MCA diameter remains constant during postural change has been justified by recent measurements of MCA diameter by MRI combined with TCD assessment of CBFV [2, 100]. The velocity is only measured in the MCA while the model predicts total cerebral blood flow, therefore we use knowledge of cerebral flow to estimate the factor. Flow to the MCA q_{MCA} is approximately 23% of total cerebral flow q_{acp} [6]. Based on an average MCA diameter of 0.29 cm [3, 100] , MCA cross-sectional area A_{MCA} can estimated at 0.066 [cm^2]. Since $q_{MCA} = v_{mCA}A_{MCA}$, where $v_{MCA} = v_{acp}$ in our model, we relate

$$v_{MCA} = v_{acp} = q_{acp}(0.23/0.066),$$

and let $A_{acp} = 0.066/0.23 = 0.29$. The size of the MCA will differ between subjects, so this value is approximate and could be fit to the specific subject. Note that A_{acp} remains

constant for a given subject.

Model equations for the baseline simulation involve a total of 53 parameters that were estimated using the Nelder-Mead optimization algorithm described in Chapter 3. Estimated parameter values are shown together with initial values in Table 5.1. The cost function

$$\begin{aligned} J \;=\; & \frac{1}{N\overline{p}^d_{af}} \sum_{i=1}^{N} \left| p^d_{af}(t_i) - p^c_{af}(t_i) \right|^2 + \frac{1}{N\overline{v}^d_{acp}} \sum_{i=1}^{N} \left| v^d_{acp}(t_i) - v^c_{acp}(t_i) \right|^2 + \\ & \frac{1}{M\overline{p}^d_{af,sys}} \sum_{i=1}^{M} \left| p^d_{af,sys}(t_i) - p^c_{af,sys}(t_i) \right|^2 + \frac{1}{M\overline{p}^d_{af,dia}} \sum_{i=1}^{M} \left| p^d_{af,dia}(t_i) - p^c_{af,dia}(t_i) \right|^2 + \\ & \frac{1}{M\overline{v}^d_{acp,sys}} \sum_{i=1}^{M} \left| v^d_{acp,sys}(t_i) - v^c_{acp,sys}(t_i) \right|^2 + \frac{1}{M\overline{v}^d_{acp,dia}} \sum_{i=1}^{M} \left| v^d_{acp,dia}(t_i) - v^c_{acp,dia}(t_i) \right|^2 , \end{aligned} \tag{5.14}$$

where p_{af} is blood pressure in the finger and $v_{acp} = q_{acp}/A_{acp}$ is CBFV. The subscripts c and d denote computed versus measured values, and N is the number of data points in the time-series. Each term in the cost function is weighted by the number of data points and the average of the data used in that term, denoted by $\bar{p}$ and $\bar{v}$. Because our model does not produce the secondary waveform of the dichrotic notch and the peak of the primary waveform in the data is narrow, the optimizer gave a flatter waveform than desired when only the two time series appeared in the cost. Therefore to get correct representation of the pulse amplitude, additional emphasis was placed on capturing both peaks and valleys of the waveform. This is done by including terms minimizing the difference between systolic and diastolic values (*sys* and *dia*, respectively). The time series to be analyzed contains M periods, thus there will be M systolic and diastolic values.

After the baseline resistances and compliances were obtained, another optimization was done including the control equations to identify the parameter values that describe the control functions. This second optimization included 27 ordinary differential equations: 11 of the form of (3.5), 2 of the form of (5.6), and 14 of the form of (5.9). These equations are solved together with the heart model described in (3.9), passive nonlinear resistances (5.3), the height used to calculate gravitational pooling in the veins (5.8), and the piecewise linear functions used to parameterize R_{acp} and R_{au}, (5.13). This second optimization gave rise to a total of 111 parameters that were optimized: 59 parameters are shown in Table 5.2, and 52 parameters used for R_{acp} and R_{au} are shown in Figures 5.5 and 5.6. During this second optimization, all parameters found during baseline optimization (i.e., during sitting, for $t < 60$ s) remained constant at the optimized values.

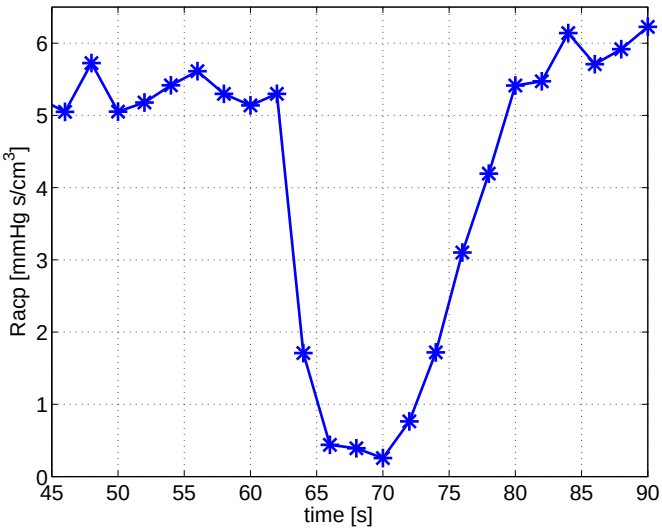

Figure 5.5: Cerebral vascular resistance $R_{acp}(t)$ for $45 \leq t \leq 90$ s, computed using a piecewise linear function (5.13), with 26 points ($*$). Shortly after transition to standing (at $t = 60$ s), cerebral autoregulation leads to a decrease in cerebrovascular resistance followed by an increase to a new steady-state value slightly higher than the steady-state value during sitting (for $t \leq 60$ s).

5.4 Results

The first results come from analysis of the pulsatile dynamics during baseline (i.e., during sitting, for $t \leq 60$ s). Nominal parameter and initial state values came from physiological considerations. The model was parameterized without including equations that describe resistances of large arteries as nonlinear functions of pressure (5.3) or active control (5.9) and (5.12). The duration of the cardiac cycles was obtained from the ECG (Figure 5.4). Simulation results in Figure 5.7 show that the parameterization resulted in an excellent agreement between the model and the data during steady-state. However, the model is not able to resolve the details of the secondary oscillation, termed the dichrotic notch, observed within each cardiac cycle. This results from pressure pulse wave propagation which we do not model here.

The second step in validating the model is illustrating the effects of venous poooling after the transition to standing. Venous pooling results in dramatic reductions of cerebral blood flow velocity and arterial pressure (Figure 5.8A); with the parameters listed in Tables 5.1 and 5.2, this decrease in blood flow velocity and pressure is reflected in the model. An increase in HR is observed not because of any control mechanisms in place, but because

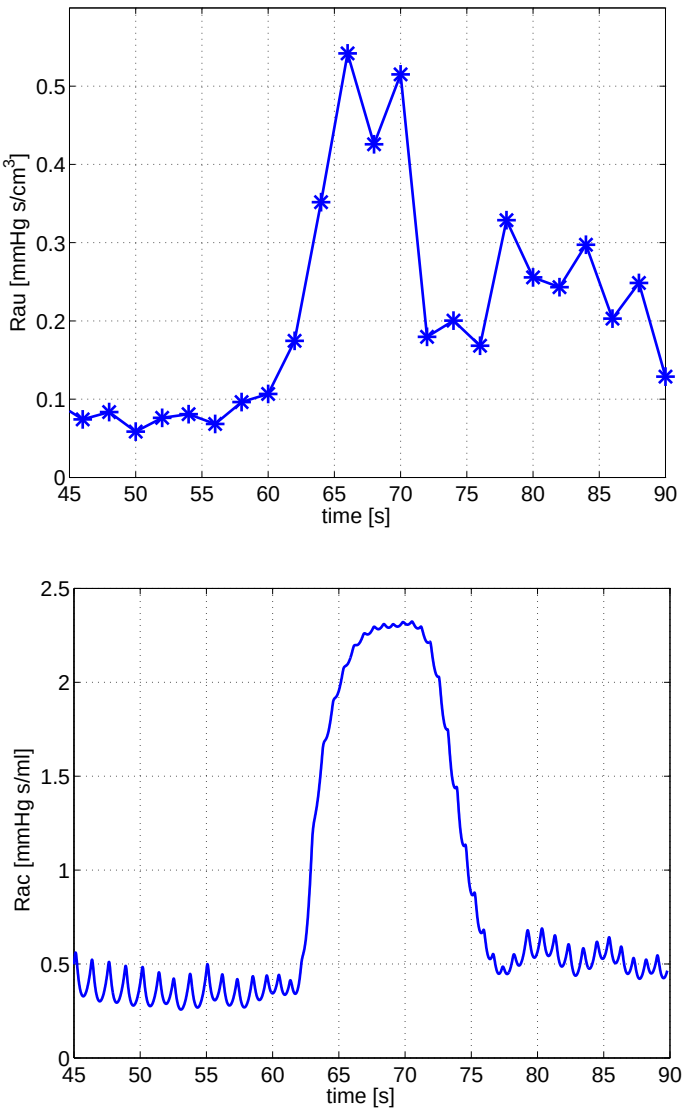

Figure 5.6: "Passive" resistances between compartments that represent large arteries. A: $R_{au}(t)$ fitted using (5.13), with 26 points ($*$). B: $R_{ac}(t)$ computed using (5.9). $R_{au}(t)$ and $R_{ac}(t)$ are depicted for $45 \leq t \leq 90$ s, increasing in response to decreasing pressure and then decreasing to a new baseline value. Models for $R_{al}(t)$ and $R_{af}(t)$ are similar to that for $R_{ac}(t)$ and show similar trends.

HR is extracted from the data (Figure 5.4). Note that although blood flow velocity and pressure drop immediately after standing (at 60 s), the pulse amplitudes for each remain small.

Next, the impact of the nonlinear relation between pressure and large artery vascu-

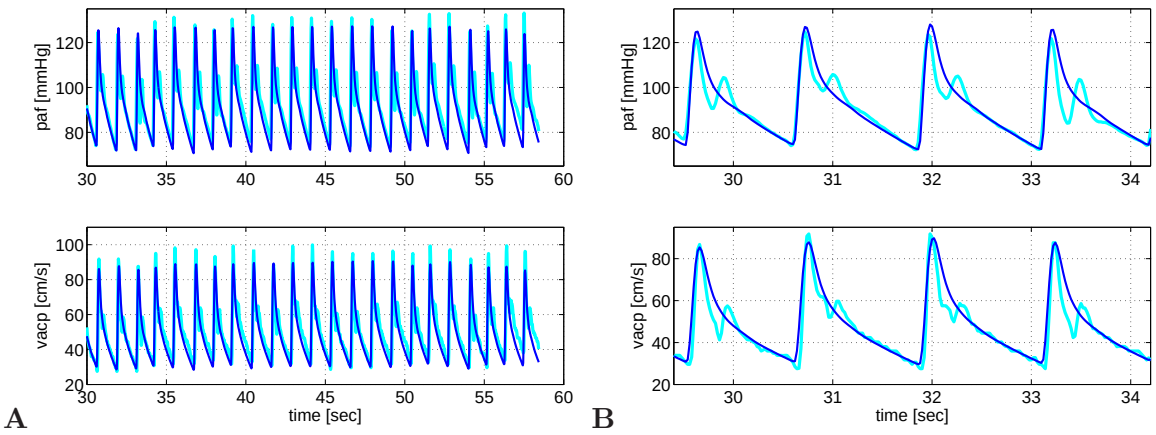

Figure 5.7: A: CBFV in the MCA v_{acp} and arterial finger blood pressure p_{af} during sitting, i.e., for $30 \leq t \leq 60$ s. B: magnification of 4 cardiac cycles from A. During baseline sitting conditions, v_{acp} and p_{af} were obtained by solving differential equations of the form of (3.5) (see Appendix A.1 for all equations). Blue traces, model simulation; cyan traces, corresponding data. Note, our model accurately predicts blood flow velocity and blood pressure profiles while the subject is sitting. As shown in B, our model is not designed to capture secondary oscillations observed in the data.

lar resistance is demonstrated; i.e. $R_{al}(\bar{p}_{au})$, $R_{ac}(\bar{p}_a)$, and $R_{af}(\bar{p}_a)$ become functions of their respective preceding pressure and optimal values for their characterizing parameters were found. The optimal values from preceding simulations are used for remaining parameters, and the result of this simulation is shown in Figure 5.8B. The pulse pressure is wider at the sit-to-stand transition point than previously; thus the model better represents measured values (cf. blue traces in Figures 5.8, A and B, in the transition region, for $60 \leq t \leq 65$ s). Finally all active control mechanisms are incorporated. Results that include effects of autonomic regulation and autoregulation are shown in Figure 5.9. The model predicts the change in the overall profile during the transition from sitting to standing. The only minor difference is that the data show a slight overshoot in pressure at the tail end of the recovery from standing.

Autonomic regulation was included using a model that predicts parameters as a function of pressure. Although this method does not delineate between separate effects of sympathetic versus parasympathetic activation, it instead represents an integrated neurogenic response. Effects of cerebral autoregulation were modeled using the empirical model described in (5.13). A total of 26 points connect the segments that represent the dynamics of cerebrovascular resistance, R_{acp}. Figure 5.5 shows that R_{acp} decreases because of

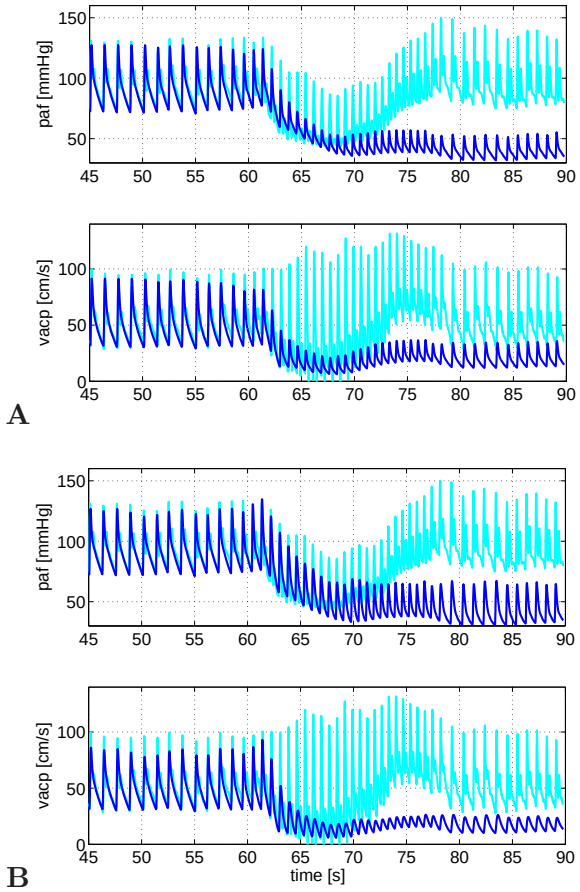

Figure 5.8: CBFV v_{acp} and arterial finger blood pressure p_{af} for $45 \leq t \leq 90$ s. Effect of standing is shown without active control mechanisms. A: Blood flow velocity and blood pressure decrease as a result of redistribution of volumes from changes in hydrostatic pressure. Blue traces, model simulation; cyan traces, corresponding data. Results were obtained by solving equations (3.5) where gravity is included as described in (5.7). B: Effect of including nonlinear functions of pressure for large arterial resistances as described in (5.3).

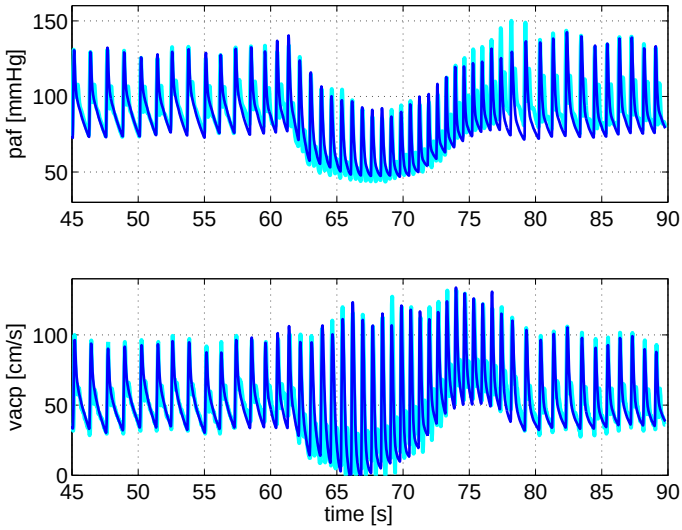

Figure 5.9: Autonomic regulation and cerebral autoregulation of arterial finger blood pressure and CBFV for $45 \leq t \leq 90$ s. The model is able to reproduce data well. Blue traces, model simulations; cyan traces, data. Results were obtained by solving cardiovascular equations of the form of (3.5), including gravity as described in (5.7), passive resistances in (5.3), and autonomic regulation and cerebral autoregulation described in (5.9) and (5.12). The main region where the model does not capture the dynamics of the data is just before returning to baseline during standing, i.e., for $75 \leq t \leq 80$ s.

autoregulation in reponse to the decrease in pressure. The resistance of the upper body arteries R_{au} was also modeled using a piecewise linear function because of the hypothesis that it may exhibit both strong active autonomic and passive behavior. Figure 5.6 shows that this resistance follows trends predicted by the other large artery resistances.

Finally, Figure 5.10 depicts the dynamics of some of the controlled variables, e.g. arterial resistance R_{aup}, cardiac contractility of the left ventricle c_{lv}, and venous compliance in the upper body C_{vu}. These results display different dynamics of the three types of variables. In particular, the compliance and peripheral resistance do not reach a steady state during the 10 s after the transition from sitting to standing (from $80 \leq t \leq 90$ s), perhaps because the dynamics that change the ventricular contractility occur over a faster time scale than those that affect resistances and compliances [53]. The dynamics of other reistances, compliances, and atrial contractility are similar to those shown in Figure 5.10.

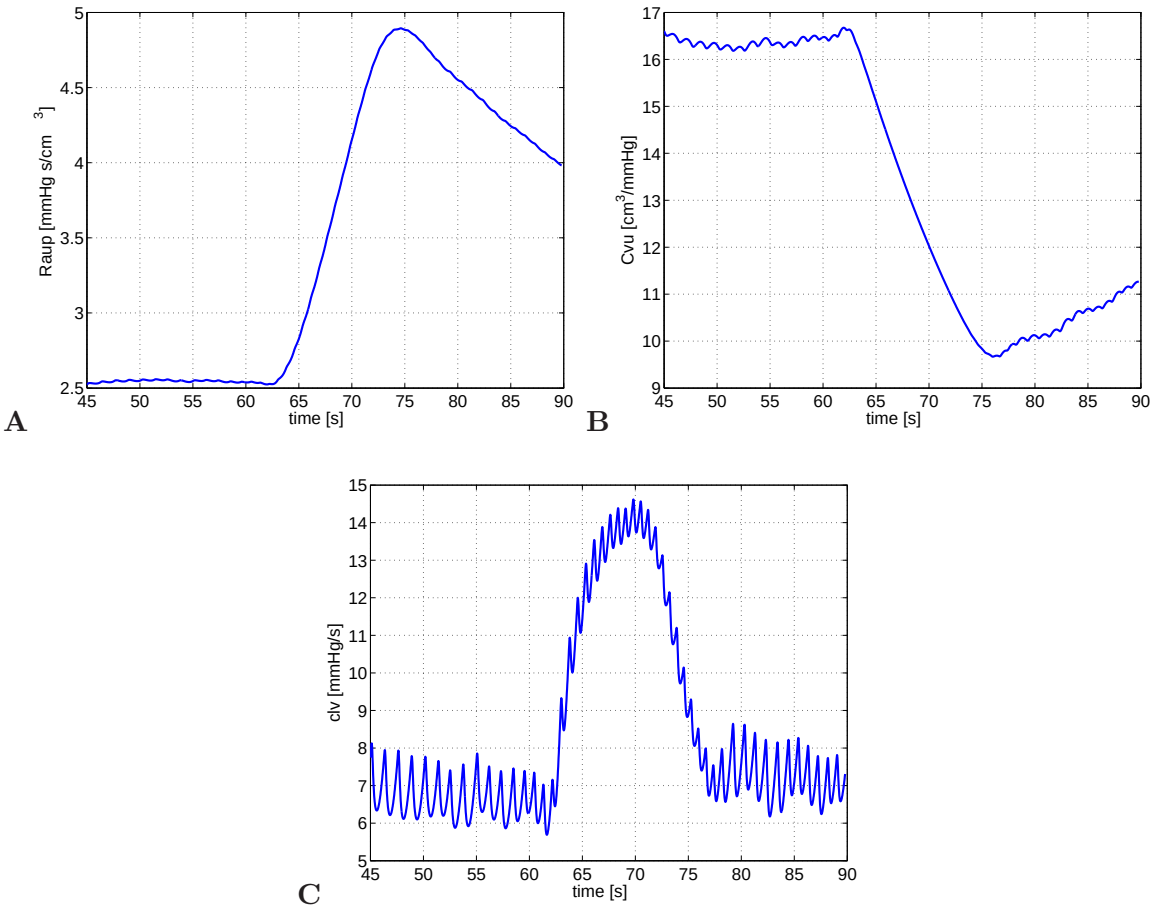

Figure 5.10: Dynamics of controlled variables for $45 \leq t \leq 90$ s. A: peripheral resistance in the upper body $R_{aup}(t)$. B: compliance of veins in the upper body $C_{vu}(t)$. C: cardiac contractility of the left ventricle $c_{lv}(t)$. Results were obtained by solving (5.9) together with equations for the cardiovascular system (3.5). Autonomic regulation yields increase in peripheral resistance, cardiac contractility, and vascular tone. The latter yields a decrease in compliance as shown. Timing of the different controls varies; especially note that cardiac contractility changes faster than resistances and compliances. Regulation of the remaining resistances, contractility, and compliances showed similar responses.

5.5 Discussion

The 11-compartment model described here predicts cerebral blood flow velocity and finger blood pressure. The model includes a physiological representation of dynamics as a response to hydrostatic pressure changes during postural change from sitting to standing. This includes nonlinear functions describing resistances of the large systemic arteries as functions of pressure. The regulatory response model includes autonomic regulation using

first-order differential equations regulating cardiac contractility, peripheral resistance, and vascular tone (compliance). An empirical model describes the dynamics of cerebraovascular resistance. Validation of the model against one data set showed that, by including the mechanisms described above, the model is able to reproduce the dynamics of blood flow velocity and blood pressure needed to compensate for hypotension observed during the postural change from sitting to standing.

Modeling of physiological responses to standing enables a better understanding of physiological mechanisms underlying disorders related to orthostatic intolerance, e.g., orthostatic hypotension and syncope. The model predicts that in the absence of regulatory mechanisms (Figure 5.8), arterial blood pressure and CBFV declined on the transition to standing and did not recover to baseline in the upright position. This modeling result has not been validated against data. However, similar responses have been observed clinically. For example, sustained blood pressure reduction in the upright position is seen in clinical syndromes with orthostatic hypotension associated with autonomic failures [52, 53]. Different etiologies and severity of autonomic failure may lead to differences in patho-physiological responses during the transition to standing. For example, severe peripheral autonomic failure, such as pure autonomic failure or diabetic neuropathy, may be associated with orthostatic hypotension with no heart rate increment. Cerebral autoregulation, which maintains cerebral perfusion over a wide range of pressure [68], may be preserved, expanded, or reduced in orthostatic hypotension. However, cerebral blood flow would decline with impairment of autoregulation and/or when blood pressure is diminished below the autoregulated range. A transient impairment of autonomic and cerebral blood flow control is common in young people with vasodepressor syncope. This is associated with a withdrawal of sympathetic tone followed by a decline of blood pressure and cerebral perfusion [44, 64, 66].

Furthermore, by including passive nonlinear responses of resistances in the large arteries, we can obtain sufficient widening of the pulse pressure amplitude observed immediately after the transition to standing. This immediate response is not regulatory but rather a purely passive response due to the nature of the underlying fluid dynamics. This model also predicts the effects of hydrostatic changes, even though this model was only validated for the transition from sitting to standing, i.e., $\cos(\phi)$=1.

The main accomplishment of this work is that the model describes how autonomic regulation and cerebral autoregulation play a synergistic role in the control of arterial blood pressure and cerebral blood flow velocity. In particular, the cerebral resistance was shown

to first decrease and then increase during active standing. Furthermore, the curve for R_{acp} displays hysteresis effects; immediately after standing, the decrease of R_{acp} is faster than the increase for $t \leq 70$ s during the phase where blood flow velocity is returning to its normal state. Hysteresis in vascular resistance in response to decreasing and increasing pressure may reflect differences between cerebral and peripheral vasculature that account for time lags between central and peripheral responses. With normal autoregulation, changes in blood flow velocity precedes changes in peripheral blood pressure, reflecting local adjustments to intracranial pressure [69]. Finally, to obtain a blood flow velocity during standing that is equivalent to that during sitting, the resistance reaches a set point that is higher during standing than during sitting. This may be a result of myogenic effects [101].

Results for parameters representative of autonomic regulation show that these parameters react as expected: peripheral resistance and cardiac contractility increase, while compliance decreases (Figure 5.10). As described in Section 5.4, the contractility increases much faster than the peripheral resistance. This could be due to the more rapid effects of parasympathetic withdrawal acting on contractility than of sympathetic activation, which has a later effect on contractility, peripheral resistance, and compliance.

Finally, the set of optimized parameters found in this study is not likely unique. The windkessel model in Section 4.4.1 was an example of a small model with an insensitive parameter (C_S) that attained two different values with two types of optimization algorithm. We suspect that this occurs in the 11-compartment model as well on a larger scale, especially since optimized parameters are found locally with respect to nominal parameter estimates and so depend on those estimates. We also observe that some of the maximum values that the Nelder-Mead method found for the resistance and compliance relationships have large values which are physiologically unrealistic. A constrained optimization algorithm could be used to bound these values to a physiologically realistic value, which may then force the optimizer to a new local minimum.

Aside from the behavior of the numerical optimization, the system of equations may lend itself to non-uniqueness due to parameter dependencies. Ottesen and Danielsen [79] point out that their heart model (3.10) gives virtually identical waveforms for ventricular pressure with multiple combinations of parameters. In particular $m = 2.2$, $n = 1$ is indistinguishable from $m = 1$, $n = 2$. With 14 parameters in the heart model it is likely that similar dependencies exist. As another example, we examine the total resistance across the systemic circulation R_{total} which is described by $R_{total} = (p_a - p_v)/q_{total}$. We have data for

only one pressure p_{af} and one velocity $v_{acp} = q_{acp}/A_{acp}$. Yet q_{total} is the sum of multiple flows, and R_{total} equals the sum of multiple resistances in series or parallel

$$R_{total} = \sum_i R_i, \text{ series,} \tag{5.15}$$

$$\frac{1}{R_{total}} = \sum_i \frac{1}{R_i}, \text{ parallel.} \tag{5.16}$$

Many values for the component resistances could sum to the same R_{total} thus leading again to similar waveforms for v_{acp} and p_{af} as related to q_{total} and p_a. We see that both numerical effects and characteristics of the model can cause problems for an optimization algorithm. These are addressed in Section 5.6.

5.6 Sensitivity analysis

Sensitivity analysis is used to begin to address the uniqueness problem. The process used here is delineated in Chapter 4 and was performed on the steady-state sitting portion of the 11-compartment model, with 11 equations and 52 parameters. Unique identification of all 52 parameters was found is likely not possible, and obtaining optimized values for these parameters was time consuming. Furthermore, the computed outcome states at locations where data are measured (i.e., finger blood pressure and CBFV) may not be sensitive to all 52 parameters. The sensitive group of parameters is identified using sensitivity analysis. Two uses of the sensitive parameter set will be discussed: (i) model validation, i.e., showing that parameter identification of the sensitive parameter set alone using nonlinear optimization can accurately fit the model to an individual data set, and (ii) model design, i.e., if the model is overdetermined for its application, adding unnecessary complexity, sensitivity analysis can be used to determine which parts of the model may be eliminated.

5.6.1 Experimental data

A different test protocol was used for this analysis. Data was collected in the Syncope and Falls in the Elderly (SAFE) Laboratory at Beth Israel Deaconess Medical Center (BIDMC). A similar protocol was used in Novak *et al.* [67]. Time-series analyzed in this study include beat-to-beat arterial pressure obtained from a cuff placed on the finger using a Portapress-2 device (FMS, Inc.) and beat-to-beat middle cerebral blood

flow velocity measurements from the index finger obtained using a Transcranial Doppler (TCD) system (MultiDop X4, Nueroscan, Inc.). All analog signals was recorded at 500 Hz using Labview NIDAQ on a Pentium Xeon 2 GHz dual processor computer and stored for offline processing. Data were down-sampled to 50 Hz prior to model analysis. All data was visually inspected for accuracy of R-wave detection, artifacts, and occasional extra systoles that were removed using a linear interpolation algorithm.

Data was recorded continuously during a 5 min interval while the subject sat on a chair with his legs elevated at 90^{O} to reduce venous pooling. After this the subject was asked to stand while recordings were continued for an additional 5 min period.

5.6.2 Parameterization

Nominal parameters for this study were found using methods discussed in Chapter 4. Section 5.6.1. In this study, total blood volume was estimated using Nadler's formula [60]

$$\text{BV, ml} = \begin{cases} 1000(0.3369(\text{height,m})^3 + 0.03219(\text{weight,kg}) + 0.6041), & \text{men} \\ 1000(0.3561(\text{height,m})^3 + 0.03308(\text{weight,kg}) + 0.1833), & \text{women,} \end{cases} \tag{5.17}$$

which for the healthy subject analyzed in this study gives $V_T = 4673$ ml. Unstressed volumes were scaled to values in Beneken and DeWit [10] as described in Section 4.1. Note that since the model only contains the systemic circulation, the sum of volumes for each of the nine arterial and venous compartment equals the total volume of the cardiovascular system V_T minus the volume of the pulmonary compartments. To adjust pressures for this subject, we assured that the nominal estimate for the finger pressure matched the mean arterial pressure obtained from Finapres measurements. Compliances and resistances, see Tables 5.4 and 5.5, are calculated using the methods described in Section 4.1. Parameter values for the left ventricle, see Table 5.6, were taken from work by Ottesen and Danielsen [79]. To estimate parameters for the left atrium we scaled the ventricle parameters to account for the difference in magnitude between atrial and ventricular systolic pressure. Finally, the scaling parameter $A_{acp} = q_{acp}/v_{acp}$ was estimated as described in Section 5.3.

The weighted least-squares cost J presented in (5.15) was used initially for the parameter optimization. Since data are only available for two locations, this least squares cost function was found to be unable to ensure correct physiological ranges for internal states.

Table 5.4: Estimates of compliance. Pressures were estimated from subject data. All other states were estimated from [10] and scaled to the subject's anthropometric data. See Figure 5.1 for location of model comparments.

Compartment	Pressure [mmHg]	Total volume [ml]	Percent stressed	Effective volume [ml]	Compliance [ml/mmHg]
Aorta (a)	73	93	35%	32	0.444
Upper body arteries (au)	70	385	30%	115	1.649
Lower body arteries (al)	68	85	16%	14	0.200
Cerebral arteries (ac)	70	99	25%	25	0.354
Finger arteries (af)	72.8	34	25%	8.4	0.115
Vena cava (v)	4	599	8%	48	11.98
Upper body veins (vu)	6	1962	8%	157	26.15
Lower body veins (vl)	8	334	8%	27	3.335
Cerebral veins (vc)	10	402	20%	80	8.040
Ventricle systolic (lv)	73.5	-	-	-	-
Ventricle diastolic (lv)	2	-	-	-	-
Atrium pressure (la)	3	-	-	-	-

Table 5.5: Initial resistances and flowrates for each pathway. Flow percentages are from [10], and scaled to the subject's blood volume. Resistances are calculated using Ohm's law (3.1). See Figure 5.1 for location of model compartments.

Pathway	Segment	Percent of cardiac output	Flowrate [ml/s]	Resistance [mmHg·s/ml]
q_{av}	Cardiac output	100%	77.88	0.006
q_{au}	Upper body	64%	62.31	0.048
q_{aup}	Upper body	64%	49.85	1.284
q_{al}	Lower body	8%	6.231	0.321
q_{alp}	Lower body	8%	6.231	9.630
q_{ac}	Cerebral (Brain)	20%	15.58	0.193
q_{acp}	Cerebral (Brain)	20%	15.58	3.852
q_{af}	Finger (Arm)	8%	6.231	0.032
q_{afp}	Finger (Arm)	8%	6.231	11.04
q_{vl}	Lower body	8%	6.231	0.321
q_{vu}	Upper body	64%	62.31	0.032
q_{vc}	Cerebral (Brain)	20%	15.58	0.385
q_{v}	Cardiac output	100%	77.88	0.013

In particular, the optimization overestimated the baseline aortic valve resistance $R_{av,open}$, which gave rise to an un-physiologically large discrepancy between the left ventricular $p_{lv,sys}$ systolic pressure and the systolic aortic pressure $p_{a,sys}$ [13], see Figure 2.4. To avoid the large pressure discrepancy, a constraint minimizing the error between the systolic ventricular pressure and the systolic aortic pressure was added. Thus an amended cost functional

can be written as

$$\hat{J} = J + \frac{1}{M\overline{p}^d_{a,sys}} \sum_{i=1}^{M} \left| p^c_{a,sys}(t_i) - p^c_{lv,sys}(t_i) \right|^2 .$$

The Nelder-Mead algorithm [45], discussed in Section 4.3, was used to identify parameters that minimize the effective cost functional J. Optimizations were run using MATLAB 6.5 on a 14-node cluster at Roskilde University, Denmark, each node with an Intel Pentium 4 2.26 GHz processor with 1GB RAM. Identification of all 52 parameters took 37 hours. Simulation results with the model using the optimized parameters are shown in Figure 5.13A and optimized parameters are listed in Table 5.6.

5.6.3 Methods

Sensitivity analysis was carried out as described in Section 5.6, with 11 state and $11 \times 52 = 572$ sensitivity equations. The automatic differentiation code as developed by Fink [27] was used to derive the sensitivities. As an example of the form of the sensitivity equations, the sensitivity $S_{paf,Ral}$ is derived by differentiating dp_{af}/dt with respect to R_{al},

$$\frac{d}{dt}\left(\frac{\partial p_{af}}{\partial R_{al}}\right) = \frac{1}{C_{af}}\left[\frac{1}{R_{af}}\left(\frac{\partial p_a}{\partial R_{al}} - \frac{\partial p_{af}}{\partial R_{al}}\right) - \frac{1}{R_{afp}}\left(\frac{\partial p_{af}}{\partial R_{al}} - \frac{\partial p_v}{\partial R_{al}}\right)\right],$$

solving for $\partial p_{af}/\partial R_{al}$, and multiplying by R_{al}/p_{af}. The resulting solution is shown in Figure 5.11, and together with Table 5.7 it is seen that maximum relative sensitivity of p_{af} with respect to R_{al} is 0.0008. In other words, this parameter is very insensitive (compare graphs on Figure 5.11). We contrast this with the relativity sensitivity with respect to c_v at 2.029, the most sensitive parameter. The remaining 571 equations are derived using similar considerations.

The derivation of sensitivity equations requires that the functions of the states with respect to each of the parameters are smooth. The system of equations analyzed in these studies includes two groups of equations that do not immediately appear to be fully differentiable: the valves (3.12) and the heart functions (3.9), (3.10). The valve equations, while piecewise continuous, are not differentiable at the cusps between the exponential function and the constant. To construct a smooth differentiable function for (3.12), a smooth approximation [18] of the form

$$\min_{\epsilon}(x_1, x_2) = -\epsilon \ln\left(\sum_{i=1}^{n} e^{-x_i/\epsilon}\right), \tag{5.18}$$

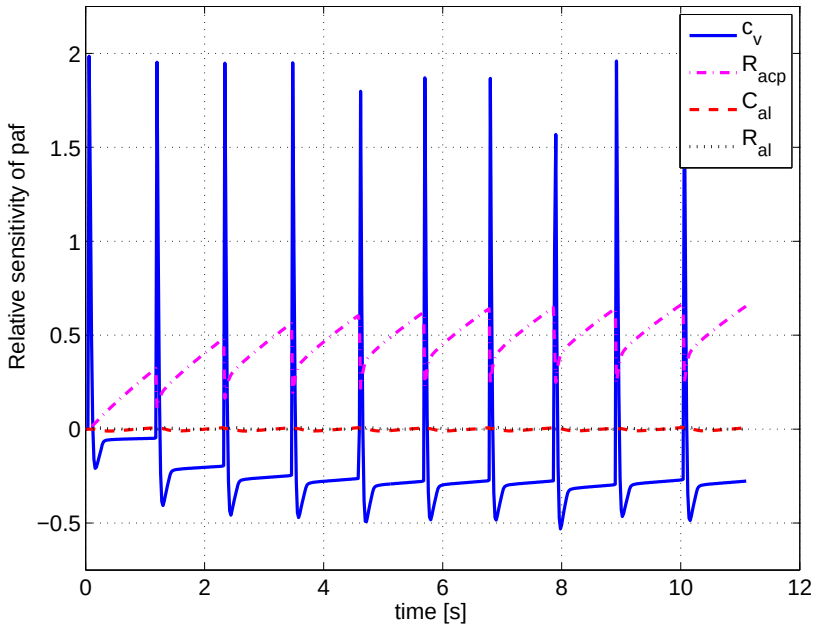

Figure 5.11: Relative sensitivities $S_{p_a f,j}$, where j denotes parameters c_v [mmHg/ml], R_{acp} [mmHg·s/ml], C_{al} [ml/mmHg], and R_{al} [mmHg·s/ml].

was adapted using $0 < \epsilon < 0.1$, where $x_1 = R_{valve,open} + e^{-k(p_{in}-p_{out})}$ and $x_2 = R_{valve,closed}$.

In the polynomial heart function, the partial derivative of the ventricle activation function f_i defined in (3.10) with respect to the parameter n in the range $0 \leq \tilde{t} \leq \beta$ is given by

$$\frac{\partial f}{\partial n} = \tilde{p} n^{-n} m^{-m} \left(\frac{\beta(n)}{n+m}\right)^{(-n-m)} \tilde{t}^n (\beta(n) - \tilde{t})^m \left(\ln(\tilde{t}) - \ln(m) - \ln\left(\frac{\beta(n)}{n+m}\right)\right) \left[t_{pv} \frac{-m}{n^2}\right],$$

which is undefined at $\tilde{t} = 0$. In the second half of the pressure waveform, $f_i = 0$ and thus $\partial f_i / \partial n = 0$. To show that f_i has a continuous derivative, L'Hospital's Rule was used to prove that $\partial f_i / \partial n \to 0$ as $\tilde{t} \to 0$ when $0 \leq \tilde{t} \leq \beta$. Letting

$$K_n = \tilde{p} n^{-n} m^{-m} \left(\frac{\beta(n)}{n+m}\right)^{(-n-m)} \left[t_{pv} \frac{-m}{n^2}\right]$$

yields the limit

$$\lim_{\tilde{t}\to 0} K_n \tilde{t}^n (\beta - \tilde{t})^m \left(\ln(\tilde{t}) - \ln(m) - \ln\left(\frac{\beta(n)}{n+m}\right)\right) = \lim_{\tilde{t}\to 0} K_n \frac{1/\tilde{t}}{-n\tilde{t}^{-n-1} m (\beta - \tilde{t})^{-m-1}} = 0.$$

Since $\tilde{t} = T$ of period $i-1$ equals $\tilde{t} = 0$ of period i, and $\partial f / \partial n = 0$ at $\tilde{t} = T$, then $\lim_{\tilde{t}\to 0} \partial f / \partial n = 0$ of i shows continuity. Analyses done for the remaining partial derivatives with respect to other parameters in the heart activation function show similar results.

5.6.4 Results

Equations (3.5) predicting pressures in each of the arterial and venous compartments and (3.6) predicting volumes of the atrium and the ventricle, coupled with the system of sensitivity equations as written in (4.8), were solved to generate the state and quasi-state sensitivity solutions. A composite sensitivity for ranking purposes was calculated as described in (4.9). Results of these calculations gave rise to the ranking shown in Figure 5.12A and Table 5.7. Results depicted on this graph suggest a decreasing exponential relationship between sensitivity $\mathbf{S_j}$ and the relative ranking. Figures 5.12B-D show the results of optimizations run with a systematic reduction in the number of parameters optimized. The weighted least squares cost, the number of optimization iterations, and computational time were recorded. Figure 5.12B indicates a continuously negligible change in cost as the number of optimized parameters are reduced from the starting number of 52. Identification of the 22 most sensitive parameters gives a cost increase of approximately 8% to 1.93, yet optimizing 21 parameters increases the cost by more than 100% to 3.63. Hence, the top 22 parameters are necessary for acceptable model behavior. Qualitatively this behavior is as good as that with 52 parameters but reducing the number of iterations needed by half. Figure 5.13 compares results for finger blood pressure and CBFV obtained when all 52 model parameters are identified (left panel), with a cost of 1.77, and when only the top 22 parameters are identified (right panel), with a cost of 1.93. Table 5.6 shows optimized parameters. These 22 parameters are referred to as sensitive and the remaining 30 are insensitive.

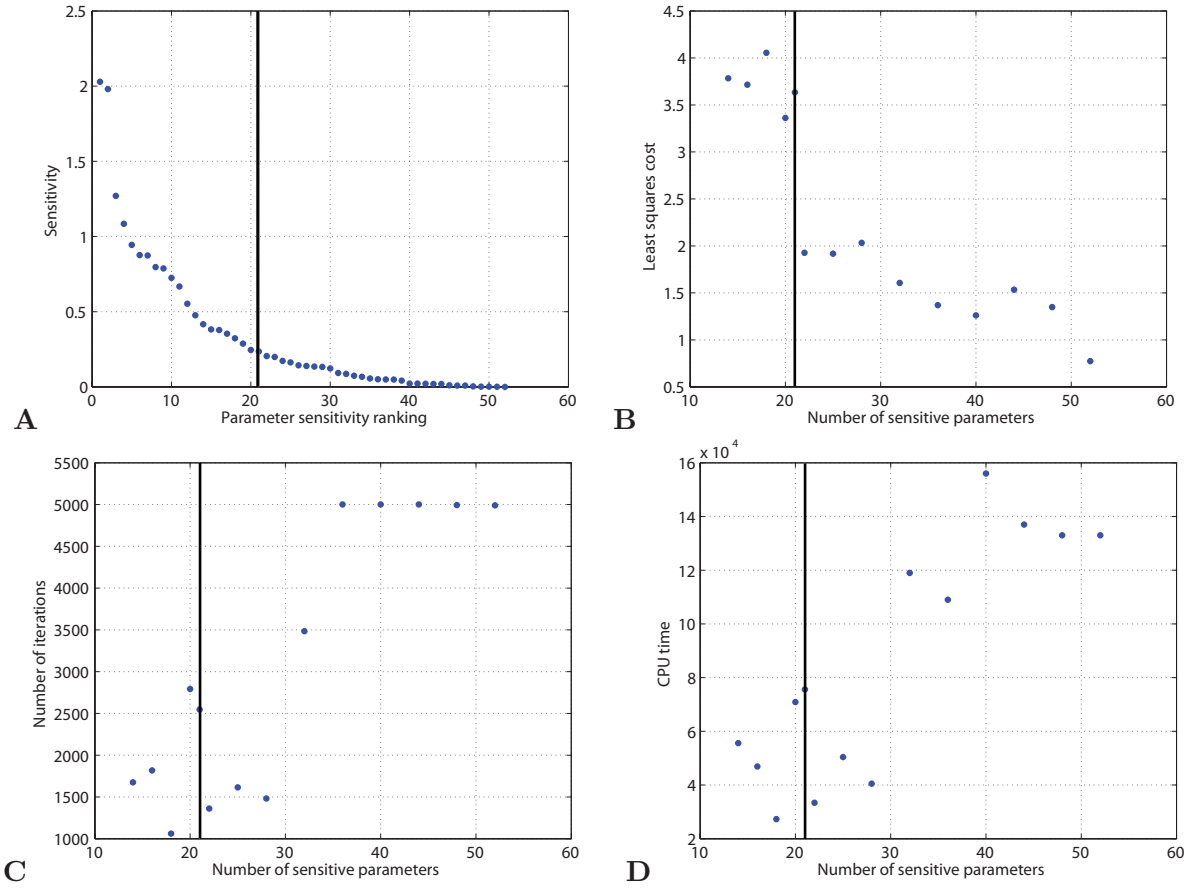

Figure 5.12: A: Sensitivities of each parameter versus their relative ranking. B-D: Results of parameterizing the system by optimizing a decreasing number of sensitive parameters while keeping an increasing number of insensitive parameters fixed at their nominal values. B, C, and D depict the least squares cost, the number of iterations, and the computational time versus the number of sensitive parameters identified, respectively. The vertical lines are each at 21, the number of sensitive parameters.

Finally, it should be noted that A_{acp} does not appear in the state equations. Therefore its sensitivity is not calculated as in the above equations and as a result it is ranked at the bottom of the sensitivity list with a sensitivity equal to zero. Optimizations run for a fixed nominal value of A_{acp} show a negligible change in cost compared to optimizations that identified A_{acp}. These results confirm the hypothesis that the parameter A_{acp} is not sensitive with respect to any of the states p_{af}, p_{ac}, or p_{vc}. However, it is noted that although this was not done in this study, sensitivities could be calculated with respect to the observation v_{acp}, a procedure explored in Chapter 6.

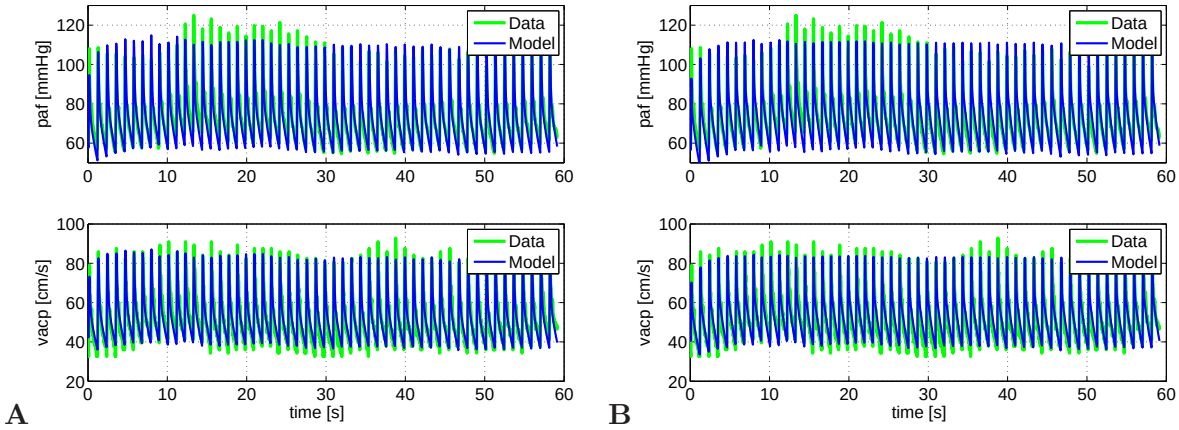

Figure 5.13: Each panel shows finger pressure p_{af} (top) and cerebral blood flow velocity v_{acp} (bottom) data and model solutions. Panel A shows the model with 52 parameters optimized, cost of 1.77. Panel B is the model with the 22 most sensitive parameters optimized, cost of 1.93.

Table 5.6: Initial and optimized parameter values used for the sensitivity analysis used in the 11-compartment model. Columns two and six are nominal parameter values. Columns three and seven give the optimized parameter values when all 52 parameters were estimated. Columns four and eight give the optimized parameter values when the top 22 sensitive parameters were estimated.

Parameter	Init	Opt, 52	Opt, 22	Parameter	Init	Opt, 52	Opt, 22
R_{av} [mmHg·s/ml]	0.006	0.004	–	ν_v	9.900	9.425	9.010
R_{au} [mmHg·s/ml]	0.048	0.104	–	θ_v [1/s]	0.951	0.871	1.323
R_{aup} [mmHg·s/ml]	1.284	1.354	1.104	$t_{diff,v}$ [s]	0.094	0.107	–
R_{al} [mmHg·s/ml]	0.321	0.449	–	$t_{min,v}$ [s]	0.186	0.177	0.101
R_{alp} [mmHg·s/ml]	9.629	9.967	9.601	$p_{min,v}$	0.842	0.563	0.659
R_{vl} [mmHg·s/ml]	0.321	0.346	–	$p_{diff,v}$	0.316	0.423	–
R_{vu} [mmHg·s/ml]	0.032	0.014	–	η_v	17.50	18.33	20.53
R_{mv} [mmHg·s/ml]	0.014	0.015	–	ϕ_v [1/s]	1.000	1.065	1.511
R_{vc} [mmHg·s/ml]	0.385	0.623	–	a_a [mmHg/ml^2]	$0.003{\cdot}10^{-2}$	$0.001{\cdot}10^{-2}$	–
R_{acp} [mmHg·s/ml]	3.852	3.832	3.688	c_a [mmHg/ml]	6.400	6.630	4.765
R_{ac} [mmHg·s/ml]	0.193	0.115	–	b_a [ml]	5.000	4.183	–
R_v [mmHg·s/ml]	0.013	0.006	–	d_a [mmHg]	1.000	1.340	–
C_a [ml/mmHg]	0.445	0.465	–	n_a	2.000	2.369	2.669
C_{au} [ml/mmHg]	1.649	1.870	1.958	m_a	2.200	1.977	–
C_{al} [ml/mmHg]	0.200	0.300	–	ν_a	9.900	10.16	–
C_{ac} [ml/mmHg]	0.354	0.180	0.079	θ_a [1/s]	0.951	0.886	0.910
C_{vl} [ml/mmHg]	3.335	3.357	1.463	$t_{diff,a}$ [s]	0.094	0.168	–
C_{vu} [ml/mmHg]	26.15	27.37	48.54	$t_{min,a}$ [s]	0.186	0.138	–
C_v [ml/mmHg]	11.98	13.10	–	$p_{min,a}$	0.842	1.055	0.600
C_{vc} [ml/mmHg]	8.040	8.585	–	$p_{diff,a}$	0.316	0.427	–
a_v [mmHg/ml^2]	0.0003	0.0004	–	η_a	17.50	17.63	–
c_v [mmHg/ml]	6.400	6.657	4.896	ϕ_a [1/s]	1.000	1.303	0.666
b_v [ml]	5.000	4.075	–	A_{acp} [cm^2]	0.300	0.289	–
d_v [mmHg]	1.000	0.997	–	C_{af} [ml/mmHg]	0.115	0.094	–
n_v	2.000	2.716	3.421	R_{af} [mmHg·s/ml]	0.032	0.074	–
m_v	2.200	1.954	1.378	R_{afp} [mmHg·s/ml]	11.04	11.57	7.105

Table 5.7: Ranked (most-to-least) sensitivities for the 11-compartment model. For each parameter, sensitivities are ranked with respect to the pressures p_f, p_{ac} and p_{vc} [mmHg]. Value in boldface designate the maximum values for each parameter.

Rank	Parameter	p_{af}	p_{ac}	p_{vc}	$\mathbf{S}_j$	Rank	Parameter	p_{af}	p_{ac}	p_{vc}	$\mathbf{S}_j$
1	c_v [mmHg/ml]	**2.029**	0.798	0.054	2.029	27	ν_a	**0.139**	0.122	0.013	0.139
2	n_v	**1.981**	1.377	0.043	1.981	28	C_a [ml/mmHg]	**0.135**	0.076	0.007	0.135
3	θ_v [1/s]	**1.270**	0.432	0.070	1.270	29	$t_{diff,v}$ [s]	**0.133**	0.039	0.007	0.133
4	R_{aup} [mmHg·s/ml]	**1.084**	1.052	0.189	1.084	30	C_v [ml/mmHg]	**0.122**	0.115	0.074	0.122
5	R_{alp} [mmHg·s/ml]	0.401	0.390	**0.944**	0.944	31	m_a	**0.092**	0.058	0.052	0.092
6	ϕ_v [1/s]	**0.876**	0.357	0.022	0.876	32	η_a	**0.086**	0.080	0.008	0.086
7	C_{vu} [ml/mmHg]	**0.874**	0.862	0.823	0.874	33	R_{vc} [mmHg·s/ml]	**0.074**	0.065	0.058	0.074
8	R_{acp} [mmHg·s/ml]	0.679	**0.797**	0.166	0.797	34	R_{au} [mmHg·s/ml]	**0.067**	0.048	0.003	0.067
9	n_a	**0.788**	0.743	0.122	0.788	35	b_v [ml]	**0.056**	0.054	0.005	0.056
10	$p_{min,v}$	**0.725**	0.279	0.019	0.725	36	C_{af}[ml/mmHg]	**0.051**	0.010	0.001	0.051
11	c_a [mmHg/ml]	**0.668**	0.625	0.066	0.668	37	$t_{diff,a}$ [s]	**0.050**	0.045	0.005	0.050
12	θ_a [1/s]	**0.553**	0.518	0.049	0.553	38	$p_{diff,v}$	**0.049**	0.021	0.001	0.049
13	$t_{min,v}$ [s]	**0.476**	0.157	0.026	0.476	39	R_{vu}[mmHg·s/ml]	**0.042**	0.030	0.036	0.042
14	C_{vl} [ml/mmHg]	0.031	0.030	**0.416**	0.416	40	b_a [ml]	0.010	0.008	**0.022**	0.022
15	R_{afp} [mmHg·s/ml]	**0.382**	0.354	0.005	0.382	41	R_{af} [mmHg·s/ml]	**0.022**	0.001	0.000	0.022
16	ν_v	**0.378**	0.110	0.018	0.378	42	R_{mv} [mmHg·s/ml]	**0.021**	0.020	0.001	0.021
17	ϕ_a [1/s]	**0.354**	0.296	0.027	0.354	43	$p_{diff,a}$	**0.020**	0.015	0.001	0.020
18	C_{au} [ml/mmHg]	**0.323**	0.284	0.048	0.323	44	R_v [mmHg·s/ml]	**0.019**	0.017	0.015	0.019
19	m_v	**0.288**	0.184	0.033	0.288	45	C_{al} [ml/mmHg]	**0.010**	0.009	0.003	0.010
20	η_v	**0.246**	0.092	0.007	0.246	46	R_{av}[mmHg·s/ml]	**0.008**	0.003	0.000	0.008
21	$p_{min,a}$	**0.236**	0.220	0.023	0.236	47	R_{al}[mmHg·s/ml]	**0.008**	0.007	0.007	0.008
22	C_{ac} [ml/mmHg]	0.035	**0.205**	0.005	0.205	48	a_v [mmHg/ml^2]	**0.003**	0.003	0.000	0.003
23	$t_{min,a}$ [s]	**0.199**	0.185	0.020	0.199	49	d_v [mmHg]	**0.002**	0.001	0.000	0.002
24	R_{vl} [mmHg·s/ml]	0.010	0.009	**0.173**	0.173	50	a_a [mmHg/ml^2]	0.001	0.001	**0.002**	0.002
25	R_{ac} [mmHg·s/ml]	0.032	**0.163**	0.003	0.163	51	d_a [mmHg]	**0.001**	0.000	0.000	0.001
26	C_{vc} [ml/mmHg]	**0.143**	0.142	0.110	0.143	52	A_{acp} [cm^2]	0	0	0	0

5.6.5 Model reduction

Sensitivity ranking of parameters shown in Table 5.7 can also be used to reduce the complexity of the model. In general, to reduce the model, compartments comprised of sensitive parameters are retained while those mainly consisting of insensitive parameters may be eliminated. However, before a compartment is eliminated several factors must be taken into account. The system must have a heart acting as a pump to raise the pressure against its gradient, so one or both heart compartments are retained. Second, separation between the brain and the rest of the body must be maintained because data used for model validation are collected both in the brain (cerebral blood flow velocity) and in the body (finger blood presure). Finally, the various model components are related, thus if one compartment is removed, it may impact dynamics of other elements, which may impact the solution. Furthermore, if the data used for model comparison are not adequate, it will not be possible to accurately predict the distribution of blood between compartments. However, instead of removing a compartment to remove a parameter, it may be possible to keep one parameter constant, while other parameters are identified by the weighted least squares optimization process.

We observed that each atrial parameter is significantly less sensitive than its corresponding ventricle parameter. This makes sense physiologically since the atrium acts primarily as a reservoir and to a lesser extent as a small priming pump, leaving the primary driver of the pressure gradient to the ventricle. Therefore the atrium was removed from the model. We next considered the portion of the system below the level of the heart. Peripheral resistances R_{alp}, R_{aup}, and R_{afp} were all sensitive, as well as compliances C_{vl}, C_{vu}, and C_{au}. Instead of concluding immediately that this entire portion of the circulation is sensitive and therefore necessary to the model, we considered these results in light of the physiology and the data. Since we only have data for the brain and the arteries near the heart, model results obtained for the remainder of the body are likely dependent upon each other. In other words, many combinations of pressures, resistances, and compliances could comprise the same total resistance and flow in the body below the heart, leading to the same solution for arterial blood pressure and cerebral blood flow velocity. The differentiation between the upper and lower bodies that was necessary for modeling the transition from sitting to standing, i.e., gravitational effects, is not necessary when only studying baseline dynamics during sitting. Therefore we conclude that sensitive parameters are such because

they are dependent upon each other to provide an effect equal to what would occur with a combined upper and lower body. In addition, note that finger parameters C_{af} and R_{af} were insensitive, ranked at 36 and 41 respectively. This is likely because the proportion of blood flowing to the arm is small compared to the rest of the body and therefore not significant to the model parameter identification problem.

In summary, we eliminated compartments representing the finger and the left atrium and combined the upper and lower body compartments. The resulting compartmental model has seven compartments representing the left ventricle, aorta and vena cava, arteries and veins in the body as well as in the brain, see Figure 5.14. Elimination of the atrium reduced the number of parameters by 15 (including R_v); at the same time, elimination of the arterial and venous compartments reduces the number of parameters by eight, hence, the proposed reduced model then has 7 differential equations and 29 parameters, compared with 11 differential equations and 52 parameters for the full model. Compared against the full model of with 52 parameters, which had a cost of 1.77, the reduced model cost is 1.58. Qualitatively the model solution fits the data similarly in both cases. Equations for the reduced model can be found in Appendix A.2.

As was done with the full model, we carried out sensitivity analysis to rank the parameters with respect to the states p_a, p_{ac}, and p_{vc} that represent the data to be studied. Similar to the full model, the heart parameters were the most sensitive (n, c, θ, ϕ, t_{min}, and p_{min}) though they appear in a slightly different order. The most sensitive non-heart parameter was R_{asp}. This compares well with the full model where R_{aup} and R_{alp} showed high sensitivity. Also both the full model and the reduced model showed high sensitivity to R_{acp} (ranked 9 and 5 in each, respectively) likely because it is explicitly part of the equations that predict the state compared with the data. Finally, it was found that 20 sensitive parameters can be accurately estimated in the small model.

5.6.6 Discussion

In this study we have shown that it is possible to accurately predict 22 of 52 parameters for a single dataset in our compartment model of systemic blood pressure and blood flow, while retaining model fit to data as seen in Figure 5.13. Sensitive parameters have physiological significance, most of which characterize the left ventricle waveform or represent lumped peripheral resistances. Hence, to identify parameter values for multiple

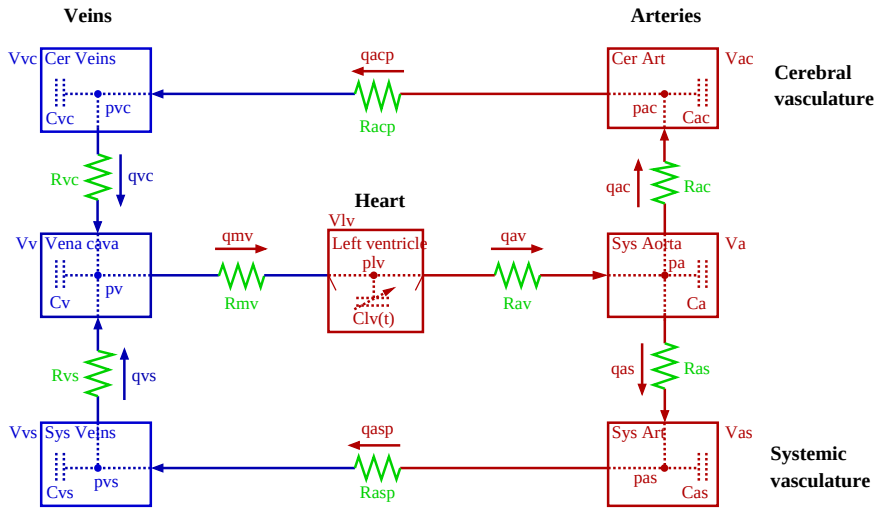

Figure 5.14: The 7-compartment model of systemic circulation, including arteries (a) and veins (v) in the cerebral vasculature (c), the systemic vasculature (s), and the left ventricle (lv). The model is constructed in the same manner as the one depicted in Figure 5.1.

datasets only the most sensitive parameters need to be identified for each of the datasets, and it would be reasonable to use literature estimates for the least sensitive parameters and keep these fixed at nominal values. Based on these predictions, one could calculate means and standard deviations for each parameter for a given group of subjects and compare values between different groups of subjects. We have also shown that it is possible to use sensitivity information to reduce the proposed model and design a simpler model with a similar number of sensitive parameters. However, we do not make any conclusions on sensitivities during a postural change. We hypothesize that during standing, differentiation between upper and lower body due to gravitational effects would be necessary.

Examining specifically at the top 22 parameters of the original model, see Table 5.8, we note that the majority of the top sensitive parameters characterize the ventricular pressure function. These parameters are largely responsible for describing the timing and magnitude of peak ventricular heart pressure p_{pv} and t_{pv} respectively. Because the heart function drives the model, and the peak pressure and waveform timing in the heart are similar to that in the aorta and nearby arteries, [13], it is consistent that the model fit would be most sensitive to these parameters. Not much is known about these parameters *a priori*, as opposed to those that are estimated from known physiological quantities, so finding parameter values for an individual patient is key for model parameterization. The

Table 5.8: The top 22 sensitive parameters and their effect on the model. Units: R, [mmHg·s/ml]; C, [ml/mmHg]; c, [mmHg/ml]; t, [s]; θ, ϕ, [1/s]; ν, η, m, n, dimensionless.

Param.	Role in Model	Effect on model with incr. in parameter value
c_v	Ventricular contractility	Incr. developed and systolic pressure
n_v	Exponent in ventricle polynomial	Peak p_{lv} moves right in time
θ_v	Median of ventricular t_p sigmoid	Incr. median time for peak p_{lv} at given HR
R_{aup}	Resistance, upper body arterioles	Incr. upper body pressure drop
R_{alp}	Resistance, lower body arterioles	Incr. lower body pressure drop
ϕ_v	Median of ventricular p_p sigmoid	Incr. median peak p_{lv} at given HR
C_{vu}	Compliance, upper body veins	Incr. p_{af} and v_{acp}
R_{acp}	Resistance, cerebral arterioles	Incr. cerebral pressure drop
n_a	Exponent in atrium polynomial	Peak p_{la} moves right in time
$p_{min,v}$	Min. of ventricular p_p sigmoid	Incr. min. possible peak p_{lv} at given HR
c_a	Atrial contractility	Incr. developed and systolic pressure
θ_a	Median of atrial t_p sigmoid	Incr. median time for peak p_{la} at given HR
$t_{min,v}$	Min. of t_p sigmoid	Incr. min. possible peak p_{lv} at given HR
C_{vl}	Compliance, lower body veins	Incr. p_{af} and v_{acp}
R_{afp}	Resistance, finger arterioles	Incr. finger pressure drop
ν_v	Steepness of ventricular t_p sigmoid	Incr. distance from median time at given HR
ϕ_a	Median of atrial p_p sigmoid	Incr. median peak p_{la} at given HR
C_{au}	Compliance, upper body arteries	Incr. p_{af} and v_{acp}, narrow waveforms
m_v	Exponent in ventricle polynomial	Peak p_{lv} moves left in time
η_v	Steepness of ventricular p_p sigmoid	Incr. distance from median time at given HR
$p_{min,a}$	Min. of atrial p_p sigmoid	Incr. min. possible peak p_{la} at given HR
C_{ac}	Compliance, cerebral arteries	Narrow v_{acp} waveform

peripheral resistances R_{aup}, R_{alp}, R_{acp}, and R_{afp} characterize the largest pressure drops, so it makes sense that they have a large impact on the solution.

Conversely, we correlate insensitivity of parameters with known physiology. Each atrial parameter is less sensitive than its corresponding ventricular parameters. This is consistent with the fact that maximum atrial pressure is approximately an order of magnitude less than maximum ventricular pressure, [13], and the atrium acts primarily as a primer pump. As another example, the position of d_v representing the volume-independent component of developed pressure for the ventricle, is at the bottom of the sensitivity ranking. Physiologically this could mean several things such as: d_v could be virtually identical between young adult subjects; it could be scaled based on the subject but its exact value is not critical for model fit; or that its place in the model is not necessary.

To reach the results in this study we used automatic differentiation to calculate the gradients used to find the sensitivities of each parameter with respect to each of the state variables. While automatic differentiation algorithms are well-developed and have long been

used in languages such as Fortran, MATLAB algorithms are fairly new, [19] and [31]. The main disadvantage of the MATLAB algorithms is that they are slow relative to Fortran and C++. One numerical solve of the model including sensitivity equations takes about 30 minutes, and an optimization run with the Nelder-Mead simplex method not including the sensitivity equations takes a day and a half. As we wish to analyze multiple subjects' data and expand to different populations, speed will become a necessity. Combining the 30-minute-per-iteration automatic differentiation with a many-iteration optimization routine in Matlab is not reasonable for this purpose. In Chapter 6 we use finite difference methods with the gradient-based optimization methods presented in Section 4.3, as well as investigate subset selection for identifying a smaller set of independent parameters within the larger parameter space, to increase the optimization performance.

Chapter 6

5-Compartment Cardiovascular Model with Subset Selection

Sensitivity analysis addresses the impact of localized parameter perturbations on model output as discussed in Chapters 4 and 5. Any given set of optimal parameters only represents a local solution to the minimization problem. Parameter values defining this local minimum may or may not be within physiological range, and there may be multiple sets of parameters that define the same model states, i.e., multiple local minima. Thus, it is essential to compute nominal parameter values using *a priori* knowledge such as height and weight, literature, or similar experiments. The solution may be insensitive to some of the model parameters, i.e., a small change in some parameters may give rise to almost no change in the output states. It is not feasible to estimate insensitive parameters as seen in Chapter 5 and Ellwein *et al.* [24], neither from a physiological nor from a numerical perspective [45]. If any of the insensitive parameters are physiologically important, designing additional experiments may be necessary to estimate these parameters. In addition, model parameters that the solution is sensitive to may depend on each other. For example, given a mean flow through two resistance vessels, an infinite combination of resistances from each vessel could combine to give the same overall resistance, thus both parameters can not be identified even though the solution will be sensitive to both parameters.

In this study we have made additional progress toward using mathematical models to estimate key parameters given limited experimental data. To illustrate our method, we employ a simple five-compartment lumped parameter model that predicts cerebral blood

flow velocity and arterial blood pressure in the systemic circulation during rest (in sitting position). Similar to the analysis in Chapter 5, model parameters were ranked from the most to the least sensitive. In addition, subset selection as described in Chapter 4 is used to specify a subset of independent candidate parameters. Results from the sensitivity analysis and subset selection were combined to identify a final subset of parameters that can be estimated using a Gauss-Newton gradient-based nonlinear optimization technique. This methodology (sensitivity analysis, subset selection, optimization) was used to extract physiological biomarkers predicting systemic and cerebrovascular resistance, arterial compliance, and time for peak systolic ventricular pressure using pulsatile finger blood pressure and cerebral blood flow velocity data obtained non-invasively from 12 healthy young and 12 healthy elderly subjects. Several known cardiovascular changes occur with aging that made these two groups good choices for comparison. With aging comes a loss of complexity in cardiovascular dynamics, one example being diminished HR variability [42]. Age is also a predictor of arterial stiffness [111], and with increased age cerebral blood flow is reduced [69].

6.1 Model construction

In this study we used a five-compartment lumped parameter cardiovascular model with similar construction as the one presented in Chapter 5. The model was simplified to only account for responses during rest (sitting). Included were two arterial compartments and two venous compartments combining vessels in the body and the brain, as well as one heart compartment representing the left ventricle, see Figure 6.1.

The model used the standard electrical circuit analog presented in Section 3.1. The model can be described by a system of five coupled ordinary differential equations with state variables representing pressure in the systemic arteries (p_{as}), the cerebral arteries (p_{ac}), the systemic veins (p_{vs}), the cerebral veins (p_{vc}), and the left ventricular volume (V_{lv}). These

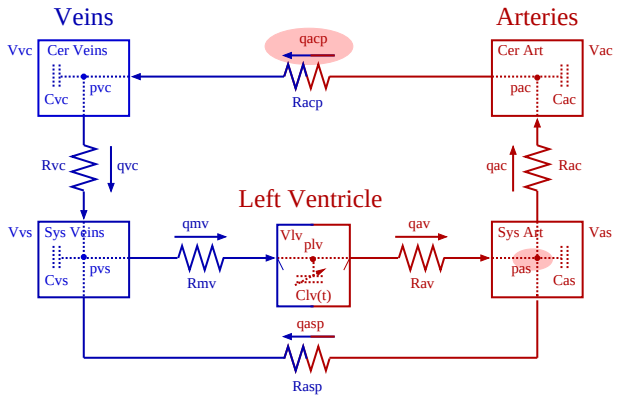

Figure 6.1: Electrical circuit representing arteries and veins in the systemic circulation including the left ventricle (lv), the systemic arteries (as), the cerebral arteries (ac), the cerebral veins (vc), and the systemic veins (vs). Each compartment contains a volume V [ml], pressure p [mmHg] and compliance (capacitor) C [ml/mmHg] (constant). Flow between compartments is marked by q [ml/s] and resistance to flow is marked by R [mmHg·s/ml] (constant). The aortic and mitral valves are marked by small lines inside the left ventricle compartment. This model uses measurements of cerebral blood flow velocity $v_{acp}(t_i) = q_{acp}(t_i)/A_{acp}$ [ml/s], where A_{acp} [cm^2] (constant) denotes the vessel area, and finger blood pressure $p_{as}(t_i)$ [mmHg]. These measurements are obtained at locations marked by red ovals.

are given by

$$\begin{aligned}
\frac{dp_{as}}{dt} &= \left(\frac{p_{lv}-p_{as}}{R_{av}} - \frac{p_{as}-p_{vs}}{R_{asp}} - \frac{p_{as}-p_{ac}}{R_{ac}}\right)/C_{as},\\
\frac{dp_{ac}}{dt} &= \left(\frac{p_{as}-p_{ac}}{R_{ac}} - \frac{p_{ac}-p_{vc}}{R_{acp}}\right)/C_{ac},\\
\frac{dp_{vs}}{dt} &= \left(\frac{p_{as}-p_{vs}}{R_{asp}} + \frac{p_{vc}-p_{vs}}{R_{vc}} - \frac{p_{vs}-p_{lv}}{R_{mv}}\right)/C_{vs},\\
\frac{dp_{vc}}{dt} &= \left(\frac{p_{ac}-p_{vc}}{R_{acp}} - \frac{p_{vc}-p_{vs}}{R_{vc}}\right)/C_{vc},\\
\frac{dV_{lv}}{dt} &= \frac{p_{vs}-p_{lv}}{R_{mv}} - \frac{p_{lv}-p_{as}}{R_{av}}.
\end{aligned}$$

Valve resistances R_{mv} and R_{av} are functions of time of the form of (3.12), with $k = 2$ and $R_{valve,closed} = 10$. The smooth approximation of (5.18) was used to ensure differentiability of the valve equations.

The elastance model in (3.8) is chosen for ventricular pressure p_{lv} because its minimal number of parameters make it more feasible for parameter estimation. The combination

of sinusoidal and rational functions ensures differentiability with respect to each of the four parameters E_{max}, E_{min}, T_M, and T_r. Because the timing changes with each cardiac cycle, we optimize $T_{M,frac} = T_M/T$ and $T_{r,frac} = T_r/T$ then calculate the parameters T_M, and T_r for each cycle.

In summary, the model discussed above can be written as

$$\frac{dX}{dt} = f(t, x, \mu),$$

where $X(t) = [p_{as}(t), p_{ac}(t), p_{vs}(t), p_{vc}(t), V_{lv}(t)]$ represents the five states. This model has a total of 16 parameters including 5 heart parameters

$$\mu_{heart} = \{V_d, E_{max}, E_{min}, T_M, T_r\} \tag{6.1}$$

and 10 cardiovascular parameters

$$\mu_{cardiovasc} = \{R_{av,open}, R_{asp}, R_{ac}, R_{acp}, R_{vc}, R_{mv,open}, C_{as}, C_{vs}, C_{ac}, C_{vc}\}.$$

The 16^{th} parameter is the scaling factor A_{acp} described in Chapter 5.

6.2 Experimental data

Data to be analyzed in this study included noninvasive finger blood pressure and cerebral blood flow velocity measurements from 12 healthy young subjects age 22-39 years (with a mean age of 28.8 ± 6.0 years) and 12 healthy elderly subjects age 56-74 years (with a mean age of 66.1 ± 6.4 years). Data were acquired in the SAFE laboratory and subjects provided informed consent signed by the Institutional Review Board at Beth Israel Deaconess Medical Center. The right and left middle cerebral arteries were insonated from the temporal windows with 2-MHz pulsed Doppler probes (MultiDop X4, DWL Neuroscan Inc. Sterling VA). Each probe was positioned to record the maximal flow velocities and stabilized using a three-dimensional head frame positioning system. Blood flow velocities were measured continuously in each of the middle cerebral arteries. In addition, peak-systolic, end-diastolic, and mean blood flow velocities were measured for each of the MCAs. Blood pressure was recorded continuously from a finger using a Finapres device (Ohmeda Monitoring Systems, Englewood, CO) and blood pressure measurements were intermittently validated using tonography. To eliminate gravitational changes in blood pressure, the finger was kept at the level of the heart. The Finapres device provides reasonably accurate

estimates of intra-arterial pressure if the finger position and temperature are kept constant (25). The electrocardiogram was measured from a modified standard lead II using a Spacelab Monitor (SpaceLab Medical Inc., Issaquah, WA). Signals were recorded at 500 Hz using a Labview Data Acquisition System (NINDAQ) (National Instruments, Austin TX). Measurements were obtained from subjects resting in a sitting position with their legs elevated at 90 degrees. Once a stable signal was obtained, data were recorded for 5 minutes in sitting position and for 3 minutes during quiet standing with eyes open. From the sitting signal 50 cardiac cycles were extracted and stored for the offline model analysis. All analysis was carried out on deidentified data. Figure 6.2 shows blood pressure (left) and blood flow velocity (right) data for a healthy young subject.

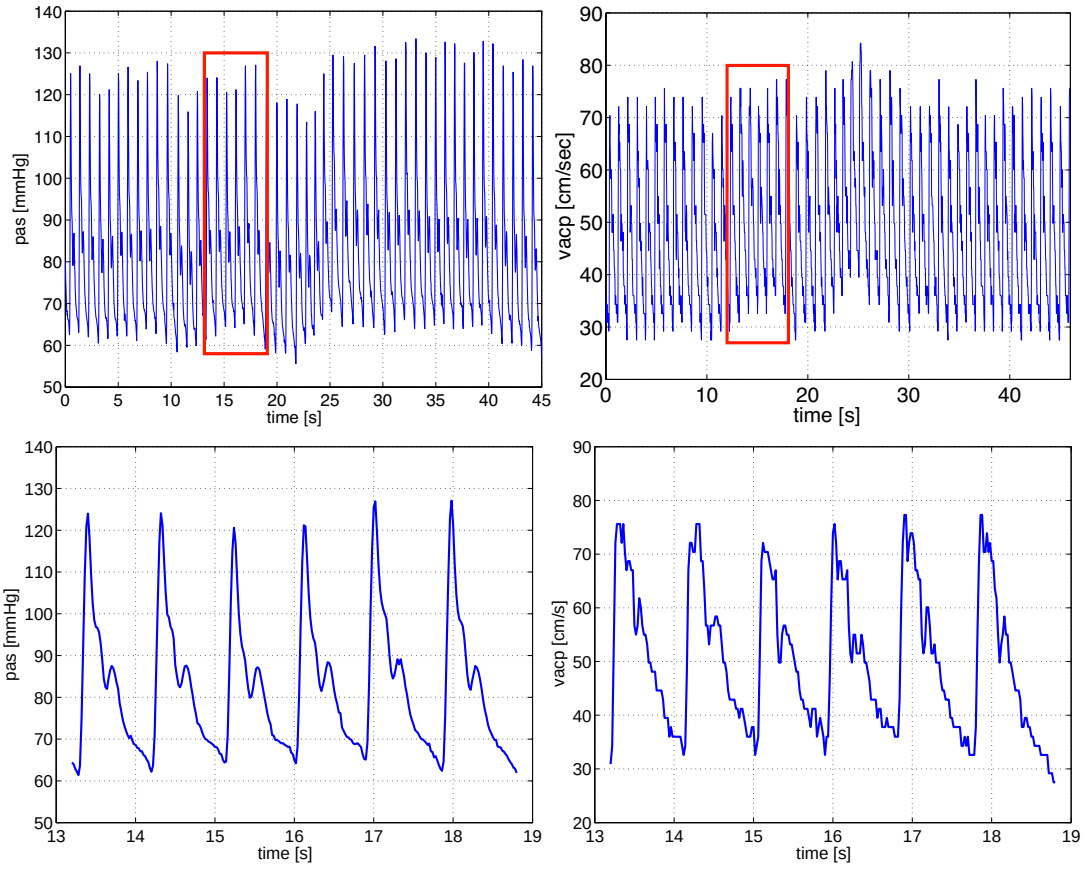

Figure 6.2: Arterial blood pressure p_{as} (left) and cerebral blood flow velocity v_{acp} (right) from a healthy young subject. The top panel shows the entire time-series and the bottom panel shows a zoom over 6 s (areas zoomed are marked by boxes in the top panel).

6.3 Parameterization

6.3.1 Model parameters

Nominal values for the cardiovascular parameters (see Table 6.1) were found from physiological considerations. Parameters for the elastance model are listed in Equation (6.1). The initial iterates for E_{min} and E_{max} [mmHg/ml] were taken from Ottesen *et al.* [80]. Parameters $T_{M,frac} = T_M/T$ and $T_{r,frac} = T_r/T$ [s/s] were predicted using the average of values given by Ottesen *et al.* [80] and Heldt [38].

Initial values for resistors and capacitors were determined separately for each subject studied. The peak systolic ventricular pressure was defined as the peak of the data finger pressure $p_{d,max} = \max(p_d)$. To allow blood flow down the pressure differential, values for systemic arterial pressure and cerebral arterial pressure were set at 99.5% and 98% of $p_{d,max}$. There is no information from the data about venous pressures, so they are set based on standard physiological considerations, see e.g. [10, 36, 103] and Chapter 4. Total BV

Table 6.1: Initial values for all model parameters. The total volume V_{tot} is defined in (6.2), equivalent to total flow q_{tot}, and p^d_{max} is the maximum of the pressure data. The parameter k is a scaling factor for particular pressures and flows. The parameter $A_{acp} = q_{acp}/v_{acp}$ relates cerebral blood flow to cerebral blood flow velocity.

Pressure [mmHg]	$k \cdot p^d_{max}$ k	Flow [ml/s]	$k \cdot q_{tot}$ k	Resistances [mmHg· s/ml]	Ohms law
$p_{lv,sys}$	1	q_{av}	1	$R_{av,open}$	$(p_{lv,sys} - p_{as})/q_{av}$
p_{as}	0.995	q_{mv}	1	$R_{mv,open}$	$(p_{vs} - p_{lv,dia})/q_{mv}$
p_{ac}	0.98	q_{asp}	0.8	R_{asp}	$(p_{as} - p_{vs})/q_{asp}$
p_{vc}	10 [mmHg]	q_{ac}	0.2	R_{ac}	$(p_{as} - p_{ac})/q_{ac}$
p_{vs}	5 [mmHg]	q_{acp}	0.2	R_{acp}	$(p_{ac} - p_{vc})/q_{acp}$
$p_{lv,dia}$	2 [mmHg]	q_{vc}	0.2	R_{vc}	$(p_{vc} - p_{vs})/q_{vc}$
Volume [ml]	$k \cdot V_{tot}$ k	Capacitors [ml/mmHg]		Heart parameters E_i [mmHg · s/ml], V_d [ml]	
V_{lv}	65 [ml]			$T_{M,frac}$	0.38
V_{as}	0.1094	C_{as}	$0.35V_{as}/p_{as}$	$T_{r,frac}$	0.18
V_{ac}	0.0193	C_{ac}	$0.35V_{ac}/p_{ac}$	E_m	0.049
V_{vc}	0.0783	C_{vc}	$0.08V_{vs}/p_{vs}$	E_M	2.49
V_{vs}	0.5634	C_{vs}	$0.08V_{vc}/p_{vc}$	V_d	10

[ml] was calculated as as a function of body surface area BSA [m^2] and gender [5] by

$$V_{tot} = \begin{cases} 1000(3.29BSA - 1.29), & \text{male} \\ 1000(3.47BSA - 1.954), & \text{female.} \end{cases} \tag{6.2}$$

This study estimated BSA using a relation originally proposed by Mosteller [57] and later reformulated by Reading and Freeman,

$$BSA = \sqrt{\frac{wh}{3600}}, \tag{6.3}$$

where h [cm] is the subject's height and w [kg] denotes the subject's weight. It follows that resistances and compliances are calculated based on methods described in Chapter 4 using these pressures and volumes. These pressures were used as initial conditions in the state equations as well.

6.3.2 Parameter estimation

Parameter estimation is conducted in a similar manner as the study in Chapter 5, adding subset selection to identify parameter dependencies. Measured data include arterial blood pressure $p_{as}(t_i)$ and cerebral blood flow velocity $v_{acp}(t_i)$. Data were sampled for $M = 50$ cardiac cycles. Nonlinear optimization was used to estimate these parameters by minimizing the residual between computed and measured pressure and velocities relative to the measured quantities over all samples t_i. To this end we define the vector y spanning both pressure and velocity, i.e., y has $2N$ entries, given by

$$y = [p_{as}(t_1), \ldots, p_{as}(t_N), v_{acp}(t_1), \ldots, v_{acp}(t_N)]^T. \tag{6.4}$$

To ensure that the model captures both the systolic values, noted by subscript *sys*, and the diastolic values, noted by subscript *dia*, of the pressure and velocity for each cardiac cycle, we defined additional vectors y_{sub}, $sub = sys, dia$ given by

$$\begin{aligned} y_{sys} &= [p_{as,sys,1}, \ldots, p_{as,sys,M}, v_{acp,sys,1}, \ldots, v_{acp,sys,M}]^T, \\ y_{dia} &= [p_{as,dia,1}, \ldots, p_{as,dia,M}, v_{acp,dia,1}, \ldots, v_{acp,dia,M}]^T. \end{aligned} \tag{6.5}$$

Note that each of these vectors concatenate pressure and velocity, i.e., each vector has $2M$ entries. These quantities are not dependent on time, but represent the minimum (diastolic) and maximum (systolic) values for each cardiac cycle.

The cost function J for parameter estimation and optimization is calculated from the residual R. Combining the vectors y, we defined the residual vector between computed ($y^c = X(\hat{\mu})$) and measured (y^d) quantities as

$$R = \left[\frac{y^c_1 - y^d_1}{\sqrt{N} y^d_1}, \ldots, \frac{y^c_{2N} - y^d_{2N}}{\sqrt{N} y^d_{2N}}, \frac{y^c_{sys,1} - y^d_{sys,1}}{\sqrt{M} y^d_{sys,1}}, \ldots, \frac{y^c_{sys,2M} - y^d_{sys,2M}}{\sqrt{M} y^d_{sys,2M}}, \right.$$
$$\left. \frac{y^c_{dia,1} - y^d_{dia,1}}{\sqrt{M} y^d_{dia,1}}, \ldots, \frac{y^c_{dia,2M} - y^d_{dia,2M}}{\sqrt{M} y^d_{dia,2M}} \right]^T .$$

Since velocity and pressure have different units and magnitudes, and since components in this vector have different lengths, the residual is scaled by both the value of the measurements and by the square root of the number of measurements (N for data, M for systolic/diastolic). This definition of the residual vector R gave rise to a least squares cost function J of the form

$$J = R^T R = \frac{1}{N} \sum_{i=1}^{N} \left| \frac{p^c_{as} - p^d_{as}}{p^d_{as}} \right|^2 + \frac{1}{N} \sum_{i=1}^{N} \left| \frac{v^c_{acp} - v^d_{acp}}{v^d_{acp}} \right|^2 + \frac{1}{M} \sum_{i=1}^{M} \left| \frac{p^c_{as,sys} - p^d_{as,sys}}{p^d_{as,sys}} \right|^2 + \tag{6.6}$$
$$\frac{1}{M} \sum_{i=1}^{M} \left| \frac{p^c_{as,dia} - p^d_{as,dia}}{p^d_{as,dia}} \right|^2 + \frac{1}{M} \sum_{i=1}^{M} \left| \frac{v^c_{acp,sys} - v^d_{acp,sys}}{v^d_{acp,sys}} \right|^2 + \frac{1}{M} \sum_{i=1}^{M} \left| \frac{v^c_{acp,dia} - v^d_{acp,dia}}{v^d_{acp,dia}} \right|^2 .$$

Several criteria discussed below are used to identify a limited set of parameters to be estimated. As in Chapter 5, sensitivity analysis was used to rank parameters from the most to the least sensitive. Subsequently, subset selection was used to identify a limited number of candidate parameters. Combining results from both analyses allowed us to select of a set of parameters to be estimated for all healthy young and healthy elderly subjects. Finally, nonlinear optimization was used to estimate the parameters.

6.3.3 Sensitivity analysis

Similar to previous work by Ellwein *et al.* [24] and presented in Chapter 5, classical sensitivity analysis was used to rank the model parameters from the most to the least sensitive. Sensitivities were computed with respect to output vector y (7.13) that concatenates pressure and velocity evaluated at times of the measured observations t_i. Note that velocities v_{acp} (the second half of y) are not state variables in the differential equation model but are obtained by scaling the cerebrovascular flow $q_{acp} = (p_{ac} - p_{vc})/R_{acp}$ by the cerebral vessel scaling factor A_{acp} (constant).

Optimization methods (discussed below) are more efficient when all parameter values are of the same order of magnitude. The nominal parameter values for our model differ by three orders of magnitude (for example, $E_d = 0.05$, while $C_v = 36$ initially). To avoid scaling issues we rescaled the parameters by the natural logarithm, i.e., the model input to the optimizer is given by $\tilde{\mu} = \ln(\mu)$.

Using the scaled parameters $\tilde{\mu}$, the relative (nondimensional) sensitivities S_{jk} of the output y_j to the k^{th} parameter is defined by

$$S_{jk}(t,\tilde{\mu})|_{\tilde{\mu}=\tilde{\mu}_0} = \left.\frac{\partial y_j}{\partial \tilde{\mu}_k}\frac{\tilde{\mu}_k}{y_j}\right|_{,\tilde{\mu}=\tilde{\mu}_0} \; X_j, \tilde{\mu}_k \neq 0 \tag{6.7}$$

in the same manner as (4.8). Note, the length of S_{jk} is 2N, since S_{jk} concatenates sensitivities of pressure and velocity with respect to each of the model parameters. The derivative was computed in the sensitivity equation using the forward difference approximation for $\partial y_j/\partial\tilde{\mu}_k$ as introduced in 4.11 because it was found to be computationally faster than AD and provided sufficient accuracy for our purposes. A scaled 2-norm was used to calculate the total sensitivity, S_k, to the k^{th} parameter

$$\mathbf{S_k} = \left(\frac{1}{2N}\sum_{i=1}^{2N} S_{jk}^2\right)^{(1/2)}. \tag{6.8}$$

Classical sensitivity analysis as described above is a local analysis, and thus sensitivities depend on the values of the parameters. The sensitivity ranking was computed using nominal parameter values because the analysis is done prior to actual parameter estimations.

6.3.4 Sensitivity to initial conditions

To analyze the dependence of solutions of these types of systems on initial conditions, the sensitivity is addressed in the same manner as for the design parameters. Sensitivity equations for initial conditions are given in the manner of (4.13) by

$$\frac{\partial}{\partial X_{0,j}}\frac{dX_l}{dt} = \sum_{k=1}^{Y}\frac{\partial F_l}{\partial X_j}\frac{\partial X_j}{\partial X_{0,j}} + \frac{\partial F_l}{\partial X_{0,j}}, \tag{6.9}$$

where the number of state equations $Y = 5$. Note that $\partial F_i/\partial X_{0,j} = 0$ for all $X_{0,j}$. The forward difference Jacobian scheme was used here as well, resembling (4.11),

$$\frac{\partial X}{\partial X_0} \approx \frac{X(X_0+\epsilon,\mu,t) - X(X_0,\mu,t)}{\epsilon}.$$

A composite sensitivity was calculated using (6.8). For this analysis, the 2-norm was used for both p_a and v_{acp}. A parameter rank was calculated for an individual dataset. Then a final rank was calculated to be the average of these ranks for 12 healthy datasets, see Figure 6.3 and Table 6.2.

Table 6.2: Sensitivities ranked with respect to initial conditions for both healthy young and elderly groups of subjects.

	Young		Elderly	
Param	Sensitivity	Rank	Sensitivity	Rank
$p_{as,0}$ [mmHg]	1.87	1	1.78	1
$p_{vs,0}$ [mmHg]	0.71	2	0.66	3
$V_{lv,0}$ [ml]	0.62	3	0.98	2
$p_{ac,0}$ [mmHg]	0.24	4	0.22	4
$p_{vc,0}$ [mmHg]	0.14	5	0.13	5

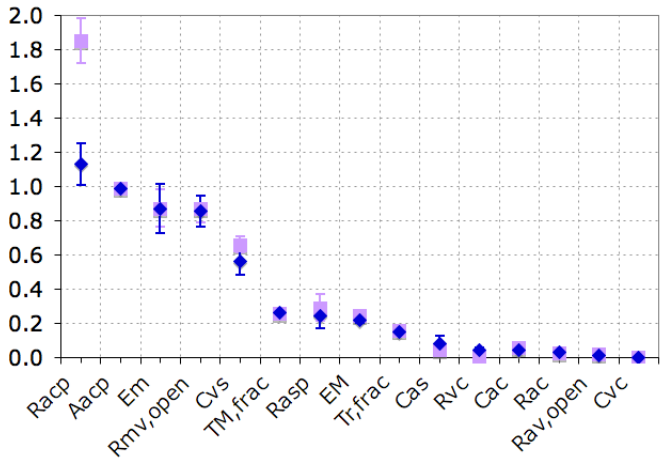

Figure 6.3: Overall ranking of the scaled model parameters $\ln(\mu)$ with one standard deviation for the healthy young subjects (blue marks) and healthy elderly subjects (lavender marks) ranked from the most to the least sensitive. Units: R, [mmHg·s/ml]; C, [ml/mmHg]; E, [mmHg/ml]; T_{frac}, [s/s]

6.3.5 Subset selection

Attempting to optimize all parameters in the model can lead to unrealistic parameter estimates and poor optimizer performance, particularly if some of the model parameters are interdependent. To determine how many and which parameters that can be identi-

fied reliably we implemented a modified version of the subset selection method detailed in Chapter 4.

The result of the subset selection process was a list of identifiable parameters and a list of parameters that should be held constant at nominal parameter values during the optimization process. To obtain physiologically relevant parameters, this method was carried out combined with expert knowledge of the system studied. For example, subset selection picked the scaling factor A_{acp} as an identifiable parameter, while the cerebrovascular resistance R_{acp} was grouped with parameters to be kept fixed. However, the parameter A_{acp} only appears once in the ODE system as a factor next to R_{acp}, while R_{acp} also appears inside one of the differential equations. Furthermore, R_{acp} is one of the biomarkers that was found important to estimate. Consequently, A_{acp} was kept at its nominal value and subsequently subset selection picked R_{acp}. Another observation was that for a healthy heart, the resistances associated with the heart valves $R_{mv,open}$ and $R_{av,open}$ should be small and should remain fixed in order to obtain a small pressure gradient at the time of peak blood flow [13]. However, in particular R_{mv} is very sensitive, which makes sense; large valve resistances could indicate a blockage of the valve, and a large change in this parameter does have a significant impact on the model solution. In this study only data from healthy subjects were analyzed, thus sensitivities were evaluated using nominal parameter values.

Results from both sensitivity analysis and subset selection in conjunction with user knowledge were combined to find a limited set of candidate parameters to be estimated for all subjects. To estimate the model parameters the Levenberg-Marquardt variant of the gradient-based Gauss-Newton optimization method introduced in Section 4.3.2 was utilized to minimize the cost J defined in (6.7). Optimizations were run with the candidate parameters against a subset of subjects and the candidate list was further adjusted based on the performance of the optimizer. If the addition of a parameter caused the optimization routine to fail to converge, the parameter was not included in the final list.

6.4 Results

Data from 12 healthy subjects age 22-39 years and 12 healthy elderly subjects age 56-74 years with characteristics summarized in Table 6.3 were analyzed. Sensitivities for each of the 15 model parameters with respect to cerebral blood flow velocity and arterial blood pressure were computed and ranked given initial values for model parameters. An overall rank (see Figure 6.3) was obtained from the average sensitivities across each group of subjects. As shown in Table 6.2, the output states ($v_{acp}(t)$ and $p_{as}(t)$) were also highly sensitive to initial values.

Table 6.3: Characteristics for both healthy young and elderly groups of subjects. For each group of subjects, entries include diastolic (D), systolic (S), and mean (M) velocities, followed by diastolic (D), systolic (S), and mean (M) pressures. Each row contains values obtained from the data (d) and the model (c). The top row gives the mean values computed as an average over all periods, the second row gives the corresponding standard deviation, and the last row gives the percent error obtained as the difference between measured and computed values relative to the measured values.

	Young							Elderly					
	Velocity [cm/s]			Pressure [mmHg]				Velocity [cm/s]			Pressure [mmHg]		
	D	S	M	D	S	M		D	S	M	D	S	M
	Mean values							Mean values					
d	42	98	63	66	116	82	d	34	80	53	73	134	94
c	48	97	71	67	129	95	c	34	67	50	69	132	98
	Standard deviation							Standard deviation					
d	8.5	15	11	7.6	14	8.4	d	6.9	16	11	4.7	11	5.6
c	9.9	15	12	8.1	14	10	c	5.9	14	9.5	3.1	13	5.6
	% Error							% Error					
	14	4.2	13	2.8	11	16		4.2	17	4.1	6.2	4	4.6

Subset selection was used to identify a set of candidate parameters. We repeated the subset selection for all datasets. Results showed that parameters R_{asp}, R_{acp}, C_a, $T_{M,frac}$, and E_M were picked for all subjects. In addition for the healthy young group, C_{ac} was picked once, while C_v and E_m were picked twice. For the healthy elderly group, C_{ac} was picked for 11 subjects, C_v was picked for 8 subjects, and E_m was picked for 3 subjects. Four of the parameters chosen by subset selection for all subjects, R_{asp}, R_{acp}, $T_{M,frac}$, and E_M were sensitive. Consequently, these parameters were included in the final set of parameters to be estimated for all subjects. The final parameter, picked for all subjects, was C_{as}, whose sensitivity is lower. For the elderly subjects two additional parameters were picked with

high frequency: C_{ac}, which was not included because it is insensitive, and C_{vs}. C_{vs} has high sensitivity and thus it should be included, but this parameter caused poor convergence of the optimizer, thus it was left out of the final set. Based on these observations the final set of parameters to be estimated for all subjects included R_{acp}, R_{asp}, $T_{M,frac}$, E_M, and C_{as}.

Optimized parameter values are summarized in Table 6.4. Results showed that R_{acp} and $T_{M,frac}$ (with 5% confidence) and C_{as} (with a 10% confidence) differ between groups. This table also showed, as expected, that the total systemic resistance differs between the two groups. A linear correlation factor (r^2 value) between computed and measured values of pressure and velocity was computed. For young subjects overall correlation coefficients for pressure and velocity were 0.84 and 0.86, respectively. For the elderly subjects, the correlation was somewhat lower, 0.80 for blood pressure and 0.78 for blood flow velocity.

We also compared diastolic, systolic, and mean values for each subject's time-series. For the young subjects, the model gave rise to mean values that were approximately 15% higher than the corresponding measured values. This can be attributed to the fact that the model does not account for wave reflection (our model does not predict the di-

Table 6.4: Mean and standard deviation for initial and optimized values for the 5 identifiable parameters R_{asp}, R_{acp}, C_a, $T_{M,frac}$, and E_M. In addition, we have predicted the total resistance and compared that between young and elderly subjects. Since this is a derived parameter no initial values are given. For each parameter the top row is obtained for the young subjects (marked by Y), while the bottom row denotes values obtained for the healthy elderly subjects (marked by E). The last column shows p-values comparing the optimized parameter values between healthy young and healthy elderly subjects.

		Initial parameters		Optimized parameters		
Parameter		Mean	Std	Mean	Std	p-value
R_{asp} [mmHg·s/ml]	Y	1.9	0.4	3.1	1.05	
	E	2	0.32	3.8	1.38	0.22
R_{acp} [mmHg·s/ml]	Y	7.1	1.5	4.6	0.82	
	E	17	3.2	6.4	1.57	0
R_{tot} [mmHg·s/ml]	Y	-	-	1.9	0.4	
	E	-	-	2.5	0.7	0.02
C_{as} [ml/mmHg]	Y	1.5	0.3	0.53	0.15	
	E	1.3	0.17	0.41	0.17	0.07
$T_{M,frac}$ [s/s]	Y	0.38	0	0.12	0.015	
	E	0.38	0	0.22	0.084	0
E_M [mmHg/ml]	Y	2.5	0	4.3	1.5	
	E	2.5	0	4	1.7	0.64

crotic notch). The model also gave rise to systolic pressures and diastolic velocities that were approximately 12% too high, while the diastolic pressures and the systolic velocities were significantly more accurate with less than 5% error. On the other hand, for the elderly subjects, the model did not systematically produce an overshoot or an undershoot. The systolic and diastolic values had a larger error, while the mean values were predicted more accurately. Even though these errors seem large, it should be noted that the model does not account for all demographic characteristics or for fluctuations due to respiration. Overall, the model predicts the data well as shown in Figure 6.4, which shows an example computation of v_{acp} and p_{as} using optimized parameters for a young subject. In addition Figure 6.5 shows all internal states including ventricular pressure $p_{lv}(t)$ and volume $V_{lv}(t)$, systemic venous pressure $p_{vc}(t)$, and cerebral arterial $p_{ac}(t)$ and venous $p_{vc}(t)$ pressure. One limitation of this model is that it under-predicts cardiac output (not shown) by about 35% and ventricular volume $V_{lv}(t)$ was shifted down toward lower values (see Figure 6.5).

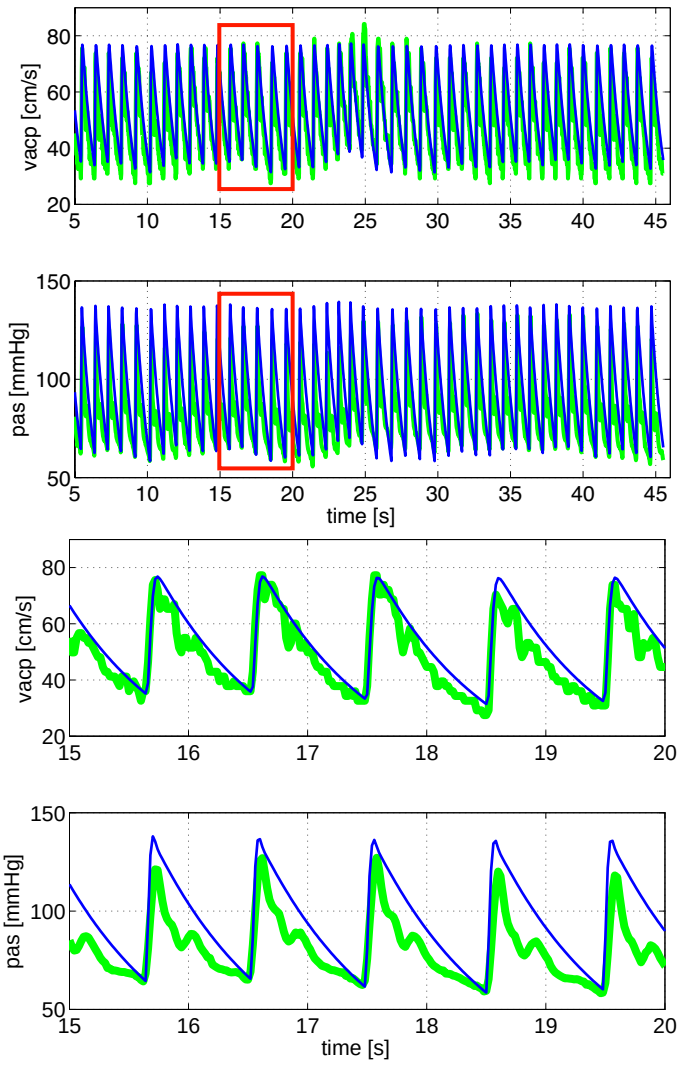

Figure 6.4: Experimental data (green) and model simulation (blue) for arterial pressure p_{as} and cerebral blood flow velocity v_{acp} for a healthy young subject. Left panel: results for the entire time-series. Right panel: zoomed window, $15 < t < 20$ s.

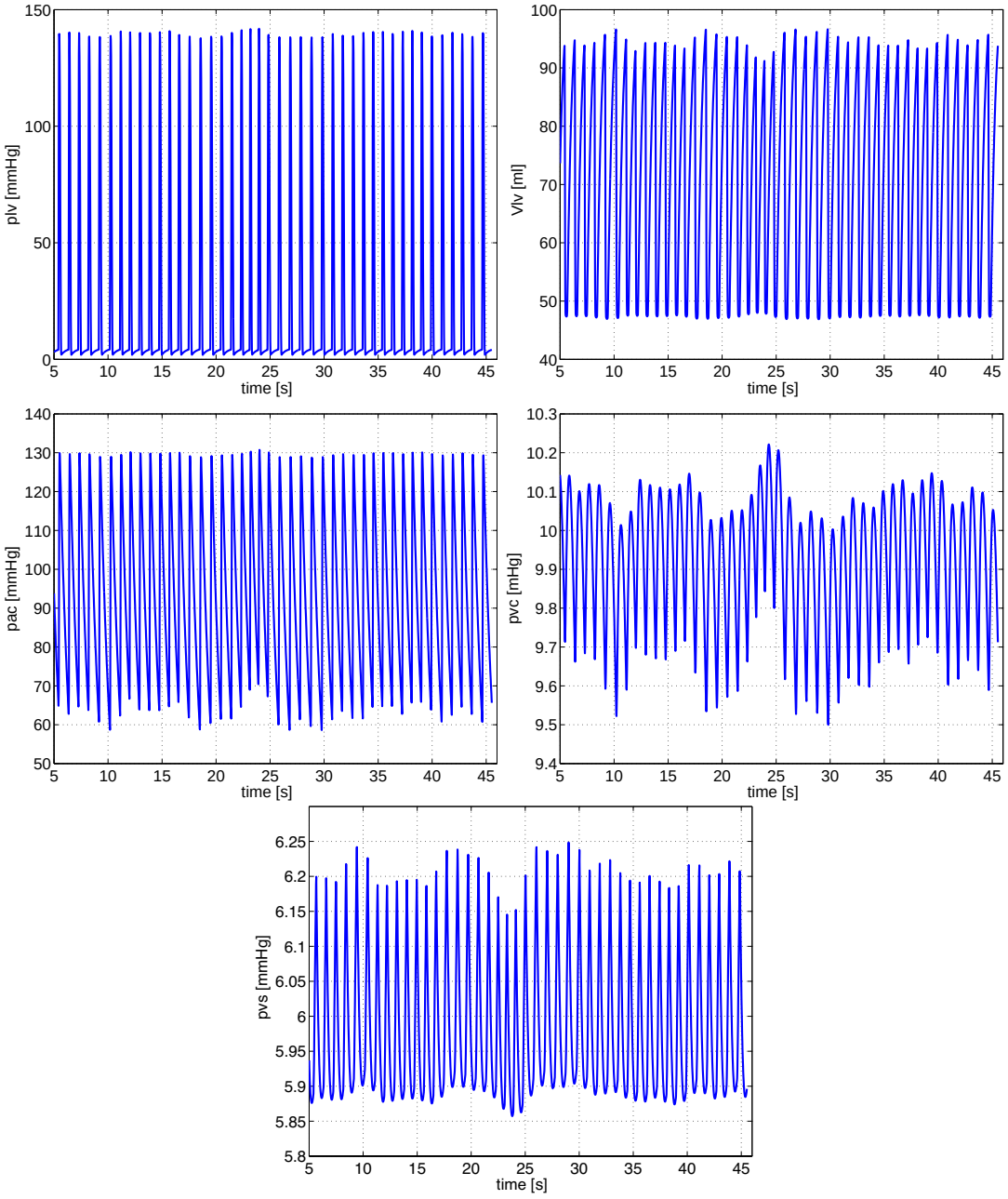

Figure 6.5: Additional model states including ventricular pressure p_{lv} and volume V_{lv}, systemic venous pressure p_{vs}, cerebral arterial pressure p_{ac}, and cerebral venous pressure p_{vc}. These results are shown for the same healthy subject depicted in Figure 6.4.

Another advantage of only identifying a limited number of parameters is that the computational efforts are significantly reduced. For most subjects, identification of 5 parameters required approximately 10 iterations. These 10 iterations lead to approximately 60 evaluations of the cost function (defined in (6.7)), one evaluation for each calculation of the cost function and 5 additional evaluations used to calculate the finite difference Jacobian. The total computation time for the optimization was approximately 800 seconds (just over 13 minutes) on a Macbook 2Ghz laptop with 2GB of memory running MATLAB 7.4.

6.5 Discussion

This study showed that sensitivity analysis and subset selection enabled us to reliably identify 5 parameters in a cardiovascular model that includes a total of 16 parameters. These results were obtained with a model that predicts cerebral blood flow velocity and arterial blood pressure using data from 12 healthy young and 12 healthy elderly subjects. The 5 identifiable parameters were cerebrovascular resistance R_{acp}, systemic resistance R_{asp}, arterial compliance C_{as}, time for peak elastance relative to the length of the cardiac cycle $T_{M,frac}$, and maximum elastance E_M. During the optimization procedure these 5 parameters were identified, while all other parameters were kept fixed at their nominal parameter values.

The major advantage of limiting the number of parameters to be identified is that the parameter estimates become more reliable. For the 24 datasets analyzed in this study (12 healthy young and 12 healthy elderly), reducing the number of parameters to be identified reduced the standard deviation for each parameter by several orders of magnitude. Furthermore, reducing the number of parameters to be optimized reduces the interdependency of the model parameters. For example, in this model, R_{acp} and A_{acp} are both sensitive (see Figure 6.3), but they appear multiplied by each other in the calculation of cerebral blood flow velocity. An infinite number of combinations of values for these two parameters could combine to give the same output states preventing parameter values from being uniquely determined. Thus, we kept A_{acp} constant, while we allowed R_{acp} to fluctuate.

However, it is important to remember that the model does depend on the remaining 11 non-optimized parameters. Consequently, it becomes essential how these are calculated, since some of these may vary by age, gender, height, mean arterial pressure etc. Nominal

values for these non-optimized parameters were found as described previously.

A limitation of this study is that subset selection does not always pick the parameters that we find the most physiologically relevant. For example, subset selection often picked A_{acp} over R_{acp}. However, considering our goal is to predict R_{acp}, we chose to keep A_{acp} fixed at its nominal value while allowing R_{acp} to vary. With this additional constraint subset selection always picked R_{acp} as one of the parameters to be estimated. Another possibility would be to create a new parameter defined as the product of these two parameters. This composite parameter could then be compared between different groups of subjects, yet it would have less physiological relevance than examining the parameters separately. Another advantage of this is that we do not have to account for subject variation in total area A_{acp}. While TCD studies by Aaslid and others [1, 48, 82] note that the MCA cross-sectional area is relatively constant over a wide range of mean flow velocities, the areas do vary between subjects. Inter-subject variation is not accounted for in this study, but A_{acp} could be determined explicitly for each subject uing vessel diameters measured on magnetic resonance angiographs.

With these modifications, subset selection picked the two major resistances R_{acp} and R_{asp}. Computations showed that R_{acp} varied significantly between groups of subjects, while R_{asp} did not. We did expect to find changes in R_{asp}. However, due to the simplicity of the cardiovascular model, and without any flow or velocity measurements for this portion of the system, we could not make any conclusions about this part of the model. On the other hand, the total systemic resistance did show significant changes between the two groups of subjects. Total peripheral resistance is classically defined as the mean arterial pressure over cardiac output [4]. Given a mean pressure of 100 mmHg and an average cardiac output of 5 l/min (83.3 ml/sec) a standard total resistance is 1.2 mmHg·sec/ml. Our results predicted R_{asp} as 1.9 for the healthy young subjects and 2.5 for the healthy elderly people. The model proposed here is validated against only cerebral blood flow velocity data and arterial blood pressure data. One limitation of this study was that the model underestimated cardiac output. For most subjects cardiac output was calculated to be about 65% of a standard cardiac output, which led to higher values for the total resistance. To ensure accurate cardiac output estimates it is essential to either include measurements of cardiac output (which would be incorporated into the cost function) or to predict cardiac output from the blood pressure measurements, as suggested by Parlikar *et al.* [83], Wesseling *et al.* [112], and Mukkamala *et al.* [58].

Another traditional measure of resistance is the resistance index defined as the pulsatile blood flow velocity (in this study v_{acp}) over the systolic velocity, i.e., $RI = (v_{sys} - v_{dia})/v_{sys}$, and the pulsatility index defined as the systolic minus the diastolic blood flow velocity over the mean blood flow velocity, i.e, $RI = (v_{sys} - v_{dia})/v_{mean}$ [63]. While these indices may be useful for detecting differences within a subject, we did not denote any differences between the two groups studied. For the healthy young subjects $RI^d = 0.51$ and $RI^c = 0.57$, while for the healthy elderly subjects $RI^d = 0.49$ and $RI^c = 0.58$. Similarly, for the healthy young subjects the pulsatility indices were $RI^d = 0.69$ and $RI^c = 0.89$, while for the healthy elderly subjects $RI^d = 0.66$ and $RI^c = 0.87$. For all indices superscript d denotes that the quantity is obtained from measurements and c denotes that the quantity is extracted from the model. All values were obtained using information summarized in Table 6.3.

Another observation was that subset selection picked C_{as} (systemic arterial compliance) rather than C_{vs} (systemic venous compliance), which is more sensitive (see Figure 6.3). From a physiological viewpoint C_{vs} may be more significant. However, C_{as} is significantly closer to the data collection site (finger arterial pressure is measured), thus this parameter likely plays a larger role in predicting the pressure data. To investigate this further, we suggest testing if subset selection would pick C_{vs} if C_{as} is kept fixed at its nominal parameter value.

We also observed that $R_{mv,open}$ was very sensitive, but physically, we know that all subjects had well functioning heart valves. Consequently, this parameter should remain small and not be optimized. In fact, subset selection did initially pick this parameter. However, optimizing it caused computed ventricular pressures to be outside of the physiological range. On the other hand, R_{av} had a low sensitivity and was never picked, thus special considerations were not required for this parameter.

Finally, we observed that for the healthy elderly subjects, subset selection picked 7 parameters rather than 5. The two additional parameters included were C_{ac}, which is highly insensitive, and C_{vs}. To study the effect of this difference, we ran simulations for the elderly optimizing all seven parameters. Including both additional parameters led to poor performance of the optimizer. This is predictable since we include an insensitive parameter (C_{ac}), which cannot easily be estimated given the data. Including 6 parameters (i.e., adding the parameter C_{vs}) also led to poor performance of the optimizer. This cannot be explained by insensitivity, but may be related to parameter dependencies not captured

by the subset-selection algorithm. More research into this will be done in future work.

Regarding the heart parameters, subset selection identified two parameters: time for maximum elastance relative to the length of the cardiac cycle ($T_{M,frac}$) and the maximum elastance (E_M). The parameter $T_{M,frac}$ differed significantly between the two groups of subjects, while no statistical significance was observed in values for E_M. The larger $T_{M,frac}$ value found in the elderly subjects can be explained by accounting for wave-reflection as described by Vlachopoulos and O'Rourke [111]. In elderly people, stiffer arteries cause the reflected pressure wave to augment the forward wave coming from the ventricle in late systole. This appears as a peak in the aortic pressure waveform that occurs later than and partially masks the systolic peak. Since the sole generator of the arterial waveform in our model is the ventricular pressure function, it is natural that this feature observed in elderly subjects appears in the $T_{M,frac}$ parameter.

It should be noted again that this study included a simple heart model, which may not capture as many physiological attributes as other more detailed models such as the 14 parameter model developed by Ottesen and Danielsen [79]. A nice feature that we found (not shown) is that if one replaces the simple 4 parameter heart model with Ottesen and Danielsens 14 parameter heart model, subset selection still identifies the same three cardiovascular parameters in addition to 3 heart parameters. In Section 6.5.1 we discuss the dynamics of the 5-compartment model using both heart models.

6.5.1 Cardiac models

As noted in earlier in Section 6.5, cardiac output was underestimated using the elastance model for ventricular pressure allowing subset selection to choose two of the four heart parameters for optimization. Under the hypothesis that the choice of ventricular pressure function influences the resulting cardiac output from optimization using subset selection, the performance of both the elastance and polynomial heart models are compared in the context of the model. Optimizations using subset selection were run on two timeseries from the same subject which we refer to as 'dataset 1' and 'dataset 2'. Tables 6.5 and 6.6 give initial and optimized parameter values using each of the two heart models.

The two models were both able to simulate model outputs p_{as} and v_{acp}, see Figures 6.6 and 6.7. One key difference arises in the left ventricular volume, see Tables 6.5 and 6.6, and Figures 6.8 and 6.9. We predict mean SV using the subject's estimated CO

Table 6.5: Maximum, minimum, and mean arterial pressures p_a, cerebral velocities v_{acp}, and left ventricular volumes V_{lv} for dataset 1. Ventricular volume dynamics and subject data are used to calculate mean SV and CO using both initial and optimized parameters.

State	Data	Init, poly	Opt, poly	Init, elast	Opt, elast
$p_{a,max}$ [mmHg]	119	115	116	84	117
$p_{a,mean}$ [mmHg]	78	99	82	70	82
$p_{a,min}$ [mmHg]	59	80	53	59	51
$v_{acp,max}$ [mmHg]	96	18	80	51	77
$v_{acp,mean}$ [mmHg]	54	15	55	42	54
$v_{acp,min}$ [mmHg]	29	12	32	34	32
$V_{lv,max}$ [mmHg]	n/a	91	107	90	85
$V_{lv,mean}$ [mmHg]	n/a	41	61	63	59
$V_{lv,min}$ [mmHg]	n/a	15	16	41	36
SV, mean [ml]	74	66	83	46	46
T, mean [s]	0.87	0.87	0.87	0.87	0.87
CO [l/min]	5.1 (est.)	4.5	5.7	3.1	3.2

Table 6.6: Maximum, minimum, and mean arterial pressures p_a, cerebral velocities v_{acp}, and left ventricular volumes V_{lv} for dataset 2. Ventricular volume dynamics and subject data are used to calculate mean SV and CO using both initial and optimized parameters.

State	Data	Init, poly	Opt, poly	Init, elast	Opt, elast
$p_{a,max}$ [mmHg]	133	128	125	92	126
$p_{a,mean}$ [mmHg]	81	108	86	76	86
$p_{a,min}$ [mmHg]	56	87	54	63	53
$v_{acp,max}$ [mmHg]	84	18	73	49	70
$v_{acp,mean}$ [mmHg]	49	15	49	40	49
$v_{acp,min}$ [mmHg]	28	12	28	40	28
$V_{lv,max}$ [mmHg]	n/a	97	114	94	88
$V_{lv,mean}$ [mmHg]	n/a	46	70	66	65
$V_{lv,min}$ [mmHg]	n/a	17	17	44	43
SV, mean [ml]	79	69	89	46.7	42
T, mean [s]	0.93	0.93	0.93	0.93	0.93
CO [l/min]	5.1 (est.)	4.4	5.8	3.0	2.7

and mean T. Given literature values for end-systolic volume (ESV) and end-diastolic volume (EDV) of 50 and 120 ml, respectively, with stroke volume at 70 ml, the two values of 74 and 79 ml seem to be reasonable estimates. The optimized elastance model consistently gives stroke volumes of about 46 and 42, well below the estimates, whereas the polynomial model when optimized gives stroke volumes of 83 and 89 . In addition, EDV and ESV differ significantly as well between the two models. The polynomial model results are overall

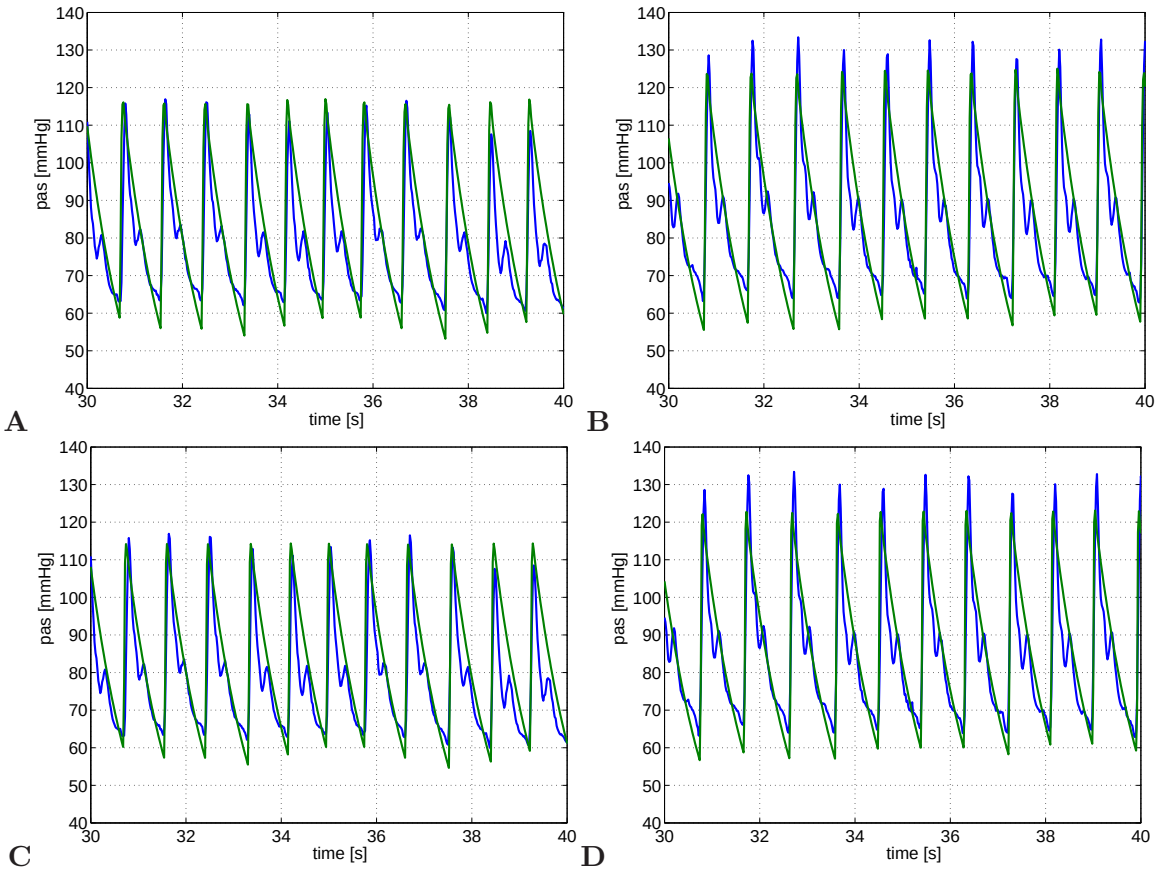

Figure 6.6: Model simulation (green) and data (blue) of arterial pressure p_{as} for both heart models for each dataset. A: Elastance model, dataset 1. B: Elastance model, dataset 2. C: Polynomial model, dataset 1. D. Polynomial model, dataset 2.

better, yet ESV is still far below average.

Subset selection picked identical cardiovascular parameters between the two models, lending credibility to the methodology, see Tables 6.7 and 6.8. The heart parameters picked in the elastance model were $T_{M,frac}$ and E_{max}, which represent time and elastance at end-systole. In general, these characterize the timing and magnitude of peak elastance. Heart parameters chosen for the polynomial model were n, θ, ϕ, and t_{min}. The parameters ϕ and θ represent medians of the sigmoidal functions of peak ventricular pressure p_p and time for peak ventricular pressure t_p. The value t_{min} is the minimum of the sigmoidal t_p relation. Finally, n characterizes contraction and affects the slope of the activation function. Peak elastance and peak pressure occur at approximately the same times, so it is consistent that the selected parameters describe similar parts of the ventricular functions.

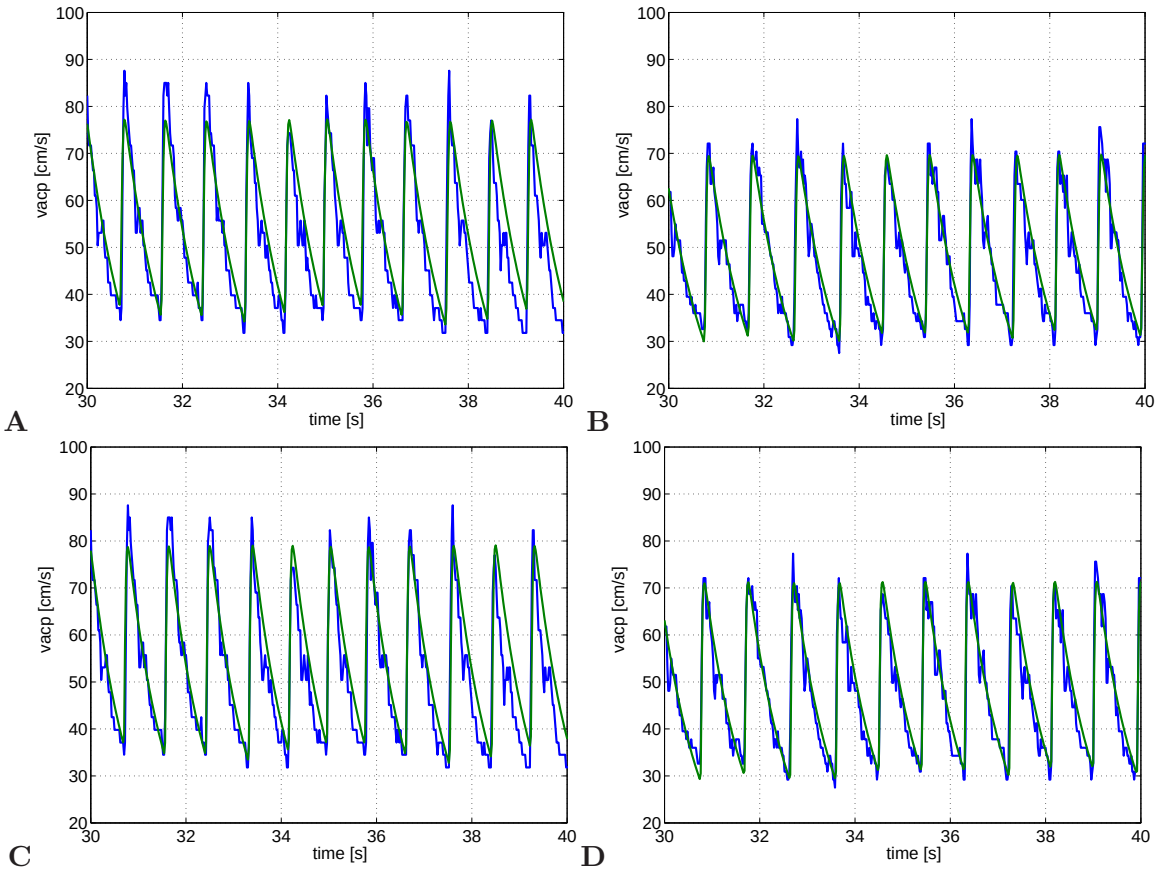

Figure 6.7: Model simulation (green) and data (blue) of CBFV v_{acp} for both heart models for each dataset. A: Elastance model, dataset 1. B: Elastance model, dataset 2. C. Polynomial model, dataset 1. D. Polynomial model, dataset 2.

The optimized values of vascular parameters found with the two models differ significantly, see Tables 6.7 and 6.8. Systemic peripheral resistance R_{asp} increased in the elastance model by about 50% but decreased in the polynomial by about 10%. In a more extreme example, the optimized cerebral resistance value R_{acp} with the elastance model was only slightly above the nomimal value, but dropped almost 75% with the polynomial. This gave an average venous cerebral pressure of about 18 mmHg, as opposed to 10 mmHg with the elastance model. Based on cerebral venous pressures found in Beneken and DeWit (4.8 mmHg) [10] and Lu *et al.* (14 mmHg), either one of these could be valid but 10 mmHg is likely more realistic. The remaining vascular parameter, C_a, dropped about 75% in the elastance model but only about 33% in the polynomial model.

Total resistance is inversely related to CO by $R_{total} = \Delta P/\mathrm{CO}$, where ΔP is the

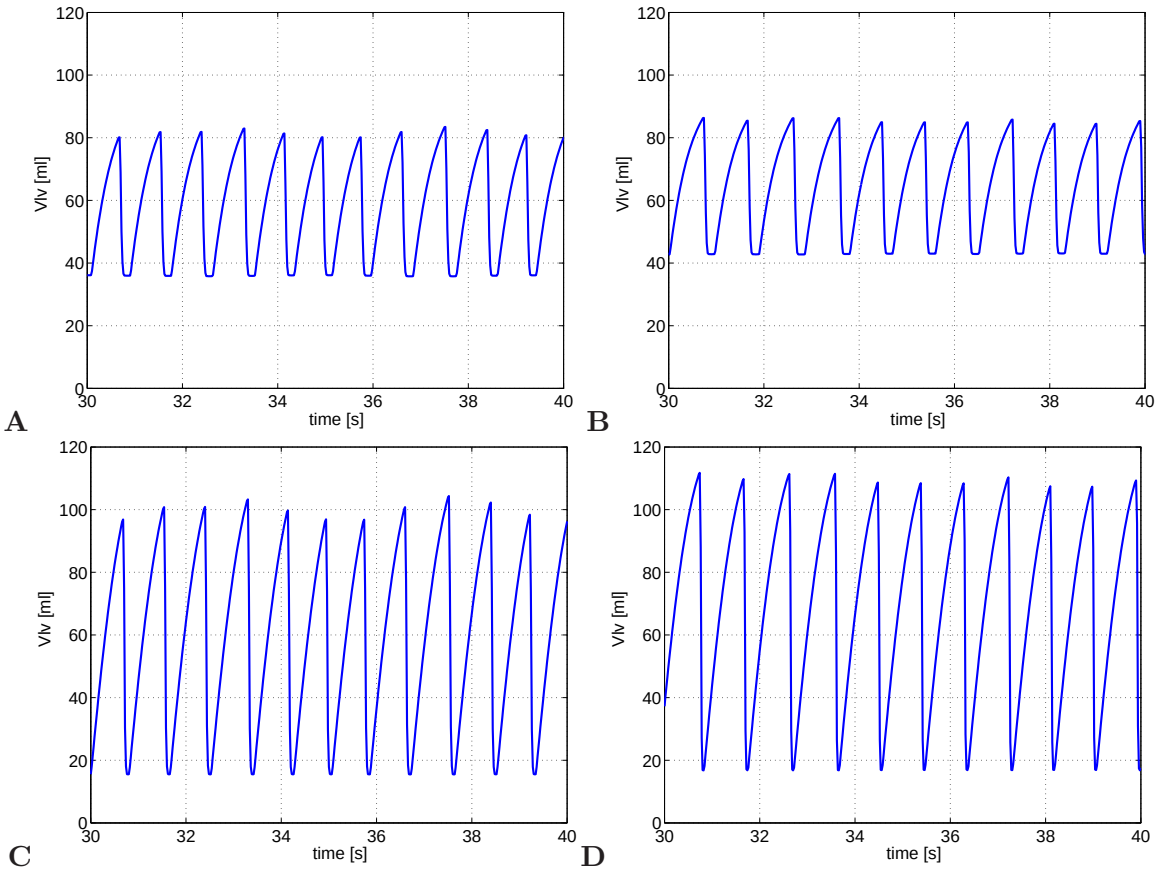

Figure 6.8: Model simulation of left ventricular volume V_{lv} for both heart models for each dataset. A: Elastance model, dataset 1. B: Elastance model, dataset 2. C. Polynomial model, dataset 1. D. Polynomial model, dataset 2.

difference between mean arterial pressure and mean venous pressure. It can be calculated as the sum of the resistances between the exit and and entrance of the left ventricle, which in this model is written as

$$R_{total} = R_{av} + R_{mv} + \left(R_{asp} + \frac{1}{R_{ac} + R_{acp} + R_{vc}} \right)^{-1}.$$

The inverse relationship is easily seen from Tables 6.5 through 6.8. The elastance model predicted a lower CO than the polynomial model by about half with both datasets (3.2 and 2.7 versus 5.7 and 5.8 l/min), and consequently R_{total} was twice as high for the elastance model (1.503 and 1.830 versus 0.852 and 0.881 mmHg/ml). Accurate estimates of cardiac output are therefore necessary for predicting R_{total}. However it may still be valid to compare between subject assuming the same methodology for all subjects.

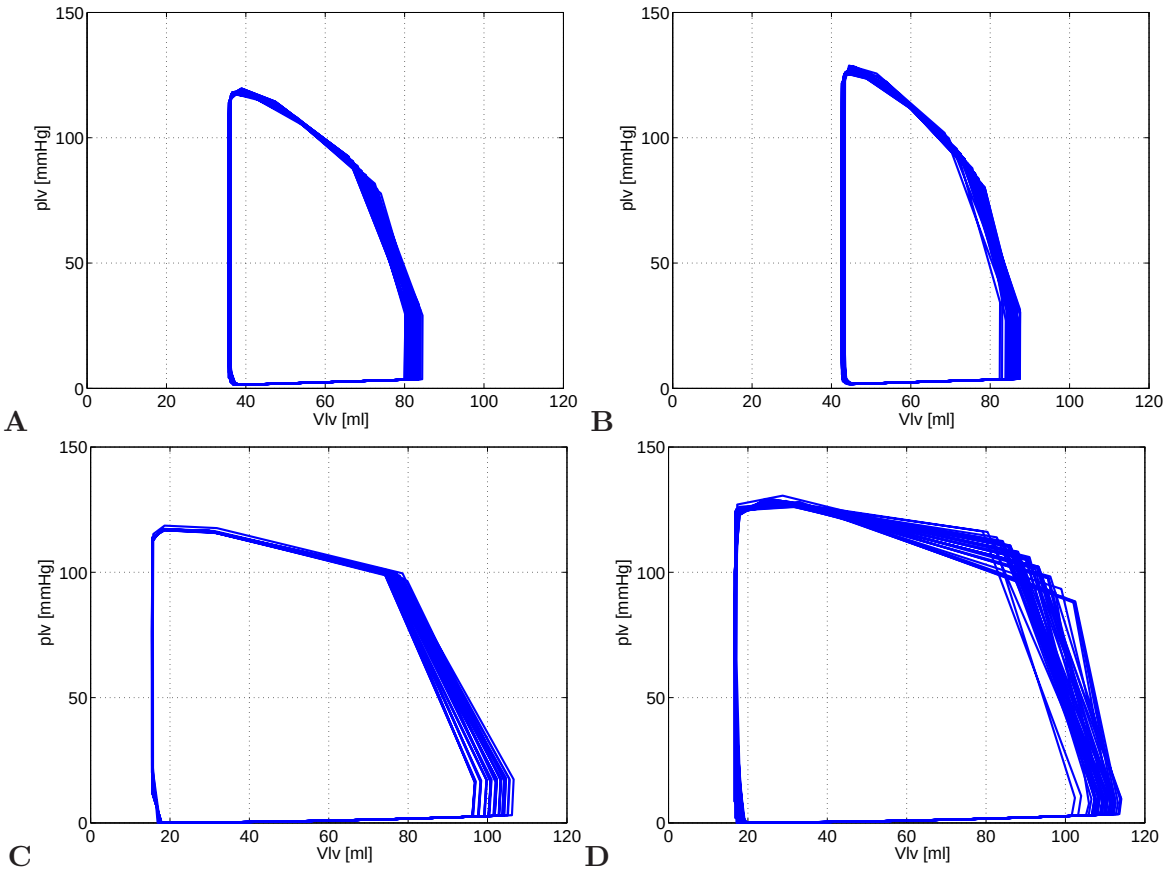

Figure 6.9: Model simulation of P-V loops obtained for both heart models for each dataset. A: Elastance model, dataset 1. B: Elastance model, dataset 2. C. Polynomial model, dataset 1. D. Polynomial model, dataset 2.

In an effort to force more accurate CO values through the elastance parameters that define ventricular volume, we pick E_m to be 0.02, lower than than the values given by Ottesen [80] and Heldt [38], and E_{max} to be 3.00, higher than the two sources. These results can be seen in Tables 6.9 and Figure 6.10. By fixing these parameters along with V_d, A_{acp}, and R_{mv} as in the previous analyses, subset selection chooses R_{asp}, R_{acp}, C_a, and $T_{M,frac}$. Because cardiac output is now higher with the more accurate stroke volume, R_{asp} optimizes to be lower, such as seen in the polynomial model. However, R_{acp} optimizes close to the higher values values that were attained with the elastance model that produced the more accurate cerebral venous pressures.

Table 6.7: Initial and optimized parameters for the elastance model for datasets 1 and 2. Subset selection chose parameters R_{asp}, R_{acp}, C_a, $T_{M,frac}$, and E_M.

Parameters	Init, dataset 1	Opt, dataset 1	Init, dataset 2	Opt, dataset 2
R_{asp} [mmHg·s/ml]	**1.531**	**1.972**	**1.731**	**2.443**
R_{acp} [mmHg·s/ml]	**5.733**	**5.252**	**6.521**	**6.258**
A_{acp} [cm^2]	0.250	0.250	0.250	0.250
C_{ac}[ml/mmHg]	0.229	0.229	0.204	0.204
R_{vc} [mmHg·s/ml]	0.294	0.294	0.294	0.293
C_a [ml/mmHg]	**1.790**	**0.478**	**1.591**	**0.398**
R_{ac} [mmHg·s/ml]	0.0967	0.0967	0.109	0.109
R_{mv} [mmHg·s/ml]	0.0353	0.0353	0.0353	0.0353
C_v [ml/mmHg]	46.001	46.001	46.001	46.001
C_{vc} [ml/mmHg]	3.197	3.197	3.197	3.197
R_{av} [mmHg·s/ml]	0.0064	0.0064	0.0073	0.0073
$T_{M,frac}$ [s/s]	**0.380**	**0.121**	**0.380**	**0.106**
$T_{r,frac}$ [s/s]	0.180	0.180	0.380	0.180
E_m [mmHg/ml]	0.0490	0.0490	0.0490	0.0490
E_M [mmHg/ml]	**2.490**	**4.462**	**2.490**	**3.769**
R_{total} [mmHg·s/ml]	1.266	1.503	1.427	1.830

Table 6.8: Initial and optimized parameters for the polynomial model for datasets 1 and 2. Subset selection chose parameters n, θ, R_{asp}, ϕ, R_{acp}, t_{min}, and $t_{diff} = t_{max-min}$.

Parameters	Init, dataset 1	Opt, dataset 1	Init, dataset 2	Opt, dataset 2
n	**2.000**	**3.733**	**2.000**	**5.079**
c_v [mmHg/ml]	6.400	6.400	6.400	6.400
θ [1/s]	**1.000**	**0.771**	**1.000**	**0.814**
R_{asp} [mmHg·s/ml]	**1.531**	**1.456**	**1.731**	**1.428**
ϕ [1/s]	1.000	0.769	1.000	0.683
R_{acp} [mmHg·s/ml]	**5.733**	**1.433**	**6.521**	**1.630**
A_{acp} [cm^2]	0.250	0.250	0.250	0.250
p_{min}	0.842	0.842	0.842	0.842
t_{min} [s]	**0.186**	**0.0938**	**0.186**	**0.0747**
ν	9.900	9.900	9.900	9.900
m	2.200	2.200	2.200	2.200
η	17.50	17.50	17.50	17.50
t_{diff} [s]	**0.0940**	**0.0940**	**0.0940**	**0.0940**
C_{ac} [ml/mmHg]	0.229	0.229	0.204	0.204
R_{vc} [mmHg·s/ml]	0.294	0.294	0.294	0.294
C_a [ml/mmHg]	1.790	1.183	1.5914	1.206
R_{ac} [mmHg·s/ml]	0.0967	0.0967	0.1088	0.109
R_{mv} [mmHg·s/ml]	0.0353	0.0353	0.0353	0.0353
C_v [ml/mmHg]	46.001	46.001	46.001	46.001
b [ml]	5.000	5.000	5.000	5.000
p_{diff}	0.316	0.316	0.3160	0.316
C_{vc} [ml/mmHg]	3.197	3.197	3.197	3.197
R_{av} [mmHg·s/ml]	0.0064	0.0064	0.0073	0.0073
a [mmHg/ml^2]	0.0003	0.0003	0.0003	0.0003
d [mmHg]	1.000	1.000	1.000	1.000
R_{total} [mmHg·s/ml]	1.266	0.852	1.427	0.881

Table 6.9: Maximum, minimum, and mean arterial pressure p_a, CBFV v_{acp}, and left ventricular volumes V_{lv} for datasets 1 and 2 using the elastance model. Computations reported in this table were carried out using fixed values for E_m, E_M, V_d, A_{acp}, and R_{mv}, while estimating parameters R_{asp}, R_{acp}, C_a, and $T_{M,frac}$.

State	Opt, dataset 1	Opt, dataset 2
$p_{a,max}$ [mmHg]	117	125
$p_{a,mean}$ [mmHg]	82	87
$p_{a,min}$ [mmHg]	52	53
$v_{acp,max}$ [mmHg]	77	70
$v_{acp,mean}$ [mmHg]	54	49
$v_{acp,min}$ [mmHg]	33	29
$V_{lv,max}$ [mmHg]	121	129
$V_{lv,mean}$ [mmHg]	79	84
$V_{lv,min}$ [mmHg]	48	51
SV, mean [ml]	67	72
T, mean [s]	0.87	0.923
CO [l/min]	4.6	4.6

Table 6.10: Initial and optimized parameters for the elastance model for datasets 1 and 2. Subset selection chose parameters R_{asp}, R_{acp}, C_a, and $T_{M,frac}$. Computations reported in this table were carried out using fixed values for E_m, E_M, V_d, A_{acp}, and R_{mv}.

Parameters	Init, dataset 1	Opt, dataset 1	Init, dataset 2	Opt, dataset 2
R_{asp} [mmHg·s/ml]	**1.534**	**1.218**	**1.731**	**1.254**
R_{acp} [mmHg·s/ml]	**5.733**	**5.268**	**6.521**	**6.288**
A_{acp} [cm^2]	0.250	0.250	0.250	0.250
C_{ac} [ml/mmHg]	0.229	0.229	0.204	0.204
R_{vc} [mmHg·s/ml]	0.294	0.294	0.294	0.294
C_a [ml/mmHg]	**1.790**	**0.797**	**1.5914**	**0.796**
R_{ac} [mmHg·s/ml]	0.0967	0.0967	0.109	0.109
R_{mv} [mmHg·s/ml]	0.0353	0.0353	0.0353	0.0353
C_v [ml/mmHg]	46.001	46.001	46.001	46.001
C_{vc} [ml/mmHg]	3.197	3.197	3.197	3.197
R_{av} [mmHg·s/ml]	0.0064	0.0064	0.0073	0.0073
$T_{M,frac}$ [s/s]	**0.380**	**0.116**	**0.1080**	**0.1080**
$T_{r,frac}$ [s/s]	0.180	0.180	0.180	0.1800
E_m [mmHg/ml]	0.0200	0.0200	0.0200	0.0200
E_M [mmHg/ml]	3.000	3.000	3.000	3.000
R_{total} [mmHg·s/ml]	1.266	1.044	1.427	1.098

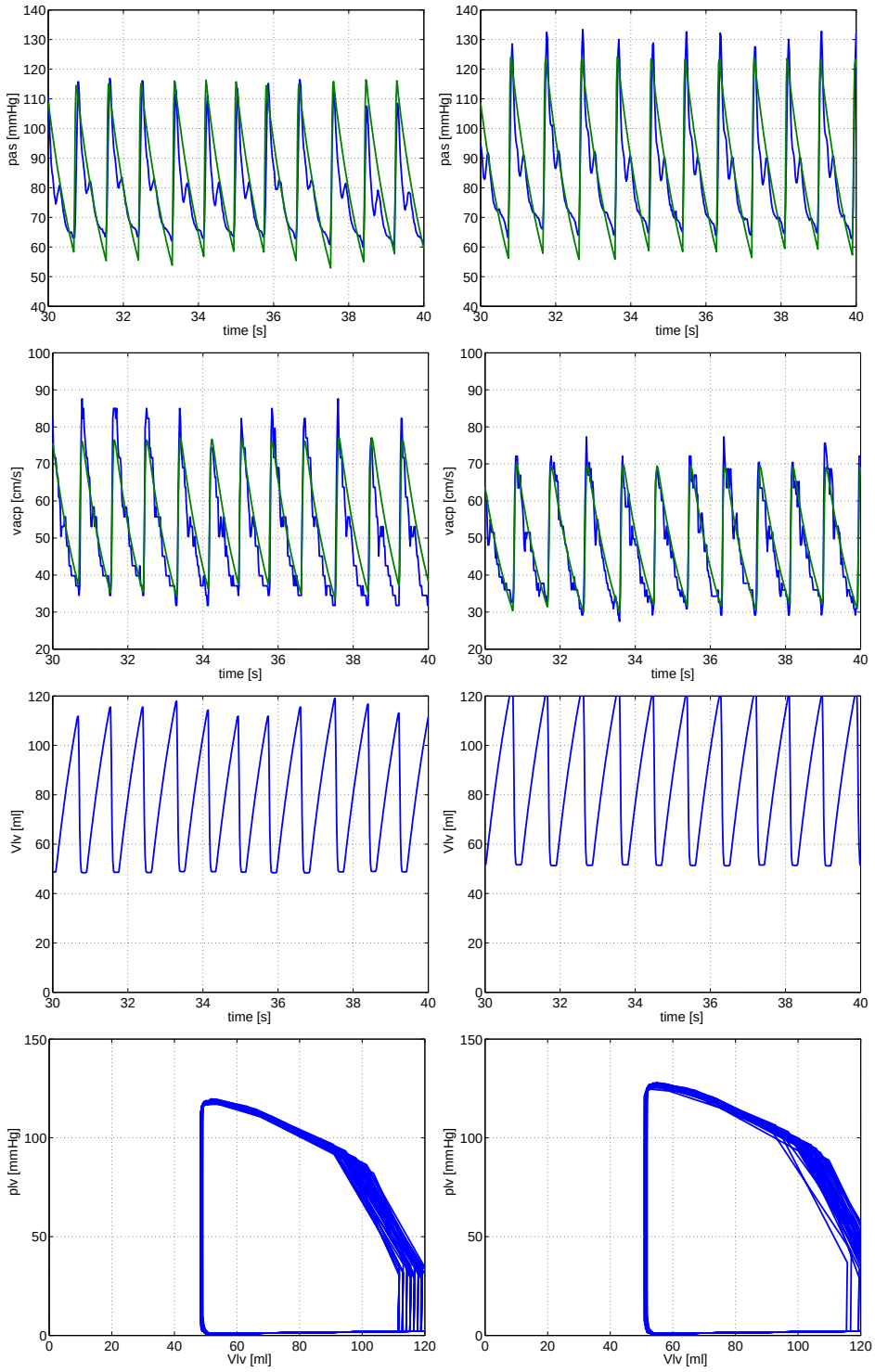

Figure 6.10: Model simulation (green) and data (blue) for p_a, v_{acp}, V_{lv}, and P-V loop, using the elastance model, fixing E_m, E_M, V_d, A_{acp}, and R_{mv} at their nominal values. Parameters estimated were R_{asp}, R_{acp}, C_a, and $T_{M,frac}$. Left: dataset 1; Right: dataset 2.

Chapter 7

Cardiorespiratory Model

7.1 Respiratory control

In this study we investigate the cardiovascular response to hypocapnia (low CO_2) and hypercapnia (high CO_2) in order to model the effects in the cerebral vasculature. To instigate hypocapnic conditions we examine data collected under voluntary hyperventilation. For hypercapnia (high CO_2) we examine data collected with constant 5% CO_2 breathing, and 5% CO_2 rebreathing.

7.1.1 Hypercapnia – CO_2 Breathing

Increased p_{a,CO_2} [mmHg] sensed by the chemoreceptors stimulates the vasomotor center, leading to peripheral vasoconstriction [8, 92] and increased ventilatory drive. In the cerebral vasculature, the opposite occurs, with increased p_{a,CO_2} causing vasodilation. It is generally accepted that with breathing 7% CO_2 air, the CBF nearly doubles due to local cerebral vasodilation [92, 13]. This can be used to guide the modeling efforts. If breathing frequency f_R is allowed to increase to expire the excess CO_2, then arterial blood pressure, CO, and HR are seen to increase significantly with total peripheral resistance falling [92, 116]. With a constant high percentage CO_2, e.g., 3-7%, the body eventually reaches a new homeostasis although it then operates under respiratory acidosis.

In CO_2 rebreathing, the subject expires into a breathing circuit consisting of a rebreathing bag with a volume ranging from 1-5 liters. The p_{a,CO_2} of the expired air will increase due to the increase in the inspired p_{a,CO_2}. The latter increases as CO_2 is expired

into the bag. As a result the p_{CO_2} in the air in the immediate vicinity of the airway continuously increases. In response to these changes, ventilatory drive, cerebral vasodilation, and peripheral vasoconstriction continue to increase according to the regulatory mechanisms previously described. Cerebral vasodilation and peripheral vasoconstriction will reach saturation levels, so eventually CBF cannot increase further. Thus CO_2 accumulates and O_2 becomes deficient which may cause syncope.

7.1.2 Hypocapnia – Hyperventilation

Hyperventilation is defined as breathing at a higher rate or volume than necessary. During hyperventilation, CO_2 is initially exhaled at a greater rate than it is produced, leading to a decrease in p_{a,CO_2} [40]. In order to study physiological responses to hyperventilation, both the effects of increased thoracic cavity movement and the decrease of p_{a,CO_2} will be considered. During normal breathing, blood pressure increases during inspiration and decreases during expiration, most likely due to a more negative intra-thoracic pressure that the heart must work against during inspiration to maintain the same pressure gradient [29]. There is also thought to be a mechanical pumping effect which would increase venous return, thus increasing stroke volume (SV) and cardiac output (CO) by the Starling mechanism [20, 29].

It is difficult to separate the mechanisms that impact cardiovascular quantities during hyperventilation. Several studies have been done analyzing the response to hyperventilation at a constant p_{a,CO_2} in attempts to isolate the effects of the mechanical action of increased breathing. De Burgh Daley [29] describes sympathetic vasodilation and increased HR during hyperventilation, likely due to the pulmonary stretch reflex. These effects were seen to take precedence over the chemoreceptor response to CO_2 when present. A study by Richardson [92] found negligible change in blood pressure, CO, HR, SV, and peripheral resistance during hyperventilation under constant p_{a,CO_2}. Other studies investigated hyperventilation while allowing changes in p_{a,CO_2}. In a study by Cummin [20] where p_{a,CO_2} was allowed to fluctuate, SV increased with minimal change in HR under increased f_R and constant tidal volume V_T. But when V_T increased, HR did as well. This appears to coincide with stimulation of the pulmonary stretch receptors inhibiting the cardioinhibitory center [13].

Studies differ on their conclusions of the impacts of hyperventilation on blood

pressure. In a study by Burnum *et al.* [15], maximal hyperventilation (breathing as hard and fast as possible) lowered blood pressure by ∼25% even though CO increased by ∼50%. Vasodilation was likely a consequence of diminished CO_2 stimulation of the vasomotor center. Yet other studies found little or no change in BP during hyperventilation, whether due to a higher V_T [56] or to rigorous breathing under constant p_{a,CO_2} [92].

The effect of hyperventilation on CBF is also not fully understood. To isolate the autoregulatory effects of CO_2 on CBF, sympathetic stimuli were removed from an extremity in the study by Richardson [92]. It was found that an increase in p_{a,CO_2} caused vasodilation, but with the sympathetic stimuli intact, CBF changes were minimal. In another study by Miyazaki, [56], in 2 of 8 patients, CBF decreased, then returned to normal levels, during hyperventilation, countering the expectation that CBF remains low during hypocapnia.

7.1.3 Summary

Figure 7.1 summarizes the chain of events that we understand to occur during hyperventilation and CO_2 breeathing. On a global level, an increase in CO_2 stimulates the chemoreceptors which activate the vasomotor, cardioinhibitory, and respiratory centers. The result is an increase in peripheral resistance and ventilation and a decrease in HR. Increased ventilation in turn decreases CO_2 and decreases HR. In the brain, increased CO_2 acts locally as a vasodilator thus decreasing cerebrovascular resistance. Cerebral blood flow increases which increases the rate of CO_2 from the cerebral vasculature. Thus the level of cerebral CO_2 are restored.

During CO_2 breathing or rebreathing, ventilation and consequently CBF increase. As a result of increased ventilation, more CO_2 is inspired, thereby negating the intended effects of the feedback mechanism. Hyperventilation induces both mechanical and chemical effects. The mechanical pumping effects of ventilation likely increase VR, SV, and CO, and the increased stimulation of the pulmonary stretch receptors cause an increased HR. The decrease in CO_2 resulting from hyperventilation triggers a decrease in ventilation via the respiratory center. However voluntary hyperventilation overrides this intended feedback response. Heart rate also decreases as a result of lowered CO_2.

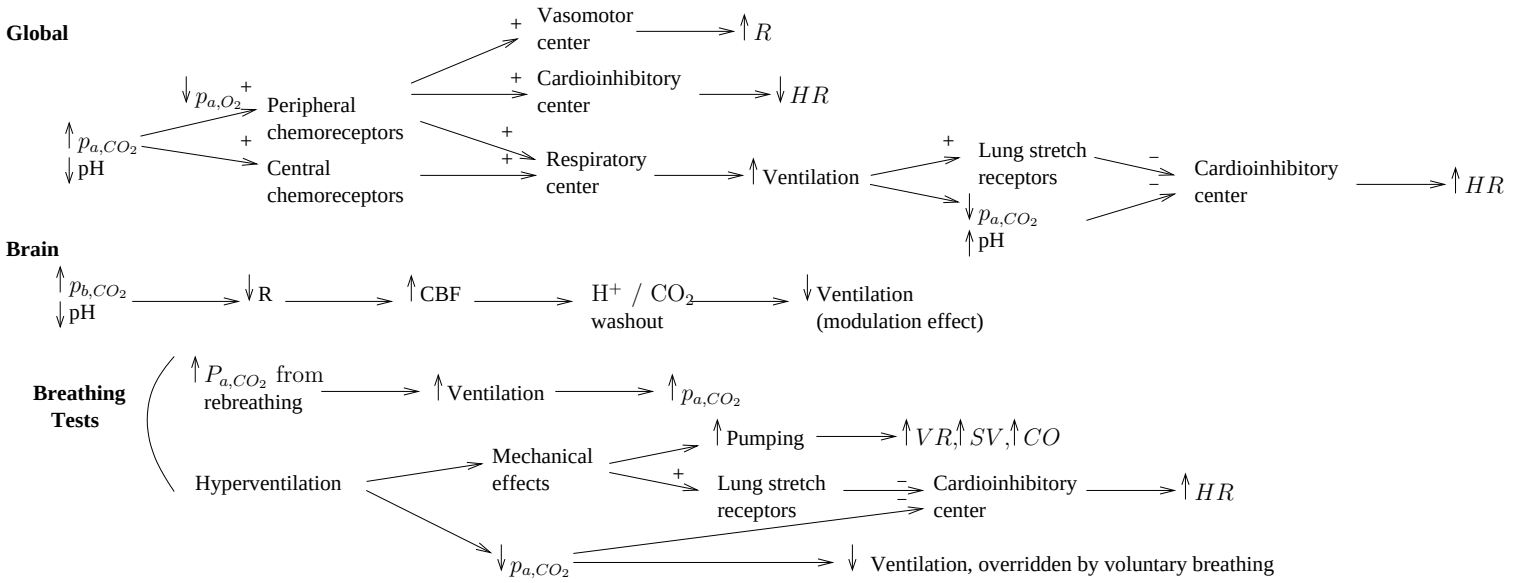

Figure 7.1: Summary of control processes involved the responses to hypercapnia and hyperventilation. Autonomic regulation mediates the system-wide response to changes in p_{a,CO_2}. Increased p_{a,CO_2} increases the firing rate of the chemoreceptors, which stimulates the regulatory centers to increase ventilation. Increased HR results from increased ventilation. Increased CO_2 acts locally on the cerebral vasculature as a vasodilator, resulting in increased CBF. During CO_2 breathing or rebreathing, increased p_{a,CO_2} drives an increase in ventilation. This causes greater inspiration of CO_2-rich air and thus further increases p_{a,CO_2}. The effects of hyperventilation cause increased venous return (VR), stroke volume (SV), cardiac output (CO), and heart rate HR. Reduced ventilatory drive is reduced as well but is overridden by voluntary hyperventilation.

7.2 Cardiorespiratory model development

The cardiorespiratory model is designed to predict arterial blood pressure p_a, cerebral blood flow velocity v_c, and expiratory CO_2 p_{exp,CO_2} during CO_2 challenges. It is constructed with equations of the type (3.5) and (3.6) first presented in Chapter 5 and is shown in Figure 7.2. The cardiovascular submodel of the cardiorespiratory model is represented by a closed loop circuit with 4 arterial compartments, 4 venous compartments, and 2 ventricular compartments. Vascular compartments represent the systemic system, including the aorta and vena cava, the body, and the brain, as well as the pulmonary system. The left and right ventricles generate the driving pressures for the systemic and pulmonary systems. A full list of the cardiovascular equations can be found in Appendix A.3.

The cardiovascular submodel is modified by adding a respiratory submodel with components allowing for gas exchange, transport, and metabolism. We model the dynamics of the two metabolite gases, O_2 and CO_2. A tissue compartment connects each peripheral arterial compartment with each peripheral venous compartment. Dynamic gas concentrations in each tissue compartment reflect O_2 consumption and CO_2 production during metabolism as well as convection via blood flow into and out of each compartment. The model also includes two pulmonary components. The alveolar space has a dynamic volume, in which O_2 and CO_2 are exchanged between the dead space and the pulmonary vasculature. Three rigid dead space compartments connect the alveolar space with the atmosphere. Gas concentrations and partial pressures are predicted in all compartments. The inputs to the model include HR and volumetric airflow $\dot{V}_{IE}$, which provides information about tidal volume V_T and ventilation frequency f_R. Typical values for pressures and volumes are given in Table 7.1.

Standard material balance equations describe respiration in the tissue compartments. We denote the total amount $A_{T,g}$ [ml] of a gas (subscript g) in a tissue (subscript T) as $A_{T,g} = V_{T,g}c_{T,g}$, the product of the tissue volume V [ml] available for the gas and the concentration c [$\text{ml}_{gas}/\text{ml}_{blood}$] of the gas in the volume. The change in amount of gas in the compartment is equal to what is utilized or formed via metabolism M [ml/s], plus what is added and removed via the bloodstream q_T [ml/s]:

$$\frac{dA_{T,g}}{dt} = \frac{dV_{T,g}}{dt}c_{T,g} + V_{T,g}\frac{dc_{T,g}}{dt} = M_{T,g} + q_T(c_{a,g} - c_{T,g}).$$

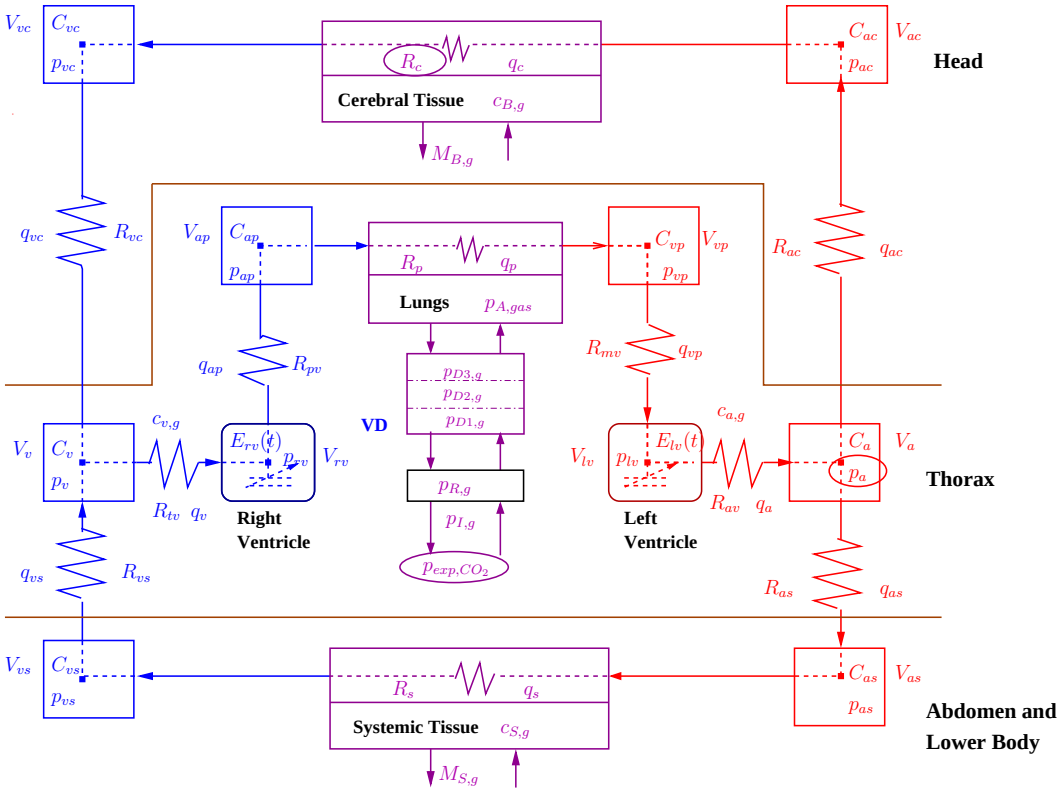

Figure 7.2: Compartmental model of systemic and pulmonary circulations (compare to Figure 5.1). The model contains arterial and venous compartment for the systemic, pulmonary, and cerebral systems, as well as the aorta and the vena cava. Three tissue capillary beds connect peripheral vascular compartments. Two ventricular compartments generate pressure for the systemic and pulmonary systemts. Four compartments represent alveolar and dead spaces in the lungs. A compartment representing the rebreathing bag (subscript R) is included for one of the studies. Cardiovascular compartments are constructed using the same notation described in detail in Figure 5.1. Respiratory components include partial pressures p [mmHg], concentrations c [ml$_{STPD}$/ml], and metabolic rates M [ml$_{STPD}$/s] for CO_2 and O_2.

Since $dV_{T,g}/dt = 0$, this equation reduces to

$$V_{T,g}\frac{dc_{T,g}}{dt} = M_{T,g} + q_T(c_{a,g} - c_{T,g}). \tag{7.1}$$

The tissue compartments are considered well-mixed with the exiting concentration equalling the mixed concentration in the compartment. We give the concentration $c_{v,g}$ in the vena cava as a mixture of the concentrations from its incoming streams such that

$$c_{v,g} = \frac{q_{s,g}q_{vs} + q_{c,g}q_{vc}}{q_{vc} \cdot q_{vc}},$$

Table 7.1: Typical values for selected parameters and states. Note that the pulmonary artery and right ventricular pressures p_{ap} and p_{rv} are lower than the aortic and left ventricular pressures p_a and p_{lv}. Ventricular volumes V_{lv} and V_{rv} are the same between both sides of the heart. Venous CO_2 is higher than arterial CO_2, whereas venous O_2 is lower than arterial O_2.

State	Value	Source
p_{a,O_2} [mmHg]	100	[32]
p_{v,O_2} [mmHg]	40	[32]
p_{a,CO_2} [mmHg]	40	[32]
p_{v,CO_2} [mmHg]	46	[32]
p_{ap} [mmHg]	8-25	[13]
p_a [mmHg]	80-120	[13]
p_{lv} [mmHg]	0-120	[13]
p_{rv} [mmHg]	0-25	[13]
V_{lv} [ml]	50-120	[13]
V_{rv} [ml]	50-120	[13]

where s and c are the systemic and cerebral concentrations of each gas. Nominal values for metabolic rates and tissue volumes are given in Table 7.2. As is standard practice, all tissue gas volumes and blood gas concentrations are given in STPD (see Chapter 3), thus units are consistent.

Alveolar gas quantities are denoted $V_{A,g} = V_A F_{A,g}$, the product of alveolar volume V_A and gas fraction $F_{A,g}$. The change in quantity of alveolar gas is represented by a similar material balance, taking into account a time-varying alveolar volume, fluid transport to and from the lungs via pulmonary capillaries, and gas transport via inspiration and expiration,

$$\frac{dV_{A,g}}{dt} = F_{A,g}\frac{dV_A}{dt} + V_A\frac{F_{A,g}}{dt} = \frac{dV_A}{dt}F_{i,g} + q_p(c_{v,g} - c_{a,g}),$$

where $i = D$ during inspiration and $i = A$ during expiration. Subscripts D, A, and p represent the dead space and alveolar space within the lungs and pulmonary tissue. Rearranging to express the rate of change of alveolar gas fraction gives

$$V_A\frac{dF_{A,g}}{dt} = \begin{cases} \dfrac{dV_A}{dt}(F_{D,g} - F_{A,g}) + q_p(c_{v,g} - c_{a,g}), & \text{inspiration} \\ q_p(c_{v,g} - c_{a,g}), & \text{expiration.} \end{cases}$$

Gas fractions are converted to partial pressures via the relationship

$$F_{A,g} = p_{A,g}/(p_{amb} - p_{water}) = p_{A,g}/713,$$

where p_{amb} is the ambient air pressure of 760 mmHg and water vapor partial pressure p_{water} equals 47 mmHg at body temperature of 37°:

$$\frac{V_A}{713}\frac{dp_{A,g}}{dt} = \begin{cases} \dfrac{dV_A}{dt}\dfrac{(p_{D,g}-p_{A,g})}{713} + q_p(c_{v,g}-c_{A,g}), & \text{inspiration} \\ q_p(c_{v,g}-c_{A,g}), & \text{expiration.} \end{cases}$$

Because blood gas concentrations are reported in [ml$_{STPD}$/ml], but alveolar volumes are in BTPS, we use the conversions from Section 3.3 to convert concentrations to BTPS. Incoming air is immediately humidified once it enters the nasal passages [11, 13] and expired air is a composition of aveolar air and dead space air at BTPS, therefore terms with those quantities are not converted. The final equations are obtained by using the conversions (3.14) and multiplying through by 713, i.e.,

$$V_A\frac{dp_{A,g}}{dt} = \begin{cases} \dfrac{dV_A}{dt}(p_{D,g}-p_{A,g}) + 863q_p(c_{v,g}-c_{A,g}), & \text{inspiration} \\ 863q_p(c_{v,g}-c_{A,g}), & \text{expiration.} \end{cases} \tag{7.2}$$

All respiratory equations are listed in Appendix A.3.2.

Additional modeling considerations concern the relationship between the pulmonary capillaries and the systemic arteries. First, an anatomical shunt is present in the pulmonary circulation. This consists of O_2-deficient blood that bypasses the alveoli

Table 7.2: Typical values for metabolic rates, tissue volumes, and gas dissociation constants for 70 kg man. All values are from Batzel *et al.* [9]. Abbreviations: S, systemic; B, brain; A, alveolar.

Variable	Literature
M_{S,CO_2} [ml$_{STPD}$/s]	3.633
M_{S,O_2} [ml$_{STPD}$/s]	4.333
M_{B,CO_2} [ml$_{STPD}$/s]	0.7
M_{B,O_2} [ml$_{STPD}$/s]	0.833
V_{S,CO_2} [ml$_{STPD}$]	14100
V_{S,O_2} [ml$_{STPD}$]	5000
V_{B,CO_2} [ml$_{STPD}$]	900
V_{B,O_2} [ml$_{STPD}$]	1000
V_{A,CO_2} [ml$_{BTPS}$]	3200
V_{A,O_2} [ml$_{BTPS}$]	2500
K_1 [ml$_{STPD}$/ml]	0.200
K_2 [mmHg^{-1}]	0.046
K_{CO_2} [ml$_{STPD}$·mmHg/ml]	0.0065
k_{CO_2} [ml$_{STPD}$/ml]	0.244

for physiological or pathological reasons. Typical shunt values range from 2-5%, wtih a larger shunt percentage possibly indicating a pathological conditions [13, 11]. The subjects studied have no known pulmonary healthy issues so we assume a 2% shunt. Therefore only 98% of the cardiac output becomes oxygenated, altering the alveolar equations to read as

$$V_A \frac{dp_{A,g}}{dt} = \begin{cases} \frac{dV_A}{dt}(p_{D,g} - p_{A,g}) + 0.98 \cdot 863 q_p (c_{v,g} - c_{A,g}), & \text{inspiration} \\ 0.98 \cdot 863 q_p (c_{v,g} - c_{A,g}), & \text{expiration.} \end{cases} \tag{7.3}$$

Second, we note that the thin alveolar wall allows for almost immediate equilibration of gases between the alveoli A and the pulmonary capillaries, which then carry the same gas concentration through the systemic arteries a. Thus we assume $p_{A,g} = p_{a,g}$ as an auxiliary equation.

Connected to the alveolar compartment are three compartments of equal volume with a total volume representing anatomical dead space. Each dead space is considered a well-mixed compartment with units V_{BTPS}, in ml. Material balance equations for the dead space compartments reflect change in gas levels due to airflow, with opposite directions of flow for inspiration versus expiration. The relation $F_{A,g} = P_{A,g}/713$ holds, and equation units are all in BTPS. Thus following the derivation of (7.3),

$$\begin{aligned} \text{Inspiration: } V_{D_1} \frac{dp_{D_1,g}}{dt} &= \frac{dV_A}{dt}(p_{I,g} - p_{D_1,g}), & (7.4) \\ V_{D_i} \frac{dp_{D_i,g}}{dt} &= \frac{dV_A}{dt}(p_{D_{i-1},g} - p_{D_i,g}), \text{ i=2,3.} & \\ \text{Expiration: } V_{D_i} \frac{dp_{D_i,g}}{dt} &= \frac{dV_A}{dt}(p_{D_i,g} - p_{D_{i+1},g}), \text{ i=1,2,} & (7.5) \\ V_{D_3} \frac{dp_{D_3,g}}{dt} &= \frac{dV_A}{dt}(p_{D_3,g} - p_{A,g}). & \end{aligned}$$

Pressure $p_{I,g}$ is the partial pressure of the gas in the inspired air.

Note that dV_A/dt is positive during inspiration and negative during expiration. The rate of change of alveolar volume dV_A/dt is equivalent to the ventilation airflow $\dot{V}_{IE}$, therefore it is written as such in future calculations. The $(\dot{\cdot})$ designation indicates a volumetric flowrate as opposed to a rate of change of volume. The airflow $\dot{V}_{IE}$ is measured during experimentation and is used as an input to the model to drive the gas concentration dynamics.

As described in Chapter 2, O_2 and CO_2 have different affinities for hemoglobin, therefore behave differently in the gas versus liquid phases. Gas dissociation laws are used

to convert alveolar gas pressures to blood gas concentrations. There are many empirical equations developed for these relationships with a multitude of characterizing parameters. In this study we use equations also used by Batzel *et al.* [9],

$$\begin{aligned} c_{T,CO_2} &= K_{CO_2} p_{T,CO_2} + k_{CO_2}, \\ c_{T,O_2} &= K_1 (1 - e^{-K_2 p_{T,O_2}})^2. \end{aligned}$$

Note that the law for CO_2 is linear while the law for O_2 is exponential. This reflects general behavior, but does not account for the the dependencies of each gas on the other as well as factors such as pH and temperature, as discussed in Chapter 2. Nominal values for dissociation constants are given in Table 7.2.

Comparing the state dynamics to data requires two conversion factors. One is the contant scaling factor of the MCA, A_c, set in the same way as A_{acp} as described in Chapter 5. Thus $v_c = (p_{ac} - p_{vc})/A_c$, where model v_c is compared with the cerebral blood flow velocity data. In the respiratory model, the expiratory CO_2 partial pressures are assumed to be almost equivalent to the dead space pressures, with a slight mixing of alveolar gas. Thus a factor f_{alv} is introduced such that

$$p_{expCO_2} = f_{alv} p_{A,CO_2} + (1 - f_{alv}) p_{D1,CO_2},$$

where p_{expCO_2} is compared to the expiratory CO_2 data. The factor f_{alv} is set depending on the data, $0 \leq f_{alv} \leq 0.1$.

To determine the connection between respiration and blood pressure we model the mechanical effect of breathing on intrathoracic pressure. The cause for the influx of air into the lungs is the negative pressure in the thorax (lung cavity) induced by the downward contraction of the diaphragm, causing the air to flow into the lungs. Consequently, any organs within the thorax will also experience the negative pressure. Equations are modified as follows:

$$\begin{aligned} \frac{dp_i}{dt} &= \frac{1}{C_i} \frac{dV_i}{dt} + \frac{dp_{IT}}{dt}, \\ p_i - p_{IT} &= E_i(t)[V_i(t) - V_d], \end{aligned}$$

where p_{IT} is intrathoracic pressure, the negative pressure in the thorax. $p_{IT} \neq 0$ affects vascular compartments $i = a, v$ heart compartments $i = lv, rv$. Pressure changes in the pulmonary vasculature are neglected in this study due to their complicated nature.

Estimated literature values for the range of pressures during the breathing function are -5 to -7.5 cm H_2O, equivalent -3.7 to -5.5 mmHg [13]. The least negative pressure occurs at the start of inspiration at minimum alveolar volume, and similarly the most negative occurs at maximum volume. The relationship between V_A and p_{IT} was estimated with a linear function [13]. We first calculated the functional residual capacity (FRC), the minimum alveolar volume during normal breathing, using the algorithm given in Stocks and Quanjer [106]. Then $\dot{V}_{IE}$ was integrated using the FRC as the initial condition, and the result was adjusted to obtain V_A such that the minimum of the result equaled the FRC. Based on maximum $V_{A,max}$, minimum $V_{A,min}$ and their difference $V_{A,diff} = V_{A,max} - V_{A,min}$, the function

$$p_{IT}(t) = \frac{-1.8}{V_{A,diff}}(V_A(t) - V_{A,min}) - 3.7 \tag{7.6}$$

estimates intrathoracic pressure p_{IT} as a function of alveolar volume V_A. Therefore differentiation p_{IT} we obtain

$$\frac{dp_{IT}}{dt} = -\frac{-1.8\dot{V}_{IE}}{V_{A,diff}}.$$

Table 7.3: Initial values for all model parameters. The total volume V_{tot} is defined in (6.2), equivalent to total flow q_{tot}, and p^d_{max} is the maximum of the pressure data. The parameter $A_{acp} = q_{acp}/v_{acp}$ relates cerebral blood flow to cerebral blood flow velocity. ($\star$) $T_{M,frac}$ was set to be the time of p^d_{max} of the first cardiac cycle.

Pressure [mmHg]	$k \cdot p^d_{max}$ k	Flow [ml/s]	$k \cdot q_{tot}$ k	Resistances [mmHg· s/ml]	Ohms law
$p_{lv,sys}$	1	q_a	1	$R_{av,open}$	$(p_{lv,sys} - p_a)/q_a$
p_a	0.99	q_v	1	$R_{tv,open}$	$(p_v - p_{rv,dia})/q_v$
p_{as}	0.97	q_{ap}	1	$R_{pv,open}$	$(p_{rv,sys} - p_{ap})/q_{ap}$
p_{ac}	0.97	q_p	1	R_p	$(p_{ap} - p_{vp})/q_p$
p_v	0.050	q_{vp}	1	$R_{mv,open}$	$(p_{vp} - p_{lv,dia})/q_{vp}$
p_{vs}	0.069	q_{as}	0.8	R_{as}	$(p_a - p_{as})/q_{as}$
p_{vc}	0.099	q_s	0.8	R_s	$(p_{as} - p_{vs})/q_s$
$p_{lv,dia}$	0.020	q_{vs}	0.8	R_{vs}	$(p_{vs} - p_v)/q_{vs}$
$p_{rv,sys}$	0.15	q_{ac}	0.2	R_{ac}	$(p_a - p_{ac})/q_{ac}$
p_{ap}	0.14	q_c	0.2	R_c	$(p_{ac} - p_{vc})/q_c$
p_{vp}	0.050	q_{vc}	0.2	R_{vc}	$(p_{vc} - p_v)/q_{vc}$
$p_{rv,dia}$	0.020				
Volume [ml]	$k \cdot V_{tot}$ k	Capacitors [ml/mmHg]		Heart parameters E_i [mmHg · s/ml], V_{str} [ml]	
V_{ap}	0.0262	C_{ap}	$0.56V_{ap}/p_{as}$	$T_{M,frac}$	($\star$)
V_{vp}	0.1131	C_{vp}	$0.10V_{vp}/p_{vp}$	$T_{r,frac}$	$T_{M,frac}/2$
V_a	0.0748	C_a	$0.34V_a/p_a$	$E_{min,l}$	0.049
V_v	0.2333	C_v	$0.08V_v/p_v$	$E_{max,l}$	2.49
V_{ac}	0.0108	C_{ac}	$0.23V_{ac}/p_{ac}$	$E_{min,r}$	0.028
V_{vc}	0.0438	C_{vc}	$0.08V_{vc}/p_{vc}$	$E_{max,r}$	0.08
V_{as}	0.0431	C_{as}	$0.21V_{as}/p_{as}$	V_d	10
V_{vs}	0.3647	C_{vs}	$0.08V_{vs}/p_{vs}$		
$V_{lv,max}$	57.6BSA [ml]				
$V_{rv,max}$	18.1BSA [ml]				

Table 7.4: Initial and optimized parameters for baseline portion of the 5% CO_2 breathing data, $0 \leq t \leq 340$ s.

Parameter	Initial value	Optimized value
R_{tv} [mmHg· s/ml]	0.0382	0.109
R_{pv} [mmHg· s/ml]	0.0127	0.0131
R_v [mmHg· s/ml]	0.115	0.127
R_{mv} [mmHg· s/ml]	0.0382	0.0381
R_{av} [mmHg· s/ml]	0.0127	0.0510
R_{ac} [mmHg· s/ml]	0.127	0.5010
R_c [mmHg· s/ml]	5.606	14.34
R_{vc} [mmHg· s/ml]	0.319	0.142
R_{as} [mmHg· s/ml]	0.0319	0.127
R_s [mmHg· s/ml]	1.449	3.6504
R_{vs} [mmHg· s/ml]	0.0318	0.116
C_{ap} [ml/mmHg]	4.936	4.737
C_{vp} [ml/mmHg]	10.65	10.56
C_a [ml/mmHg]	1.198	0.229
C_v [ml/mmHg]	17.58	11.71
C_{ac} [ml/mmHg]	0.119	0.477
C_{vc} [ml/mmHg]	1.650	1.198
C_{as} [ml/mmHg]	0.435	0.109
C_{vs} [ml/mmHg]	19.63	23.21
A_c [cm^2]	0.25	0. 625
$T_{M,frac}$ [s/s]	0.197	0.194
$T_{r,frac}$ [s/s]	0.0984	0.530
$E_{min,l}$ [mmHg/ml]	0.049	0.536
$E_{max,l}$ [mmHg/ml]	2.49	1.909
$E_{min,r}$ [mmHg/ml]	0.028	0.0244
$E_{max,r}$ [mmHg/ml]	0.8	0.566
f_{alv}	0.001	-
K_1 [ml_{STPD}/ml]	0.20	-
K_2 [$mmHg^{-}1$]	0.046	-
K_{CO_2} [ml_{STPD}·mmHg/ml]	0.0065	-
k_{CO_2} [ml_{STPD}/ml]	0.244	-
M_{CO_2} [ml_{STPD}/s]	4.893	-
M_{O_2} [ml_{STPD}/s]	5.835	-
V_{A,CO_2} [ml_{STPD}]	150	-
V_{A,O_2} [ml_{STPD}]	3200	-
V_{T,CO_2} [ml_{STPD}]	2500	-
V_{T,O_2} [ml_{STPD}]	15,000	-
V_{B,CO_2} [ml_{STPD}]	6000	-
V_{B,O_2} [ml_{STPD}]	900	-
M_{B,CO_2} [ml_{STPD}/s]	0.790	-

Table 7.5: Initial and optimized parameters for baseline portion of the hyperventilation / 5% CO_2 rebreathing data, $20 \leq t \leq 580$ s.

Parameter	Initial value	Optimized value
R_{tv} [mmHg· s/ml]	0.0406	-
R_{pv} [mmHg· s/ml]	0.0135	-
R_v [mmHg· s/ml]	0.122	-
R_{mv} [mmHg· s/ml]	0.0406	-
R_{av} [mmHg· s/ml]	0.0135	-
R_{ac} [mmHg· s/ml]	0.135	-
R_c [mmHg· s/ml]	5.948	-
R_{vc} [mmHg· s/ml]	0.338	-
R_{as} [mmHg· s/ml]	0.0338	-
R_s [mmHg· s/ml]	1.538	1.668
R_{vs} [mmHg· s/ml]	0.0338	-
C_{ap} [ml/mmHg]	4.652	-
C_{vp} [ml/mmHg]	10.04	-
C_a [ml/mmHg]	1.129	1.391
C_v [ml/mmHg]	16.57	-
C_{ac} [ml/mmHg]	0.113	-
C_{vc} [ml/mmHg]	1.555	-
C_{as} [ml/mmHg]	0.410	-
C_{vs} [ml/mmHg]	18.50	-
A_c [cm^2]	0.25	0.292
$T_{M,frac}$ [s/s]	0.255	0.236
$T_{r,frac}$ [s/s]	0.128	-
$E_{min,l}$ [mmHg/ml]	0.049	0.0333
$E_{max,l}$ [mmHg/ml]	2.49	1.501
$E_{min,r}$ [mmHg/ml]	0.028	-
$E_{max,r}$ [mmHg/ml]	0.8	-
f_{alv}	0.02	-
K_1 [ml_{STPD}/ml]	0.20	-
K_2 [$mmHg^{-1}$]	0.046	-
K_{CO_2} [ml_{STPD}·mmHg/ml]	0.0065	-
k_{CO_2} [ml_{STPD}/ml]	0.244	-
M_{CO_2} [ml_{STPD}/s]	4.292	-
M_{O_2} [ml_{STPD}/s]	5.117	-
V_{A,CO_2} [ml]	150	-
V_{A,O_2} [ml]	3200	-
V_{T,CO_2} [ml]	2500	-
V_{T,O_2} [ml]	15,000	-
V_{B,CO_2} [ml]	6000	-
V_{B,O_2} [ml]	900	-
M_{B,CO_2} [ml_{STPD}/s]	0.693	-

7.2.1 Model validation

Several actions were necessary to validate the physiological feasibility of the model. First we considered the effect of the dead space compartments on the model. A succession of adjacent small compartments is a better representation than one large compartment of the branching of the rigid airways that make up the dead space. We see that modeling the dead space with several compartments gives flatter peaks and valleys of the expiratory CO_2 curve and the dead space compartment closest to the mouth. This matches physiological reality of the end-tidal and end-inspiration portions of the respiratory cycle [105] and is seen in the p_{exp,CO_2} data used for these models. Figure 7.3 also shows that p_{A,CO_2} and p_{D,CO_2} are slightly out of phase, as would be expected. This is a result of the short time lag for the transfer of gas between successive compartments. Simulations by Khoo [47] and Lu *et al.* [54] display similar behavior. The final test for the validity of the dead space construction in the model is verifying that a negligible dead space volume results in a higher p_{A,O_2} and lower p_{A,CO_2}. Results for this are shown in Figure 7.4.

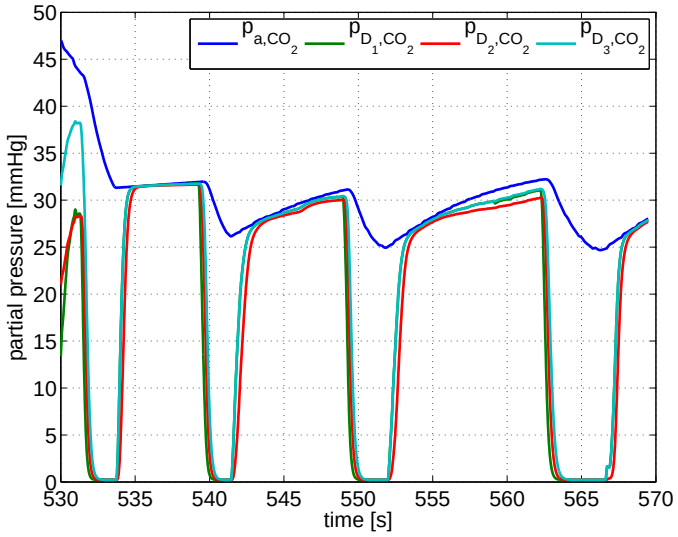

Figure 7.3: Dynamics of the partial pressure of alveolar CO_2 p_{a,CO_2} and the partial pressure of CO_2 in each of the three dead space compartments p_{D_i,CO_2}, with total volume of 150 ml. Dead space compartment 1 is closest to the mouth. Note, the end-tidal portion of the curve, at the end of expiration, is the peak of each respiratory cycle.

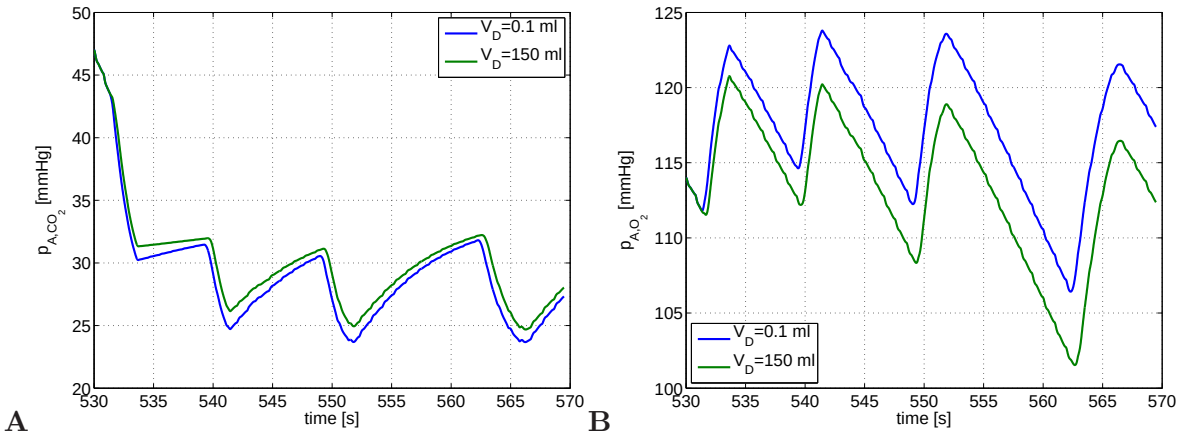

Figure 7.4: Dynamic alveolar partial pressures of CO_2 (A) and O_2 (B), using dead space volumes of 150 ml and 0.1 ml. Note p_{A,CO_2} is lower and p_{O_2} is higher with negligible dead space.

7.2.2 Regulation

The three experimental conditions that were investigated are hyperventilation, 5% CO_2 breathing, and 5% CO_2 rebreathing, which will point to the effects of hypocapnia and hypercapnia. The cerebral autoregulatory response to changes in CO_2 regulates cerebral blood flow by controlling cerebrovascular resistance R_c. The autonomic responses to CO_2 and $\bar{p}_a$ regulate peripheral systemic resistance R_s. Ventilation rate $\dot{V}_{IE}$ and HR change as well, but we extract these from the data for use as inputs to the model.

We approach modeling of the regulatory responses with two methods first used in Chapter 5 and Olufsen *et al.* [74]. As discussed in Chapters 2 and 5, the autonomic nervous system may play a role in cerebrovascular resistance changes and the possible interactions with autoregulation is still unknown, we empirically developed a piecewise cubic spline function with nine unknown coefficients to obtain a representative function that shows the behavior of the time-varying response of the cerebrovascular resistance. The result could then interpreted in terms of the suspected underlying physiology. We chose a spline instead of a linear function to maintain differentiability. The same method was used to initially estimate the behavior of the peripheral resistance R_s because its response is a function of the two stimuli CO_2 and $\bar{p}_a$.

An alternative method was to model the controlled parameters using first-order differential equations with set-point functions dependent on p_{CO_2} or $\bar{p}_a$ in the manner of

(5.9). To obtain a decrease in baseline cerebrovascular resistance $R_{c,s}$ with an increase in p_{b,CO_2} and a decrease in peripheral systemic resistance $R_{s,s}$ with increase in mean pressure $\bar{p}_a$, the following set-point functions could be used,

$$\begin{aligned} R_c(p_{b,CO_2}) &= (R_{c,max} - R_{c,min})\frac{p_{b,0}^k}{(p_{b,CO_2}^k + p_{b,0}^k)} + R_{c,min}, \text{ where} \\ p_{b,0} &= p_{b,CO_2,goal}\left(\frac{R_{c,s} - R_{c,min}}{R_{c,max} - R_{c,s}}\right)^{(1/k)} \end{aligned} \tag{7.7}$$

and

$$\begin{aligned} R_s(p_{am}) &= (R_{s,max} - R_{s,min})\frac{p_{a,0}^k}{(p_{am}^k + p_{a,0}^k)} + R_{s,min}, \text{ where} \\ p_{a,0} &= \bar{p}_{a,goal}\left(\frac{R_{s,s} - R_{s,min}}{R_{s,max} - R_{s,s}}\right)^{(1/k)}. \end{aligned} \tag{7.8}$$

The targeted cerebral partial pressure $p_{b,CO_2,goal}$ could be estimated from the baseline simulated cerebral concentration $c_{b,CO_2,goal}$. Mean pressure can be calculated as in (5.6).

Peripheral systemic resistance increases in response to increased p_{a,CO_2}. Thus for R_s, the set-point function is

$$\begin{aligned} R_s(p_{a,CO_2}) &= (R_{s,max} - R_{s,min})\frac{p_{a,CO_2}^k}{(p_{a,CO_2}^k + p_{a,0}^k)} + R_{s,min}, \text{ where} \\ p_{a,0} &= p_{a,CO_2,goal}\left(\frac{R_{s,max} - R_{s,s}}{R_{s,s} - R_{s,min}}\right)^{(1/k)}. \end{aligned} \tag{7.9}$$

The target arterial partial pressure $p_{a,CO_2,goal}$ could be estimated from the baseline simulated p_{a,CO_2}.

5% CO_2 increase

We observed from the data that effect of 5% CO_2 occurs not instantaneously but gradually. We modeled the increase from 0% to 5% CO_2 in the environment exterior to the mouth as a step change. Then the p_{I,CO_2} at the mouth reaches the 5% CO_2 level with dynamics following Newton's Law of Heating:

$$\frac{dp_{I,CO_2}}{dt} = k(38 - p_{I,CO_2}),$$

where a partial pressure of 38 mmHg is equivalent to 5% CO_2. The parameter k characterizes the rate of increase of p_{I,CO_2}. With a constant new atmospheric level of p_{a,CO_2}, ventilation and p_{exp,CO_2} reach new baseline oscillatory levels.

Rebreathing

In the rebreathing experiment, a rebreathing bag is introduced into the breathing circuit connected to a tube, making a closed-loop respiratory system. In the compartmental model, the tube is represented by an additional dead space compartment at the exit of the mouth and the rebreathing bag is a compartment attached to the tube with no other outlet. Material balance equations are derived as for the other pulmonary compartments. The rebreathing bag has a dynamic volume similar to the alveolar compartment, but there is no addition or removal of gases via cardiovascular flow. This results in no change in gas fraction within the rebreathing bag during inspiration. All volumes are expressed in BTPS. In the model, these differential equations are inactive during baseline simulations and are activated when the rebreathing bag is added to the circuit. Equations for the connecting tube (subscript *tube*) and rebreathing bag (subscript R) are derived in the same way as (7.3),

$$\text{Inspiration: } V_{tube}\frac{dp_{tube,g}}{dt} = \frac{dV_R}{dt}(p_{tube,g} - p_{R,g}), \qquad \text{connecting tube,} \tag{7.10}$$

$$V_R\frac{dp_{R,g}}{dt} = 0, \qquad \text{rebreathing bag,}$$

$$\text{Expiration: } V_{tube}\frac{dp_{tube,g}}{dt} = \frac{dV_R}{dt}(p_{D_1,g} - p_{D_{tube,g}}), \qquad \text{connecting tube,} \tag{7.11}$$

$$V_R\frac{dp_{R,g}}{dt} = \frac{dV_R}{dt}(p_{tube,g} - p_{R,g}), \qquad \text{rebreathing bag.}$$

Note that $dV_R/dt = -\dot{V}_{IE}$.

7.3 Experimental data

In this study we investigate data from two different test protocols that encompass the three breathing challenges including hyperventilation, 5% breathing, and 5% rebreathing.

7.3.1 Hyperventilation and CO_2 rebreathing

This test protocol and data are obtained from the SAFE laboratory. Instrumentation for physiological measurements takes 30 minutes. During the entire experiment, the subject was in supine position. Continuous measurements included HR, beat-to-beat blood pressure, CBFV in the MCA, respiration airflow, O_2, and CO_2. Heart rate was measured

with a 3-lead electrocardiogram and beat-to-beat arterial pressure from a finger cuff using a Portapress-2 device (FMS, Inc), corroborated by standard measurements of arterial BP on the upper arm (Dynamap). Respiration was measured using a nasal thermistor. End-tidal CO_2 and O_2 values were taken using an infrared end-tidal volume gas monitor (Capnomac Ultima, Ohmeda Inc.) attached to a face mask. A TCD system (MultiDop X4, Neuroscan, Inc.) was used to measure BFV in the MCA insonated from the temporal windows using the 2-MHz probes. Each probe was positioned to record the maximal BFV and fixed at the desired angle using a 3-dimensional positioning system.

The subject was a healthy female age 52 with no known cardiovascular disease. The test began with supine rest for 10 minutes. Then the subjects hyperventilated to reduce CO_2 to 25 mmHg for 3 minutes. Then the subject breathed a mixture of 5% CO_2 and 95% air (21% O_2 and balanced nitrogen) from a 5 liter rebreathing bag to increase CO_2 above baseline to 45 mmHg for 3 minutes, followed by approximately 2 minute rest to equilibrate p_{a,CO_2}. The rebreathing bag is attached to the breathing circuit via a tube with approximate dimensions of 45 cm long and 2 cm diameter. In this particular experiment the subject was instructed to start breathing very slow deep breaths while breathing normally for about 30 seconds after the end of hyperventilation. p_{exp,CO_2} was seen to rise above 25 mmHg to normal levels quickly, and the subject was instructed to continue breathing slowly. Then the rebreathing circuit was attached.

7.3.2 5% CO_2 breathing

This test protocol and data are published in a study done by Ailiang Xie [116]. The subject is a male age 55 with congestive heart failure but no known sleep apnea syndrome. The hypercapnia trial lasted 5 minutes. A gas mixture of 5% CO_2 (about 38 mmHg) with 21% O_2 and the balance nitrogen was added to the breathing circuit.

A 2-MHz pulsed Doppler ultrasound system (Neurovision 500 M; Multigon Industries, Yonkers, NY) was used to continuously measure peak CBFV in the proximal segment of the MCA. The MCA was insonated through the right temporal bone window using search techniques described in Otis and Ringelstein [76]. After detection and optimization of the Doppler signal, the probe was mechanically secured using a headband device and probe holder to provide a fixed angle of insonation for the duration of the experiment. The subject was studied in the semirecumbent position and was asked to keep his head still and eyes

open throughout the experiment. End-tidal CO_2 was sampled from a leak-free mask and measured by a gas analyzer (Model CD-3A; Ametek, Pittsburgh, PA). Heart rate, arterial pressure in arm and finger, V_T, f_R, and S_{a,O_2} (arterial O_2 saturation) were measured as previously described by Przybylowski *et al.* [87]. Sampling rate was 128 Hz.

7.4 Parameterization

7.4.1 Baseline gas concentrations

In order for us to evaluate the changes in model states in response to CO_2 challenges, we must ensure that baseline dynamics are established model states, which we assume are in steady state in the experimentation prior to the challenges. The time for a model state to reach steady-state can be estimated by examining the first order dynamics. In the equation for p_{ac} from the 11-compartment model of Chapter 5,

$$\frac{dp_{ac}}{dt} = \left(\frac{p_a - p_{ac} + \rho g h_c}{R_{ac}} - \frac{p_{ac} - p_{vc}}{R_{acp}} \right) / C_{ac},$$

the time constant is approximately $(C_{ac}R_{ac}R_{acp})/(R_{ac}+R_{acp}) = 0.027$ s. The cardiovascular states reach their baseline steady-state dynamics much quicker than the duration of the experiment. In contrast, the time constants in the gas state equations are given by the tissue volumes which are of much larger magnitude, the largest of which is seen in the state equation for systemic CO_2 concentration c_{S,CO_2},

$$V_{S,CO_2} \frac{dc_{S,CO_2}}{dt} = M_{S,CO_2} + q_s(c_{a,CO_2} - c_{S,CO_2}).$$

The values of $V_{S,CO_2} = 14,100$ ml and $q_s = 66.6$ ml/s give an approximate time constant of 210 seconds. We analyze an exponential with a steady-state concentration c_s represented as a vertical shift to look at the time required for a desired reduction in the derivative.

$$c = Ae^{-k/t} + c_s$$
$$\frac{dc}{dt} = \frac{-1}{k} Ae^{-t/k} = \frac{-(c - c_s)}{k}.$$

Given the initial value $c_0 = A + c_s$ at $t = 0$, The initial derivative dc/dt_0 will decrease by a rate r to give dc/dt at time t:

$$\left.\frac{dc}{dt}\right|_0 = \frac{-A}{k},$$
$$\frac{dc}{dt} = r \left.\frac{dc}{dt}\right|_0 = \frac{-rA}{k} = \frac{-c + c_s}{k}.$$

We rearrange the above to obtain

$$rA = c - c_s.$$

Solving for t in the original expression,

$$t = -k \ln \left(\frac{c - c_s}{A} \right) = -k \ln r.$$

We can see from the following sample calculation that for $r = 0.1$, $t = 485$ s, and for $r = 0.01$ $t = 972$ s. It is generally not computationally feasible to parameterize the model against such a large timespan of data.

We address these problems in two ways. First we chose initial conditions for the gas states that are closer to the steady-state concentrations. These were found by solving the model equations using a simple sinusoidal airflow profile with dynamics similar to the data airflow seen from baseline data

$$\dot{V}_{IE,sine} = 320 \sin(2\pi t/5). \tag{7.12}$$

We use the vector of variable heart rate obtained from the data. We used nominal values for metabolic rates and volumes to generate dynamics with the sinusoidal respiration function (7.12), shown in Figure 7.5. Mean values used as initial conditions for the baseline dynamics are given in Table 7.6. Note that initial pressures and parameters were not taken from data but from literature values. After good estimates for initial conditions for the baseline gas dynamics were found, we ran model simulations for the length of the baseline data available for a particular study to reach as close to steady-state as possible. Note that fluctuations in the heart rate and ventilation appear in the actual data that will prevent the gas levels from reaching a true steady-state.

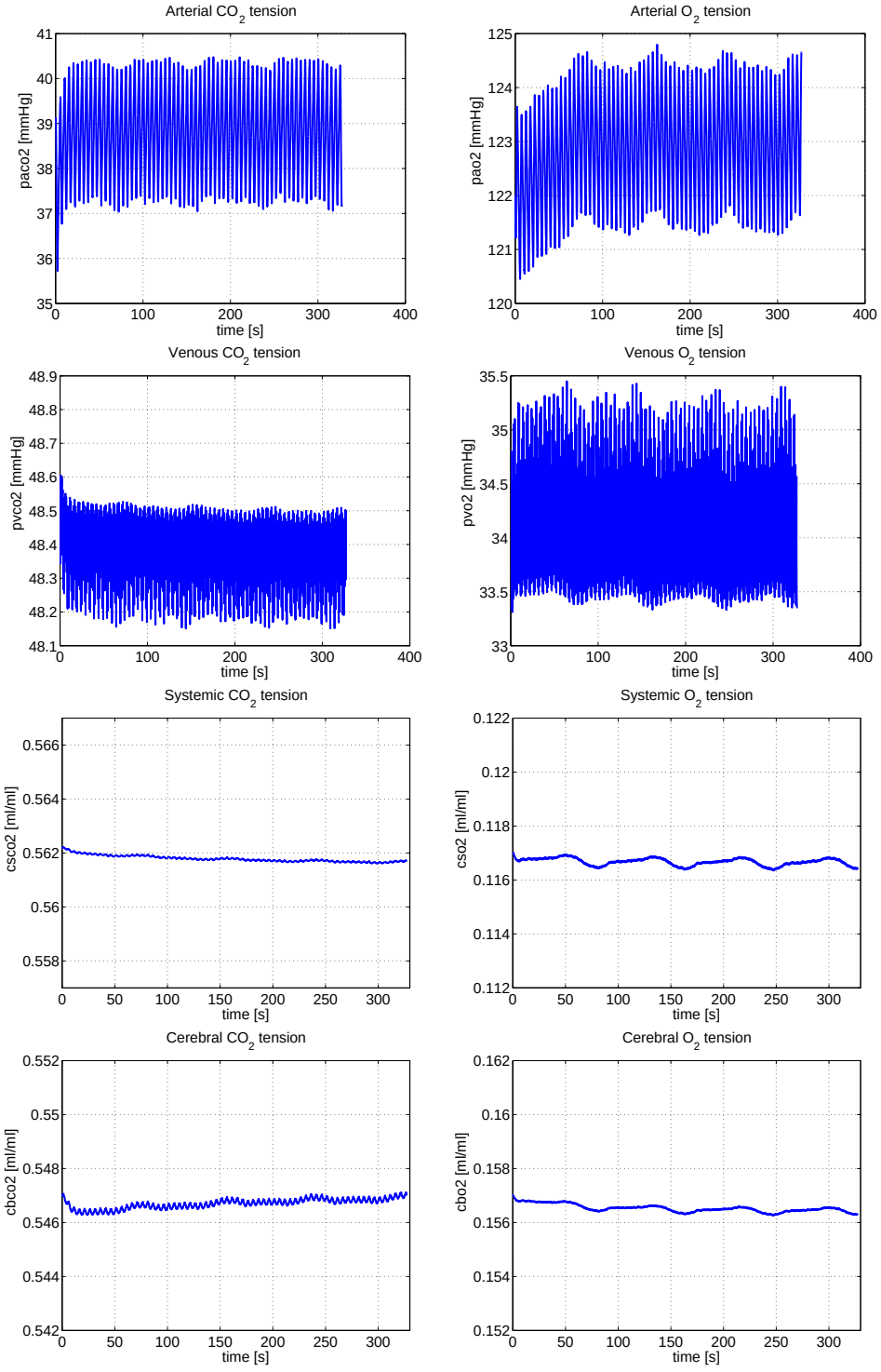

Figure 7.5: Baseline dynamic behavior with sinusoidal airflow input. From top to bottom: $p_{a,g}$, $p_{v,g}$, $c_{s,g}$, and $c_{b,g}$, for gas g. Left column, CO_2. Right column, O_2.

Table 7.6: Steady-state values obtained from computations using a sinusoidal respiration function (7.12). This function was defined using visual estimates from the state output shown in Figure 7.5. Estimated initial condition values were used to generate baseline dynamics for model simulations with actual airflows.

Variable	Value
p_{a,CO_2} [mmHg]	39
p_{a,O_2} [mmHg]	122
p_{v,CO_2} [mmHg]	48.5
p_{v,O_2} [mmHg]	33.8
c_{S,CO_2} [ml$_{STPD}$/ml]	0.562
c_{S,O_2} [ml$_{STPD}$/ml]	0.117
c_{B,CO_2} [ml$_{STPD}$/ml]	0.547
c_{B,O_2} [ml$_{STPD}$/ml]	0.157

7.4.2 Model parameters

Nominal parameter values and initial conditions were estimated from the subject's anthropometric measurements. Height and weight are used to calculate BSA [m^2] using (6.3) and BV [ml] using (6.2) [5] as described in Chapter 6. Maximum and minimum left ventricular volumes LV_{max} and LV_{min} [ml] were found as functions of BSA based on a study by Salton [97]:

$$LV_{max} = \begin{cases} 57.6BSA, & \text{male} \\ 49.8BSA, & \text{female} \end{cases}$$

$$LV_{min} = \begin{cases} 18.1BSA, & \text{male} \\ 14.8BSA, & \text{female.} \end{cases}$$

Right and left ventricular minimum and maximum volumes are approximately the same, therefore the right and left heart volumes were estimated to be equal [13]. All other volumes were calculated as in other studies based on the stressed volume percentages shown in Table 4.1 and scaled to the subject's blood volume.

The maximum, or systolic, heart pressure $p_{l,max}$ was set to be the maximum pressure found in the data. Mean pressures used for nomimal resistance and compliance calculations were set relative to $p_{l,max}$ based on literature values for means. The initial condition for p_a was set to be the initial data point of the arterial pressure data. Initial conditions for remaining pressures were set with the same ratios as for the mean pressures.

Since we start simulations at the beginning of a cardiac cycle, we set initial conditions for the ventricular volume equations at the corresponding LV_{max}.

The timing fraction $T_{M,frac}$ was set to be equal to the timing of the peak pressure in the first cycle of the ABP data. Similar to the model used by Heldt [39], the fraction $T_{r,frac}$ was set to be 1/2 of $T_{M,frac}$. The elastance parameters $E_{max,l}$ and $E_{min,l}$ for the left ventricle were set to the values used by Ottesen *et al.* [79]. Then with the knowledge that the volume profiles are are expected to be the same between the left and right ventricles, elastance parameters $E_{max,r}$ and $E_{min,r}$ were set to be less than the left, as suggested by Ottesen, adjusted to get similar ventricular volume dynamics between the two ventricles.

Metabolic rates were set using standard allometric scaling proportional body mass by the power of 3/4 [114, 115] using values in Table 7.2.

7.4.3 Parameter estimation

Parameter estimation was done in a similar manner as in earlier studies, see Chapters 5 and 6. Measured data include arterial blood pressure $p_a(t_i)$ [mmHg], cerebral blood flow velocity $v_c(t_i)$ [cm/s], and expiratory CO_2 $p_{exp,CO_2}(t_i)$ [mmHg]. Nonlinear optimization was used to estimate parameters by minimizing the residual between computed and measured pressure and velocities relative to the measured quantities over all samples t_i. To this end we define the vector y spanning both pressure and velocity, i.e., y has $3N$ entries, given by

$$y = [p_a(t_1), \ldots, p_a(t_N), v_c(t_1), \ldots, v_c(t_N), p_{exp,CO_2}(t_1), \ldots, p_{exp,CO_2}(t_N)]^T. \tag{7.13}$$

We define vectors of systolic and diastolic values of p_a and v_c as

$$\begin{aligned} y_{sys} &= [p_{a,sys,1}, \ldots, p_{a,sys,M}, v_{c,sys,1}, \ldots, v_{c,sys,M}]^T, \\ y_{dia} &= [p_{a,dia,1}, \ldots, p_{a,dia,M}, v_{c,dia,1}, \ldots, v_{c,dia,M}]^T. \end{aligned} \tag{7.14}$$

as was done in the study in Chapter 6. Each vector has $2M$ entries where M is the number of cardiac cycles. In addition, we define a vector for end expiration values of p_{exp,CO_2}, i.e., the maximum flat region of each respiratory cycle, which includes only Q values above a user-defined threshold,

$$y_{CO_2} = [p_{exp,CO_2,1}, \ldots, p_{exp,CO_2,Q}]. \tag{7.15}$$

The cost function J for parameter estimation and optimization is calculated from the residual R. Combining the vectors y, we defined the residual vector between computed ($y^c = X(\hat{\mu})$) and measured (y^d) quantities as

$$\begin{aligned} R &= \left[\frac{y_1^c - y_1^d}{\sqrt{N} y_1^d}, \ldots, \frac{y_{2N}^c - y_{2N}^d}{\sqrt{N} y_{2N}^d}, \frac{y_{sys,1}^c - y_{sys,1}^d}{\sqrt{M} y_{sys,1}^d}, \ldots, \frac{y_{sys,2M}^c - y_{sys,2M}^d}{\sqrt{M} y_{sys,2M}^d}, \right. \\ & \left. \frac{y_{dia,1}^c - y_{dia,1}^d}{\sqrt{M} y_{dia,1}^d}, \ldots, \frac{y_{dia,2M}^c - y_{dia,2M}^d}{\sqrt{M} y_{dia,2M}^d}, \frac{y_{CO_2,1}^c - y_{CO_2,1}^d}{\sqrt{Q} y_{CO_2,1}^d}, \ldots, \frac{y_{CO_2,Q}^c - y_{CO_2,Q}^d}{\sqrt{Q} y_{CO_2,Q}^d} \right]^T . \end{aligned}$$

The residual is scaled by both the value of the measurements and by the square root of the number of measurements (N for pressure/velocity, M for systolic/diastolic, Q for CO_2). This definition of the residual vector R gave rise to a least squares cost-function J of the form

$$\begin{aligned} J &= R^T R = \frac{1}{N} \sum_{i=1}^{N} \left| \frac{p_{as}^c - p_{as}^d}{p_{as}^d} \right|^2 + \frac{1}{N} \sum_{i=1}^{N} \left| \frac{v_{acp}^c - v_{acp}^d}{v_{acp}^d} \right|^2 + \frac{1}{M} \sum_{i=1}^{M} \left| \frac{p_{as,sys}^c - p_{as,sys}^d}{p_{as,sys}^d} \right|^2 + \\ & \frac{1}{M} \sum_{i=1}^{M} \left| \frac{p_{as,dia}^c - p_{as,dia}^d}{p_{as,dia}^d} \right|^2 + \frac{1}{M} \sum_{i=1}^{M} \left| \frac{v_{acp,sys}^c - v_{acp,sys}^d}{v_{acp,sys}^d} \right|^2 + \frac{1}{M} \sum_{i=1}^{M} \left| \frac{v_{acp,dia}^c - v_{acp,dia}^d}{v_{acp,dia}^d} \right|^2 + \\ & \frac{1}{Q} \sum_{i=1}^{Q} \left| \frac{p_{exp,CO_2}^c - p_{exp,CO_2}^d}{p_{exp,CO_2}^d} \right|^2 . \end{aligned} \tag{7.16}$$

The Levenberg-Marquardt variant of the Gauss-Newton optimization method introduced in Section 4.3.2 was used to minimize the cost J (7.17) for parameter estimation. We present the method for estimating baseline parameters for each test protocol below. Note that we chose to fix all respiratory parameters at their nominal values parameter estimation under both protocols.

5% CO_2 breathing

1. Solve equations using baseline timespan $1 \leq t \leq 340$ s to establish baseline gas concentrations.

2. Choose 20 s at the end of the baseline data for baseline parameter estimation.

3. To predict baseline dynamics, optimize all cardiovascular parameters for optimization.

4. Use two 9-node piecewise cubic spline functions to estimate parameters that predict dynamics of R_s and R_c for data $345 \leq t \leq 445$ s.

Hyperventilation and 5% CO_2 rebreathing

1. Solve equations using baseline timespan $20 \leq t \leq 580$ s to establish steady-state gas concentrations.

2. Choose 30 seconds at the end of the baseline data for parameter estimation.

3. To predict baseline dynamics, use subset selection to choose cardiovascular parameters for optimization.

4. Use first-order differential equations to estimate parameters that predict dynamics of R_s and R_c for data $550 \leq t \leq 650$ s and $800 \leq t \leq 950$ s.

7.5 Results

Preliminary results are presented here. The first results come from the analysis of the dynamics for the 5% CO_2 breathing test. Nominal parameter values for the baseline data come from the physiological considerations outlined in Table 7.3 and are shown with optimized baseline parameters values in Table 7.4. The residual R was composed only of y, y_{sys}, and y_{dia}.

Next the CO_2 breathing transition ($345 \leq t \leq 445$ s) dynamics were analyzed. A piecewise spline was constructed with 9 nodes each for R_c and Rs. Spline nodes are given in Table 7.7. Data and model simulated dynamics of p_a, v_c, and p_{exp,CO_2} are given in Figure 7.6 and 7.7. Dynamic resistances R_c and R_s are shown in Figure 7.8.

In the results from the hyperventilation / rebreathing experiment shown here, we used subset selection with the cardiovascular parameters to identify a set of parameters that characterize the baseline model state dynamics. We modeled the control of R_c and R_s under hyperventilation and CO_2 rebreathing with the first-order differential equations given in (7.8)-(7.10). Control parameters for the control equations were manually tuned, with values shown in Table 7.8. The same parameters are used for control functions describing both CO_2 challenges and for the response of R_s to both $\bar{p}_a$ and CO_2.

Table 7.7: Piecewise cubic spline nodes used in dynamic R_c and R_s functions for CO_2 breathing data, $1 \leq t \leq 445$ s.

Time	R_c	R_s
40	15.05	3.65
140	15.05	3.65
240	15.05	3.65
340	15.05	3.65
360	14.75	3.95
380	14.45	4.25
400	14.15	4.55
420	14.05	4.65
440	14.05	4.65

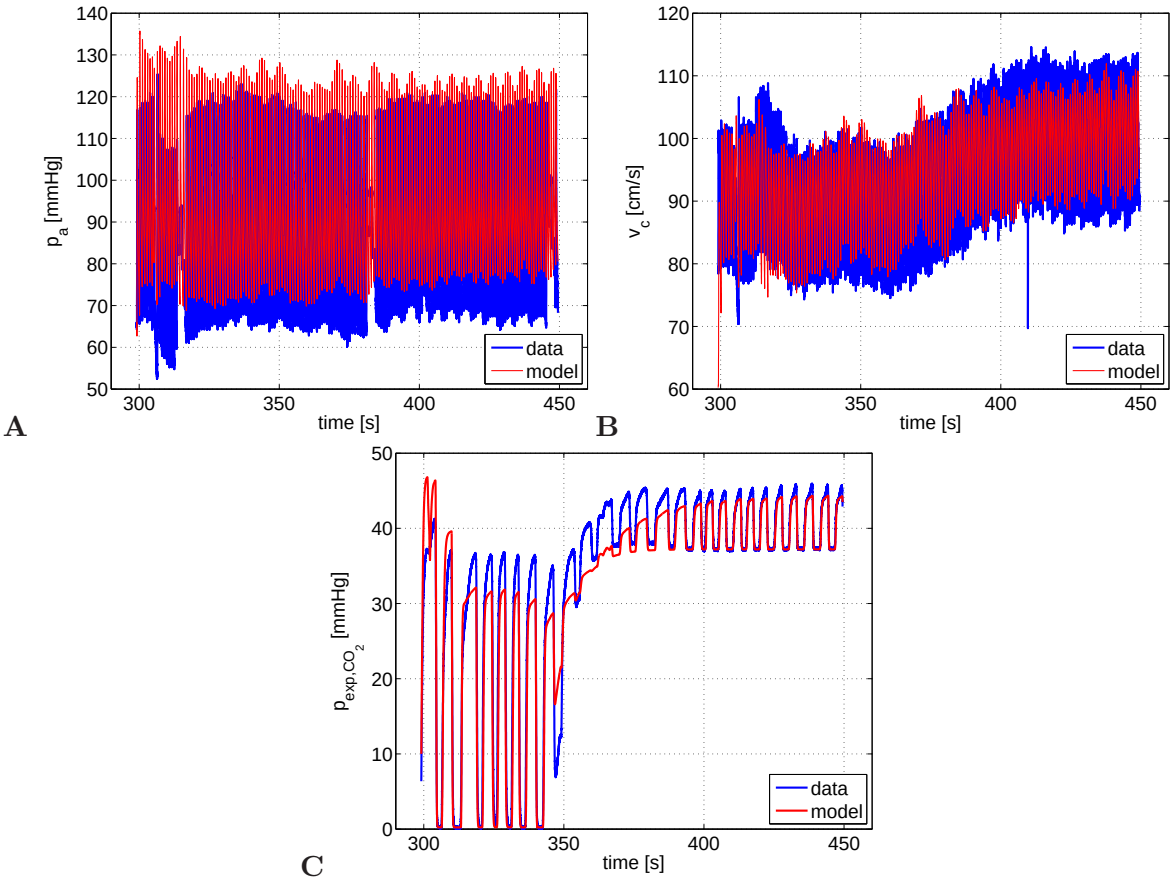

Figure 7.6: Model simulation compared to data for p_a (A), v_c (B), and p_{exp,CO_2} (C) during 5% CO_2 breathing, $300 \leq t \leq 450$ s. Breathing of 5% CO_2 begins at 343 s.

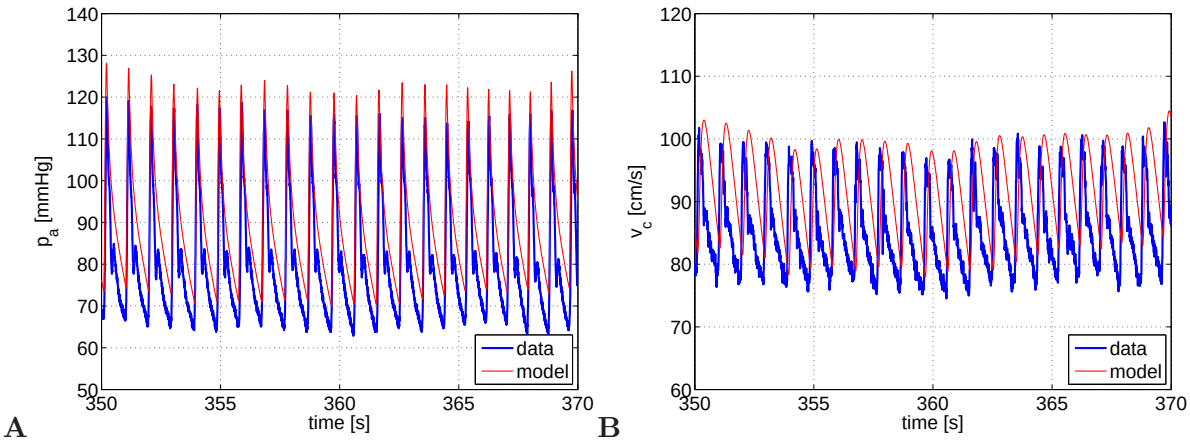

Figure 7.7: Model simulation compared to data for p_a (A) and v_c (B) during 5% CO_2 breathing, zoomed in to the interval $350 \leq t \leq 370$ s.

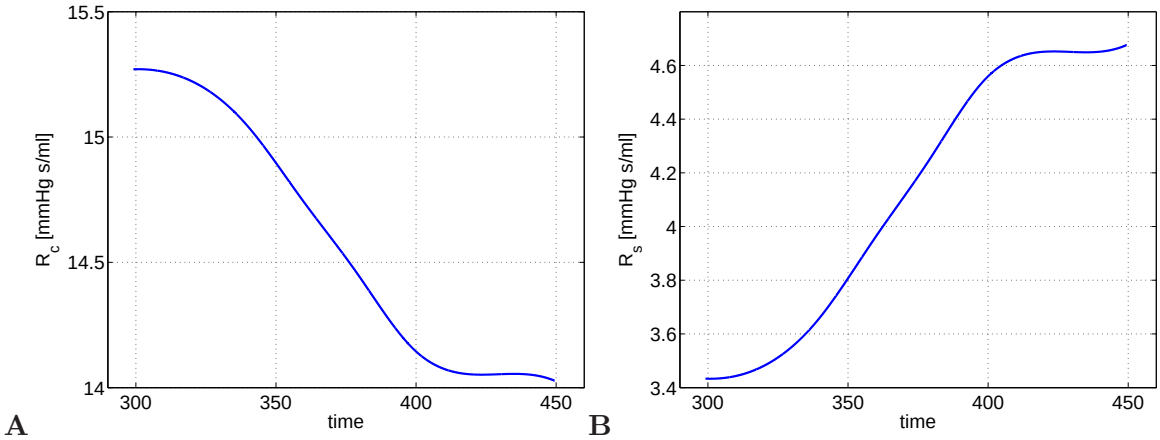

Figure 7.8: Simulated dynamic resistances R_c (A) and R_s (B) during 5% CO_2 breathing, $300 \leq t \leq 450$ s.

Table 7.8: Control parameters for hyperventilation and CO_2 rebreathing simulations. The same parameters were used for hyperventilation and rebreathing, and for R_s as a function of both CO_2 and $\bar{p}_a$. Note that the two R_s responses are added to obtain the total R_s.

Parameter	Value
$R_{c,CO_2,max}$	11.95
$R_{c,CO_2,min}$	3.948
k_c	50
τ_c	5
$R_{s,max}$	2.361
$R_{s,min}$	0.974
k_s	5
τ_s	5

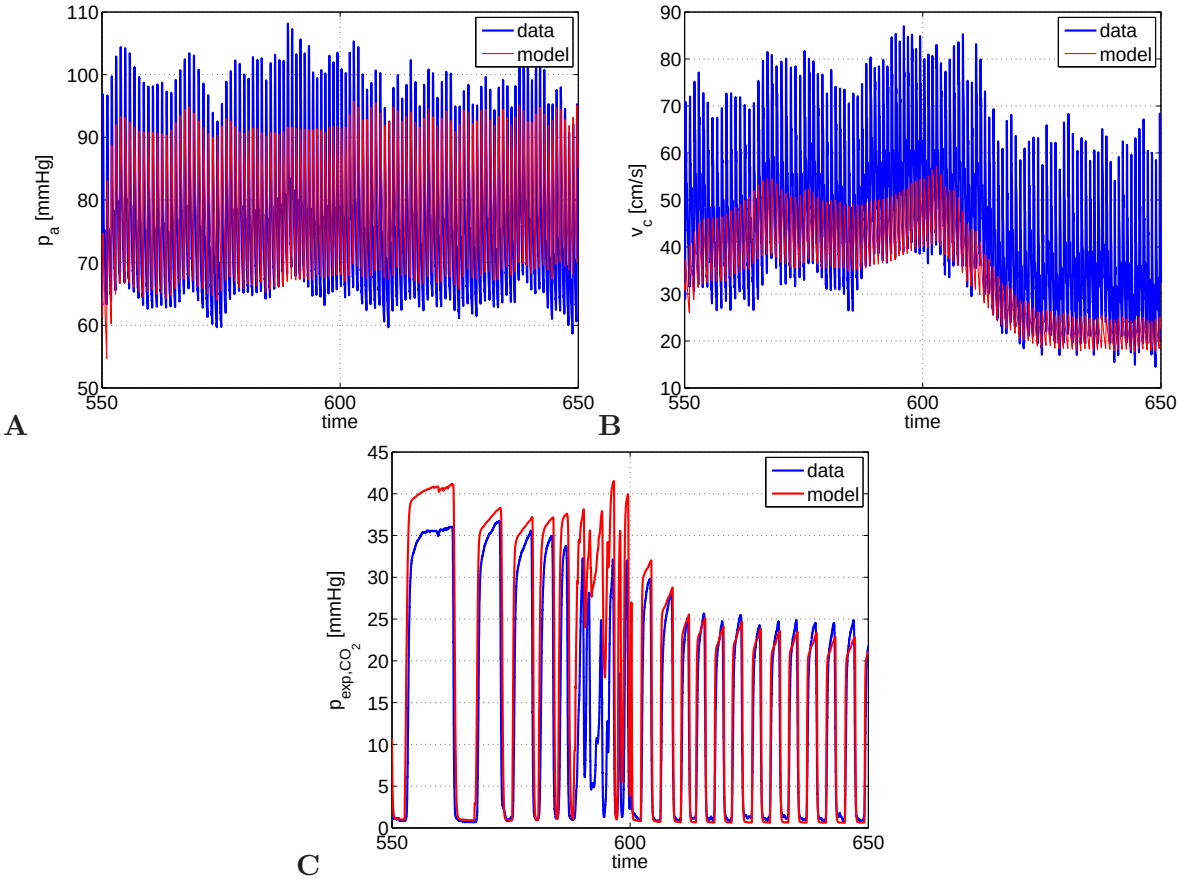

Figure 7.9: Model simulation compared to data for p_a (A), v_c (B), and p_{exp,CO_2} (C) during hyperventilation, $550 \leq t \leq 650$ s. Hyperventilation begins at 590 s.

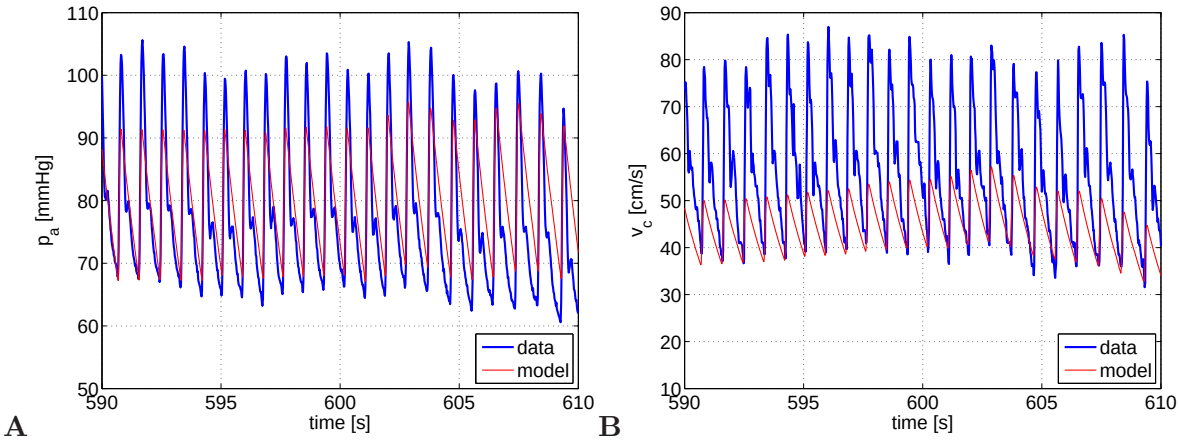

Figure 7.10: Model simulation compared to data for p_a (A) and v_c (B) during hyperventilation, zoomed in to the interval $590 \leq t \leq 610$ s.

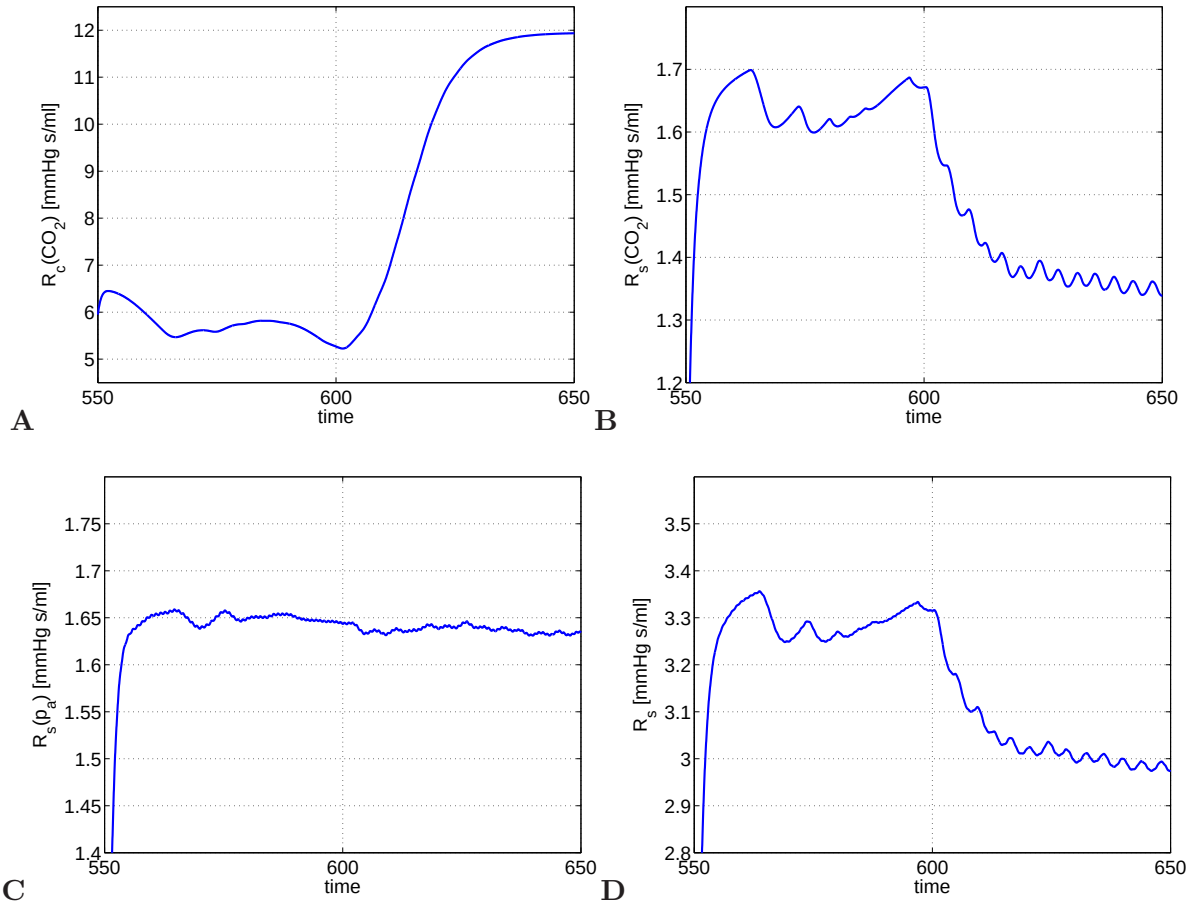

Figure 7.11: Simulated dynamic resistances during hyperventilation, $550 \leq t \leq 650$ s. A: $R_c(CO_2)$, B: $R_s(CO_2)$, C: $R_s(p_a)$, D: total R_s.

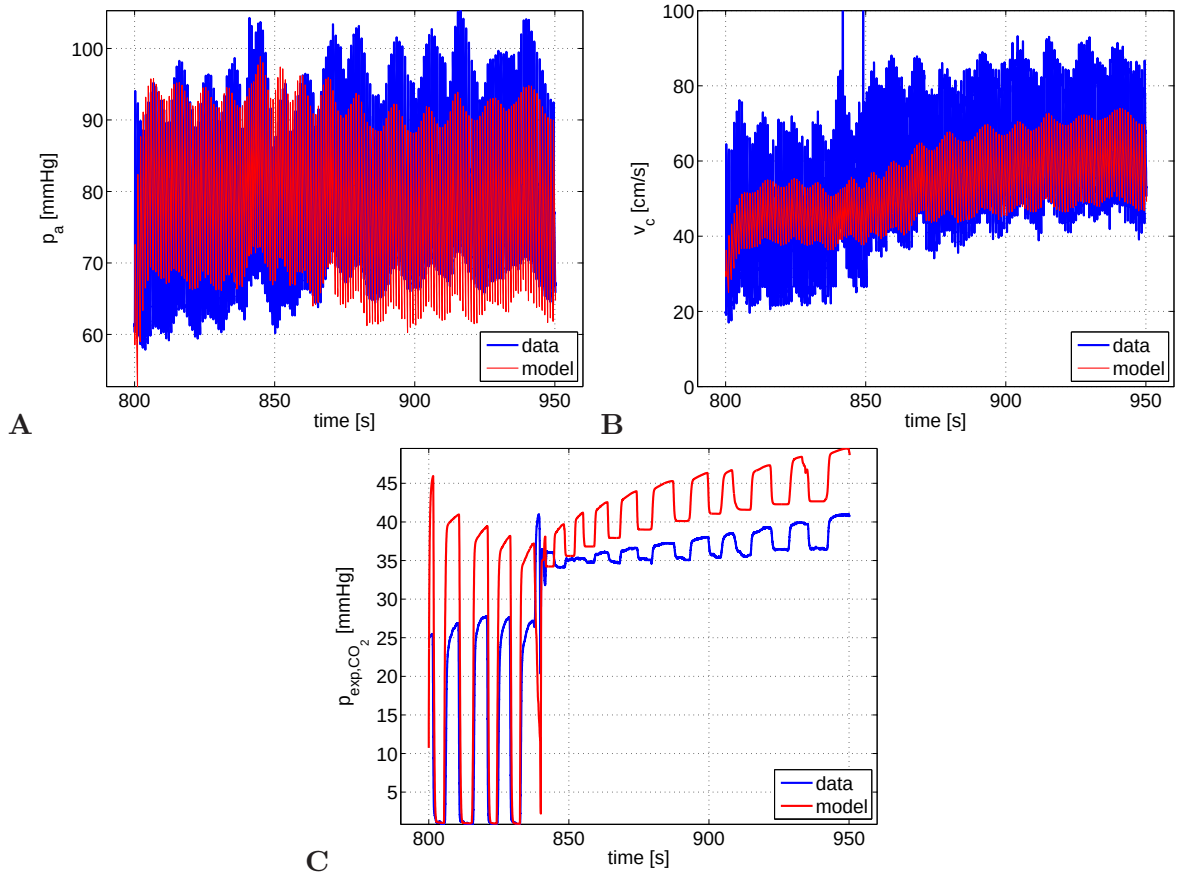

Figure 7.12: Model simulation compared to data for p_a (A), v_c (B), and p_{exp,CO_2} (C) during CO_2 rebreathing, $800 \leq t \leq 950$ s. CO_2 rebreathing is at 840 s.

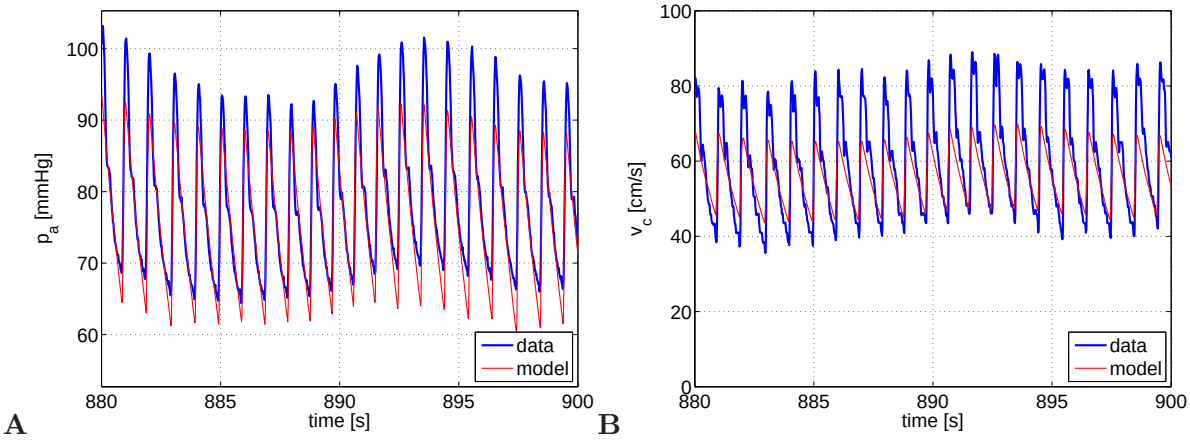

Figure 7.13: Model simulation compared to data for p_a and v_c during CO_2 rebreathing, zoomed in to the interval $880 \leq t \leq 900$ s.

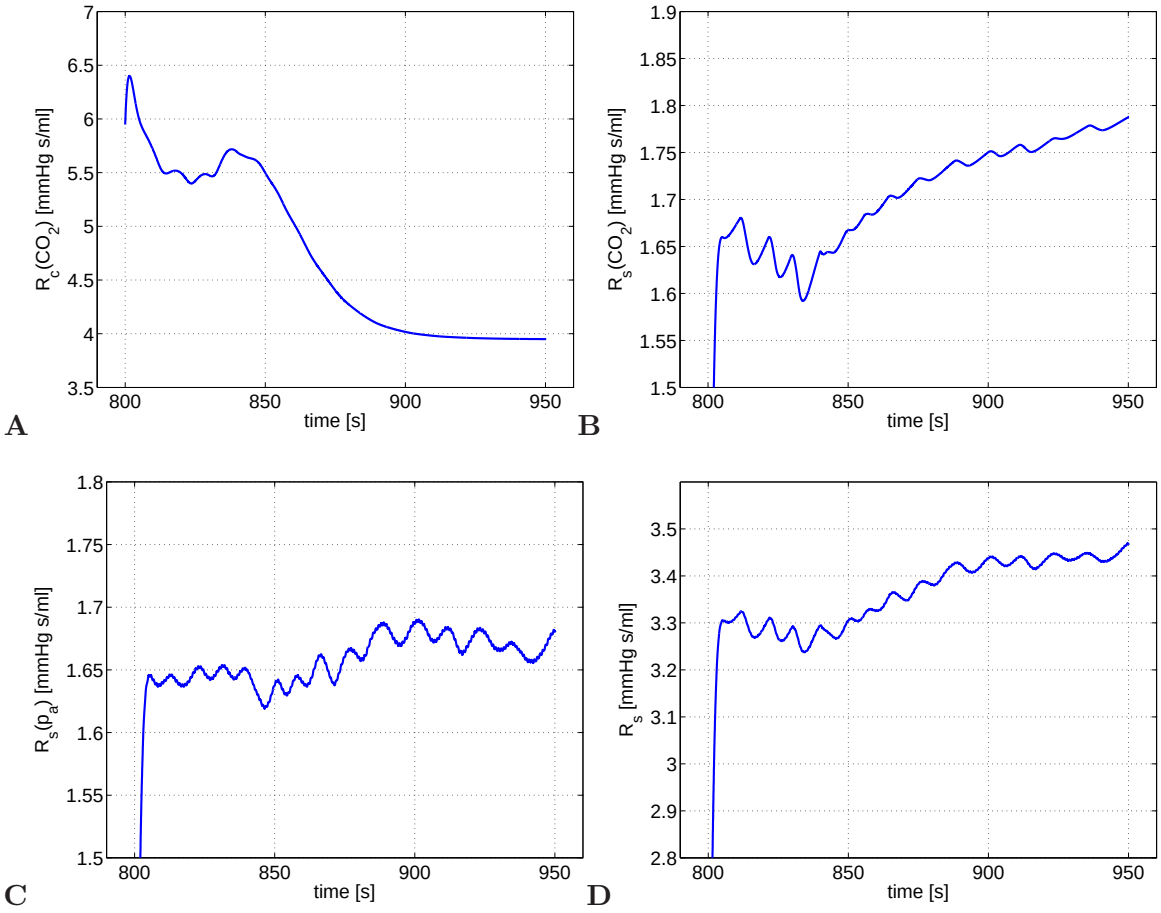

Figure 7.14: Simulated dynamic resistances during CO_2 rebreathing, $800 \leq t \leq 950$ s. A: $R_c(CO_2)$, B: $R_s(CO_2)$, C: $R_s(p_a)$, D: total R_s.

7.6 Discussion

The cardiorespiratory model described here is designed to predict cerebral blood flow velocity, finger blood pressure, and expiratory CO_2 dynamics. Baseline parameters were predicted using nonlinear optimization. Empirical models using piecewise cubic splines and first-order differential equations were parameterized to predict responses of cerebrovascular resistance and peripheral systemic resistance to changes in CO_2 and $\bar{p}_a$. The model shows potential for simulating the dynamics of all three observations under the three CO_2 challenges. The p_a, v_c, and p_{exp,CO_2} waveforms were captured. We note especially the qualitative behavior of the end-inspiration (valley) and end-tidal (peak) portions of p_{exp,CO_2}. The piecewise spline and first-order differential equation control functions were able to generate the appropriate change in controlled resistances R_c and R_s in response to $\bar{p}_a$ and CO_2. The resistance changes caused the expected increase in v_c during CO_2 breathing and rebreathing, and a decrease in v_c during hyperventilation.

The clearest difference between the model simulations and the data is the underestimated velocity pulse magnitude in simulated v_c. This is most evident with the hyperventilation / rebreathing protocol in both the baseline data and the CO_2 test data. We also observe a delay in the CO_2 breathing simulations between the time at which CO_2 begins to increase and when R_c decreases and v_c increases. These issues are best addressed with improvements in the control functions and the parameterization scheme. We also discuss several alternatives for the components of the respiratory submodel.

We first address several non-regulatory facets of the model. As seen in Figure 5.8, including passive resistances for large arteries contributed to pressure pulse widening in the model of Chapter 5. Including passive resistances in the cardiorespiratory model could more accurately describe output dynamics. The delay seen in the CO_2 breathing simulations may be an inherent effect of circulatory transport. The latency of the various autonomic responses also likely contributes to the delay, which could be accounted for in the time constants τ in the regulatory differential equations.

The control functions used in these modeling efforts were preliminary attempts at characterizing regulatory dynamics of the responses to changes in CO_2. The spline functions used to represent the dynamics of R_c and R_s during CO_2 breathing were not based on physiology but merely gave the proposed dynamics of the changes in R_c and R_s that could cause an increase in v_c. The differential equations used for both hyperventilation and

CO_2 rebreathing were parameterized with manual tuning with little physiological basis. In addition, the same parameterization was used for both R_s functions and the same time constant was assumed for all three functions. However, the actual responses of each resistance to changes in $\bar{p}_a$ versus CO_2 likely have different timing and magnitude. Hysteresis in the response of vascular resistance to increasing and decreasing gas levels requires modeling the response differently under hyperventilation versus CO_2 breathing. Following the study described in Chapter 5 and in Olufsen *et al.* [74] we propose including autonomic regulation for all small arteries and venous compliances. These additions could produce a wider velocity pulse observed in the earlier study.

Parameter estimation presents many opportunities for improvement. Using subset selection and the cost function (7.17) we were unable to identify a set of parameters that could predict baseline dynamics with the correct p_a and v_c pulse magnitudes. Removing the respiratory parameters from the optimizable parameter space improved cardiovascular parameter estimates but inaccurately predicted p_{exp,CO_2} pulse magnitude, particularly in the CO_2 rebreathing simulation. We chose with the CO_2 baseline data to optimize all of the cardiovascular parameters, including both R_c and A_c, because subset selection produced undesirable results. A_c is only in the output equation for v_c, but R_c appears in the differential equations as well and so influences the state dynamics. In spite of the dependency seen in the output equation for v_c we suggest that both of these parameters are critical to the parameterization of the model. Obtaining measurements that lead to a more accurate calculation of A_c could aid in solving this problem. With the hyperventilation / rebreathing data we attempted to optimize all cardiovascular parameters but this gave a less accurate model output than what was simulated with nominal values. When we used subset selection to choose the candidate parameters, A_c was chosen but not R_c. More knowledge of the system could aid in choosing candidate parameters for optimization. Including the respiratory parameters could lead to more accurate simulation of p_{exp,CO_2} during CO_2 rebreathing.

Additional parameter estimation methods from earlier studies could be utilized for this model. Combining sensitivity analysis with subset selection as in Chapter 6 could aid in eliminating parameters from the set of candidates as was done in Chapter 5. Direct-search and other non-gradient-based algorithms are options for optimization not yet explored with the cardiorespiratory model. If gradient-based optimization is retained the choice of bounds should be examined. Finally, the cost function could be constructed differently or have weights placed on the portions about which we are most concerned.

Although simulated p_{exp,CO_2} dynamics represented the data well in most cases, we recognize that we use simple components in our respiratory submodel. Greater accuracy in gas concentration dynamics could be predicted using a more complex model, leading to a better understanding to the control responses to changes in CO_2. The lung model in this study consists of one alveolar compartment and three dead space compartments in series, a simple representation of lung mechanics. This ignores much of the complicated functionality of the lungs. Many other models exist, including both circuit-based compartmental models and spatially-distributed models. As examples we point to the models included in Ottesen *et al* [80] and Lu *et al.* [54], which contain multiple resistances and compliances similar to our cardiovascular submodel and consider explicit equations for gas diffusion. In addition, as first mentioned in Chapter 2, levels of arterial O_2 and CO_2 each are influenced by each other, by temperature, and by pH. We chose simple dissociation relations for each gas independent from each other. These were computationally easy to use but not as physiologically accurate. To increase complexity we could implement a model such as the implicit relation given in Ottesen *et al.* [80].

Chapter 8

Concluding Remarks

In these studies we have considered the parameterization of several lumped parameter cardiovascular and cardiopulmonary models. In the first study, the 11-compartment model was able to predict arterial blood pressure and cerebral blood flow velocity during postural change from sitting to standing using equations describing passive tension in large arteries, actively regulated tension in the small arteries and veins, and gravitational effects. Model parameters were optimized using the Nelder-Mead simplex method. No methods for parameter space reduction were used which led to inefficient parameter optimization and the potential for non-unique parameters. In a follow-up study we used sensitivity analysis to reduce the 11-compartment model to 7 compartments, and the parameter space from 52 to 22 parameters, producing the same model solution.

In our next study we showed that using subset selection and sensitivity analysis combined with measurements of cerebral blood flow velocity and arterial blood pressure can be used to identify five sensitive, independent model parameters that characterized a simple 5-compartment cardiovascular model. Having a limited number of parameters allowed us to identify two biomarkers that vary between healthy young and elderly groups of subjects: our modeling revealed, as expected, that cerebrovascular resistance and time for peak elastance was higher in healthy aging. While these physiological results were not new they showed that the proposed parameter identification methodology has potential to be applied to clinical studies. This was our first use of the gradient-based Levenberg-Marquardt algorithm for nonlinear parameter optimization.

Our first attempts at including the cerebrovascular response to carbon dioxide were presented in our third study. Our compartmental cardiorespiratory model was designed to

predict arterial blood pressure, cerebral blood flow velocity, and expiratory partial pressure of CO_2 during hyperventilation, CO_2 breathing, and 5% CO_2 rebreathing. Gradient-baed optimization was used to identify baseline parameters for data from two subjects. A piecewise spline was used as a first attempt to characterize the dynamics of the relevant regulation. Physiologically-based equations were proposed for regulatory responses.

As with any mathematical model there are limitations to our methodology. Compartmental models by their construction are spatially homogeneous, therefore we were unable to examine the spatial variability of the state variables. One future approach is developing multiscale model whereby system-level lumped parameter models and multidimensional localized models are combined for a more accurate representation of the physiology. We also did not include an inductor in our model, a common component of compartmental cardiovascular models. This would introduce second-order dynamics such as are seen in the dichrotic notch of the pressure waveform.

More specifically, while we were able to simulate dynamics of the data with our model output, the dynamics of internal states were often not as predicted with regard to the subject's anthropometric data. We should expect that known physiological quantities will be consistent with our models. This is important when analyzing their physiological relevance and viability for clinical use. Cardiac output and associated stroke volume is a clear example of this issue, as we are able to estimate them both for the data and the model output and parameterization affects the model output. We have found that in most cases, optimal parameters for predicting model output also predict simulated cardiac output and stroke volume that are much lower that for the data. Ensuring accurate cardiac output is a possibility for future work.

Finally, we remark that the parameterization methods developed in these studies using subset selection and sensitivity analysis show progress toward addressing issues in large system parameter estimation problems. Expert knowledge of the system is still required for the use of these algorithms, e.g., choosing to fix one of two parameters when a dependence between them is known and one is physiologically more relevant. User intervention is also required when setting numerical tolerances. More refined methodologies for parameter space reduction is another area of future investigation that will be welcomed among physiological modelers.

Bibliography

[1] R Aaslid, K-F Lindegaard, W Sorteberg, and H Nornes. Cerebral autoregulation dynamics in humans. *Stroke*, 20:45–52, 1989.

[2] R Aaslid, TM Markwalder, and H Nornes. Noninvasive transcranial doppler ultrasound recording of flow velocity in basal cerebral arteries. *J Neurosurg*, 57:769–774, 1982.

[3] J Alastruey, KH Parker, J Peiro, SM Byrd, and SJ Sherwin. Modelling the circle of willis to assess the effects of anatomical variations and occlusions on cerebral flows. *J Biomech*, 40(8):1794–1805, 2006.

[4] F Aletti, E Lanzarone, ML Constantino, and G Baselli. Non-linear modulation of total peripheral resistance due to pulsatility: a model study. *Comp Cardiol*, 33:653–656, 2006.

[5] RJ Baker, DD Kozoll, and KA Meyer. The use of surface area as a basis for establishing normal blood volume. *Surg Gynecol Obstet*, 104(2):183–189, 1957.

[6] R Bammer, TA Hope, M Aksoy, and MT Alley. Time-resolved 3d quantitative flow mri of the major intracranial vessels: Initial experience and comparative evaluation at 1.5t and 3.0t in combination with parallel imaging. *Mag Res Med*, 57:127–140, 2007.

[7] H.T. Banks and D. Bortz. A parameter sensitivity methodology in the context of hiv delay equation models. *Journal of Mathematical Biology*, 50(6):607–25, 2005.

[8] JJ Batzel. *Modeling and stability analysis of the human respiratory control system*. PhD thesis, North Carolina State University, 1998.

[9] JJ Batzel, F Kappel, and S Timischl-Teschl. A cardiovascular-respiratory control system model including state delay with application to congestive heart failure in humans. *Journal of Mathematical Biology*, 50(3):293–335, 2005.

[10] J Beneken and B DeWit. A physical approach to hemodynamic aspects of the human cardiovascular system. In E.B. Reeve and A.C. Guyton, editors, *Physical Bases of Circulatory Transport: Regulation and Exchange*, pages 1–45. Saunders, Philadelphia, 1967.

[11] RM Berne and MN Levy. *Physiology*. C.V. Mosby Company, St. Louis, second edition, 1988.

[12] K Bischoff and R Brown. Drug distribution in mammals. *Chemical Engineering Progress Symposium Series*, 62(66):33–45, 1966.

[13] W Boron and E Boulpaep. *Medical physiology*. Elsevier, Philadelphia, 2003.

[14] B Bortz and Nelson P. Sensitivity analysis of nonlinear lumped parameter models of hiv infection dynamics. *Bulletin of Mathematical Biology*, 66(5):1009–1026, 2004.

[15] JF Burnum, JB Hickam, and HD McIntosh. The effect of hypocapnia on arterial blood pressure. *Circulation*, 9:89–95, 1954.

[16] M Burth, GC Verghese, and MV Valerez-Reyes. Subset selection for improved parameter estimation in on-line identification of a synchronous generator. *IEEE Trans Power Systems*, 14:218–225, 1999.

[17] G Carmichael, A Sandu, and F Potra. Sensitivity analysis for atmospheric chemistry models via automatic differentiation. *Atmos Environ*, 31(3):475–489, 1997.

[18] X Chen, L Qi, and K-L Teo. Smooth convex approximation to the maximum eigenvalue function. *Journal of Global Optimization*, 30:253–270, 2004.

[19] T Coleman and A Verma. Admat: An automatic differentiation toolbox for matlab. Technical report, Cornell University, NY, 1998.

[20] ARC Cummin, VI Iyawe, N Mehta, and KB Saunders. Ventilation and cardiac output during the onset of exercise, and during voluntary hyperventilation, in humans. *Journal of Physiology*, 370:567–583, 1986.

[21] M Danielsen. *Modeling of feedback mechanims which control the heart function in a view to implementation in cardiovascular models*. PhD thesis, Roskilde University, Roskilde, Denmark, 1998.

[22] M Danielson and J Ottesen. Describing the pumping heart as a pressure source. *Journal of Theoretical Biology*, 212:71–81, 2001.

[23] T Ebert. Sensitivity of fitness to macro-parameter changes: an analysis of survivorship and individual growth in sea urchin life histories. *Oecologia (Berlin, Germany)*, 65:461–467, 1985.

[24] LM Ellwein, HT Tran, C Zapata, V Novak, and MS Olufsen. Sensitivity analysis and model assessment: Mathematical models for arterial blood flow and blood pressure. *Cardiovasc Eng*, 2008.

[25] M Eslami. *Theory of sensitivity in dynamic systems: an introduction*. Spring-Verlag, Berlin, 1994.

[26] H-H Fan and MCK Khoo. Pneuma a comprehensive cardiorespiratory model. *Eng Med Biol*, 2:1533–1534, 2002.

[27] M Fink. *Open-source automatic differentiation code, http://gosh.gmxhome.de/*, 2007.

[28] M Fink, JJ Batzel, and F Kappel. An optimal control approach to modeling the cardiovascular-respiratory system: an application to orthostatic stress. *Cardiovascular Engineering*, 4(1):27–38, 2004.

[29] AP Fishman, editor. *The respiratory system*, volume 3:II:2 of *Handbook of Physiology*. American Physiological Society, Bethesda, MD, 1983.

[30] L Formaggia, F Nobile, A Quarteroni, and V Alessandro. Multiscale modelling of the circulatory system: a preliminary analysis. *Computing and Visualization in Science*, 2:75–83, 1999.

[31] S Forth and R Ketzscher. High-level interfaces for the mad (matlab automatic differentiation) package. In P Neitaanmäki *et al*, editor, *ECCOMAS 2004: Fourth European Congress on Computational Methods in Applied Sciences and Engineering, European Community on Computational Methods in Applied Sciences*, 2004.

[32] SI Fox. *Human Physiology*. Wm. C. Brown Publishers, Dubuque, IA, fourth edition, 1993.

[33] P Frank. *Introduction to Sensitivity Theory*. Academic Press, New York, 1978.

[34] GH Golub, VC Klema, and GW Stewart. Rank degeneracy and least squares problems. Technical report, Stanford University, Stanford, CA, USA, 1976.

[35] GH Golub and CF Van Loan. *Matrix computations*. The Johns Hopkins University Press, Baltimore, MD, 1989.

[36] A Guyton and J Hall. *Textbook of medical physiology*. WB Saunders, Philadelphia, ninth edition, 1996.

[37] E Hamel. Perivascular nerves and the regulation of cerebrovascular tone. *J Appl Physiol*, 100:1059–1064, 2006.

[38] T Heldt. *Computational models of cardiovascular response to orthostatic stress*. PhD thesis, Massachusetts Institute of Technology, 2004.

[39] T Heldt, E Shim, R Kamm, and R Mark. Computational modeling of cardiovascular response to orthostatic stress. *J Appl Physiol*, 92(3):1239–1254, 2002.

[40] MP Hlastala and AJ Berger. *Physiology of Respiration*. Oxford University Press, Oxford, second edition, 2001.

[41] FC Hoppensteadt and CS Peskin. *Modeling and Simulation in Medicine and the Life Sciences*. Spring-Verlag, New York, 1992.

[42] DT Kaplan, MI Furman, SM Pincus, SM Ryan, LA Lipsitz, and AL Goldberger. Aging and the complexity of cardiovascular dynamics. *Biophys J*, 59(4):945–949, 1991.

[43] F Kappel and R Peer. A mathematical model for fundamental regulation processes in the cardiovascular system. *J Math Biol*, 31:611–631, 1993.

[44] H Kaufmann. Syncope. a neurologist's viewpoint. *Cardiol Clin*, 15:177–194, 1997.

[45] CT Kelley. *Iterative Methods for Optimization*. Society for Industrial and Applied Mathematics, Philadelphia, 1999.

[46] RCP Kerckhoffs, ML Neal, Q Gu, JB Bassingthwaighte, JH Omens, and AD McCulloch. Coupling of a 3d finite element model of cardiac ventricular mechanics to lumped systems models of the systemic and pulmonic circulation. *Annals of Biomedical Engineering*, 35(1):1–18, 2007.

[47] MCK Khoo. A model-based evaluation of the single-breath co2 ventilatory response test. *Journal of Applied Physiology*, 58(1):393–399, 1990.

[48] DS Kimmerly, E Tutungi, TD Wilson, JM Serrador, AW Gelb, RL Hughson, and JJK Shoemaker. Circulation norepinephrine and cerebrovascular control in conscious humans. *Clin Physiol Funct Imaging*, 23:314–319, 2003.

[49] LD Landau and EM Lifshitz. *Fluid Mechanics*. Pergamon, Oxford, UK, 1993.

[50] LA Lipsitz, S Mukai, J Hamner, M Gagnon, and V Babikian. Dynamic regulation of middle cerebral artery blood flow velocity in aging and hypertension. *Stroke*, 31:1897–1903, 2000.

[51] L Loufrani, S Lehoux, A Tedgui, B Lèvy, and D Henrion. Stretch induces mitogen-activated protein kinase activation and myogenic tone through 2 distinct pathways. *Arteriosclerosis, Thrombosis, and Vascular Biology: Journal of the American Heart Association*, 19(12):2878, 1999.

[52] PA Low. Autonomic nervous system function. *J Clin Neurophysiol*, 10:14–27, 1993.

[53] PA Low, editor. *Clinical Autonomic Disorders*. Lippincott-Raven, Philadelphia, 1997.

[54] K Lu, JE Clark, FH Ghorbel, DL Ware, and A Bidani. A human cardiopulmonary system model applied to the analysis of the valsalva maneuver. *Am J Physiol*, 281:H2661–H2679, 2001.

[55] S Middleman. *Transport Phenomena in the Circulatory System*. Wiley-Interscience, New York, 1972.

[56] M Miyazaki. Effect of some respiratory maneuvers on cerebral and peripheral circulation, with special reference to maximum breathing, voluntary hyperventilation, and the valsalva maneuver. *Japanese Circulation Journal*, 37(5):455–460, 1973.

[57] RD Mosteller. Simplified calculation of bsa. *NEJM*, 317:1098, 1987.

[58] R Mukkamala, AT Reisner, HM Hojman, RG Mark, and RJ Cohen. Continuous cardiac output monitoring by peripheral blood pressure waveform analysis. *IEEE Trans Biomed Eng*, 53:459–467, 2006.

[59] JP Mulier. *Ventricular pressure as a function of volume and flow*. PhD thesis, University of Leuven, Belgium, 1994.

[60] S Nadler, J Hidalgo, and T Bloch. Prediction of blood volume in normal human adults. *Surgery*, 51:224–232, 1962.

[61] ML Neal and JB Bassingthwaighte. Subject-specific model estimation of cardiac output and blood volume during hemorrhage. *J Cardiovasc Eng*, 7:97–120, 2007.

[62] JA Nelder and R Mead. A simplex method for function minimization. *Computer Journal*, 7:308–313, 1965.

[63] DW Newell and R Aaslid. *Transcranial Doppler*. Raven Press, New York, 1992.

[64] PC Njemanze. Cerebral circulation dysfunction and hemodynamic abnormalities in syncope during upright tile test. *Can J Caridiol*, 9:238–242, 1993.

[65] A Noordergraaf. *Circulatory system dynamics*. Academic Press, New York, 1978.

[66] V Novak, G Honos, and R Schondorf. Is the heart "empty" at syncope? *J Auton Nerv Syst*, 60:83–92, 1996.

[67] V Novak, K Hu, M Vyas, and LA Lipsitz. Cardiolocomotor coupling in young and elderly people. *Journal of Gerontology A Biol Sci Med Sci*, 62(1):86–92, 2007.

[68] V Novak, P Novak, JM Spies, and PA Low. The autoregulation of cerebral blood flow in orthostatic hypotension. *Stroke*, 29:104–111, 1998.

[69] V Novak, ACC Yang, L Lepicovsky, AL Goldberger LA Lipsitz, and CK Peng. Multimodel pressure-flow method to assess dynamics of cerebral autoregulation in stroke and hypertension. *BioMed Eng Online*, 3:39, 2004.

[70] JB Olansen, JW Clark, D Khoury, FH Ghorbel, and A Bidani. A closed-loop model of the canine cardiovascular system that includes ventricular interaction. *Comp Biomed Res*, 33:260–295, 2000.

[71] MS Olufsen, A Nadim, and L Lipsitz. Dynamics of cerebral blood flow regulation explained using a lumped parameter model. *Am J Physiol Regulatory Integrative Comp Physiol*, 282:R611–R622, 2002.

[72] MS Olufsen, HT Tran, and J Ottesen. Modeling cerebral flood flow control during posture change from sitting to standing. *Journal of Applied Physiology*, 4(1):47–58, 2004.

[73] MS Olufsen, HT Tran, J Ottesen, REU, L Lipsitz, and V Novak. Modeling baroreflex regulation of heart rate during orthostatic stress. *American Journal of Physiology*, 4:R1455–R1368, 2006.

[74] MS Olufsen, HT Tran, JT Ottesen, LM Ellwein, LA Lipsitz, and V Novak. Blood pressure and blood flow variation during postural change from sitting to standing - modeling and experimental validation. *Journal of Applied Physiology*, 99(4):1523–1537, 2005.

[75] K Ono, T Uozumi, C Yoshimoto, and T Kenner. The optimal cardiovascular regulation of the arterial blood pressure. In T Kenner, R Busse, and H Hinghofer-Szalkay, editors, *Cardiovascular System Dynamics: Model and Measurements*, pages 119–139. Plenum, New York, 1997.

[76] SM Otis and EB Ringelstein. The transcranial doppler examination: principles and applications of transcranial doppler sonography. In CH Tegeler, VL Babikian, and CR Gomez, editors, *Neurosonology*, pages 113–128. Mosby, St. Louis, MO, 1996.

[77] J Ottesen. Modeling of the baroreflex-feedback mechanism with time-delay. *Journal of Mathematical Biology*, 36:41–63, 1997.

[78] J Ottesen. Nonlinearity of baroreceptor nerves. *Survey Math Ind*, 7:187–201, 1997.

[79] JT Ottesen and M Danielsen. Modeling ventricular contraction with heart rate changes. *Journal of Theoretical Biology*, 222(3):337–346, 2003.

[80] JT Ottesen, MS Olufsen, and JK Larsen. *Applied Mathematical Models in Human Physiology*. Society of Industrial and Applied Mathematics, Philadelphia, 2004.

[81] JL Palladino and A Noordergraaf. A paradigm for quantifying ventricular contraction. *Cellular and Molecular Biology Letters*, 7(2):331–335, 2002.

[82] RB Panerai, H Coughtrey, JM Rennie, and DH Evans. A model of the instantaneous pressure-velocity relationships of the neonatal circulation. *Physiol Meas*, 14:411–418, 1993.

[83] TA Parklikar, T Heldt, GV Ranade, and GC Verghese. Model-based estimation of cardiac output and total peripheral resistance. *Comp Cardiol*, 34:379–382, 2007.

[84] OB Paulson, S Strandgaard, and L Edvinsson. Cerebral autoregulation. *Cerebrovascular and Brain Metabolism Reviews*, 2:161–192, 1990.

[85] CS Peskin and DM McQueen. A three-dimensional computational method for blood flow in the heart. i. immersed elastic fibers in a viscous incompressible fluid. *Journal of Computational Physics*, 81(2):372–405, 1989.

[86] WH Press, BP Flannery, SA Tenkolsky, and WT Vettering. *Numerical Recipes*. Cambridge University Press, Cambridge, UK, 1986.

[87] T Przybylowski, MF Bangash, K Reichmuth, and M Fisher. Mechanisms of the cerebrovascular response to apnoea in humans. *J Physiol*, 548:323–332, 2003.

[88] A Quarteroni, R Sacco, and F Saleri. *Numerical Mathematics*. Springer, New York, 2000.

[89] H Rabitz, M Kramer, and D Dacol. Sensitivity analysis in chemical kinetics. *Annual review of physical chemistry*, 34:419–461, 1983.

[90] BD Reading and B Freeman. Simple formula for the surface area of the body and a simple model for anthropometry. *Clin Anat*, 18:126–130, 2005.

[91] DM Regen, WC Howe, JT Peterson, and WC Little. Characteristic of single isovolumic left-ventricular pressure waves of dog hearts in situ. *Heart Vessels*, 8:136–148, 1993.

[92] DW Richardson, AJ Wasserman, and Jr. JL Patterson. General and regional circulatory responses to change in blood ph and carbon dioxide tension. *J Clin Invest*, 40(1):31–43, 1960.

[93] V Rideout. *Mathematical and Computer Modeling of Physiological Systems*. Prentice Hall, New Jersey, 1991.

[94] D Robertson, Low PA, and RJ Polinsky. *Primer on the Autonomic Nervous System*. Academic Press, San Diego, 1996.

[95] S Forth S and M Edvall. *User Guide for MAD - a Matlab Automatic Differentiation Toolbox. Version 1.1, the Forward Mode*, 2006.

[96] K Sagawa. The ventricular pressure-volume diagram revisited. *Circulation Research*, 43:677–687, 1978.

[97] CJ Salton, ML Chuang, CJ O'Donnell, MJ Kupka, MG Larson, KV Kissinger, RR Edelman, D Levey, and WJ Manning. Gender differences and normal left ventricular anatomy in an adult population free of hypertension: A cardiovascular magnetic resonance study of the framingham heart study offspring cohort. *J Am College of Cardiol*, 39:1055–1060, 2002.

[98] GS Schroff, JS Janicki, and KT Weber. Left ventricular systolic dynamics in terms of its chamber mechanical properties. *Am J Physiol Heart Circ Physiol*, 14:H110–H124, 1983.

[99] P Segers, HA Leather, P Verdonck, Y-Y Sun, and PF Wouters. Preload-adjusted maximal power of right ventricle: contribution of end-systolic p-v relation intercept. *Am J Physiol Heart Circ Physiol*, 283:1681–1687, 2002.

[100] JM Serrador, PA Picot, BK Rutt, JK Shoemaker, and RL Bondar. Mri measures of middle cerebral artery diameter in conscious human during simulated orthostasis. *Stroke*, 31:1672–1678, 2000.

[101] JT Shepherd and FM Aboud, editors. *The cardiovascular system*. Handbook of Physiology. American Physiological Society, Bethesda, MD, 1983.

[102] T Shishido, K Hayashi, K Shigemi, T Sato, M Sugimachi, and K Sunagawa. Single-beat estimation of end-systolic elastance using bilinearly approximated time-varying elastance curve. *Circulation*, 102:1983–1989, 2000.

[103] JJ Smith and JP Kampine. *Circulatory Physiology – the essentials*. Williams and Wilkins, Baltimore, third edition, 1990.

[104] N Stergiopoulos, J Meister, and N Westerhof. Determinants of stroke volume and systolic and diastolic aortic pressure. *Am J Physiol*, 270:H2050–H2059, 1996.

[105] RE St.John. End-tidal carbon dioxide monitoring. *Crit Care Nurse*, 23(4):83–88, 2003.

[106] J Stocks and PH Quanjer. Reference values for residual volume, functional residual capacity and total lung capacity. *Eur Respir J*, 8:492–506, 1995.

[107] JS Stroud, SA Berger, and D Saloner. Numerical analysis of flow through a severely stenotic carotid artery bifurcation. *Journal of Biomechanical Engineering*, 124(1):9–20, 2002.

[108] H Suga, K Sagawa, and AA Shoukas. Load independence of the instantaneous pressure-volume ratio of the canine left ventricle and effects of epinephrine and heart rate on the ratio. *Circulation Research*, 32:314–322, 1973.

[109] M Ursino. Interaction between carotid baroregulation and the pulsating heart: a mathematical model. *American Journal of Physiology*, 44:H1733–H1747, 1998.

[110] M Velez-Reyes. *Decomposed algorthms for parameter estimation*. PhD thesis, Massachusetts Institute of Technology, 1992.

[111] C Vlachopoulos and M O'Rourke. Diastolic pressure, systolic pressure, or pulse pressure. *Curr Hyperten Rep*, 2:271–279, 2000.

[112] KH Wesseling, JRC Jansen, JJ Settels, and JJ Screuder. Computation of aortic flow from pressure in humans using a nonlinear three-element model. *J Appl Physiol*, 74:2566–2573, 1993.

[113] KH Wesseling, JJ Stettels, G Walstra, HJ Van Esch, and JH Donders. Baromodulation as the cause of short-term blood pressure variability. In G Alberi, Z Bajzer, and P Baxa, editors, *Application of Physics to Medicine and Biology*, pages 247–276. World Scientific, Singapore, 1982.

[114] GB West, JH Brown, and BJ Enquist. A general model for the origin of allometric scaling laws in biology. *Science*, 276(5309):122–126, 1997.

[115] CR White and RS Seymour. Allometric scaling of mammalian metabolism. *J Exp Biol*, 208:1611–1619, 2005.

[116] A Xie, JB Skatrud, R Khayat, J Dempsey, B Morgan, and D Russell. Cerebrovascular response to carbon dioxide in parients with congestive heart failure. *American Journal of Respiratory and Critical Care Medicine*, 172:371–378, 2005.

[117] R Zhang, JH Zuckerman, I Kenichi, TE Wilson, CG Crandall, and BD Levine. Autonomic neural control of dynamic cerebral autoregulation in humans. *Circulation*, 106:1814–1820, 2002.

Appendix A

Appendix A

A.1 Equations, 11-compartment model

A.1.1 State equations

$$
\begin{aligned}
\frac{dp_a(t)}{dt} &= \left(\frac{p_{lv}(t)-p_a(t)}{R_{av}} - \frac{p_a(t)-p_{au}(t)+\rho g h_u}{R_{au}} - \frac{p_a(t)-p_{ac}(t)+\rho g h_c}{R_{ac}} - \frac{p_a(t)-p_{af}(t)}{R_{af}}\right)/C_a \\
\frac{dp_{au}(t)}{dt} &= \left(\frac{p_a(t)-p_{au}(t)}{R_{au}} - \frac{p_{au}(t)-p_{al}(t)-\rho g h_u+\rho g h_l}{R_{al}} - \frac{p_{au}(t)-p_{vu}(t)}{R_{aup}}\right)/C_{au} \\
\frac{dp_{al}(t)}{dt} &= \left(\frac{p_{au}(t)-p_{al}(t)-\rho g h_u+\rho g h_l}{R_{al}} - \frac{p_{al}(t)-p_{vl}(t)}{R_{alp}}\right)/C_{al} \\
\frac{dp_{af}(t)}{dt} &= \left(\frac{p_a(t)-p_{af}(t)}{R_{af}} - \frac{p_{af}(t)-p_v(t)}{R_{afp}}\right)/C_{af} \\
\frac{dp_{ac}(t)}{dt} &= \left(\frac{p_a(t)-p_{ac}(t)+\rho g h_c}{R_{ac}} - \frac{p_{ac}(t)-p_{vc}(t)}{R_{acp}}\right)/C_{ac} \\
\frac{dp_v(t)}{dt} &= \left(\frac{p_{vu}(t)-p_v(t)-\rho g h_u}{R_{vu}} + \frac{p_{vc}(t)-p_v(t)-\rho g h_c}{R_{vc}} + \frac{p_{af}(t)-p_v(t)}{R_{afp}} - \frac{p_v(t)-p_{la}(t)}{R_v}\right)/C_v \\
\frac{dp_{vu}(t)}{dt} &= \left(\frac{p_{vl}(t)-p_{vu}(t)-\rho g h_l+\rho g h_u}{R_{vl}} + \frac{p_{au}(t)-p_{vu}(t)}{R_{aup}} - \frac{p_{vu}(t)-p_v(t)-\rho g h_u}{R_{vu}}\right)/C_{vu} \\
\frac{dp_{vl}(t)}{dt} &= \left(\frac{p_{al}(t)-p_{vl}(t)}{R_{alp}} - \frac{p_{vl}(t)-p_{vu}(t)-\rho g h_l+\rho g h_u}{R_{vl}}\right)/C_{vl} \\
\frac{dp_{vc}(t)}{dt} &= \left(\frac{p_{ac}(t)-p_{vc}(t)}{R_{acp}} - \frac{p_{vc}(t)-p_v(t)-\rho g h_c}{R_{vc}}\right)/C_{vc} \\
\frac{dV_{lv}(t)}{dt} &= \frac{p_{la}(t)-p_{lv}(t)}{R_{mv}(t)} - \frac{p_{lv}(t)-p_a(t)}{R_{av}(t)} \\
\frac{dV_{la}(t)}{dt} &= \frac{p_v(t)-p_{la}(t)}{R_v} - \frac{p_{la}(t)-p_{lv}(t)}{R_{mv}(t)}
\end{aligned}
$$

Parameters include R_i [mmHg·s/ml], C_i [ml/mmHg].

Constants include $\rho = 1.055$ [g/ml], $g = 981$ [cm/s^2], $h_i = 0$ [cm] during sitting.

A.1.2 Valve equations, R_{av}, R_{mv}, and R_{vu} [mmHg·s/ml]

$$
\begin{aligned}
R_{av} &= min(R_{av,open} + e^{(-10(p_{lv}-p_a))}, 5000) \\
R_{mv} &= min(R_{mv,open} + e^{(-10(p_{la}-p_{lv}))}, 5000) \\
R_{vu} &= min(R_{vu,open} + e^{(-10(p_{vu}-p_v))}, 5000)
\end{aligned}
$$

A.1.3 Heart equations, left ventricle and atrium

Ventricle

$$
\begin{aligned}
p_{lv}(t) &= a_v(V_{lv}(t) - b_v)^2 + (c_v V_{lv}(t) - d_v) f_v(t) \\
f_v(t) &= \begin{cases} p_{pv}(H) \dfrac{\tilde{t}^n (\beta_v(H) - \tilde{t})^{m_v}}{n_v^{n_v} m_v^{m_v} [(\beta_v(H))/(m_v + n_v)]^{m_v+n_v}} & 0 \le \tilde{t} \le \beta_v(H) \\ 0 & \beta_v(H) < \tilde{t} \le T \end{cases} \\
\tilde{t} &= \mathrm{mod}(t, T) \\
t_{pv} &= (t_{max,v} - t_{min,v}) \frac{\theta_v^{\nu_v}}{H^{\nu_v} + \theta_v^{\nu_v}} + t_{min,v} \\
p_{pv} &= (p_{max,v} - p_{min,v}) \frac{H^{\eta_v}}{H^{\eta_v} + \phi_v^{\eta_v}} + p_{min,v} \\
\beta_v(H) &= \frac{n_v + m_v}{n_v} t_{pv}(H)
\end{aligned}
$$

Atrium

$$
\begin{aligned}
p_{la}(t) &= a_a(V_{la}(t) - b_a)^2 + (c_a V_{la}(t) - d_a) f_a(t) \\
f_a(t) &= \begin{cases} p_{pa}(H) \dfrac{\tilde{t}^n (\beta_a(H) - \tilde{t})^{m_v}}{n_a^{n_a} m_a^{m_a} [(\beta_a(H))/(m_a + n_a)]^{m_a + n_a}} & 0 \le \tilde{t} \le \beta_a(H) \\ 0 & \beta_a(H) < \tilde{t} \le T \end{cases} \\
\tilde{t} &= \mathrm{mod}(t, T) \\
t_{pa} &= (t_{max,a} - t_{min,a}) \frac{\theta_a^{\nu_a}}{H^{\nu_a} + \theta_a^{\nu_a}} + t_{min,a} \\
p_{pa} &= (p_{max,a} - p_{min,a}) \frac{H^{\eta_a}}{H^{\eta_a} + \phi_a^{\eta_a}} + p_{min,a} \\
\beta_a(H) &= \frac{n_a + m_a}{n_a} t_{pa}(H)
\end{aligned}
$$

Parameters include a_i [mmHg/ml^2], b_i [ml], c_i [mmHg/ml], d_i [mmHg],
n_i, m_i, θ_i [1/s], ϕ_i [1/s], η_i, ν_i,
$t_{diff,i}$ [s], $t_{min,i}$ [s], $p_{diff,i}$, $p_{min,i}$
where $t_{diff,i} = t_{max,i} - t_{min,i}, p_{diff,i} = p_{max,i} - p_{min,i}$.

H is extracted from the data.

A.2 Equations, 7-Compartment Model

A.2.1 State equations

$$
\begin{aligned}
\frac{dp_a}{dt} &= \left(\frac{p_{lv}-p_a}{R_{av}} - \frac{p_a-p_{as}}{R_{as}} - \frac{p_a-p_{ac}}{R_{ac}}\right)/C_a \\
\frac{dp_v}{dt} &= \left(\frac{p_{vs}-p_v}{R_{vs}} + \frac{p_{vc}-p_v}{R_{vc}} - \frac{p_v-p_{lv}}{R_{mv}}\right)/C_v \\
\frac{dp_{as}}{dt} &= \left(\frac{p_a-p_{as}}{R_{as}} - \frac{p_{as}-p_{vs}}{R_{asp}}\right)/C_{as} \\
\frac{dp_{vs}}{dt} &= \left(\frac{p_{as}-p_{vs}}{R_{asp}} - \frac{p_{vs}-p_v}{R_{vs}}\right)/C_{vs} \\
\frac{dp_{ac}}{dt} &= \left(\frac{p_a-p_{ac}}{R_{ac}} - \frac{p_{ac}-p_{vc}}{R_{acp}}\right)/C_{ac} \\
\frac{dp_{vc}}{dt} &= \left(\frac{p_{ac}-p_{vc}}{R_{acp}} - \frac{p_{vc}-p_v}{R_{vc}}\right)/C_{vc} \\
\frac{dV_{lv}}{dt} &= \frac{p_v-p_{lv}}{R_{mv}} - \frac{p_{lv}-p_a}{R_{av}}
\end{aligned}
$$

Parameters include R_i [mmHg·s/ml], C_i [ml/mmHg].

A.2.2 Valve equations, R_{av} and R_{mv} [mmHg·s/ml]

$$
\begin{aligned}
R_{mv} &= \min(R_{mv,open} + e^{(-2(p_v-p_{lv}))}, 20) \\
R_{av} &= \min(R_{av,open} + e^{(-2(p_{lv}-p_a))}, 20)
\end{aligned}
$$

A.2.3 Heart equations, left ventricle

See Appendix A.1.3

A.3 Equations, Cardiorespiratory Model

A.3.1 Cardiovascular equations

$$
\begin{aligned}
\frac{dp_{ap}}{dt} &= \left(\frac{p_{rv}-p_{ap}}{R_{ap}} - \frac{p_{ap}-p_{vp}}{R_{pv}}\right)/C_{ap} \\
\frac{dp_{vp}}{dt} &= \left(\frac{p_{ap}-p_{vp}}{R_{p}} - \frac{p_{vp}-p_{lv}}{R_{mv}}\right)/C_{vp} \\
\frac{dp_{a}}{dt} &= \left(\frac{p_{lv}-p_{a}}{R_{av}} - \frac{p_{a}-p_{ac}}{R_{ac}} - \frac{p_{a}-p_{as}}{R_{as}}\right)/C_{a} \\
\frac{dp_{v}}{dt} &= \left(\frac{p_{vc}-p_{v}}{R_{vc}} + \frac{p_{vs}-p_{v}}{R_{vs}} - \frac{p_{v}-p_{rv}}{R_{tv}}\right)/C_{v} \\
\frac{dp_{ac}}{dt} &= \left(\frac{p_{a}-p_{ac}}{R_{ac}} - \frac{p_{ac}-p_{vc}}{R_{c}}\right)/C_{ac} \\
\frac{dp_{vc}}{dt} &= \left(\frac{p_{ac}-p_{vc}}{R_{c}} - \frac{p_{vc}-p_{v}}{R_{vc}}\right)/C_{vc} \\
\frac{dp_{as}}{dt} &= \left(\frac{p_{a}-p_{as}}{R_{as}} - \frac{p_{as}-p_{va}}{R_{s}}\right)/C_{as} \\
\frac{dp_{vs}}{dt} &= \left(\frac{p_{as}-p_{vs}}{R_{s}} - \frac{p_{vs}-p_{v}}{R_{vs}}\right)/C_{vs} \\
\frac{dV_{lv}}{dt} &= \frac{p_{vp}-p_{lv}}{R_{vp}} - \frac{p_{lv}-p_{a}}{R_{a}} \\
\frac{dV_{rv}}{dt} &= \frac{p_{v}-p_{rv}}{R_{v}} - \frac{p_{rv}-p_{ap}}{R_{ap}}
\end{aligned}
$$

A.3.2 Respiratory equations

Inspiration equations

$$
\begin{aligned}
V_{D1}\frac{dp_{D1,CO2}}{dt} &= \dot{V}_{ie}(p_{i,CO_2} - p_{D1,CO_2}) \\
V_{D1}\frac{dp_{D1,O2}}{dt} &= \dot{V}_{ie}(p_{i,O_2} - p_{D1,O_2}) \\
V_{D2}\frac{dp_{D2,CO2}}{dt} &= \dot{V}_{ie}(p_{D1,CO_2} - p_{D2,CO_2}) \\
V_{D2}\frac{dp_{D2,O2}}{dt} &= \dot{V}_{ie}(p_{D1,O_2} - p_{D2,O_2}) \\
V_{D3}\frac{dp_{D3,CO2}}{dt} &= \dot{V}_{ie}(p_{D2,CO_2} - p_{D3,CO_2}) \\
V_{D3}\frac{dp_{D3,O2}}{dt} &= \dot{V}_{ie}(p_{D2,O_2} - p_{D3,O_2}) \\
V_{A}\frac{dp_{a,CO_2}}{dt} &= 863 \cdot 0.98 \cdot q_p(c_{v,CO_2} - c_{a,CO_2}) + \dot{V}_{ie}(p_{D3,CO_2} - p_{a,CO2}) \\
V_{A}\frac{dp_{a,O_2}}{dt} &= 863 \cdot 0.98 \cdot q_p(c_{v,O_2} - c_{a,O_2}) + \dot{V}_{ie}(p_{D3,O_2} - p_{a,O_2}) \\
V_{S,CO_2}\frac{dc_{S,CO_2}}{dt} &= M_{S,CO_2} + q_s(c_{a,CO_2} - c_{S,CO_2}) \\
V_{S,O_2}\frac{dc_{S,O_2}}{dt} &= -M_{S,O_2} + q_s(c_{a,O_2} - c_{S,O_2}) \\
V_{B,CO_2}\frac{dc_{B,CO_2}}{dt} &= M_{B,CO_2} + q_c(c_{a,CO_2} - c_{B,CO_2}) \\
V_{B,O_2}\frac{dc_{B,O_2}}{dt} &= -M_{B,O_2} + q_c(c_{a,O_2} - c_{B,O_2}) \\
V_{tube,CO_2}\frac{dp_{tube,CO_2}}{dt} &= \dot{V}_{ie}(p_{R,CO_2} - p_{tube,CO_2}) \\
V_{tube,O_2}\frac{dp_{tube,O_2}}{dt} &= \dot{V}_{ie}(p_{R,O_2} - p_{tube,O_2}) \\
V_{R,CO_2}\frac{dp_{R,CO_2}}{dt} &= 0 \\
V_{R,O_2}\frac{dp_{R,O_2}}{dt} &= 0
\end{aligned}
$$

Expiration equations

$$
\begin{aligned}
V_{D1}\frac{dp_{D1,CO2}}{dt} &= \dot{V}_{ie}(p_{D1,CO2} - p_{a,CO2}) \\
V_{D1}\frac{dp_{D1,O2}}{dt} &= \dot{V}_{ie}(p_{D1,O2} - p_{a,O2}) \\
V_{D2}\frac{dp_{D2,CO2}}{dt} &= \dot{V}_{ie}(p_{D2,CO2} - p_{D1,CO2}) \\
V_{D2}\frac{dp_{D2,O2}}{dt} &= \dot{V}_{ie}(p_{D2,O2} - p_{D1,O2}) \\
V_{D3}\frac{dp_{D3,CO2}}{dt} &= \dot{V}_{ie}(p_{D3,CO2} - p_{D2,CO2}) \\
V_{D3}\frac{dp_{D3,O2}}{dt} &= \dot{V}_{ie}(p_{D3,O2} - p_{D2,O2}) \\
V_{A}\frac{dp_{a,CO2}}{dt} &= 863 \cdot 0.98 \cdot q_p(c_{v,CO2} - c_{a,CO2}) \\
V_{A}\frac{dp_{a,O2}}{dt} &= 863 \cdot 0.98 \cdot q_p(c_{v,O2} - c_{a,O2}) \\
V_{S,CO2}\frac{dc_{S,CO2}}{dt} &= M_{S,CO2} + q_s(c_{a,CO2} - c_{S,CO2}) \\
V_{S,O2}\frac{dc_{S,O2}}{dt} &= -M_{S,O2} + q_s(c_{a,O2} - c_{S,O2}) \\
V_{B,CO2}\frac{dc_{B,CO2}}{dt} &= M_{B,CO2} + q_c(c_{a,CO2} - c_{B,CO2}) \\
V_{B,O2}\frac{dc_{B,O2}}{dt} &= -M_{B,O2} + q_c(c_{a,O2} - c_{B,O2}) \\
V_{tube,CO_2}\frac{dp_{tube,CO_2}}{dt} &= \dot{V}_{ie}(p_{tube,CO_2} - p_{D_1,CO_2}) \\
V_{tube,O_2}\frac{dp_{tube,O_2}}{dt} &= \dot{V}_{ie}(p_{tube,O_2} - p_{D_1,O_2}) \\
V_{R,CO_2}\frac{dp_{R,CO_2}}{dt} &= \dot{V}_{ie}(p_{R,CO_2} - p_{tube,CO_2}) \\
V_{R,O_2}\frac{dp_{R,O_2}}{dt} &= \dot{V}_{ie}(p_{R,O_2} - p_{tube,O_2})
\end{aligned}
$$

Respiratory parameters include $M_{i,g}$ [ml/s], V_i [ml], $V_{i,g}$ [ml].

$\dot{V}_{IE}$ is extracted from data.